Investigating Interfaces between Heterogeneous Catalysts and Metal-Organic Frameworks for Catalytic Selectivity Control

Wei-Shang Lo

A dissertation

submitted to the Faculty of

the department of Chemistry

in partial fulfillment

of the requirements for the degree of

Doctor of Philosophy

Boston College
Morrissey College of Arts and Sciences
Graduate School

August 2022

Investigating Interfaces between Heterogeneous Catalysts and Metal-Organic Frameworks for Catalytic Selectivity Control

Wei-Shang Lo

Advisor: Professors Matthias M. Waegele and Chia-Kuang Tsung

ABSTRACT

Depositing metal-organic frameworks (MOFs) on the surfaces of metal nanoparticles (NPs) to enhance catalytic selectivity has recently attracted great attention; however, a solid understanding of how the NP-MOF interface promotes catalytic selectivity is lacking. In this thesis, we have conducted three fundamental studies and further applied the knowledge to other types of catalysts using enzymes. The first part of this thesis focuses on understanding the NP-MOF interfacial structures and their impact on catalytic performance. We have systematically probed the NP-MOF interface generated by three commonly used approaches by IR and Raman spectroscopy. We have revealed significant differences in interfacial chemical interactions between them, and have found that these differences in interfacial structure dramatically impact selectivity. For example, the interface generated by the coating approach contains trapped capping agents. This trapped capping agent reduces crotyl alcohol selectivity for the hydrogenation of crotonaldehyde.

The second part of this thesis focuses on addressing the trapped capping agents at the NP-MOF interface. We developed an approach to creating a direct NP-MOF interface by utilizing weakly adsorbed capping agents during the MOF coating process. Their dynamic nature allows for their gradual dissociation from the NP surface with the assistance of the organic MOF linkers. Thus, direct chemical interactions can be built between NP and MOF, generating a clean and well-defined interface. Direct evidence on capping agent dissociation and formation of chemical interactions was obtained by Raman and IR spectroscopy. Combined with transmission electron

microscopy and X-ray diffraction, we have revealed the relative orientation and facet alignment at the NP-MOF interface.

The third part of this thesis investigates how various MOF components affect the selectivity of hydrogenation reactions catalyzed at the MOF-NP interface. We found that the replacement of Zr-oxo nodes with Ce-oxo nodes yields the highest selectivity for cinnamyl alcohol (~87%), whereas the functionalization of the terephthalic acid linker with -OH, CH_3, $-NO_2$ and NH_2 groups only moderately modulates the selectivity relative to the Zr-UiO-66 (~58%). Reaction kinetics studies demonstrate that coating Pt NPs with Ce-UiO-66 increases the rate of C=O hydrogenation, which infrared spectroscopic observations suggest is due to the interaction of the C=O group with the Ce-oxo node. This work highlights the critical role of metal-oxo nodes in regulating the catalytic selectivity of metal NPs in specific reactions.

The fourth part of this thesis extends the interface control to other catalysts involving enzymes. We compared the interfacial interactions of catalase in solid and hollow MOF microcrystals. The solid sample with confined catalase was prepared through a reported method. The hollow sample was generated by hollowing the MOFs crystal, sealing freestanding enzymes in the central cavities of the hollow MOF. By monitoring this hollowing process, we observed that the enzymes gradually changed from a confined form to a freestanding form. The freestanding enzymes in the hollow MOFs show higher activity in the decomposition of hydrogen peroxide, attributed to their lesser chemical interactions and confinement. This study highlights the importance of the freestanding state for the biological function of encapsulated enzymes. Taken together, the four sections in this thesis establish design rules for refining MOF-based catalyst design.

Table of Contents

List of Figures

List of Tables

Acknowledgment

I want to foremost acknowledge my advisor, Prof. Chia-Kuang (Frank) Tsung. Frank was a passionate scientist and a great mentor. Thank you for guiding me to tackle challenges from every angle, and we will pass on your legacy into the future. I am grateful to Prof. Matthias M. Waegele for allowing me to learn from his team on vibrational spectroscopy, and for endless support after Frank's passing. I wish to thank a number of mentors from Boston College. Thank you to Prof. Dunwei Wang and Prof. Udayan Mohanty for serving on my committee and giving me valuable suggestions. I want to thank the members of the Tsung group for making my life enjoyable: Dr. Xiaoyuan Liu, Dr. Allison P. Young, Dr. Zhehui Li, Dr. Benjamin P. Williams, Dr. Yang Li, Dr. Furui Zhang, Mr. Chenhao Ren, Mr. Adam Bensalah, Mr. Banruo Li, and Mr. Connor Gallacher. I find memories working with Waegele's group members. especially with Dr. Charuni M. Gunathunge, Dr. Jingyi Li, and Dr. Xiang Li. I thank all of our collaborators around the world: Prof. Wenyu Huang, Prof. Xingyi Ling, Prof. Hiang Kwee Lee, Prof. Omar K. Farha, Prof. SonBinh T. Nguyen, Prof. Lien-Yang Chou, Prof. Hsiao-Ching Yang, Prof. Fa-Kuen Shieh, Prof. Li Li, and Prof. Hao Pei. I want to acknowledge the funding support from Boston College and National Science Foundation. I want to acknowledge the following people from the chemistry department who gave me guidance throughout my graduate career: Prof. Kenneth R. Metz, Prof. Lynne A. O'Connell, Prof. Daniel Fox, Prof. Jianmin Gao, Dr. Ian B. Parr, Mrs. Dale L. Mahoney, and Mrs. Lynne Pflaumer. I thank the many friends I have made in Shanghai and Boston for catalyzing my life. Finally, I want to express my heartfelt thanks to my parents, 羅振全 and 彭美惠, and my sisters 羅千雅 and 羅佩佩 for their continuous support and encouragement. Thank you all for your support.

This page is on purposely left in blank

1.0 Chapter 1:

Introduction

1.1 Thesis Goal and Outline

The central theme of the thesis focuses on improving heterogeneous catalysts (**Figure 1.1**). Specifically, we aim to design metal nanoparticle (NP) composite catalysts with high catalytic selectivity. Our strategy is to introduce microenvironment control around catalyst active sites by coating them with geometrically and chemically ordered materials, namely metal-organic frameworks (MOFs). While this strategy is promising, the development of efficient MOF-based heterogeneous catalysts remains at the trial-and-error stage instead of following rational design. This bottleneck stems from a lack of understanding of how to control complicated hybrid interfaces between metal catalysts and MOFs. To fill this knowledge gap, we have conducted three fundamental studies, including (1) developing a spectroscopic protocol to study complicated hybrid interfaces,[1] (2) designing synthetic tools to control interfaces,[2] and (3) revealing the critical components of the MOFs design to promote selectivity on metal catalysts. By collaborating with researchers from different disciplines, we have applied this understanding to molecular catalysts and biomolecules. [3]

This dissertation is organized into eight chapters. **Chapter 1** is a background review of heterogeneous catalysis, metal NPs, and MOFs. **Chapter 2** describes the impact of the NP-MOF interface on the selectivity control, and we observed that trapped capping agents reduce the crotyl alcohol selectivity for the hydrogenation of crotonaldehyde. **Chapter 3** address the issue of trapped capping agents by using weakly adsorbed capping agents, generating a clean and well-defined NP-MOF interface. **Chapter 4** reveals that preferential activation from inorganic MOF

clusters is critical to achieving high selectivity. Meanwhile, we have developed a directional engraving process to realize the hierarchical control in the MOF microcrystals. By using the hierarchical control in the MOF microcrystals, **Chapter 5** demonstrates that chemical interactions between enzymes and MOFs are critical for maintaining the biological functions of encapsulated enzymes. **Chapter 6** summarizes achievements in this dissertation and the future directions.

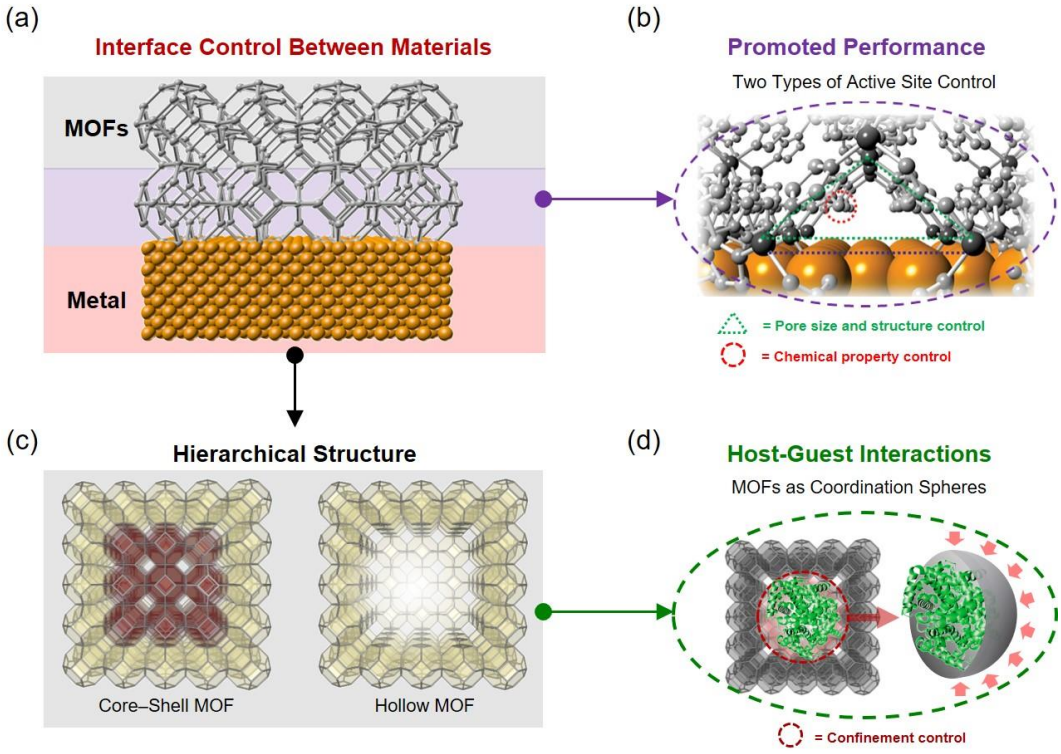

Figure 1.1: Overview of the research achievements from this thesis: (a, b) controlling the interface between metal NPs and MOFs to promote catalytic selectivity, (c) designing MOF structures to realize the hierarchical control in the MOF microcrystals, and (d) tuning the host-guest interactions to direct catalytic behaviors of biomolecules.

1.2 Developments in Heterogeneous Catalysis

Catalysis is at the center of our society, and nearly all commercial products require the use of catalysts during manufacture.[4] One of the earliest catalytic processes is the fermentation of sugar to produce alcohol which has been in use for thousands of years. Although many catalytic processes have been known from the beginning of human history, the term "catalysis" was only proposed in recent decades (1835, by Jöns Jacob Berzelius).[5] A heterogeneous catalytic process involves more than one phase.[6] In this case, the state of heterogeneous catalysts is usually solid, and the reactants are in the gas or liquid phase. Because of the solid nature of heterogeneous catalysts, they can be recycled with ease, generating less chemical waste. [7] With this advantage in hand, the process development in industry began to study heterogeneous catalysts. Since that, a series of key milestones in heterogeneous catalysis has been developed.[8] For example, the catalytic hydrogenation by the Ni-based heterogeneous catalyst was invented by Paul Sabatier, who was awarded the Nobel Prize in Chemistry in 1912.[9] Fritz Haber and Carl Bosch were awarded the Nobel Prize in Chemistry in 1918 for the development of ammonia synthesis.[10] By focusing on the molecular-level picture, several key breakthroughs have been made in catalyst design, characterization, and the associated mechanisms. For example, Hugh Taylor introduced the term "active site" in the 1920s, establishing the concept that distinct sites on a catalyst are responsible for chemical reactions.[11] Later in the mid-1920s, scientists disclosed the theory of chemical kinetics and the associated mechanisms (*Details on the historical development of kinetic in relation to catalysis can be found in "Fifty Years of Chemical Kineticists" by Hugh Taylor*). It is worth pointing out that Langmuir's concept of fixed intermediates on active sites became particularly important because it allowed a first quantitative analysis of the possible mechanism.[12]

Building on these milestones, a general picture of heterogeneous catalysis began to form: (1) reactants must be transported to the catalyst surface where at least one reactant chemisorbs, (2) the intermediates react to give adsorbed products, and then (3) products desorb and leave away from the catalyst (**Figure 1.2**). With this picture in mind, researchers began to collect more molecule-level information.[13] For example, developing single-crystal model systems to study complex issues of catalysis,[14] building an *operando* setup to monitor the reaction,[15] and establishing computational methods to characterize the transition states of reactions.[16] All of these efforts build the fundamental frameworks of heterogeneous catalysis, making it possible to develop catalysts with high catalytic performance.

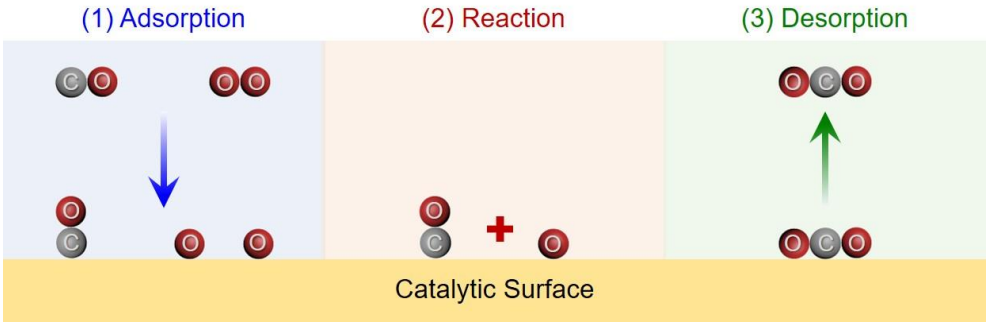

Figure 1.2: Schematic illustration of heterogeneous catalysis. The reaction cycle of catalytic oxidation of CO by O_2 was used as the demonstration. (grey spheres represent carbon atoms and red spheres represent oxygen atoms.)

1.3 Challenges in Heterogeneous Catalysis

Heterogeneous catalysis provides access to many chemicals, materials, and fuels needed for modern society. For example, platinum-tin catalysts are active and selective for propane dehydrogenation to produce propylene,[17-18] which can be further converted into value-added materials, such as polypropylene, propylene oxide, and acrylonitrile.[19] Promoting the catalytic reactivity and selectivity to desired products has been the primary focus in the field. One of the

challenges in heterogeneous catalysis is to reduce the cost while increasing the activity and selectivity of catalysts. For example, the total value of platinum group metals (PGMs, Pt, Pd, Rh etc.) claimed from used catalytic converters was $3 billion in 2010.[20] Although finding other transition metal catalysts with a lower cost could address the problem, the high catalytic activity and selectivity could be significantly compromised. Therefore, a major focus in catalyst design is to achieve the same activity and selectivity with a smaller amount of PGMs. For example, the Department of Energy launched the "*Basic Research Needs for Synthesis Science*" in 2021.[21] To reach this goal, a fundamental understanding of promoting the catalytic activity and selectivity of active sites in heterogeneous catalysts is crucial.

One approach to promote the catalytic activity and selectivity of active sites is by introducing modifiers.[22] Modifiers could interact with the active sites, and influence the catalytic performance. In the following section, we discuss the developments of modifiers.

1.4 Developments in Using Modifiers to Promote Catalytic Performance

Applying modifiers on active sites of metal surfaces can tailor the surface environment and influence catalytic performance.[22] One of the earliest examples is the Lindlar catalyst, developed by Herbert Lindlar in 1952, for selective hydrogenations of alkynes.[23] By introducing organic (e.g., quinoline) and inorganic (e.g., lead, Pb) modifiers on a palladium/$CaCO_3$, the hydrogenation of alkynes to undesirable alkanes can be greatly suppressed, resulting in high selectivity to alkenes (around 85.0 % at full conversion). Owing to the high selectivity to alkenes, the Lindlar catalyst has been one of the most widely studied catalysts. Kinetic studies found that the selectivity profiles are greatly influenced by the relative population of alkyne and alkene groups.[23] The mechanistic study suggests that modifiers alter the electronic structures of Pd sites and hinder the formation of

Pd hydride for hydrogenation.[24-25] Inspired by the mechanistic picture of the Lindlar catalyst, a number of surface modifications have been developed. In the following section, we discuss approaches utilizing metal oxides and organic ligands to enhance the catalytic performance of metal NPs.

1.5 Inorganic Modifiers of Metal Oxides

Supporting metal NPs on inorganic modifiers of metal oxides could generate new interfaces between metal surfaces and oxide supports. Depending on the interfacial interactions and structures, such metal/metal oxide interfaces can have a profound impact on the catalytic performance of the metal NPs.[26] In the following discussion, we focus on how metal-support interfaces promote catalytic stability, reactivity, and selectivity (**Figure 1.3**).

Firstly, supporting small metal NPs on metal oxides can stabilize catalytic performance by preventing the sintering of metal NPs (**Figure 1.3a**). For example, in ammonia synthesis, the Fe-based catalysts greatly degrade over time because the catalyst reconstructs to crystallite iron oxide particles (Fe_2O_3).[27] Supporting Fe-based catalysts on alumina (Al_2O_3) could prevent catalyst reconstruction, improving the catalytic stability. Secondly, the metal/metal oxide interfaces can change the electronic structure of active sites. The change in electronic structure can influence the adsorption of intermediates, optimizing the energy landscape of the reaction (**Figure 1.3b**). For example, in CO oxidation, supporting Au NPs on titanium oxide (TiO_2) can facilitate electron transfer at the Au-TiO_2 interface.[28] The electron transfer from TiO_2 to the active sites of Au NPs can promote O_2 activation in the CO oxidation reaction, enhancing the catalytic performance.

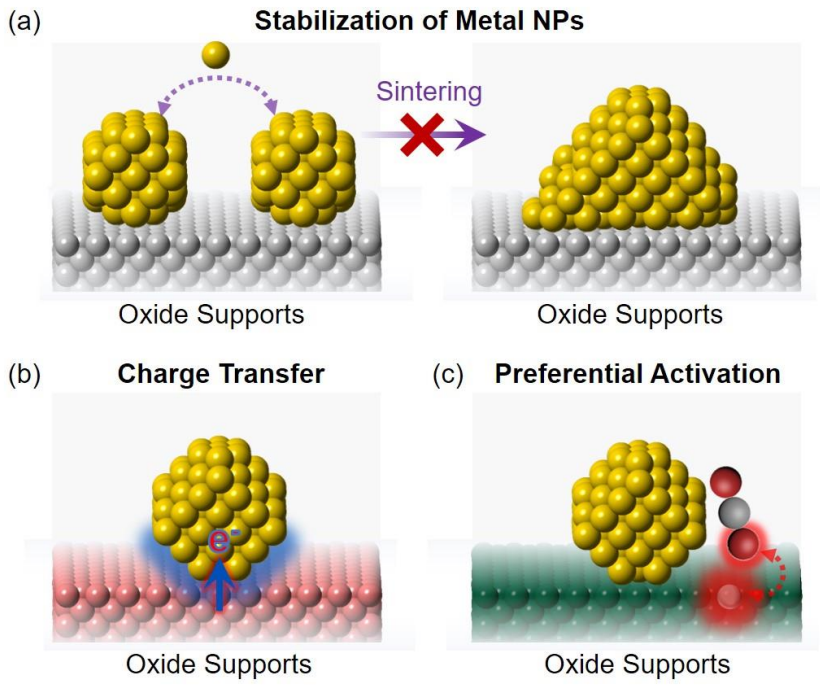

Figure 1.3: Schematic illustration of using metal/metal oxide interfaces to (a) prevent the metal NPs from sintering, (b) transfer charge to alter electronic properties of metal NPs, and (c) preferentially activate a specific chemical bond in intermediates.

Thirdly, the Lewis acidic nature of metal oxides at metal-support interfaces can activate a specific bond in reactants (**Figure 1.3c**). The preferential activation of chemical bonds from metal oxides are thought to promote the catalytic selectivity of a specific product. For example, in CO_2 hydrogenation, zirconium oxides and cerium oxides have been proposed to activate CO_2 to form formate and methoxide intermediates, enhancing the selectivity to methanol (**Figure 1.4a**).[29-30] Furthermore, tuning the Lewis acid strength of metal oxides from Zr to Ti and Nb could promote methanol formation rates and selectivities (**Figure 1.4b**).[31-32] The same concept has been also applied to other catalytic reactions such as the selective hydrogenation of nitroaromatics by Pt NP supported on $Fe(OH)_x$ catalysts.[33]

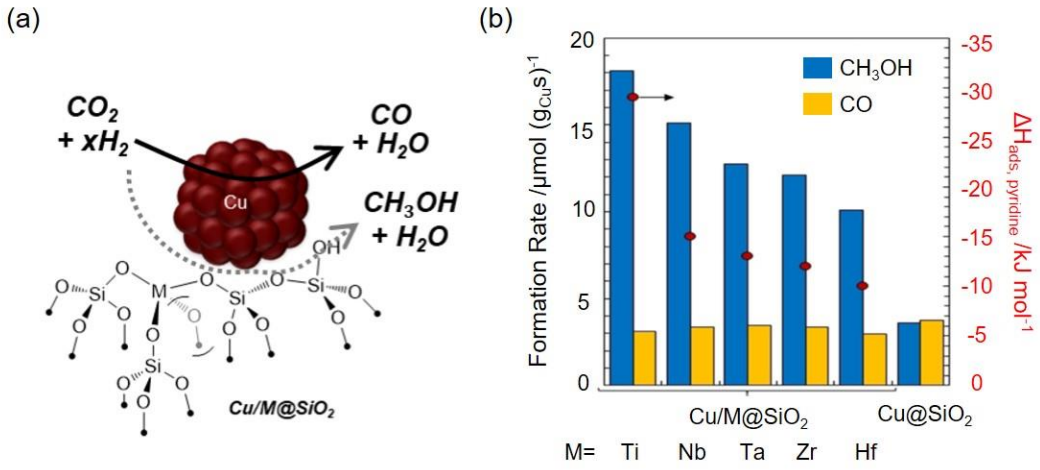

Figure 1.4: (a) Scheme of site requirements for CO_2 hydrogenation pathways. CO is formed on the same site as Cu/SiO_2 (indicated by the black arrow) and CH_3OH is formed on a Cu-M interfacial site (indicated by the grey dashed arrow). (b) The product formation rate of CO_2 hydrogenation and enthalpies of pyridine adsorption. Figure adapted from ref. [31].

In addition to metal oxides, alkaline cations can also serve as inorganic modifiers to promote catalytic performance. Alkali cation can alter the electronic structure of active sites and influence the bonding of intermediates.[34] For example, in ammonia synthesis, potassium ion (K^+) could greatly enhance ammonia productivity. The alkaline cations at active sites may weaken the bonding of the NH_3 product at active sites, allowing the product to desorb with ease.

1.6 Organic Modifiers of Organic Ligands

Organic modifiers can be present in several kinds of forms including polymers, dendrimers, and ligands. Because polymers and dendrimers are built from ligands, the following discussion will mainly focus on using organic ligands as modifiers to promote the catalytic performance of metal NPs. Similar to inorganic modifiers, putting organic ligands on the surface of metal NPs could

generate new interfaces between metal surfaces and organic ligands. Here, we focus on how metal-ligand interfaces promote chemoselectivity and enantioselectivity (**Figure 1.5**).

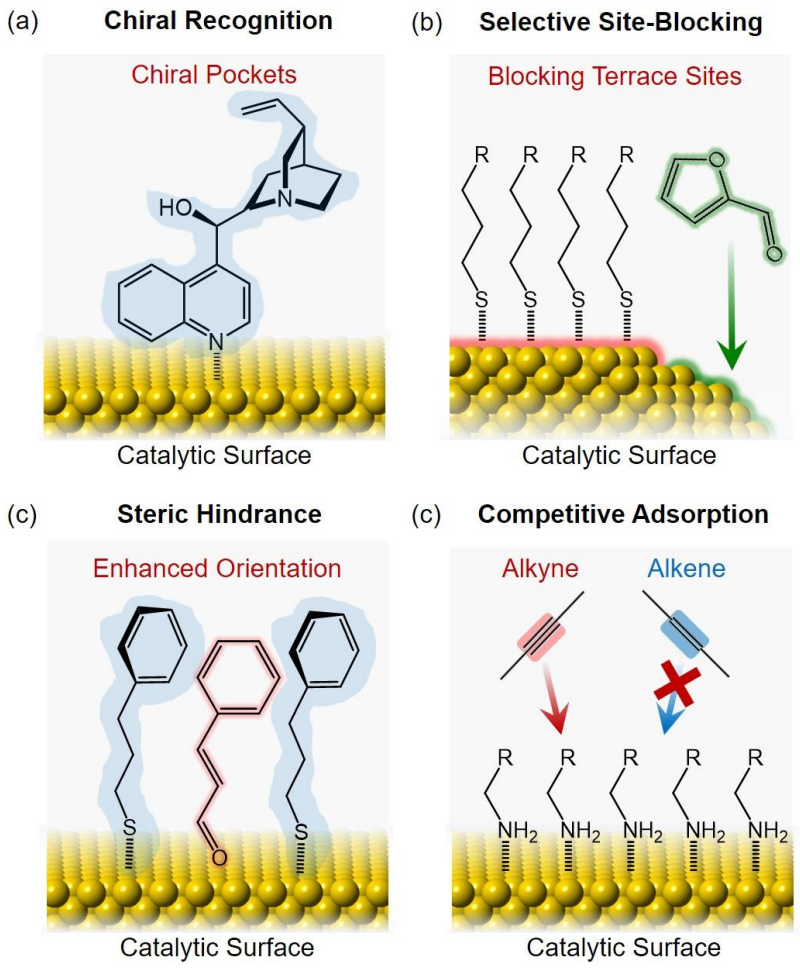

Figure 1.5: Schematic illustration of using metal-ligand interfaces to (a) create chiral pockets by adding chiral ligands, (b) block specific types of active sites on catalytic surfaces, (c) sterically hinder intermediates, and (d) facilitate the competition adsorption between intermediates and adsorbed ligands.

One of the earliest examples is adding cinchonidine to Ni catalysts for the asymmetric hydrogenation of α-ketoesters (**Figure 1.5a**).[35] The chiral nature of cinchonidine on the metal surface only allows the substrate to contact active sites through a specific conformation, resulting

in high enantioselectivity at around 95.0 % in favor of the (*R*)-α-hydroxyesters. To be more specific, it is thought to believe that the cinchonidine modifier forms a weak complex with the reactant and places the reactant within its chiral pocket, forcing the carbonyl group to adopt a specific orientation with only one side of the molecular plane available for reaction.[36-38]

Self-assembled monolayers (SAMs) are another attractive surface modification. The most commonly studied system is thiolate-based SAMs on metal surfaces.[39] Therefore, the following discussion will focus primarily on SAMs formed from thiol-based organic ligands. Firstly, the SAM modifications can selectively block specific types of reactive sites, and preferentially expose active sites that favor a desirable reaction pathway (**Figure 1.5b**). For example, in furfural hydrogenation, the SAMs consist of alkyl thiol chains of 18 carbons. They can selectively block active sites associated with the undesired reaction of decarbonylation and ring hydrogenation.[40] By suppressing the undesired reaction, SAM-modified Pd/Al_2O_3 presents high selectivity to furfural while the undesired product of furan remains low. Secondly, the SAM monolayers could sterically restrict the orientation of reactants, only allowing the terminal site of reactants to contact the active sites (**Figure 1.5c**). For example, in cinnamaldehyde hydrogenation, SAM-modified Pt/Al_2O_3 may impose the steric interactions to prevent cinnamaldehyde from lying flat on the surface of catalysts (**Figure 1.6**), only allowing cinnamaldehyde to contact active sites through the terminal site of the aldehyde group.[41] The result of the steric hindrance is the greatly enhanced selectivity to unsaturated alcohol (> 90.0 %). Similarly, the promoted selectivity has also been observed in using amine-based organic ligands.[42] By increasing the tail length of ligands from C4 to C18, the selectivity to unsaturated alcohol could be promoted to more than 90.0 %.

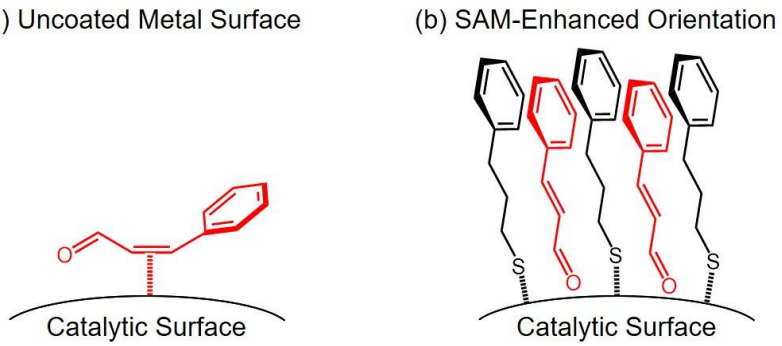

Figure 1.6: Schematic illustration of cinnamaldehyde on catalytic surfaces: (a) cinnamaldehyde interacting with an uncoated metal surface through the C=C double bond, and (b) 3-Phenyl-1-propanethiol SAMs favoring aldehyde hydrogenation by favoring an upright orientation. Figure adapted from ref. [41]

In addition to the two mechanistic pictures described above, the organic modifier can show competitive adsorption with intermediates, inhibiting the conversion of specific intermediates (**Figure 1.5d**). For example, in the hydrogenation of 4-octyne, the alkylamine modifier presents stronger binding energy than intermediate alkenes, but weaker than alkynes.[43] After converting alkynes to alkenes, the alkylamines would dominate the competitive adsorption with alkenes, preventing further hydrogenation of alkenes into alkanes. The same concept of competitive adsorption mechanism has also been applied to polymers in acetylene hydrogenation.[44-45]

1.7 Challenges in Tuning Catalysis with Catalytic Modifiers

Both types of modifiers have been intensively studied over the past few decades, but the mechanisms for improvement are still poorly understood as compared to the molecular catalysts. The major challenge in modifiers is the lack of defined structural information. Therefore, a detailed descriptor of the proposed mechanisms is still missing.[39] Furthermore, the stability of the organic species under demanding reaction conditions (high pressures or temperatures or both) is another

concern. In contrast, rigid inorganic modifiers on NP surfaces do not have the concern of transient structures, but the ill-defined coverage of these oxide clusters is still an issue. As a result, there has been growing interest in developing more consistent, highly-ordered structures that can provide a systematic approach for mechanistic studies.

In response to the challenge mentioned above, recent efforts have been focused on extending the concept to ordered nanoporous materials, such as zeolites and MOFs. This thesis primarily focuses on using MOFs as the catalytic modifiers because of the relatively milder synthetic condition as compared to zeolites.[46-48] We envision that the fundamental information, once established, can be applied in zeolites. It is worth noting that researchers have also combined organic and inorganic modifiers by coating oxide layers onto molecular templates via atomic layer deposition (ALD).[49] However, the active site may still remain ill-defined due to the desorption of the molecular template during the ALD coating process. A crystalline MOF material thus stands as an ideal platform for this task.

1.8 Selectivity Control based on Metal-Organic Frameworks

MOFs are crystalline nanoporous materials composed of metal nodes and organic linkers (**Figure 1.7a**).[50] The crystalline nature of MOFs can potentially form an ordered structure on the NP surfaces, enabling the understanding of the structural information at interfaces. Because of the well-developed chemistry to design inorganic clusters and organic ligands, the pore structures of MOFs could be further designed, [51-54] creating a more favorable microenvironment for specific product formation during catalysis (**Figure 1.7b**). A number of recent studies from our team and others have already shown that the MOF coating could indeed alter the catalytic performance.[55-81] However, the true potential of this strategy has not been demonstrated because the NP-MOF

interfaces were not well-controlled. In the flowing paragraph, we will discuss the progress of using MOFs as the catalytic regulator, and how the NP-MOF interfaces were not well-controlled.

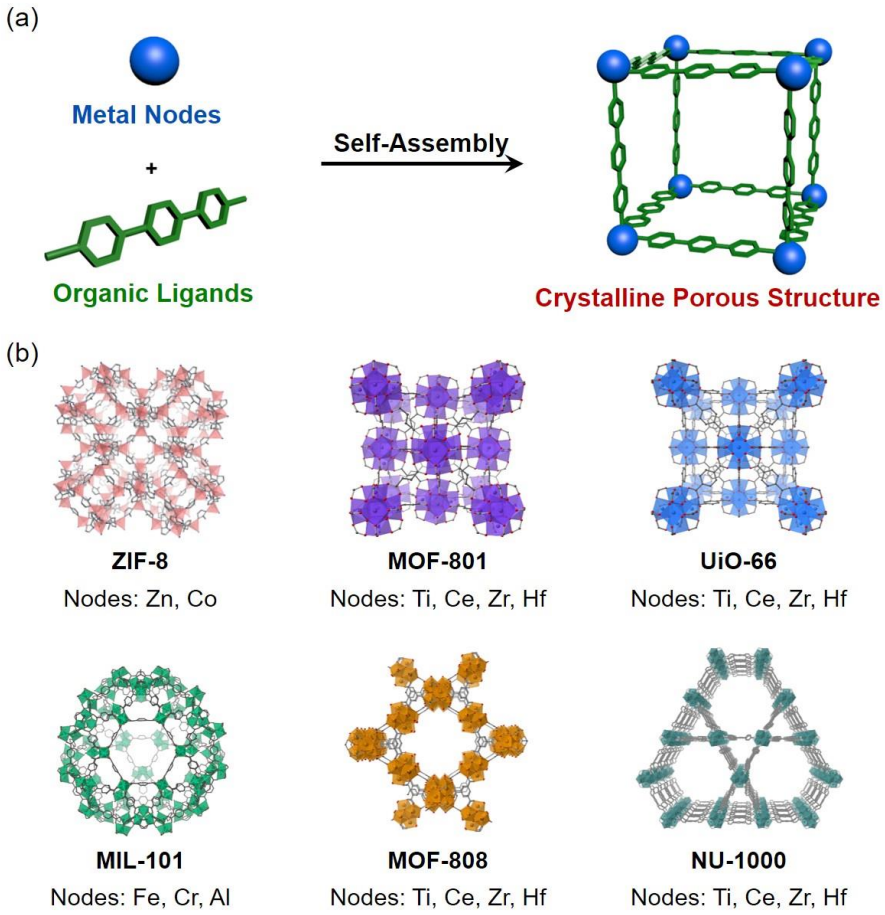

Figure 1.7: (a) Schematic illustration of MOF structures formed by the self-assembly of metal nodes and organic ligands, and (b) six representative MOFs to demonstrate the tunability of the pore structures.

Two types of selectivity have been reported: reactant size-exclusion and intermediate control. The size-exclusion mechanism is straightforward. The MOF coated on the catalyst surfaces excludes sterically bulky reactants from approaching the metal surface (**Figure 1.8**). For example, our team has utilized the tunability of MOFs to develop size-selective catalysts by encapsulating Pd NPs in zeolitic-imidazolate framework-8 (ZIF-8).[71] The uncoated Pd NPs are

active in the hydrogenation of ethylene and cyclooctene. When encapsulated Pd catalysts are used, the hydrogenation of cyclooctene is greatly suppressed while the hydrogenation of ethylene and cyclohexene remains active.

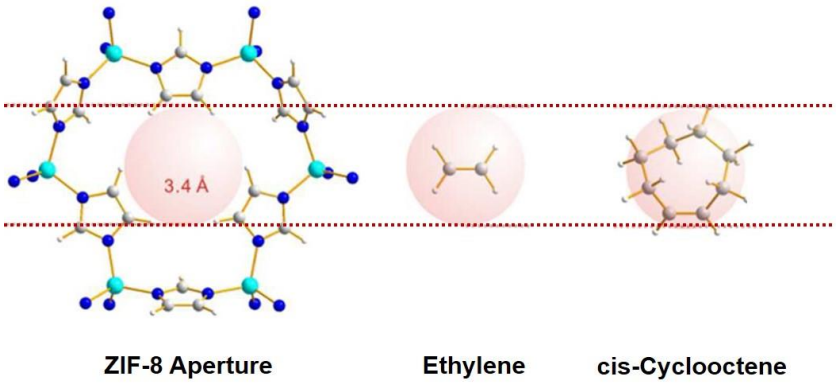

Figure 1.8: Schematic illustration of size-selective catalysis showing the aperture size of ZIF-8, the molecule size of ethylene, and cis-cyclooctene. Figure adapted from ref. [71]

As compared to the size-exclusion mechanism, the intermediate control mechanism is more complicated, and the concept is similar to the proposed mechanisms mentioned in metal oxides and organic ligands. In this concept, the MOF modulates the intermediates adsorbed at the NP-MOF interface to alter the product distribution, and the mechanistic picture includes steric hindrance, preferential activation, and confinement (**Figure 1.9**).

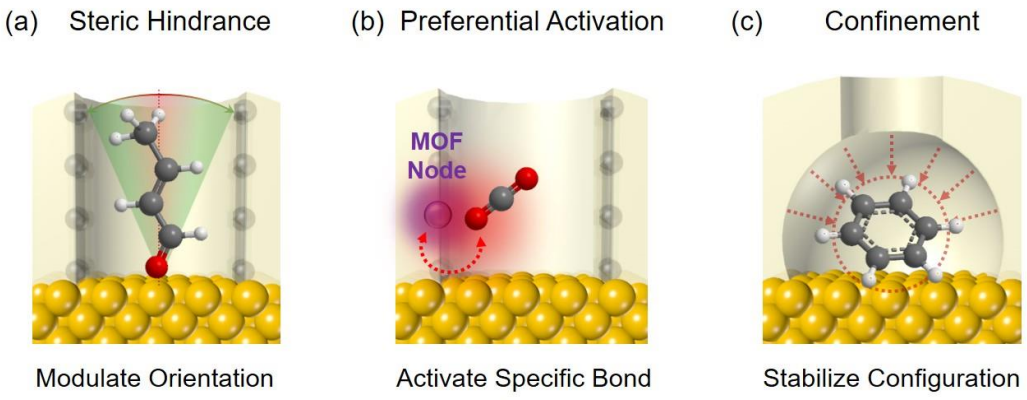

Figure 1.9: Schematic illustration of using NP-MOF interfaces to (a) sterically restrict the orientation of intermediates, (b) preferentially activate a specific chemical bond in intermediates, and (c) confine intermediates by stabilizing them in a specific configuration.

Firstly, it has been proposed that the MOF channel could sterically regulate the orientation of intermediates (**Figure 1.9a**). The allowed orientation results in only a specific site of intermediates interacting with the catalytic surface. Taking cinnamaldehyde hydrogenation as an example, when the cinnamaldehyde molecules are bound to a metal surface, they prefer a laid-down configuration in which both C=C and C=O can be hydrogenated. When NP-MOF catalysts are used, the steric hindrance provided by the chosen MOF may place intermediates in the up-right orientation, favoring the hydrogenation of the terminal C=O bond.[61] The same concept of the steric hindrance has also been proposed to control the selective oxidation of hexane-1,5-diol.[56]

Secondly, it has been hypothesized that selectivity could be promoted by the activation of a specific chemical bond (**Figure 1.9b**). The preferential activation relies on the ability of the inorganic nodes of the selected MOFs to interact with a bond of the intermediates. For example, the hydrogenation of acrolein is thermodynamically favored to occur at the C=C bond rather than the C=O bond.[82] When NP-MOF catalysts are used, the inorganic nodes of the chosen MOF (e. g., iron-based and zirconium-based MOFs) selectively interact with C=O bonds and promote the reaction toward the formation of allyl alcohol. The same concept of preferential activation has also been applied to the selective CO_2 hydrogenation to form methanol.[55, 83-85]

For the third type of selectivity control, the defined MOF cavity can stabilize a certain product shape while limiting the formation of others (**Figure 1.9c**). For instance, ring-opening and cracking are energetically favorable in methylcyclopentane isomerization.[57-58] When NP-MOF

catalysts are used, the pore structure of the chosen MOFs suppresses ring-opening and promotes ring enlargement, leading to the formation of C6-cyclic products.

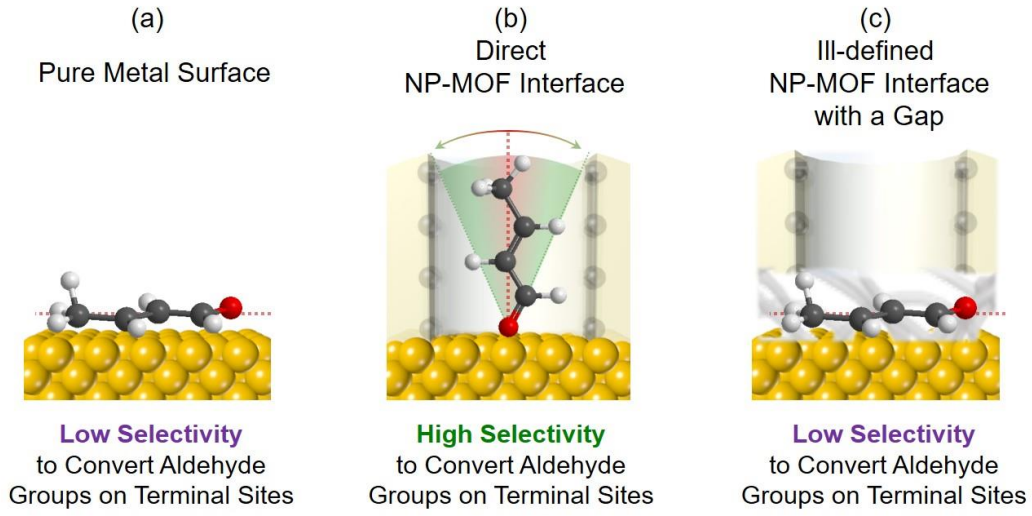

Figure 1.10: Schematic illustration of the possible selectivity control on the metal surface: (a) ordinary intermediate orientation on pure metal surfaces, (b) orientation directed by a direct NP−MOF interface. (c) orientation poorly controlled by an ill-defined NP−MOF interface. A crotonaldehyde molecule was used as a model reactant.

1.9 Challenges in MOF-based Catalyst Design

In all of the proposed mechanisms, MOF must be directly coated on the metal surface without any gap or chemicals in between (**Figure 1.10**). This is because the intermediates are adsorbed at the surface of metal NPs, and only MOF layers directly coated on the metal surface can modulate intermediates. However, this important interfacial feature has been overlooked in previous studies. Therefore, MOF-based selectivity control is largely stuck at the try-and-error stage because it is challenging to establish a structure-selectivity relationship if there is no direct and well-defined interface. The detailed descriptor of the proposed mechanisms is still missing. For example, how does tuning the identity of inorganic nodes and steric bulkiness of organic ligands influence catalytic selectivity? In the following paragraph, we discuss two commonly used syntheses to prepare NP-MOF catalysts. The two methods are the impregnation and coating methods (**Figure 1.11**).

In the impregnation method, MOFs are synthesized first and serve as a matrix to immobilize metal precursors that are reduced to form encapsulated NPs (**Figure 1.11a**).[86] In the coating method, colloidal metal NPs are synthesized first and then introduced into a MOF growth solution to coat MOF on the NPs (**Figure 1.11b**).[87] These two methods all generate NP-MOF interfaces; however, their detailed interfacial structures could be greatly different due to differences in their formation process. Firstly, the impregnation method is the most straightforward way to make heterogeneous catalysts. It could generate a direct NP-MOF interface, but it is challenging to completely avoid the growth of NPs on the external surface of the preformed MOFs. In addition, impregnating metal precursors in preformed MOFs could also damage the MOF structure. For the coating method, because MOFs are coated around pre-synthesized NPs, the colloidally synthesized NPs could be of a well-defined structure. However, the capping agents

used to stabilize colloidal NPs are hard to remove from the surface of metal NPs, preventing direct interaction between NP and MOF. As a result, a systematic method to coat MOF layers on the metal surface to form a well-defined NP-MOF interface is still missing.

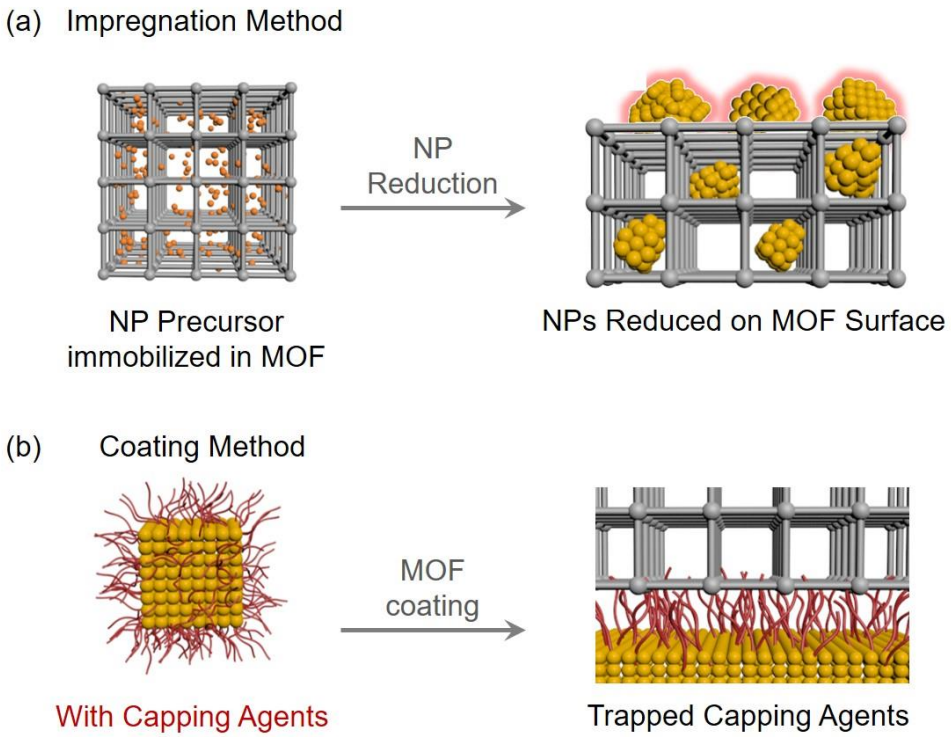

Figure 1.11. Schematic illustration of two synthetic methods to obtain NP-MOF catalysts: (a) impregnation methods and (b) coating methods.

Besides the synthetic challenge described above, characterizing the NP-MOF interfacial structures around active centers is another challenge. While MOF morphology, porosity, and crystallinity will be characterized by electron microscopy (EM), nitrogen sorption, and powder X-ray diffraction (XRD), it is more challenging to gather chemical information about the interface. To this end, the two critical challenges in synthesis and characterization limit the development of MOF-based selectivity control.

1.10 Thesis Objectives

We aim to address the key challenge described above by answering three fundamental questions, including (1) how to characterize the complicated hybrid NP-MOF interfaces, (2) how to allow MOF layers directly coated on the metal surface to form a well-defined NP-MOF interface, and (3) how to tune the identity of inorganic nodes and steric bulkiness of organic ligands influence catalytic selectivity. Furthermore, we expect to apply the understanding to promote other types of catalysts, such as molecular catalysts and biomolecules. The synthetic methods developed in this thesis are expected to benefit the hierarchical control in the MOF microcrystals. Ultimately, this thesis provides key knowledge to promote the design of MOF-based heterogeneous catalysts and serve as the foundation to realize the conventional modifiers of metal oxides and organic ligands.

This page is on purposely left in blank

2.0 Chapter 2:

Probing the Interface between Encapsulated Nanoparticles and Metal-Organic Frameworks for Catalytic Selectivity Control

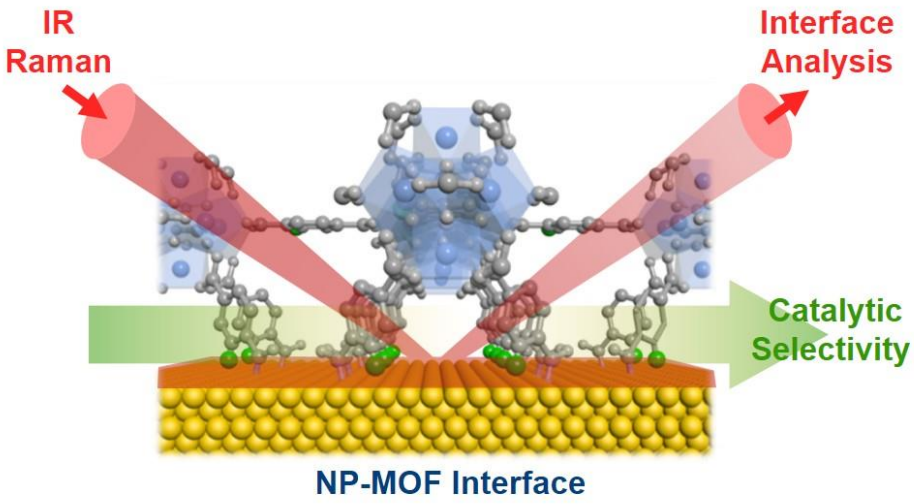

A significant portion of the work described in this chapter has been published in:

Lo, W. –S.; Chou, L. –Y.; Young, A. P.; Ren, C.; Goh, T. W.; Williams, B. P.; Li, Y.; Chen, S. –Y.; Ismail, M. N.; Huang, W.; Tsung, C. –K. Probing the Interface between Encapsulated Nanoparticles and Metal-Organic Frameworks for Catalytic Selectivity Control. *Chem. Mater.,* **2021**, 33, 1946–1953. Copyrights 2021 American Chemical Society. Portions of this chapter may be seen in Allison P. Young's 2018 dissertation titled "Using Lattice Engineering and Porous Materials Gating to Control Activity and Stability in Heterogeneous Catalysis", and Chenhao Ren's 2021 thesis titled "Investigating Catalytic Selectivity of Nanoparticles encapsulated in MOFs". I thank them for the use of this material as a co-author of the above-mentioned manuscript.

2.1 Introduction

Controlling the catalytic performance of metal nanoparticles (NPs) is a longstanding research topic in heterogeneous catalysis because they are at the center of many key industrial processes.[24-25, 88] Within this field, expanding and improving selectivity remains one of the most challenging aims. It is well-known that selectivity can be influenced by reaction conditions, NP sizes, and NP compositions,[89] but a molecular-level design of selectivity control remains elusive. More recently, introducing organic ligands to the NP surface has proved to be an effective way to rationally tune selectivity by directing intermediates on a molecular level,[90] and numerous organic ligands have been applied to effectively control selectivity.[38, 42, 91-92] Recently, intermediate control has been extended from surface adsorbed ligands to crystalline solids, metal-organic frameworks (MOFs).[50] The crystalline nature of the frameworks prevents the transient structure of the organic ligands that could be a potential issue during certain catalytic reactions.[39] Selectivity for a great number of important reactions has indeed been demonstrated using MOFs as intermediate-directing agents, such as the selective hydrogenation of α, β-unsaturated aldehydes, the selective oxidation of diols, and the isomerization of methylcyclopentane.[56, 58, 61, 68, 75, 93-95] Even the challenging selective hydrogenation of acrolein has been demonstrated, which has never been reported using organic ligands alone.[82]

The superior selectivity control provided by MOFs can be understood through the underlying mechanisms. The intermediate-directing agents control selectivity by modifying the electronic structure of NPs or directing the conformation of intermediates.[96] For example, in α, β-unsaturated aldehyde hydrogenation, both adsorbed ligands and coated MOFs on the catalytic surface can generate steric effects to prevent intermediates lying down in a flat conformation, allowing only the terminal C=O bond to be hydrogenated and leading to high chemoselectivity for

unsaturated alcohol.[42, 61] The crystalline nature of MOFs could further provide a more uniform steric control to direct intermediates at the interfaces between NPs and MOFs.[97] The tunable nature of MOFs allows this steric control to be fine-tuned.[53]

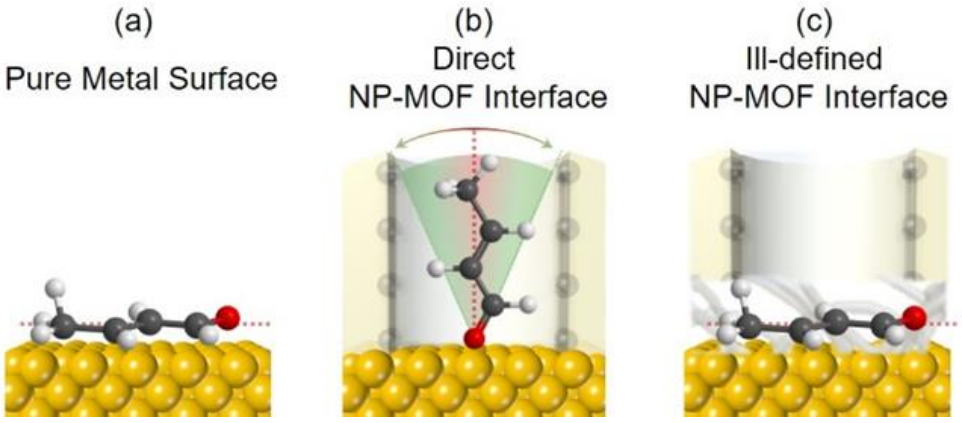

Figure 2.1: Schematic illustration of the possible intermediate conformations at the interface. (a) Ordinary intermediate conformation on a pure metal surface. (b) Conformation directed by a direct NP-MOF interface. (c) Conformation poorly controlled by an ill-defined NP-MOF interface. A crotonaldehyde molecule was used as a model reactant. These possible conformations are adopted from previous DFT reports.[77, 98]

Based on this mechanism of intermediate directing, the detailed structure at the interface is very important. In order for the sterics of the MOF pores to direct the intermediate for selectivity control, the MOF must be directly coated on the metal surface without any gap or chemicals in between (**Figure 2.1**). However, this important feature has been overlooked in many previous works. Only a well-defined and direct interface between NPs and MOFs could provide selectivity control.[77, 99-100] In this work, we aim to probe the interfacial structures and their impact on selectivity control. We first generate NP-MOF interfaces by three commonly used approaches, impregnation, coating, and one-pot.[70, 101-103] Then, we use infrared and Raman spectroscopy to gain chemical information at the interface generated by each approach. After understanding the

interface, we tested the selectivity of the catalysts for a model reaction, the hydrogenation of an α, β-unsaturated aldehyde.

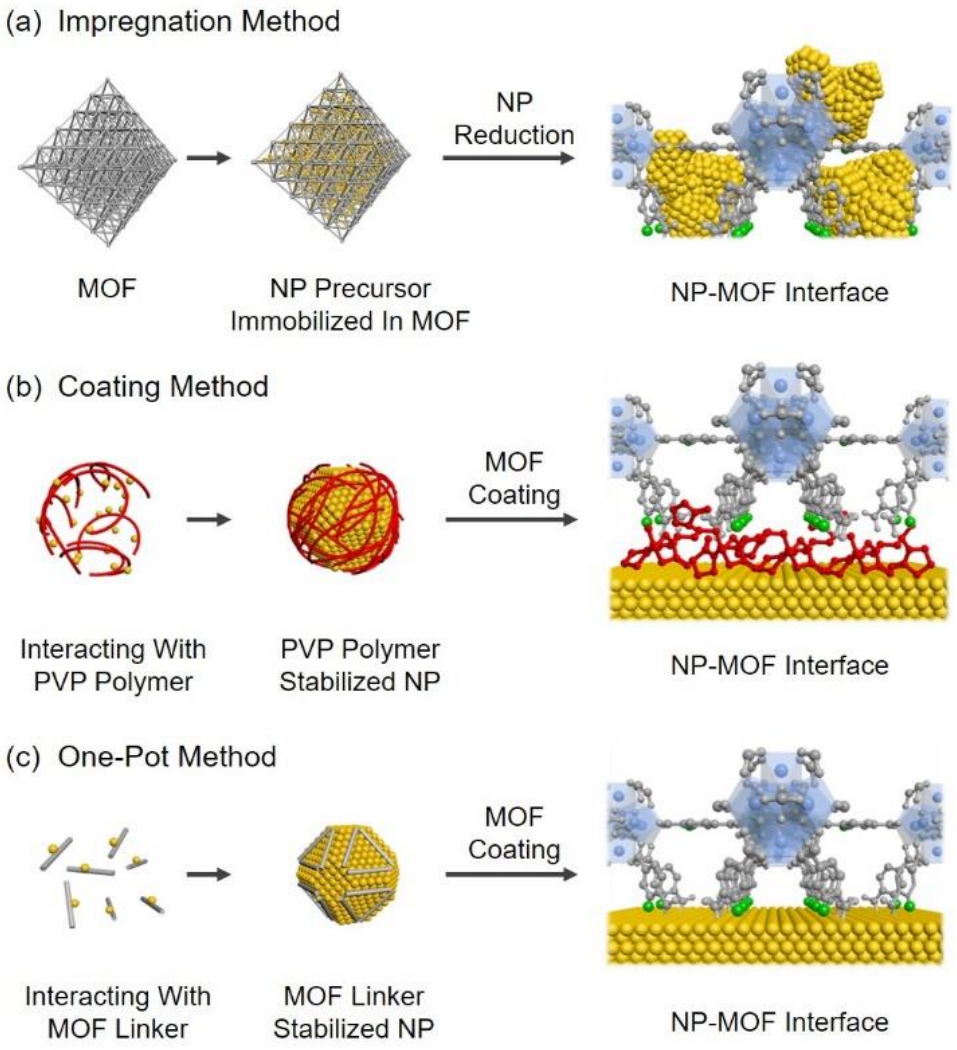

Figure 2.2: Schematic illustration of three different approaches to form the NP@MOF catalyst: (a) impregnation, (b) coating, and (c) one-pot. The illustrated sizes of the NPs in the scheme are used to emphasize the differences between the methods.

As mentioned, the three methods used to form NP@MOF catalysts are impregnation, coating, and one-pot. In the impregnation method, MOFs are synthesized first and serve as a matrix

to immobilize metal precursors that are reduced to form encapsulated NPs.[104] In the coating method, colloidal metal NPs are synthesized first and then introduced into a MOF growth solution to coat MOF on the NPs.[87] In the one-pot method, metal NPs and MOF precursors are mixed in one pot and then heated to form metal NPs and simultaneously coat MOF. These three methods all generate a NP-MOF interface; however, we hypothesize that their detailed interfacial structure could vary due to differences in their formation process (**Figure 2.2**). The impregnation method is the most conventional way to make heterogeneous catalysts. It could generate a direct NP-MOF interface, but it is challenging to completely avoid the growth of NPs on the external surface of the preformed MOFs. In addition, the size of formed NPs is less tunable, as most previous methods could only generate NPs with small size (**Figure 2.2a**).[61, 105] For the coating method, because MOFs form around pre-synthesized NPs, the colloidally synthesized NPs could be of well-defined morphologies and compositions. However, the capping agent used to stabilize colloidal NPs and provide an anchor for MOF growth could be trapped at the interface, preventing direct interaction between NP and MOF (**Figure 2.2b**). For the one-pot method, it has a great potential to form direct interfaces because no capping agent is added (**Figure 2.2c**); however, the syntheitic condition of this relatively new method is not fine-tuned for the interface control.[66] These hypothesized differences motivated us to perform a detailed study to provide direct comparisons between the methods.

2.2 Results and Discussions

Chemically stable UiO-66-NH_2 (University of Oslo-66-NH_2) is selected as the host MOF for this study.[106] UiO-66-NH_2 is formed by the assembly of zirconium clusters and 2-aminoterephthalic acid (BDC-NH_2). The amino group has a high affinity to metal NPs, [63, 107-108] and also provides a

probe for later spectroscopic study.[61, 63] We used reported methods for the encapsulation of Pd NPs in UiO-66-NH_2 to generate the impregnation and coating samples (**Details in experimental procedures; Figures 2.3a, 2.3b and A2.1**).[57, 61, 108-109] Because there is no reported one-pot method for NP@UiO-66-NH_2, we have developed a method modified from previous reports for NP@UiO-66.[66] In a typical experimental condition, metal precursors (salts of sodium tetrachloropalladate) and MOF precursors (zirconium tetrachloride, and BDC-NH_2) are mixed in the solvent. The solution is kept at 120 ^oC for 24 hours without stirring. Pd NPs form within the first 15 minutes of heating, followed by the formation of UiO-66-NH_2 (**Figure A2.2**). Uniform Pd@UiO-66-NH_2 nanocrystals were produced (**Figure 2.3c**). Powder X-ray diffraction (PXRD) patterns of Pd@UiO-66-NH_2 composites show no difference compared to simulated UiO-66 (**Figure A2.3**). The presence of metal salts does not affect MOF formation (**Figure A2.4**). The loading of Pd in Pd@UiO-66-NH_2 was identified by inductively coupled plasma optical emission spectrometry (ICP-OES) as 3.0 wt. %.

Although the newly developed one-pot synthesis is not the focus of this work, we want to emphasize its advantages, primarily its potential to form controlled NP-MOF interfacial structures. The procedure has improved upon previously reported one-pot methods through the use of BDC-NH_2, which plays two roles here. First, BDC-NH_2 can promote the formation of NP nuclei and accelerate the formation of NPs.[110] Second, its affinity for metals allows it to stabilize the metal surface and prevent NP aggregation without additional capping agents. The BDC-NH_2 stabilized NPs are thus formed first and then encapsulated into MOFs ((**Figure 2.2c**). When native BDC is used as the MOF linker under the same reaction conditions, the synthesized NPs formed a series of aggregates outside of the UiO-66 crystals (**Figure A2.5**). Using BDC-NH_2, the size and composition of encapsulated NPs can further be easily tuned by changing the reaction temperature

and metal precursor(s), respectively. At higher temperatures, the nucleation rate is accelerated, leading to smaller particles. Pd NP sizes can be tuned from 3.6 ± 1.0 nm to 9.9 ± 1.8 nm by decreasing the synthesis temperature from 150 ˚C to 90 ˚C (**Figures A2.6 and A2.7**). PdPt alloy NPs were used to demonstrate composition control. When a mixture of Pd and Pt precursors were introduced, a series of alloyed NPs formed (**Figures A2.8)**. A volcano relationship between activity and Pd:Pt ratio was observed (**Figures A2.9 and Table A2.1**), indicating that the encapsulated metal NPs are indeed alloyed.[111] A linear relationship was observed while using a mixture of pure Pt and Pd NPs (**Figure A2.10**).

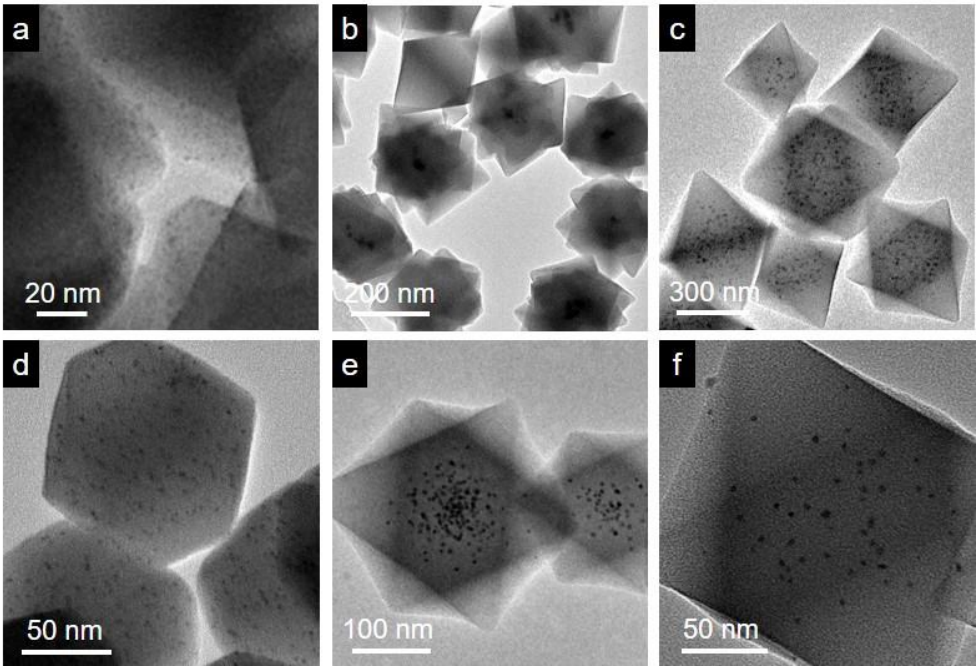

Figure 2.3: Characterization of the NP@UiO-66-NH_2. TEM images of Pd@UiO-66-NH_2 generated by (a) impregnation, (b) coating and (c) one-pot methods. TEM images of Pt@UiO-66-NH_2 generated by (d) impregnation, (e) coating and (f) one-pot methods. See supporting information for the loading and size distribution of encapsulated NPs.

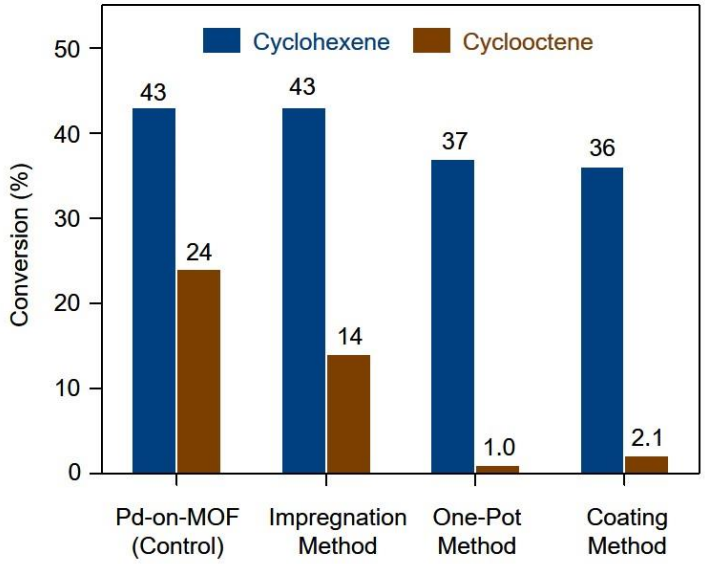

Figure 2.4: Size-selective alkene hydrogenation over Pd NPs on UiO-66-NH_2, and Pd@UiO-66-NH_2 obtained using the coating, one-pot, and impregnation methods. The catalyst activity was normalized by ethylene hydrogenation held at 40% conversion. Ethylene hydrogenation is run at 0 ˚C, cyclohexene hydrogenation is run at 25 ˚C, and cyclooctene hydrogenation is run at 40 ˚C.

Before studying the interfacial structures generated by the three different methods, we tested whether the metal NPs are encapsulated by carrying out size-selective alkene hydrogenation, using ethylene, cyclohexene, and cyclooctene, and comparing the results with a control sample, in which NPs are on the external surface of UiO-66-NH_2. The loading and size distribution of encapsulated Pd NPs in each sample were summarized in **Table A2.2** and **Figure A2.11**. Due to the smaller size of NPs formed in the impregnation sample,[61, 105] the metal NP surface areas of the four samples were normalized through a standard method of ethylene hydrogenation (to 40 % conversion, **Table A2.3**).[112] Because the MOF aperture size is bigger than cyclohexene and smaller than cyclooctene, we observe low activity for cyclooctene hydrogenation over impregnation, coating, and one-pot samples (**Figure 2.4)**, while the control sample (Pd-on-MOF) shows high

activity for both cyclohexene and cyclooctene hydrogenation. This result indicates that most of the metal NPs are indeed encapsulated. Because we used the impregnation method, higher activity of cyclooctene hydrogenation could be related to NPs on the external surface, which has been reported.[113] It is worth mentioning that these NPs on the external surface of MOFs can be avoided when extra synthetic steps were introduced.[113]

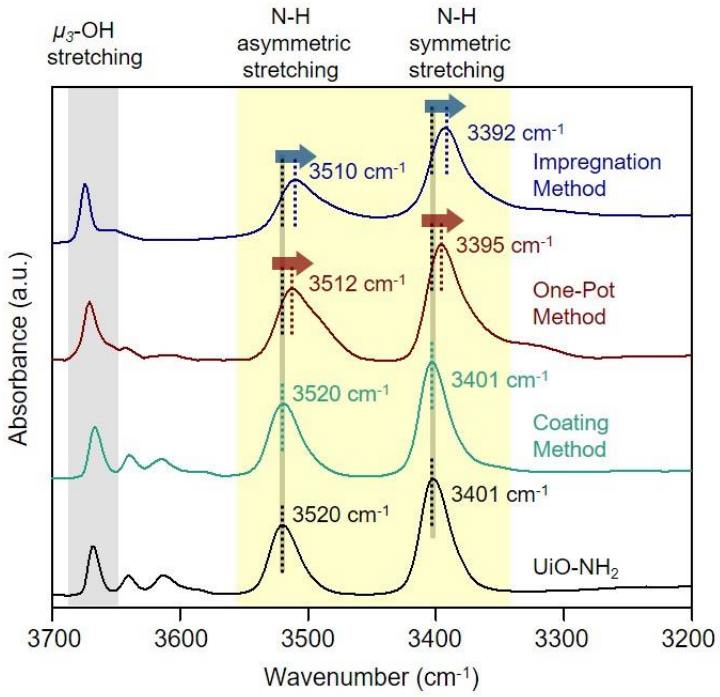

Figure 2.5: DRIFTS, with the characteristic stretches of the amine group highlighted, for UiO-NH_2 and Pd@UiO-66-NH_2 obtained using impregnation, one-pot, and coating methods. Significant shifts in the N-H stretch indicate that the MOF chemically interacts with the Pd surface.

After investigating the encapsulation of NPs into MOFs, we next studied the NP-MOF interfacial structure. Although the structures look similar under TEM and identical under XRD, these characterizations methods provide little insight into the interfacial structure (Figure 1). In light of this, the formation of chemical interactions at the interface was investigated through IR

and Raman spectroscopy. Different NP-MOF interfacial structures lead to different chemical bonding between NP and MOF. These chemical interactions can be probed by measuring changes in the chemical properties of either the MOF linkers or the NP surface. To study change in the MOF linkers after the formation of NP-MOF, we used diffuse reflectance infrared Fourier transform spectroscopy (DRIFTS) to monitor the stretching of the amine group of BDC-NH_2. Interaction between NP and MOF should lead to a weaker N-H bond, resulting in a red-shift of the N-H stretch IR frequency.[61] As shown in **Figure 2.5**, four samples were compared: pure UiO-NH_2 and Pd@UiO-NH_2 generated by each of the three methods, impregnation, coating, and one-pot. In the spectra, the bands at 3520 cm^{-1} and 3401 cm^{-1} are attributed to the N−H asymmetric and symmetric stretching vibration peak, respectively, and the band at 3670 cm^{-1} corresponds to the μ_3-OH stretching of the zirconium cluster.[114] The impregnation sample showed the greatest red-shift, indicating that the MOF linkers are chemically interacting with the encapsulated metal NPs. While lesser, the red-shift of the one-pot sample also indicates the MOF linkers are chemically interacting with encapsulated NPs. In contrast, no noticeable shift was observed for the coating sample, signifying that there is little interfacial interaction between MOF and NP. We attribute this limited contact to residues trapped at interface, which will be discussed in detail in a later section. The greater shift observed in the impregnation sample indicates that there are more chemical bonds at NP-MOF interface likely due to the smaller NP size generated by impregnation method (**Figure A2.10**).

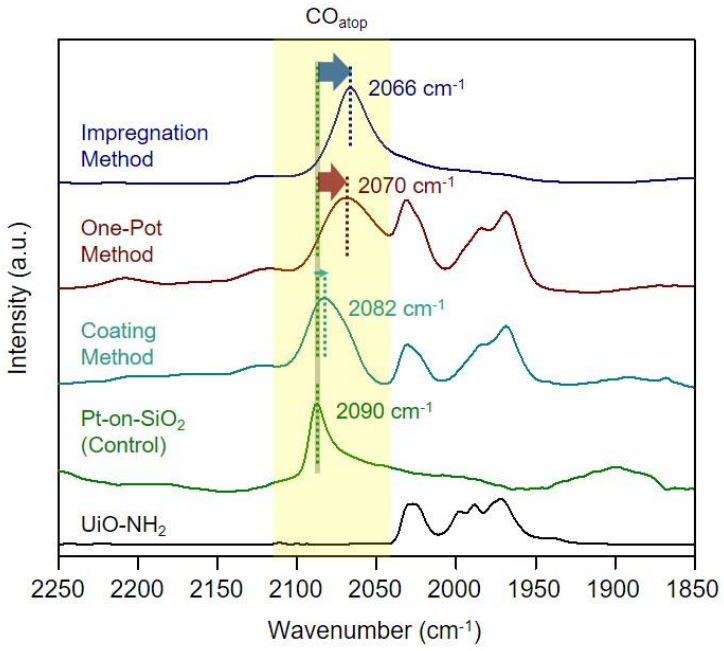

Figure 2.6: DRIFTS of CO adsorbed on Pt-on-SiO_2 and Pt@UiO-66-NH_2 obtained using impregnation, one-pot and coating methods. Significant shifts in CO_{atop} indicate that the MOF chemically interacts with the Pt surface, changing the electronic structure of Pt.

To probe changes in the NP electronic structure, we introduced carbon monoxide (CO) as a probe molecule, because the stretching frequency of CO adsorbed on a metal surface is sensitive to the electronic structure of the metal.[115] The small size of CO further allows it to easily pass through the UiO-66 aperture. For these studies, Pd NPs were replaced by Pt NPs, as the Pt surface yields well-defined (and well-understood) CO signals.[116-117] Pt@UiO-66-NH_2 samples were synthesized via the same routes as Pd@UiO-66-NH_2 (TEM images and PXRD pattern were shown in **Figures 2.3d-2.3f** and **Figure A2.12,** respectively).[57, 61] The loading and size distribution of encapsulated Pt NPs in each sample were summarized in **Table A2.2** and **Figure A2.13**. The more bonds formed at the NP-MOF interface, the more red-shifted the CO stretch frequency, as the electron-donating amine group increases charge density on the metal surface, resulting in increased

electron back donation to CO antibonding orbitals, weakening the CO bond.[118] As shown in **Figure 2.6**, four samples were again compared: Pt NPs-on-SiO_2, as the control, and Pt@UiO-66-NH_2 synthesized using the impregnation, coating, and one-pot methods. In the spectra, the band between 2050 and 2100 cm^{-1} is attributed to CO linearly bound on Pt atoms(CO_{atop}). [115] The frequency of CO_{atop} in the Pt-on-SiO_2 sample, ~2090 cm^{-1}, was used as a reference for comparison.[115] Compared to this reference frequency, the CO_{atop} frequency of the impregnation sample shows a red-shift from 2090 cm^{-1} to 2066 cm^{-1}, further indicating the chemical interaction between the linkers and metals in the impregnation sample. As expected, the one-pot method also shows a similar red-shift (~20 cm^{-1}) due to the chemical interaction. In contrast, a relatively small red-shift (~8 cm^{-1}) of CO_{atop} is observed in coating sample. Similar to the NH_2 stretching study, it implies a less chemical interaction at the interface in coating sample. Importantly, this study also suggests that insights provided by the Pd@UiO-66-NH_2 system can be extended to other metal NPs. Next, we studied the mechanisms causing the differences in NP-MOF interactions.

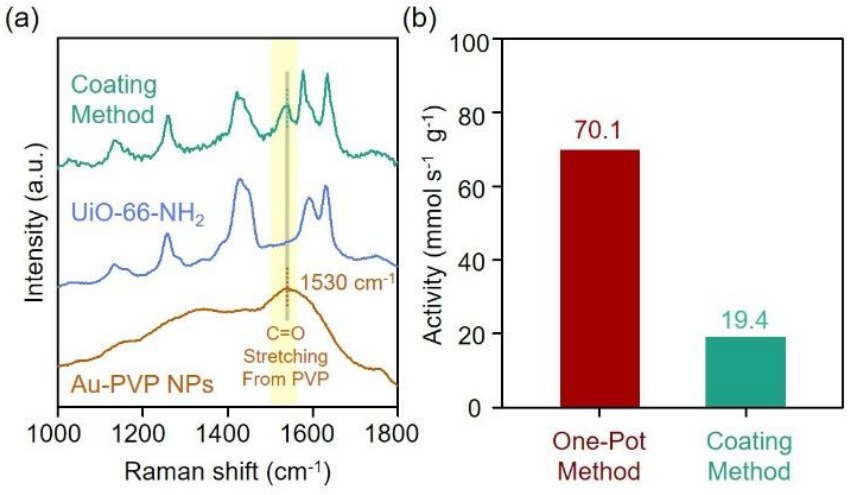

Figure 2.7: (a) Raman spectra of Au-PVP NPs, UiO-NH_2, and Au@UiO-66-NH_2 formed using the coating method. (b) Ethylene hydrogenation over Pt@UiO-66-NH_2 obtained using the one-pot and coating methods. Ethylene hydrogenation is run at 0 ˚C.

Capping agents are used to stabilize NPs for colloidal synthesis.[119-120] We hypothesize that the capping agents on the surface of colloidal NPs that are trapped at the interface after MOF coating. These trapped organic ligands block chemical interaction between MOF and NP, generating an ill-defined interface. To test this hypothesis, we used Raman spectroscopy to investigate interfacial capping agents. The same coating method and capping agent, polyvinylpyrrolidone (PVP), were used, but the metal NPs were switched to Au for its surface enhancement (**Figures A2.14-16**).[121] Because the surface plasmon resonance of Au NPs largely promotes the Raman signal of molecules close to the Au surface, the information is very interface specific.[122] As shown in **Figure 2.7**, the non-coated Au-PVP NPs showed a band at 1530 cm^{-1}, corresponding to stretching vibrations of the C=O moiety on PVP, in agreement with the literature.[123] After coating with UiO-66-NH_2, which has no characteristic peaks in this region, the peak can be clearly seen. The presence of PVP signal in the composite suggests that the capping agents used to stabilize colloidal metal NPs are indeed trapped inside the coated MOF. In contrast, no PVP signal was observed for the samples generated by impregnation and one-pot methods (**Figure A2.17**). To further examine the influence of this trapped interfacial capping agent, we compared the activity for ethylene hydrogenation of Pt@UiO-66-NH_2 synthesized by the coating and one-pot methods with similar Pt loading and particle size. (The NP sizes generated by the impregnation method cannot be controlled, so it was excluded from this study.) As shown in **Figure 2.7**, the coating sample shows much lower activity than the one-pot sample, which is attributed to active site blocking by PVP residues.[124-125]

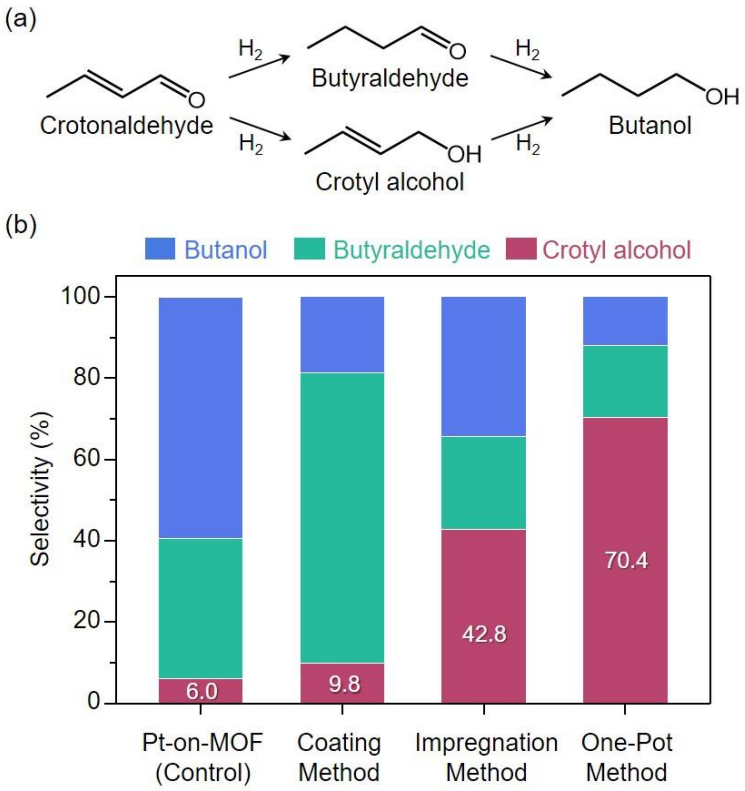

Figure 2.8: (a) Two pathways for the hydrogenation of crotonaldehyde. (b) Selectivity for crotonaldehyde hydrogenation over Pt NPs on UiO-66-NH_2 and Pt@UiO-66-NH_2 obtained using the coating, impregnation, and one-pot methods. To compare the selectivity of our samples, the conversion of each reaction was kept at 30 %. Crotyl alcohol is the preferred product, and selectivity was determined by its ratio to the sum of all three products. Reaction conditions: 2 mL of isopropanol, 100 µL of crotonaldehyde, 30 bar H_2, 70 °C, reaction time of 18 h.

After gaining an initial understanding of the NP-MOF interfacial structure, we carried out a model reaction, crotonaldehyde hydrogenation (**Figure 2.8a**). Numerous studies suggest that this type of α, β-unsaturated aldehyde hydrogenation over a NP@MOF catalyst favors the hydrogenation of the C=O bond, which is originally thermodynamically less favorable than the hydrogenation of the C=C bond.[61, 68, 74, 81-82, 126-127] Although many different mechanisms have been proposed, such as steric[61] or activation effects,[82] a direct interface is required for high selectivity

in all hypothesized mechanisms (**Figure 2.1**). For example, it has been proposed that the improved selectivity is due to the MOFs ability to regulate the orientation of intermediates.[61] Such regulation is dependent on a clean and direct NP-MOF interface. For our study, Pt@UiO-66-NH_2 was chosen because it produces fewer byproducts than Pd.[128] To compare the selectivity of our samples, the conversion of each reaction was kept at 30 % (**Table A2.4**). As shown in **Figure 2.8**, four samples were compared: pure Pt NPs on UiO-66-NH_2 and Pt@UiO-66-NH_2 synthesized through the coating, impregnation, and one-pot methods. The sample of pure Pt NPs on the MOF surface, which serves a control (Pt-on-MOF), shows a 6.0 % selectivity to crotyl alcohol. For the impregnation sample, selectivity increased (42.8 %), indicating promotion of the hydrogenation of C=O due to the presence of a direct NP-MOF interface. However, the sample generated by the coating method shows only a marginal increase in selectivity (9.8 %), which is attributed to the ill-defined interface suggested by our spectroscopic studies. The highest selectivity of crotyl alcohol (70.4 %) was observed in the one-pot sample, also due to direct interface revealed by our spectroscopy study. Although both samples have a direct interface, NP size control allows the one-pot sample to show higher catalytic activity than the impregnation samples (**Figures A2.11 and A2.13**). It has been reported that larger Pt NPs promote the formation of unsaturated alcohol.[129-130] The impregnation method can only generate NPs with small size that disfavors the formation of unsaturated alcohol.[61, 105] Besides providing a fundamental understanding of the interface, our study also reveals the potential of the one-pot synthesis method when the metal-linker interaction is controlled, and the formation sequence is regulated. We hypothesize that, if the conditions are optimized, NPs will form first, stabilized by linkers with high metal affinity. At this stage, the morphology and composition of the NPs can be controlled by colloidal methods because the MOF is not formed yet. Then, the MOF precursors will bond to the linkers on the NP surface and form

MOF around the NPs, forming a clean and direct interface. We believed that this process could lead to highly controlled and active interfacial structures.

2.3 Conclusions

In summary, we have developed a spectroscopic protocol to probe the chemical interactions at the interface by combining IR and Raman spectroscopy. We have used this toolbox to reveal differences in the chemical interactions at the interfaces generated by several common synthesis methods. We have found that although the coating method allows for better control over the encapsulated NPs than the impregnation method, the interface generated by the coating approach contains trapped capping agent. This trapped capping agent reduces crotyl alcohol selectivity for the hydrogenation of crotonaldehyde. Our developed one-pot method, on the other hand, shows the highest selectivity to the unsaturated alcohol, due to the direct NP-MOF interface and size-control of the encapsulated NPs. While the encapsulation of metal NPs into MOFs has been shown to be a route to promising composite catalysts, our current study shows that it is essential to fine-tune the interfacial structures between NPs and MOFs. The toolbox and understanding established in this work could offer perspective for further optimization of MOF-based heterogeneous catalyst design.

This work is supported by National Science Foundation (CHE-1566445) and Boston College. Authors thank Prof. Matthias Waegele at Boston College for helpful comments on the spectroscopic study.

2.4 Experimental Procedures

Chemicals: Unless otherwise stated, all the reactions were carried out in the air without taking any precaution to protect reactions from oxygen or moisture. Zirconium(IV) chloride ($ZrCl_4$, Aldrich, 99.5%), zirconium(IV) oxychloride octahydrate ($ZrOCl_2 \cdot 8H_2O$, Sigma-Aldrich, 99.5%), terephthalic acid (BDC, Sigma-Aldrich, 98%), 2-aminoterephthalic acid (BDC-NH_2, Sigma-Aldrich, 99%), acetic acid (Sigma-Aldrich, 99.7%), N,N-dimethylformamide (DMF, Sigma-Aldrich, 99.8%), sodium tetrachloropalladate(II) trihydrate ($Na_2PdCl_4 \cdot 3H_2O$, Strem Chemicals, 99.0%), chloroplatinic acid hexahydrate ($H_2PtCl_6 \cdot 6H_2O$, Sigma-Aldrich, 99.995%), gold(III) chloride trihydrate ($HAuCl_4 \cdot 3H_2O$, Sigma-Aldrich, ≥99.0%), sodium citrate tribasic dihydrate (Sigma-Aldrich, ≥99.0%), potassium tetrachloroplatinate (II) (K_2PtCl_4, Sigma-Aldrich, 98%), ammonium tetrachloroplatinate ($(NH_4)_2PtCl_4$, Sigma-Aldrich, 99%), cyclohexene (Sigma-Aldrich, 99%), cis-cyclooctene (Sigma-Aldrich, 95%), sodium hydroxide (NaOH, Sigma-Aldrich, 98%), polyvinylpyrrolidone (PVP, MW 40,000, Aldrich), tetramethylammonium bromide (Sigma-Aldrich, 99%), ethylene glycol (Sigma-Aldrich, ≥99%) were purchased from the indicated sources and used without further purification. The control sample of Pt on SiO_2 (5.0 wt% of Pt loading, Strem Chemicals) was used for CO-DRIFTS study. Carbon monoxide (Airgas, 99.999%) and nitrogen (Airgas, 99.999%) were used for CO-DRIFTS measurement. Hydrogen (Airgas, 99.999%), ethylene (Airgas, 99.995%) and helium (Airgas, 99.999%) were used for heterogeneous gas phase catalysis. Crotonaldehyde (Sigma-Aldrich, ≥99.0%) and hydrogen (Airgas, 99.999%) were used for crotonaldehyde hydrogenation. The Pd and Pt standards (1000 ppm, Inorganic Ventures) were used for inductively coupled plasma optical emission (ICP-OES) analysis.

Characterizations: Transmission electron microscope (TEM) images were obtained on JEOL JEM2010F operated at 200 kV. Scanning transmission electron microscope (STEM) and

Energy-dispersive X-ray spectroscopy (EDS) mapping experiments were performed on a FEI Probe Cs corrected Titan operating at 200 kV. Scanning electron microscope (SEM) images were obtained on a JEOL JSM6340F. The powder x-ray diffraction patterns (PXRD) were collected on a Bruker AXS diffractometer with Cu Kα radiation (λ= 1.5418 Å) in the 2-theta range of 4 to 40 degrees. ICP-OES spectrometry was performed using an Agilent 5100 instrument. The quantitative analysis of Pd and Pt was carried out by the calibration using known concentrations of standard solutions. Infrared measurement of chemisorbed carbon monoxide was carried out using a Bruker Tensor-27 IR spectrometer with a linearized mercury−cadmium−telluride detector, Harrick diffuse reflection accessory and Praying Mantis high-temperature reaction chamber. Raman spectra were collected on a Micro-Raman system (XploRA, Horiba) with 532 nm laser excitation.

Synthesis of Pd@UiO-66-NH_2 using one-pot method: In general, 14.5 mg of BDC-NH_2 (0.08 mmol) and 2.78 mg of $Na_2PdCl_4 \cdot 3H_2O$ (0.008 mmol) were dissolved in 7.622 mL DMF in a 20 mL scintillation vial, then 1.378 mL acetic acid was added into the solution to make the final volume to 9 mL. Next, 1 mL of DMF containing 18.6 mg of $ZrCl_4$ (0.08 mmol) was introduced into the above solution. The solution was heated to 120 ˚C in an oil bath for 24 hours. After cooling, the formed Pd@UiO-66-NH_2 powder was collected by centrifugation (8000 rpm, 10 minutes). The sample was washed with DMF three times. Then, the as-synthesized Pd@UiO-66-NH_2 powder was activated by solvent exchange to remove residues trapped in the framework. Activation was performed by washing with DMF and methanol three times every 12 h. The activated Pd@UiO-66-NH_2 sample was dried at 80 ˚C for 24 h.

Synthesis of Pt@UiO-66-NH_2 using one-pot method: In general, 14.5 mg of BDC-NH_2 (0.08 mmol) and 4.14 mg of $H_2PtCl_6 \cdot 6H_2O$ (0.008 mmol) were dissolved in 7.622 mL DMF in a 20 mL scintillation vial, then 1.378 mL acetic acid was added into the solution to make the final

volume to 9 mL. Next, 1 mL of DMF containing 18.6 mg of $ZrCl_4$ (0.08 mmol) was introduce into the above solution. The solution was heated to 120 ˚C in an oil bath for 24 hours. After cooling, the formed Pt@UiO-66-NH_2 powder was collected by centrifugation (8000 rpm, 10 minutes). The sample was washed with DMF three times. Then, the as-synthesized Pt@UiO-66-NH_2 powder was activated by solvent exchange to remove residues trapped in the framework. Activation process was performed by washing with DMF and methanol three times every 12 h. The activated Pt@UiO-66-NH_2 sample was dried at 80 ˚C for 24 h.

Synthesis of size controlled Pd@UiO-66-NH_2 using one-pot method: In general, 14.5 mg of BDC-NH_2 (0.08 mmol) and 2.78 mg of $Na_2PdCl_4 \cdot 3H_2O$ (0.008 mmol) were dissolved in 4 mL DMF as solution A. Solution A was heated to the desired temperature (90, 120 and 150 ˚C) in an oil bath for 2 hours with a magnetic stir at 200 rpm. While Solution A was heating, 18.6 mg of $ZrCl_4$ (0.08 mmol) was dissolved in 4.622 mL DMF, then 1.378 mL acetic acid was added into the solution to take the final volume of Solution B to 6 mL. Solution B was preheated to 120 ˚C in an oil bath. Solution A was then added into the solution B. The mixture was heated at 120 ˚C in an oil bath for 24 hours. After cooling, the formed Pd@UiO-66-NH_2 powder was collected by centrifugation (8000 rpm, 10 minutes). The sample was washed with DMF three times. Then, the as-synthesized Pd@UiO-66-NH_2 powder was activated by solvent exchange to remove residues trapped in the framework. Activation was performed by washing with DMF and methanol three times every 12 h. The activated Pd@UiO-66-NH_2 sample was dried at 80 ˚C for 24 h.

Synthesis of size controlled Pt@UiO-66-NH_2 using one-pot method: In general, 14.5 mg of BDC-NH_2 (0.08 mmol) and 4.14 mg $H_2PtCl_6 \cdot 6H_2O$ (0.008 mmol) were dissolved in 3.5 mL DMF, then 0.5 mL ethanol was added into the above solution to make the final volume to 4 mL as Solution A. Solution A was heated to the desired temperature (90, 120 and 150 ˚C) in an oil bath

for 2 hours with a magnetic stir at 200 rpm. While Solution A was heating, 18.6 mg of $ZrCl_4$ (0.08 mmol) was dissolved in 4.622 mL DMF, then 1.378 mL acetic acid was added into the solution to take the final volume of Solution B to 6 mL. Solution B was preheated to 120 ˚C in an oil bath. Then Solution A was then added into Solution B. The mixture was heated at 120 ˚C in an oil bath for 24 hours. After cooling, the formed Pt@UiO-66-NH_2 powder was collected by centrifugation (8000 rpm, 10 minutes). The sample was washed with DMF three times. Then, the as-synthesized Pt@UiO-66-NH_2 powder was activated by solvent exchange to remove residues trapped in the framework. Activation was performed by washing three times with DMF and methanol every 12 h. The activated Pt@UiO-66-NH_2 sample was dried at 80 ˚C for 24 h.

Synthesis of PdPt@UiO-66-NH_2 composite using one-pot method: Following a similar procedure as the synthesis of Pd@UiO-66-NH_2 composite, differing nominal loadings of potassium tetrachloropalladate (K_2PdCl_4) or potassium tetrachloroplatinate (K_2PtCl_4) were dissolved in the DMF prior to the heating step. The total amount of metal precursor in the synthesis was kept at 8×10^{-3} mmol, and the stoichiometry between K_2PdCl_4 and K_2PtCl_4 was varied to form alloy nanoparticles with different compositions. These reactions were then run for 24 hours at 120 ˚C, and collected by centrifugation (8000 rpm, 10 minutes). The as-synthesized PdPt@UiO-66-NH_2 powder was activated by the solvent exchange to remove the residues trapped in the framework. Activation was performed by washing with DMF and methanol three times every 12 h. The activated PdPt @UiO-66-NH_2 sample was dried at 80 ˚C for 24 h. The compositions of Pd and Pt in PdPt@UiO-66-NH_2 were tested by ICP-OES spectroscopy (**Table S1**).

Synthesis of Au@UiO-66-NH_2 using one-pot method: In general, 14.5 mg of BDC-NH_2 (0.08 mmol) and 6.28 mg of $HAuCl_4 \cdot 3H_2O$ (0.016 mmol) were dissolved in 4 mL DMF as solution A. Solution A was heated to 150 ˚C in an oil bath for 40 min with a magnetic stir at 200 rpm.

While Solution A was heating, 18.6 mg of $ZrCl_4$ (0.08 mmol) was dissolved in 4.622 mL DMF, then 1.378 mL acetic acid was added into the solution to take the final volume of Solution B to 6 mL. Solution B was preheated to 120 ˚C in an oil bath. Solution A was then added into the solution B. The mixture was heated at 120 ˚C in an oil bath for 24 hours. After cooling, the formed Au@UiO-66-NH_2 powder was collected by centrifugation (8000 rpm, 10 minutes). The sample was washed with DMF three times. Then, the as-synthesized Au@UiO-66-NH_2 powder was activated by solvent exchange to remove residues trapped in the framework. Activation was performed by washing with DMF and methanol three times every 12 h. The activated Au@UiO-66-NH_2 sample was dried at 80 ˚C for 24 h.

Synthesis of Pd@UiO-66-NH_2 composite using impregnation method: The synthesis of NP@UiO-66-NH_2 composite using the impregnation method was performed based on a previous report.[108] In general, pure UiO-66-NH_2 was synthesized first and served as a matrix to immobilize metal precursors that are reduced to form NPs in MOFs. To synthesized pure UiO-66-NH_2, 48.0 mg of $ZrCl_4$ (0.20 mmol) and 37.2 mg of BDC-NH_2 (0.20 mmol) were dissolved in 12 mL DMF in a 20 mL scintillation vial. Then, 15 μL H_2O was added into the solution. The solution was heated to 120 ˚C in an oil bath for 24 hours. After cooling, the formed UiO-66-NH_2 powder was collected by centrifugation (8000 rpm, 10 minutes). The sample was washed with DMF three times. Then, the as-synthesized UiO-66-NH_2 powder was activated by solvent exchange to remove residues trapped in the framework. Activation was performed by washing three times with DMF and methanol every 12 h. The activated UiO-66-NH_2 sample was dried at 80 ˚C for 24 h. To form Pd@UiO-66-NH_2 composites using the impregnation method, 100.0 mg of activated UiO-66-NH_2 powder was dispersed in 5 mL of dichloromethane followed by sonication for 40 minutes at room temperature. Then, 5 mL of dichloromethane containing 7.0 mg of palladium acetate was added

dropwise to the above solution with magnetic stirring at 900 rpm. The mixture was stirred at 500 rpm for 24 h at ambient temperature. The as-synthesized Pd^{2+}-impregnated UiO-66-NH_2 was centrifuged and washed with dichloromethane three times. The sample was further washed by dichloromethane three times every 12 h to remove the remaining palladium precursor adsorbed on the surface of UiO-66-NH_2. The resulting sample was then air-dried and reduced under a 10 % H_2 flow (50 mL/min, balanced with helium) at 200 °C for 2 h.

Synthesis of Pt@UiO-66-NH_2 composite using impregnation method: The synthesis of NP@UiO-66-NH_2 composite using the impregnation method was performed based on a previous report.[61] In general, pure UiO-66-NH_2 was synthesized first and served as a matrix to immobilize metal precursors that are reduced to form NPs in MOFs. To synthesize pure UiO-66-NH_2, 48.0 mg of $ZrCl_4$ (0.20 mmol) and 37.2 mg of BDC-NH_2 (0.20 mmol) were dissolved in 12 mL DMF in a 20 mL scintillation vial. Then, 15 µL H_2O was added into the solution. The solution was heated to 120 ˚C in an oil bath for 24 hours. After cooling, the formed UiO-66-NH_2 powder was collected by centrifugation (8000 rpm, 10 minutes). The sample was washed with DMF three times. Then, the as-synthesized UiO-66-NH_2 powder was activated by solvent exchange to remove residues trapped in the framework. Activation was performed by washing three times with DMF and methanol every 12 h. The activated UiO-66-NH_2 sample was dried at 80 ˚C for 24 h. To form Pt@UiO-66-NH_2 composites using the impregnation method, 200.0 mg of activated UiO-66-NH_2 powder was dispersed in 12 mL of H_2O followed by sonication for 40 min at room temperature. Then, 2 mL of an aqueous solution containing 13.0 mg of K_2PtCl_4 was added dropwise to the above solution with magnetic stirring at 900 rpm. The mixture was stirred at 500 rpm for 24 h at ambient temperature. The as-synthesized Pt^{2+}-impregnated UiO-66-NH_2 was centrifuged and

washed with H_2O three times. The resulting sample was vacuum dried and reduced under a 10 % H_2 flow (50 mL/min, balanced with helium) at 200 °C for 1 h.

Synthesis of Au@UiO-66-NH_2 composite using impregnation method: The synthesis of NP@UiO-66-NH_2 composite using the impregnation method was performed based on a previous report.[131-132] In general, pure UiO-66-NH_2 was synthesized first and served as a matrix to immobilize metal precursors that are reduced to form NPs in MOFs. To synthesized pure UiO-66-NH_2, 48.0 mg of $ZrCl_4$ (0.20 mmol) and 37.2 mg of BDC-NH_2 (0.20 mmol) were dissolved in 12 mL DMF in a 20 mL scintillation vial. Then, 15 µL H_2O was added into the solution. The solution was heated to 120 ˚C in an oil bath for 24 hours. After cooling, the formed UiO-66-NH_2 powder was collected by centrifugation (8000 rpm, 10 minutes). The sample was washed with DMF three times. Then, the as-synthesized UiO-66-NH_2 powder was activated by solvent exchange to remove residues trapped in the framework. Activation was performed by washing three times with DMF and methanol every 12 h. The activated UiO-66-NH_2 sample was dried at 80 ˚C for 24 h. To form Au@UiO-66-NH_2 composites using the impregnation method, 50.0 mg of activated UiO-66-NH_2 powder was dispersed in 5 mL of ethanol followed by sonication for 40 minutes at room temperature, and 10 uL of 10 wt.% $HAuCl_4 \cdot 3H_2O$ solution was added dropwise to the above solution with magnetic stirring at 900 rpm followed by 5 mL of dichloromethane. The above solution with magnetic stirring at 500 rpm for 1 hour at ambient temperature. Then, the solution was mixed with 30 mL hexane (the sample should precipitate at this stage). The as-synthesized Au^{3+}-impregnated UiO-66-NH_2 was centrifuged and washed with hexane three times. The resulting sample was then air-dried and reduced under a 10 % H_2 flow (50 mL/min, balanced with helium) at 200 °C for 30 min.

Synthesis of Pd nanocrystals using a colloidal method: The synthesis was performed based on a previous report.[133] A total of 0.025 mmol of Na_2PdCl_4, 0.75 mmol of tetramethylammonium bromide, and 0.5 mmol of polyvinylpyrrolidone (in terms of the repeating unit, MW 40 000) were dissolved into 5 mL of ethylene glycol in a 25 mL round-bottom flask at room temperature. The solution was bubbled with Ar for 15 minutes to remove the oxygen in solution. The mixed solution was and heated to 200°C under stirring in an oil bath under reflux for 20 min. After cooling, the formed Pd NPs were mixed with acetone and centrifuged at 8000 rpm for 10 minutes to remove the unreacted residues. The as-synthesized Pd NPs were purified by washing with a mixture of 3.0 mL ethanol and 27 mL hexane three times using centrifugation (8000 rpm, 10 minutes). The resulting Pd NPs were dispersed into 5 mL of methanol to give a Pd NP concentration of 0.5 mg/mL. Before introduction into the synthesis of Pd@UiO-66-NH_2, 1 mL of the Pd NPs (0.5 mg/mL) in methanol were centrifuged at 8000 rpm for 10 min and dispersed in 1 mL DMF.

Synthesis of Pt nanocrystals using a colloidal method: The synthesis was performed based on a previous report.[133] A total of 0.025 mmol of K_2PtCl_4, 0.75 mmol of tetramethylammonium bromide, and 0.5 mmol of polyvinylpyrrolidone (in terms of the repeating unit, MW 40 000) were dissolved into 5 mL of ethylene glycol in a 25 mL round-bottom flask at room temperature. The solution was bubbled with Ar for 15 minutes to remove the oxygen in solution. The mixed solution was and heated to 200°C under stirring in an oil bath under reflux for 20 min. After cooling, the formed Pt NPs were mixed with acetone and centrifuged at 8000 rpm for 10 minutes to remove the unreacted residues. The as-synthesized Pt NPs were purified by washing with a mixture of 3.0 mL ethanol and 27 mL hexane three times using centrifugation (8000 rpm, 10 minutes). The resulting Pt NPs were dispersed into 5 mL of methanol to give a Pt

NP concentration of 0.5 mg/mL. Before introduction into the synthesis of Pt@UiO-66-NH_2, 1 mL of the Pt NPs (0.5 mg/mL) in methanol were centrifuged at 8000 rpm for 10 min and dispersed in 1 mL DMF.

Synthesis of Au nanocrystals using a colloidal method: The synthesis was performed based on a previous report.[134] 1.25 mL of 0.01 m $HAuCl_4$ aqueous solution was introduced into 48.25 mg H_2O in a 100-mL two-neck round bottom flask. Then, the solution was stirred and refluxed at 110 °C oil bath for 20 min. After that, 0.5 mL of the aqueous solution containing 3 wt% sodium citrate tribasic dihydrate was introduced to the above solution and the reaction was held in reflux at 110 °C oil bath for 3 min. (The pink color should form at this stage, indicating the formation of Au NP.) The solution was cooled to room temperature. Then, 1.0 mL of the aqueous solution containing 55.5 mg of polyvinylpyrrolidone was added into the formed Au NP solution and stirred for 10 min. The formed Au NPs protected by polyvinylpyrrolidone were centrifuged at 13000 rpm for 20 min to remove the unreacted residues. The as-synthesized Au NP was purified by washing with methanol twice using centrifugation (14000 rpm, 20 minutes). The resulting Au NPs were dispersed into 0.5 mL of methanol to give a concentration of Au NPs (5.0 mg/mL). The Au NPs in methanol were introduced into the synthesis of Au@UiO-66-NH_2 using coating method without the solvent exchange using DMF.

Synthesis of Pd@UiO-66-NH_2 composite using coating method: The synthesis of Pd@UiO-66-NH_2 composites using the coating method was modified from a previous report.[109] In general, 25.8 mg of $ZrOCl_2 \cdot 8H_2O$ (0.08 mmol) and 14.5 mg of BDC-NH_2 (0.08 mmol) were dissolved in 7.622 mL DMF in a 20 mL scintillation vial, then 1.378 mL acetic acid was added into the solution to take the final volume to 9 mL. Next, 1 mL of Pd NPs (0.5 mg/mL in DMF, synthesized from the colloidal method using PVP as capping agents) were introduced into the

above solution, and the solution was heated at 120 ˚C in an oil bath for 2 hours. After cooling, the formed Pd@UiO-66-NH_2 powder was collected by centrifugation (8000 rpm, 10 minutes). The sample was washed with DMF three times. Then, the as-synthesized Pd@UiO-66-NH_2 powder was activated by solvent exchange to remove residues trapped in the framework. The activation process is carried out by washing three times with DMF and methanol every 12 h.

Synthesis of Pt@UiO-66-NH_2 composite using coating method: The synthesis of Pt@UiO-66-NH_2 composites using the coating method was modified from a previous report.[57] In general, 18.6 mg of $ZrCl_4$ (0.08 mmol) and 14.5 mg of BDC-NH_2 (0.08 mmol) were dissolved in 7.622 mL DMF in a 20 mL scintillation vial, then 1.378 mL acetic acid were added into the solution to take the final volume to 9 mL. Next, 1 mL of Pt NPs (0.5 mg/mL in DMF, synthesized from the colloidal method using PVP as capping agents) was introduced into the above solution, and the solution was heated at 120 ˚C in an oil bath for 24 h. After cooling, the formed Pt@UiO-66-NH_2 powder was collected by centrifugation (8000 rpm, 10 minutes). The sample was washed with DMF three times. Then, as-synthesized the Pt@UiO-66-NH_2 powder was activated by solvent exchange to remove residues trapped in the framework. Activation was performed by washing three times with DMF and methanol every 12 h. The activated Pt@UiO-66-NH_2 sample was dried at 80 ˚C for 24 h.

Synthesis of Au@UiO-66-NH_2 composite using coating method: The synthesis of Au@UiO-66-NH_2 composite using coating method is based on the previous report with modifications.[121] In general, 54.0 mg of BDC-NH_2 (0.30 mmol) was dissolved in 2 mL DMF in a 20 mL scintillation vial, then 980 µL acetic acid was added into the solution. Next, 2 mL DMF containing 21.0 mg of $ZrOCl_2 \cdot 8H_2O$ (0.066 mmol) and 0.1 mL of Au NPs (5 mg/mL in methanol, synthesized from the colloidal method using PVP as capping agents) were introduce in to the above

solution, and the solution was heated at 120 ˚C in an oil bath for 18 h. After cooling, the formed Au@UiO-66-NH_2 powder was collected by centrifugation (8000 rpm, 10 minutes). The sample was washed with DMF three times. Then, the as-synthesized Au@UiO-66-NH_2 powder was activated by solvent exchange to remove residues trapped in the framework. Activation was performed by washing three times with DMF and methanol every 12 h. The activated Au@UiO-66-NH_2 sample was dried at 80 ˚C for 24 h.

Synthesis of UiO-66-NH_2 for DRIFTS measurements: The synthesis of UiO-66-NH_2 is based on a previous report.[135] In general, 18.6 mg (0.08 mmol) $ZrCl_4$ and 14.5 mg (0.08 mmol) BDC-NH_2 were dissolved in 8.622 mL DMF in a 20 mL scintillation vial. Then 1.378 mL acetic acid was added into the above solution, and the resulting solution was heated for 24 hours in a 120 ˚C oil bath. After cooling, the formed UiO-66-NH_2 powder was collected by centrifugation (4000 rpm, 10 minutes). The sample was washed with DMF three times. Then, as-synthesized the UiO-66-NH_2 powder was activated by the solvent exchange to remove the residues trapped in the framework. Activation was performed by washing three times with DMF and methanol every 12 hours. The activated UiO-66-NH_2 sample was dried at 80 ˚C for 24 hours.

Synthesis of Pd on the external surface of UiO-66-NH_2 for alkene hydrogenation: To prepare the samples of Pd NPs deposited on the external surface of UiO-66-NH_2 (Pd-on-MOF), 6 mL of the colloidal Pd NPs (0.5 mg/ mL, in DMF) was mixed with 100.0 mg of UiO-66-NH_2 in 5 mL DMF in a 20 mL scintillation vial. The mixture was sonicated for 10 min and stirred for 24 h at 25 ˚C. Then, the brown precipitates were separated by centrifugation (4000 rpm, 10 min), washed with ethanol four times, and dried in the vacuum oven overnight.

Synthesis of Pt on external surface of UiO-66-NH_2 for crotonaldehyde hydrogenation: To prepare the samples of Pt NPs deposited on the external surface of UiO-66-NH_2 (Pt-on-MOF),

6 mL of the colloidal Pt NPs (0.5 mg/ mL, in DMF) was mixed with 100.0 mg of UiO-66-NH_2 in 5 mL DMF in a 20 mL scintillation vial. The mixture was sonicated for 10 min and stirred for 24 h at 25 ˚C. Then, the brown precipitates were separated by centrifugation (4000 rpm, 10 min), washed with ethanol four times, and dried in the vacuum oven overnight.

DRIFTS measurement: Diffuse reflectance infrared Fourier transform spectroscopy (DRIFTS) spectra were collected using a Bruker Tensor 27 with a mercury-cadmium-telluride detector (MCT) and a Harrick diffuse reflectance accessory. The beam alignment and calibration were performed before each measurement. Both CO-DRIFTS spectra and DRIFTS spectra and were carried out using this instrumental setup. To carry out CO-DRIFTS analysis, the sample was packed in the sample cup and sealed in a Praying Mantis high-temperature IR reaction chamber. The sample was then activated in the IR reaction chamber under a 10 % H_2 flow (50 mL/min, balanced with helium) at 200 °C for 1 h. The temperature is controlled by a PID controller with a type-K thermocouple. The sample was cooled to room temperature under He flow (50 mL/min) and a spectrum of the sample was recorded as a background. The adsorption of carbon monoxide (CO) on the sample was performed by introducing CO (10 mL/min) into the IR reaction chamber with N_2 flow (50 mL/min) for 20 min. The series of CO-DRIFTS spectra were measured by flushing with N_2 flow (50 mL/min) to remove gaseous CO. All spectra were collected with 160 scans at a resolution of 4 cm^{-1} from 1750 cm^{-1} to 3000 cm^{-1}. We observed two distinct signals for all Pt@UiO-66-NH_2 samples. The band from 2050 cm^{-1} to 2100 cm^{-1} is attributed to CO adsorbed linearly atop the Pt atom. The band from 1950 cm^{-1} to 2050 cm^{-1} is attributed to CO adsorbed in the MOF scaffold, which is in agreement with the spectrum measured by using the control sample of UiO-66-NH_2. Before carrying out the DRIFTS spectra, all samples (25.0 mg) were activated by incubation in 0.1 M HCl (10.0 mL) at 60 °C for 8 hours. The sample was washed three times with

DMF and methanol and dried at 80°C for 24 hours. Before each measurement, the samples (10.0 mg) was mixed with KBr (10.0 mg) and placed in oven at 80 °C for 24 hours. Then, it was packed in the sample cup and sealed in a Praying Mantis high-temperature IR reaction chamber. To remove adsorbed water in the MOFs, the sample was activated in the high-temperature IR reaction chamber followed by DRIFTS measurements after the sample was cooled to room temperature. The activation process was performed by heating the sample under a He flow (50 mL/min) at 200 °C for 1 h. The temperature was controlled by PID controller with a type-K thermocouple. KBr was used as a spectra background and all spectra were collected with 160 scans at a resolution of 4 cm^{-1} from 3000 cm^{-1} to 4000 cm^{-1} under a He atmosphere. We observed two distinct signals for sample contained UiO-66-NH_2. The peaks around 3520 and 3401 cm^{-1} are attributed to N−H asymmetric and symmetric stretches, respectively. The signal at around 3670 cm^{-1} corresponds to the μ_3-OH stretching of the zirconium cluster of UiO-66-NH_2

Raman measurement: Raman spectra were collected on a Micro-Raman system (XploRA, Horiba) with a 632 nm laser excitation at room temperature. Before each measurement, samples (Au@UiO-66-NH_2 or Au-PVP) were dropcast on a Si wafer (1.0 cm × 1.0 cm) and dried at 80 °C for 24 hours. Due to the low Raman signal of UiO-66-NH_2, the samples of UiO-66-NH_2 were dropcast on a Au coated Si wafer (1.0 cm × 1.0 cm, 50 nm thickness of Au). Considering the sensitivity of MOFs to laser excitation, a low output power (10 mW) was used to carry out the Raman measurement. The laser alignment and calibration at 632 nm were performed before each measurement using a Si wafer. All spectra were collected by averaging 10 accumulations with an accumulation time of 10 seconds.

Sample preparation for ICP-OES measurement: To prepare the sample for ICP-OES measurement, 5.0 mg of NP-in-UiO-66-NH_2 samples was quantitatively transferred into a 3.0 mL

Teflon vial, and the samples were dispersed in 300 μL of DMSO by sonication for 10 min. To digest the samples, 1 drop of 15 wt% aqueous hydrofluoric acid solution was added into the above solution and left for 3 h. To remove the hydrofluoric acid and DMSO, the digested samples were heated to approximately 150 °C overnight in a sand bath in a fume hood. The resulting solid was dissolved by 1.5 mL of aqua regia and the acidic solution was diluted to 25 mL with deionized water using a volumetric flask. Before the ICP-OES measurement, the solution was filtered through a filter membrane (0.22 μm). The quantitative analysis of Pd and Pt was carried out against calibration using known concentrations of standard solutions. ICP-OES spectrometry was performed using an Agilent 5100 instrument.

Alkene Hydrogenation: Samples were diluted with low surface area quartz and loaded into U-shaped glass reactors. The glass reactor was then connected to a home-built gas-phase flow system for alkene hydrogenation. Gas flows, including helium, hydrogen, and ethylene were regulated using calibrated mass flow controllers. The desired partial pressure of cyclohexene or cis-cyclooctene was achieved by bubbling He through the liquid and assuming saturation.[112] For all reactions, gas composition was analyzed with a mass spectroscope (MKS special V2000P). Temperature was controlled by a furnace (CARBOLITE) and PID controller (Diqi-Sense) with a type-K thermocouple. To test whether the metal NPs are encapsulated, the catalyst activity was normalized by ethylene hydrogenation kept at 40% conversion. To normalize the metal NP surface areas, the catalyst amount was carefully adjusted to have ethylene hydrogenation of 40%. The same amount of catalysts were used to perform the hydrogenation of cyclohexene and cyclooctene. Ethylene hydrogenation was run at 0 ˚C, cyclohexene hydrogenation is run at 25 ˚C, and cyclooctene hydrogenation was run at 40 ˚C. To test the alloy nature of encapsulated PdPt NP, 10 mg sample with similar loading (0.01 wt% Pd, Pt and Pd_xPt_1 alloy) of

encapsulated NP in UiO-66-NH_2 was diluted with low surface area quartz and loaded into glass reactors for ethylene hydrogenations activity measurement, run at 70 ˚C. The turnover frequency of ethylene hydrogenation was normalized by using the percentage of surface atoms following the palladium cluster diameter.[136]

Crotonaldehyde Hydrogenation: Catalysts were dispersed in 2 mL isopropanol solution in the 10-mL ampule, and then 40 μL crotonaldehyde (0.4 mmol) was added into the above solution. To compare the selectivity of our samples, the conversion of each reaction was kept at 30 %. Before catalysis, the high-pressure reactor vessel (Wattacas Inc., 500 mL) was pre-heated to 70 ˚C. Temperature was controlled using a hot plate (RCT basic, IKA) with a type-K thermocouple. Subsequently, the ampule was transferred into a high-pressure reactor vessel. The autoclave was purged 5 times with H_2 to remove air. Then, the hydrogenation of crotonaldehyde was carried at 30 bar H_2 at 70 ˚C for 18 h with magnetic stirring at 500 rpm. After that, the catalysts were separated by centrifugation, and the reaction solution was filtered through a filter membrane (0.22 μm). The products were analyzed on a gas chromatography-mass spectrometry (Shimadzu QP2010 Ultra, column: Rtx-5, 30 m × 0.25 mm × 0.25 μm). The response factors of each component were determined with standard samples and were used to calculate the conversion and selectivity.

2.5 Appendix

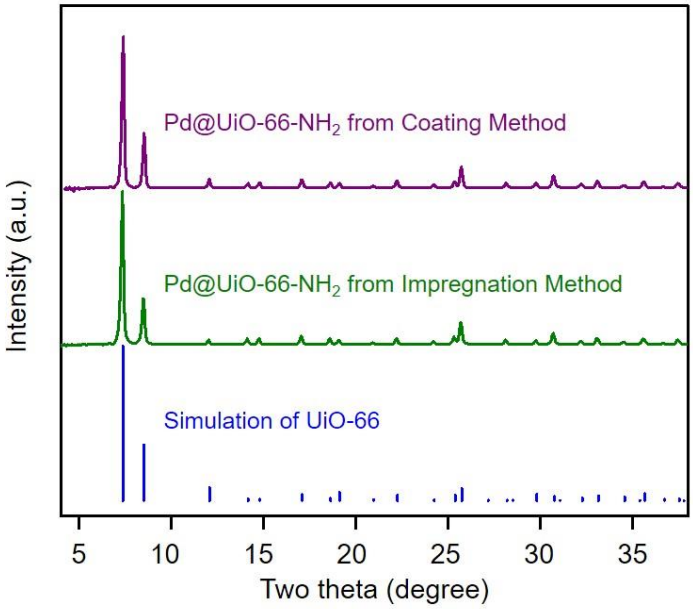

Figure A 2.1: PXRD patterns of Pd@UiO-NH_2 generated from impregnation and coating methods.

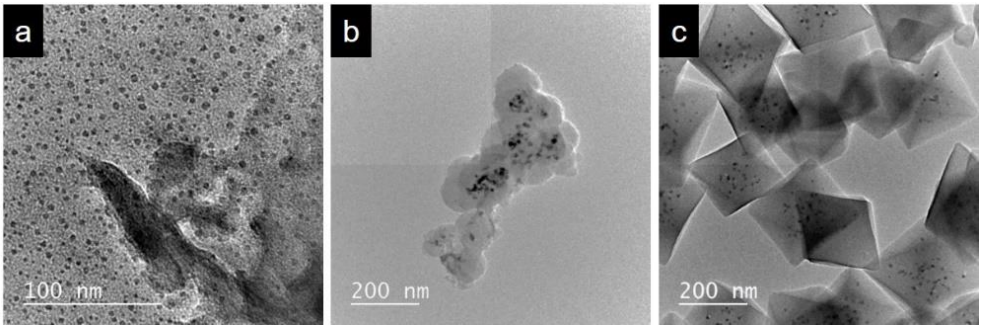

Figure A 2.2: Time study of the synthesis of Pd@UiO-66-NH2 using the one-pot method at reaction times of (a) 0.25 hours, (b) 1.25 hours, and (c) 6.5 hours.

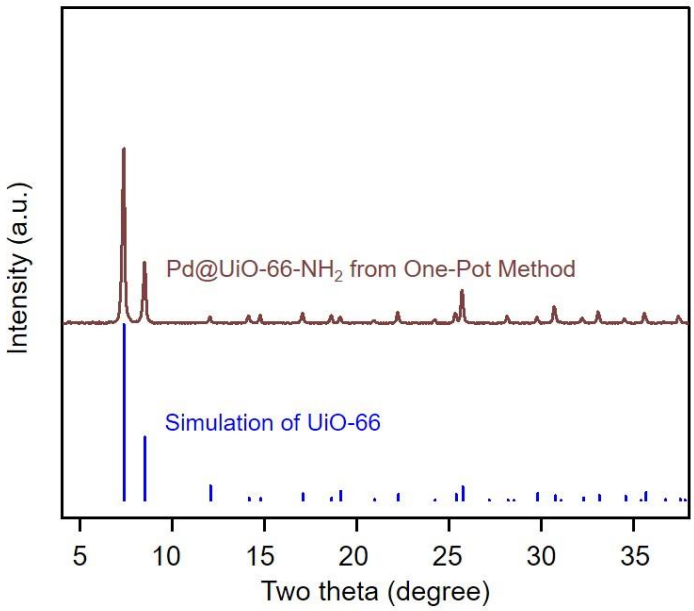

Figure A 2.3: PXRD patterns of Pd@UiO-66-NH_2 obtained using the one-pot method, and the simulation of UiO-66.

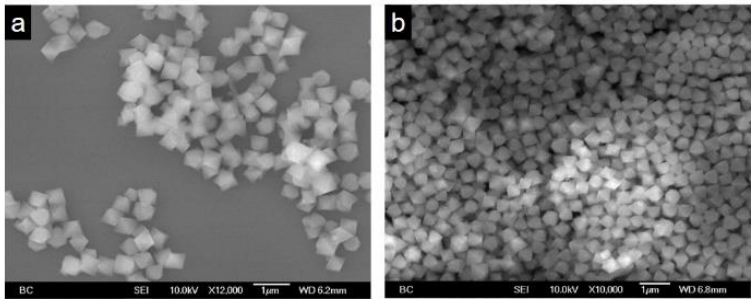

Figure A 2.4: SEM images of (a) pure UiO-66-NH_2 and (b) Pd@UiO-66-NH_2 obtained using the one-pot method.

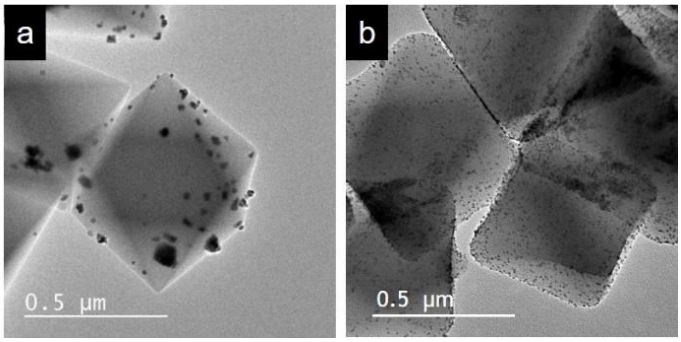

Figure A 2.5: TEM images of the one-pot synthesis using BDC without the amino-functionalization as MOF linkers, resulting in a series aggregates of (a) Pd and (b) Pt on the external surface of UiO-66.

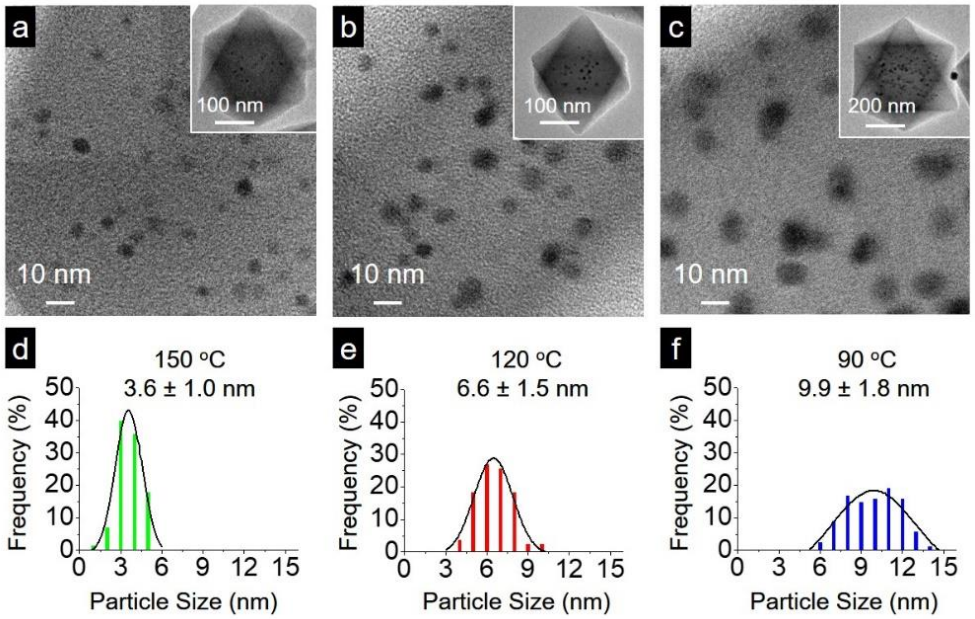

Figure A 2.6: TEM images and size distribution of the one-pot samples of Pd@UiO-66-NH_2 with controlled NP size synthesized at (a, d) 150 ˚C, (b, e) 120 ˚C and (c, f) 90 ˚C.

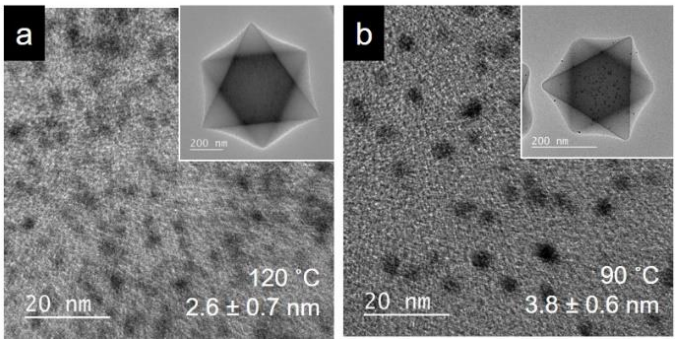

Figure A 2.7: TEM images of the one-pot samples of Pt@UiO-66-NH_2 with controlled NP size synthesized at (a) 120 ˚C and (b) 90 ˚C. The size distribution of each sample is shown in the figure.

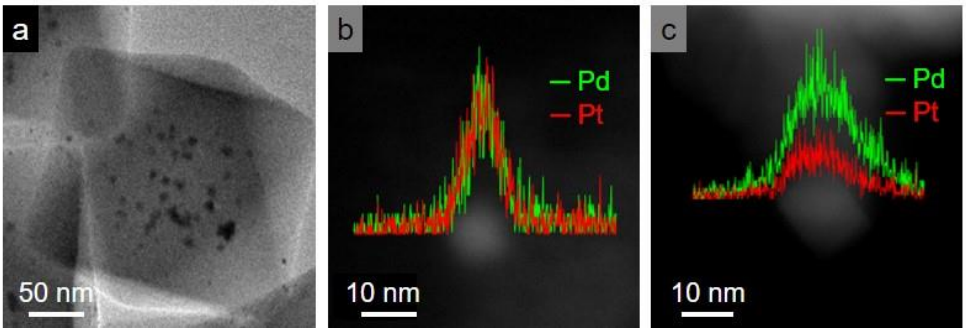

Figure A 2.8: (a) TEM images of $Pd_{0.7}Pt_{1.0}$@UiO-66-NH_2. (b, c) EDS line mapping of $Pd_{0.7}Pt_{1.0}$@UiO-66-NH_2 and $Pd_{3.2}Pt_{1.0}$@UiO-66-NH_2, respectively. Green color represents Pd, and red color represents Pt.

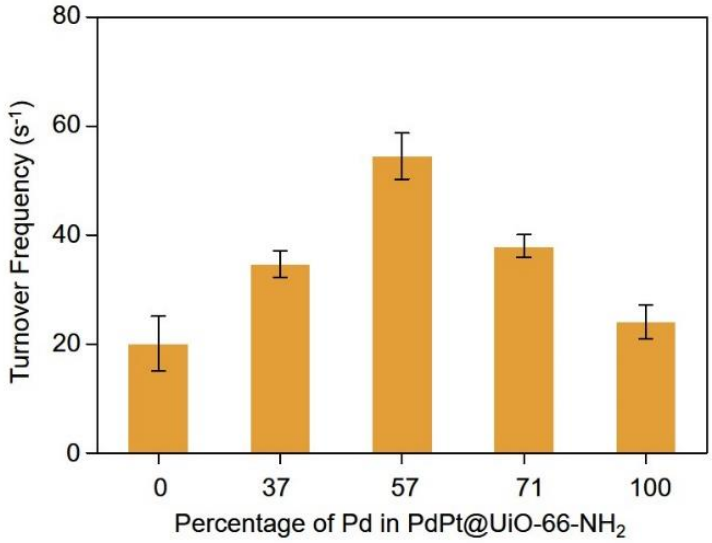

Figure A 2.9: Ethylene hydrogenation with the catalysts of the encapsulated PdPt alloy in UiO-66-NH_2. Ethylene hydrogenation is performed at 70 ˚C.

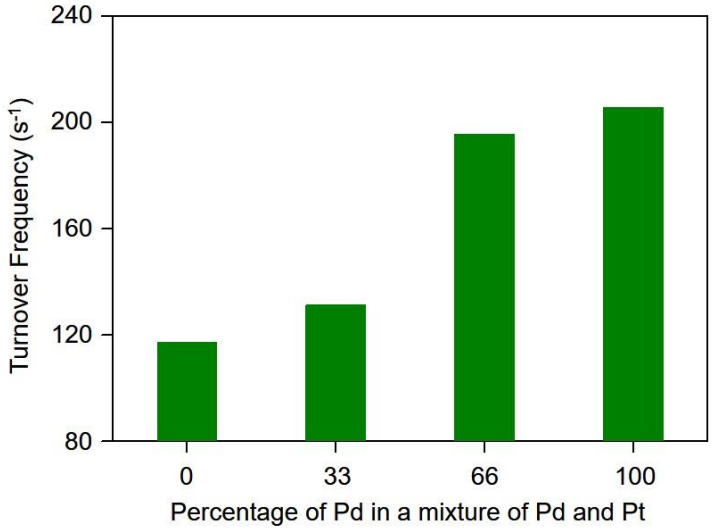

Figure A 2.10: Ethylene hydrogenation with the mixtures of Pd and Pt NPs. Ethylene hydrogenation was performed at 70 ˚C.

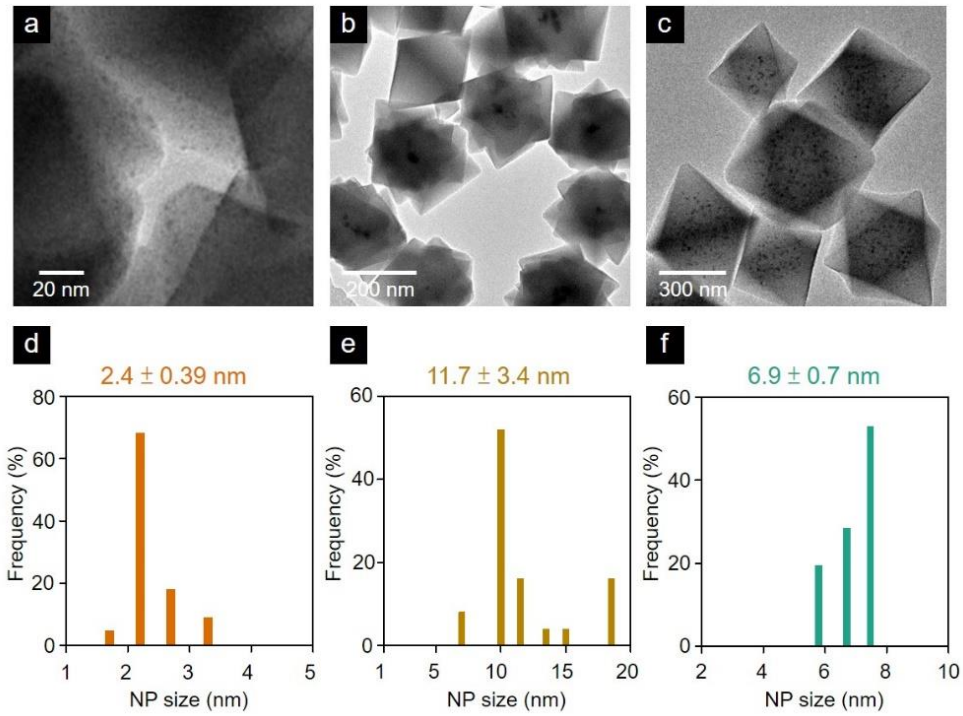

Figure A 2.11. TEM images and NP size distributions of Pd@UiO-NH_2 generated from (a, d) impregnation method, (b, e) coating method and (c, f) one-pot method.

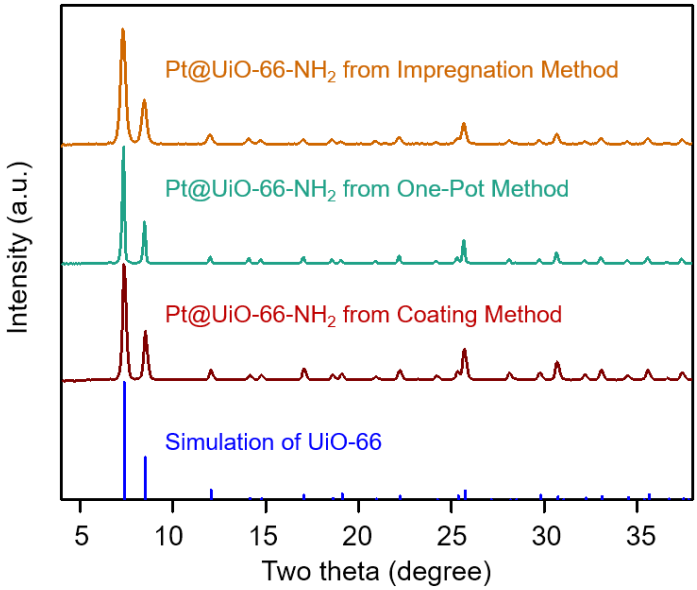

Figure A 2.12: PXRD patterns of Pt@UiO-NH_2 generated from impregnation method, coating method and one-pot method.

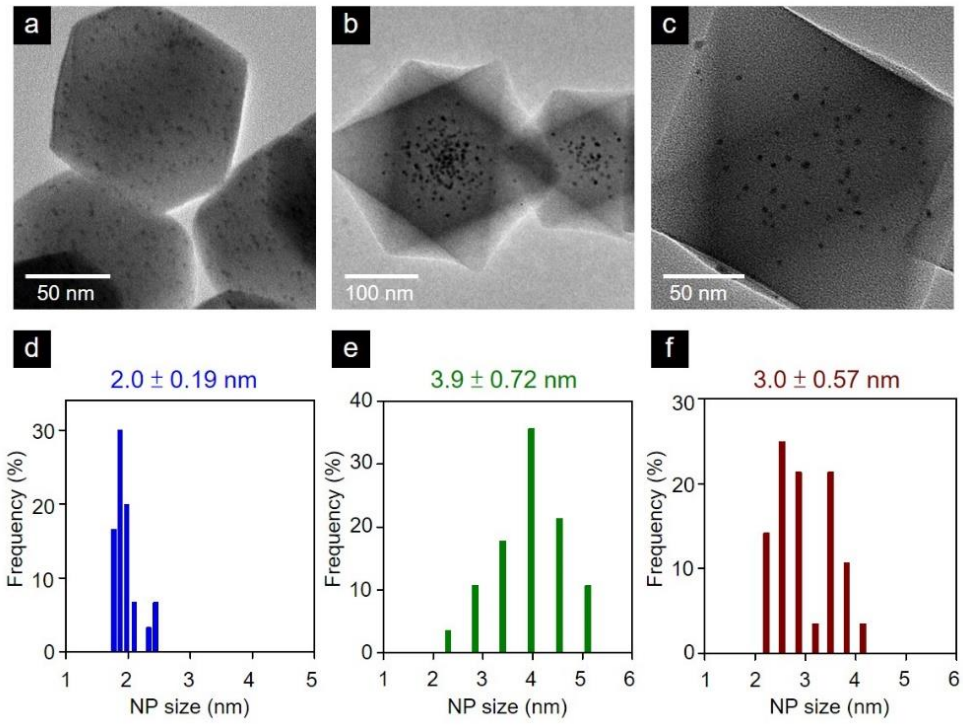

Figure A 2.13: TEM images and NP size distributions of Pt@UiO-NH_2 generated from (a, d) impregnation method, (b, e) coating method and (c, f) one-pot method.

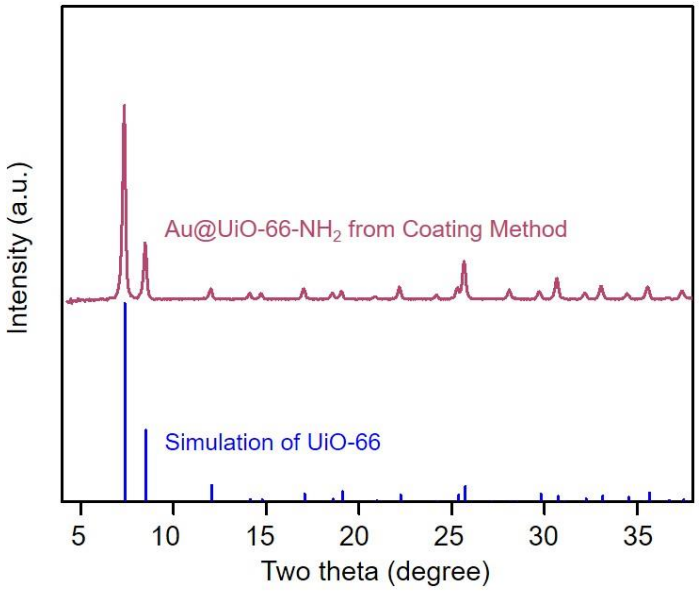

Figure A 2.14: PXRD patterns of Au@UiO-66-NH_2 obtained using the coating method

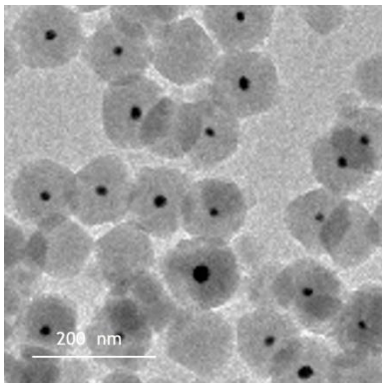

Figure A 2.15: TEM image of Au@UiO-66-NH_2 obtained using the coating method.

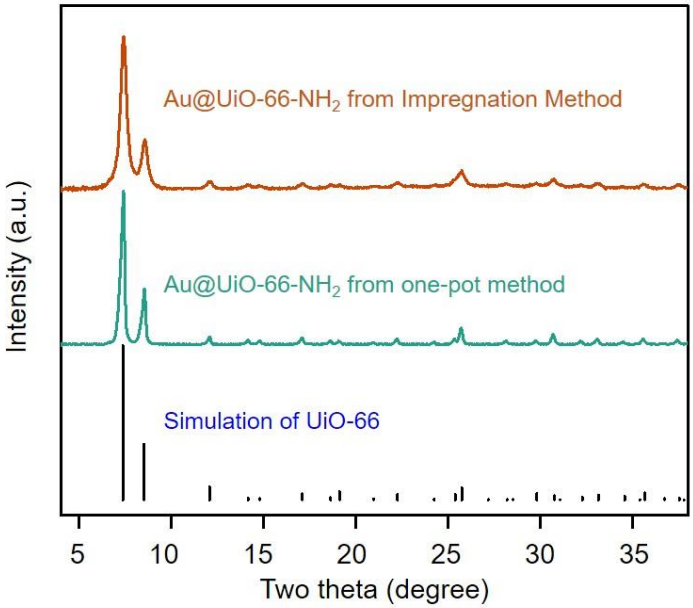

Figure A 2.16: PXRD patterns of Au@UiO-66-NH_2 obtained using the impregnation and one-pot method.

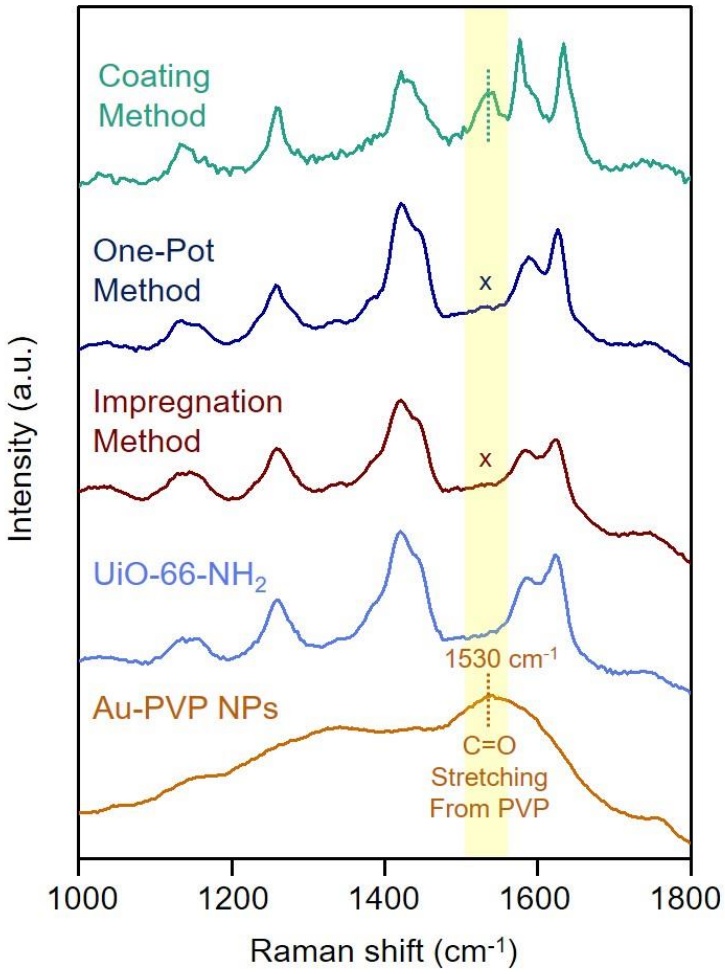

Figure A 2.17: Raman spectra of Au-PVP NPs, UiO-NH_2, and Au@ UiO-66-NH_2 samples generated by impregnation, one-pot and coating methods.

Table A 2.1: Summary of PdPt@UiO-66-NH_2 samples with various compositions

Sample	Pd (ppb)	Pt (ppb)	Mole ratio (Pd:Pt)
$Pd_{3.2}Pt_1$	1607	916	3.22
$Pd_{1.3}Pt_1$	1290	1767	1.34
$Pd_{0.7}Pt_1$	577	1472	0.72

Table A 2.2: Summary of NP loading in UiO-66-NH_2 samples

Sample	Metal loading (wt. %)
Pd-in-MOF Coating Method	2.5
Pd-in-MOF Impregnation Method	3.0
Pd-in-MOF One-Pot Method	3.0
Pt-in-MOF Coating Method	2.1
Pt-in-MOF Impregnation Method	3.0
Pt-in-MOF One-Pot Method	2.7

Table A 2.3: Summary of alkene hydrogenation and corresponding ethylene hydrogenation to normalize the catalyst surface areas.

Sample	Catalyst Amount (mg)	Conversion of Ethylene Hydrogenation (%)	Conversion of Cyclohexene Hydrogenation (%)	Conversion of Cyclooctene Hydrogenation (%)
Pd-on-MOF (control sample)	6.4 [a]	42.0	43.0	24.0
Pd-in-MOF Coating Method	16.8	40.0	36.0	2.1
Pd-in-MOF Impregnation Method	4.0 [b]	43.0	43.0	14.0
Pd-in-MOF One-Pot Method	1.2	44.0	37.0	1.0

[a] 6.4 mg of 0.5 wt% Pd on UiO-66-NH_2 samples. [b] 4.0 mg of the diluted catalysts prepared by mixing 25.2 mg UiO-66-NH_2 with 2.8 mg Pd@UiO-66-NH_2 generated by coating method.

Table A 2.4: Summary of selectivity for crotonaldehyde hydrogenation

Catalyst	Conversion (%)	Selectivity to Crotyl alcohol (%)	Selectivity to Butyraldehyde (%)	Selectivity to Butanol (%)
Pt-on-MOF (Control)	37.5 ± 3.2	6.0 ± 2.6	34.5 ± 9.3	59.4 ± 8.7
Pt-in-MOF Coating Method	31.7 ± 2.5	9.8 ± 0.2	71.3 ± 2.3	18.7 ± 2.5
Pt-in-MOF Impregnation Method	26.4 ± 6.0	42.8 ± 2.7	22.7 ± 0.49	34.2 ± 2.5
Pt-in-MOF One-Pot Method	32.1 ± 4.0	70.4 ± 4.9	17.4 ± 2.9	12.0 ± 2.0

Selectivity was determined by its ratio to the sum of all three products (crotyl alcohol, butyraldehyde and butanol). The standard deviation was obtained based on three independent measurements.

This page is on purposely left in blank

3.0 Chapter 3:

Creating an Aligned Interface between Nanoparticles and MOFs via Concurrent Replacement of Capping Agents

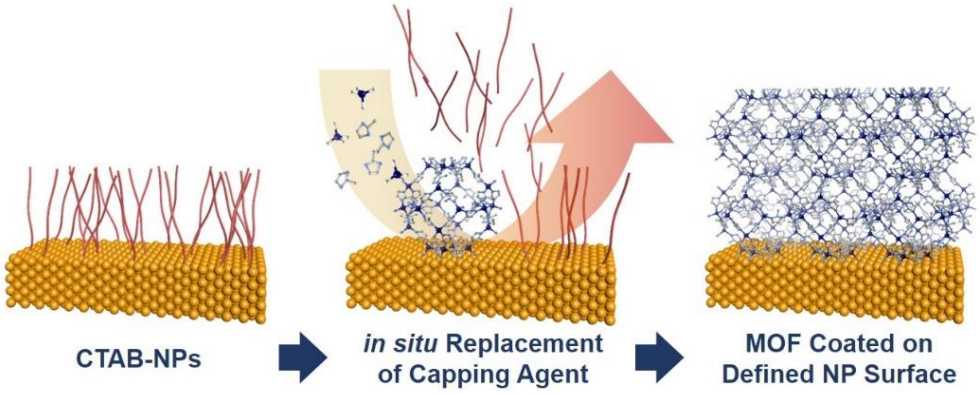

A significant portion of the work described in this chapter has been published in:

Li, Y.[#]; **Lo, W. –S.[#] (co-first author)**; Zhang, F.[#]; Si, X.; Chou, L. –Y.; Liu, X. –Y.; Williams, B. P.; Li, Y. –H.; Jung, S. –H.; Hsu, Y. –S.; Liao, F. -S.; Shieh, F. –K.; Ismail, M. N.; Huang, W.; Tsung, C. –K. Creating an Aligned Interface between Nanoparticles and MOFs by Concurrent Replacement of Capping Agents. *J. Am. Chem. Soc.* **2021**, 143, 5182–5190. Copyrights 2021 American Chemical Society. Portions of this chapter may be seen in Furui Zhang's 2017 thesis titled "Mechanism and Interface Study of One-to-one Metal NP/Metal Organic Framework Core-shell Structure, and in Yang Li's 2021dissertation titled "MOFs across Dimensions: Engineering Heterostructures and Thin Films for Catalysis and Energy Conversions". I thank them for the use of this material as a co-author of the above-mentioned manuscript.

3.1 Introduction

Great effort has been devoted to designing interfaces, as their structure shows a large influence on the performance of the whole system in various fields, such as electronics, biomedicines, and separations.[137-141] Recently, focus has been extended to complicated interfaces, which are composed of materials with distinct chemical components or crystal lattices.[141-144] For instance, to improve the selectivity of metal nanoparticle (NP) catalysts, applying metal-organic frameworks (MOFs) to the metal surface has recently been identified as an apt strategy for this long-standing and challenging goal.[101, 145-146] Selectivity control in this strategy relies on the structure of the NP-MOF interface, but interfacial structure remains difficult to control because metals and MOFs have distinct chemical compositions and structural dimensions that differ by orders of magnitude.

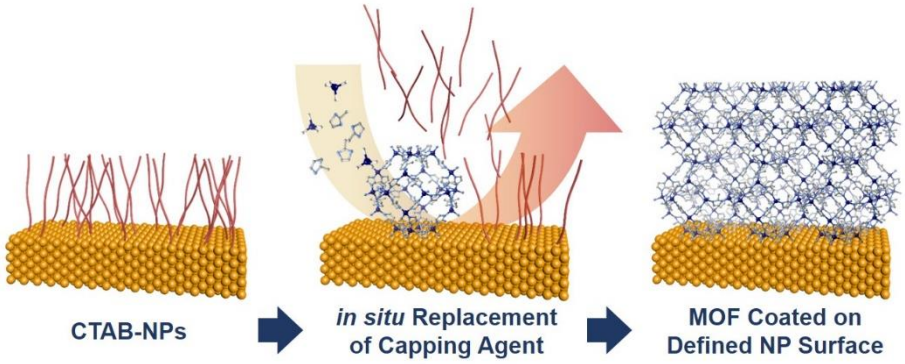

Figure 3.1: The formation of a direct NP-MOF interface using dynamic, weakly-adsorbed capping agents.

Currently, the most common approach to generate a controlled interface is to first synthesize shaped NPs through colloidal methods and then coat them with MOFs.[87] Compared to conventional impregnation methods,[103, 147] this approach indeed provides better control over the morphology and size of the metal NPs. However, it relies on adding capping agents, such as long-

chain hydrocarbon surfactants (e.g., oleic acid) or polymers (e.g., polyvinylpyrrolidone), which are normally trapped at the NP-MOF interface during coating, interrupting MOF growth and preventing direct contact between the NP and MOF.[70, 148] This interfacial residue is a general dilemma in many composite materials.[149] To solve this issue, we herein propose a new strategy to generate a well-defined interface in hybrid materials by introducing weakly adsorbed capping agents to mediate MOF growth (**Figure 3.1**). During growth, these capping agents gradually dissociate from the metal surface and the MOF directly grows on the gradually exposed NP surface. We hypothesize that when this *in situ* replacement is well mediated, a controlled interface between the MOF and NP can form.

To demonstrate this concept, we first selected zeolitic imidazolate framework-8 (ZIF-8) as the MOF and shaped metal NPs with cetyltrimethylammonium bromide (CTAB) as the surfactant.[73, 150] We introduced CTAB-capped NPs into a solution with fine-tuned amounts of MOF precursors. Because it has been reported that the gradual dissociation of CTAB can be trigged by changes in the chemical environment.[151-153] The rates of dissociation and *in situ* MOF growth were balanced by adjusting the CTAB and MOF precursor concentrations. Under optimized conditions, we obtained a core-shell structure with one metal NP encapsulated in one single-crystalline ZIF-8 nanocrystal, showing specific facet alignment at the interface. Coupling the information gained from diffuse reflectance infrared Fourier transform spectroscopy (DRIFTS) and Raman spectroscopy, the *in situ* replacement of capping agents by MOFs, leading to the formation of a direct interface, was revealed. With this understanding, we then applied our approach to encapsulate NPs into a more chemically stable Zr-based MOF. UiO-66-type (University of Oslo 66) MOFs have distinct chemical properties and crystal topologies from ZIF-8, demonstrating the generality of our method. Finally, a model reaction, the hydrogenation of an

α,β-unsaturated aldehyde, was carried out over samples generated with and without the well-mediated process. The well-defined interface showed over 99.0 % selectivity toward the desired unsaturated alcohol, outperforming the sample without a well-controlled interface (85.1 % selectivity). This work sheds light on the process of creating well-defined interface between materials with vastly different structural dimensions.

3.2 Results and Discussions

Cubic Pd NPs capped by CTAB (Pd-CTAB NPs) were synthesized through an established method that has been used to synthesize various metal NPs with defined shapes,[154] sizes,[155] and compositions.[156] The Pd-CTAB NPs were then added into a solution containing ZIF-8 precursors (2-methyl imidazole (2-mim) and $Zn(NO_3)_2$). We found that CTAB dissociation was indeed triggered after the NPs were exposed to aqueous 2-mim (**Figure A3.1**). The amount of CTAB in the supernatant was found to increase with time, as shown in **Figures A3.2 and A3.3**, suggesting that CTAB gradually and continuously dissociates from the metal surface, finally resulting in agglomeration of the metal NPs. To control the dissociation of CTAB while avoiding the aggregation of metal NPs during the MOF coating, the concentration of each component was controlled to fine-tune the kinetics of each process. The detailed concentrations and procedures can be found in the supporting information. Under the optimized conditions, ZIF-8 was evenly coated on individual Pd NPs, forming Pd@ZIF-8 with a one-to-one, core-shell structure (**Figures 3.2a-b**). The single-crystalline nature of ZIF-8 coating was revealed by selected area electron diffraction (SAED) taken along the [001] zone axis (**Figure 3.2c**), where spots from the {200} and {110} planes can be clearly observed. The well-defined NP shape was also preserved after coating. Clear electron diffraction patterns indicating single-crystalline Pd was observed while decreasing

the working distance, showing {200} and {220} planes along the [001] zone axis (**Figure 3.2d**). With further analysis of the relationship between two diffraction patterns, we have observed that the [100] direction of the ZIF-8 crystal aligns well with the [100] direction of the Pd nanocrystals, indicating a facet alignment along the [001] direction despite the vastly different structural dimensions **(Figure 3.2e)**. This alignment was also observed by powder X-ray diffraction (XRD). When the core-shell particles are well assembled on the substrate, both Pd and ZIF-8 showed enhanced diffraction intensity corresponding to the {100} facets **(Figure 3.2f)**. This unique alignment is discussed in detail later.

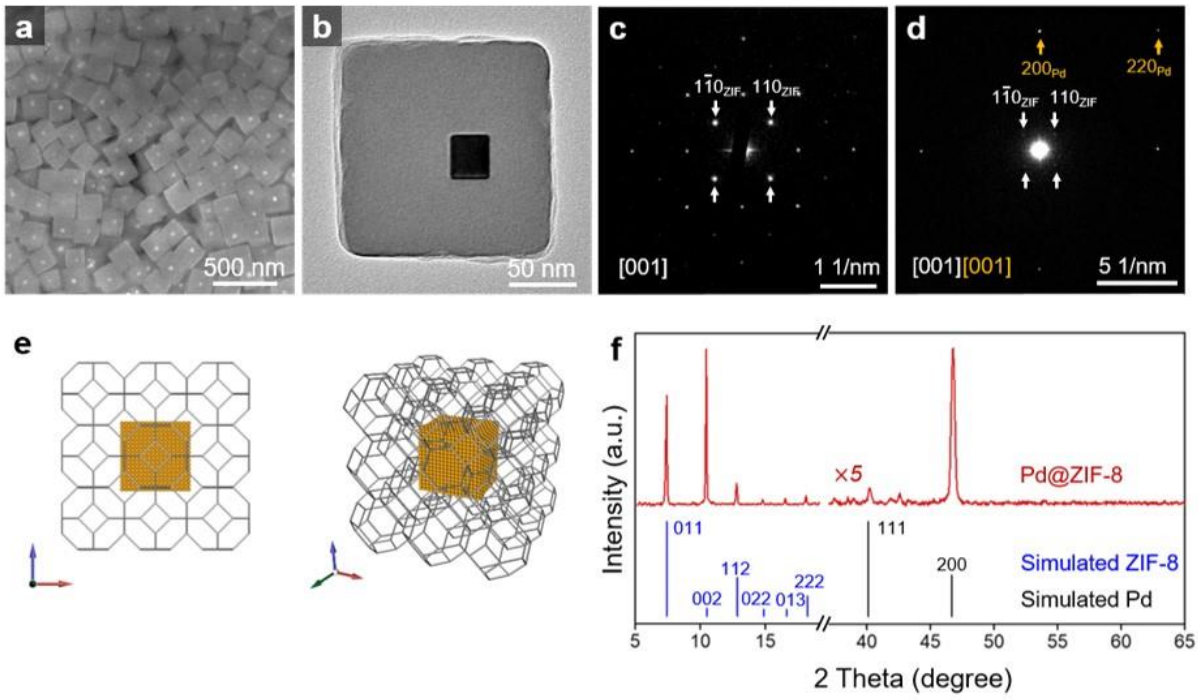

Figure 3.2: One-to-one encapsulation of metal NPs in ZIF-8. (a) SEM image, (b) TEM image, (c-d) SAED patterns of Pd and ZIF-8 along [001] directions, (e) 3D modeling projections at [001] directions, and (f) XRD patterns of Pd@ZIF-8.

Since global techniques like SEM, TEM, and XRD do not provide direct evidence of the interfacial structure, diffuse reflectance infrared Fourier transform spectroscopy (DRIFTS) and

Raman spectroscopy were used to characterize the interfacial structures of Pd@ZIF-8 composites. We sought to understand the interface from two perspectives: First, is capping agent trapped at the NP-MOF interface? Second, is the MOF coated directly onto the metal surface?

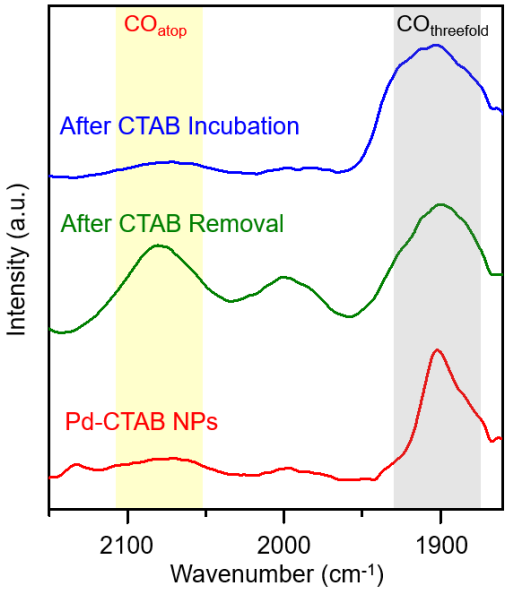

Figure 3.3: CO-DRIFTS spectra of Pd-CTAB NPs, the clean Pd surface, and the clean Pd surface after adding CTAB.

To answer the first question, we employed carbon monoxide as a probe molecule to test the metal surface through CO-DRIFTS.[157-158] The small size of CO allows for its diffusion through the ZIF-8 shell to access the metal surface, and the vibrational stretching mode of adsorbed CO is sensitive to the nature of the metal surface.[159] Therefore, the characteristic CO stretching frequency can be used to determine the amount of adsorbed capping agent on the metal surface.[160-161] To establish a reference for our system, we first carried out CO-DRIFTS on pure Pd NPs, with or without CTAB, supported on an inert substrate. As shown in **Figure 3.3**, three clear IR bands were observed for the clean Pd surface, which can be grouped into three binding modes: 2050-2100 cm^{-1} for linearly bound CO (CO_{atop}), 1950-2000 cm^{-1} for bridging bound CO (CO_{bridge}), and 1875-1925

cm^{-1} for threefold bound CO ($CO_{threefold}$).[115, 162] On the other hand, when CTAB adsorbed on the Pd surface, only the $CO_{threefold}$ band was observed. To verify that this difference can be used to monitor changes in adsorption behavior at the metal surface, we added CTAB to the clean Pd surface. We were indeed able to observe conversion from three distinct bands to one threefold band. These data clearly show that the CO_{atop} band is sensitive to the adsorbed CTAB and changes in its intensity can be used to monitor the Pd NP surface.

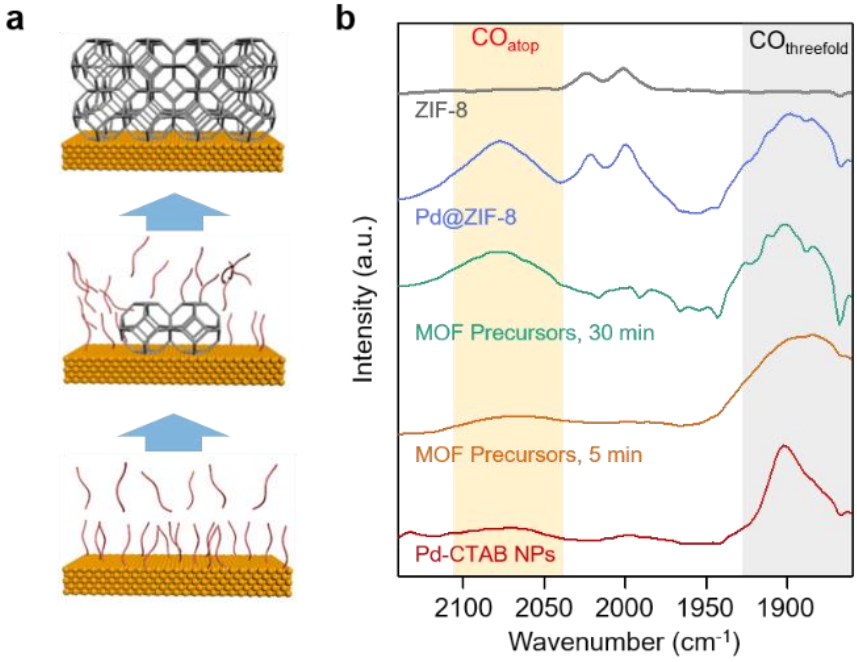

Figure 3.4: (a) Schematic illustration of CTAB dissociation during MOF coating. (b) CO-DRIFTS spectra of Pd-CTAB NPs, Pd-CTAB NPs incubated in MOF precursor (2-mim) for 5 min and 30 min, Pd@ZIF-8 with direct interface, and ZIF-8.

Using CO-DRIFTS, we investigated the changes of the CTAB on Pd NP surface in the presence of ZIF-8 precursor. As shown in **Figure 3.4**, the intensity of the CO_{atop} peak (~ 2080 cm^{-1}) increased with precursor treatment time, indicating the gradual dissociation of surface CTAB. Notably, for the Pd@ZIF-8 product after coating, a high-intensity CO_{atop} mode was seen, along

with two distinct peaks at 2020 cm^{-1} and 2000 cm^{-1} attributed to ZIF-8. This observation fits well with our hypothesis that the weakly-adsorbed capping agent gradually dissociates from the metal surface during the formation of the MOF shell.

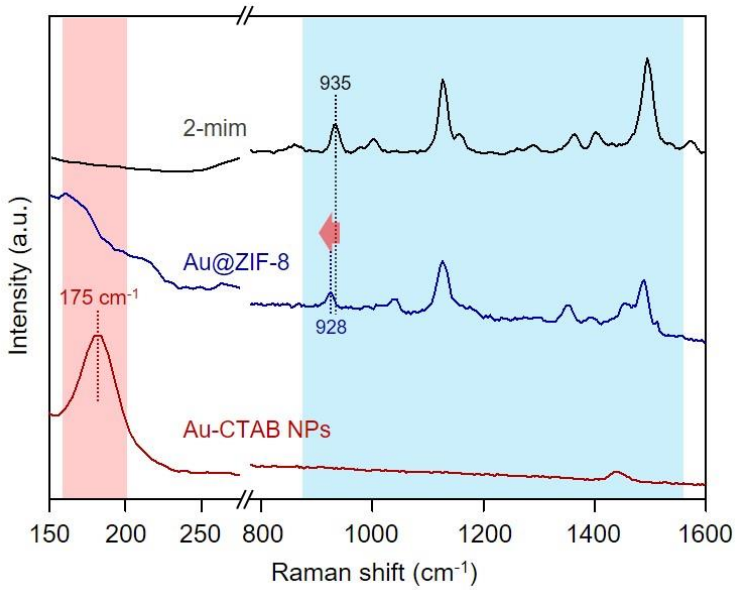

Figure 3.5: *in situ* Raman spectra for the formation of Au@ZIF-8 with a direct interface. The capping agents were observed to dissociate during MOF coating, forming direct contact between ZIF-8 and the metal surface.

To further study the behavior of CTAB at the interface and determine whether there is a direct contact between the MOF shell and the metal surface, Au NPs (Au-CTAB NPs, **Figure A3.4**) were employed to allow for surface-enhanced Raman spectroscopy (SERS) studies.[163] As shown in **Figure 3.5**, Au-CTAB NPs showed a vibrational signal at 175 cm^{-1}, referring to the stretching of the bond between the Au surface and the adsorbed Br^- of the capping agent.[164-165] After the introduction of the Au-CTAB NPs to the ZIF-8 precursor, however, the vibrational signal at 175 cm^{-1} greatly decreased. This result indicates CTAB dissociates from the metal surface in the presence of MOF precursors, which agrees well with the IR observations. Interestingly, it also

suggests that CTAB dissociation is accomplished by removal of the whole surfactant molecule, including both cations and anions. A set of bands also appeared in the 800-1500 cm^{-1} region (**Figure 3.5**), which was assigned to the vibrations of 2-mim in ZIF-8 (**Table A3.1**).[166] It has been reported that the 2-mim could interact with the metal surface through the imidazole "pyridine N", so we compared the spectral feature of out-of-plane bending modes of NH (γ(NH)) at around 928 cm^{-1}.[167-168] The stretching of NH was absent in bulk ZIF-8 due to the deprotonation of 2-mim when forming Zn-N bonds (**Figure A3.5**). Therefore, the observation of NH bending at 928 cm^{-1} in Au@ZIF-8 could be attributed to the 2-mim at the NP-MOF interface. After the NH moiety interacted with the metal surface, the interaction would lead to a weaker NH bending, resulting in a redshift of the N-H bending frequency. In the spectra, Au@ZIF-8 sample showed a redshift of the NH bending mode (928 cm^{-1}) compared to free 2-mim (935 cm^{-1}), suggesting the adsorption of ZIF-8 on the metal surface through the imidazole "pyridine N" (see **Figure A3.5** for more detailed discussion). This result provides further evidence that ZIF-8 has direct contact with the metal surface.

Next, we investigated the correlation between the capping agent dissociation process and the resulting interfacial and material properties. To that end, we carried out a control experiment where the kinetically inefficient dissociation of CTAB was intentionally designed by introducing excess CTAB into the solution during the ZIF-8 coating (**Figure 3.6**). Indeed, the dissociation of CTAB was significantly suppressed with an increased amount of exogenous CTAB as shown by the missing of CO_{atop} band in CO-DRIFTS (**Figure 3.6**). This suggests that the sluggish desorption kinetics kept the CTAB molecules on the metal surface, trapping them at the interface in the final encapsulated Pd@ZIF-8 sample and resulting in an indirect interface.

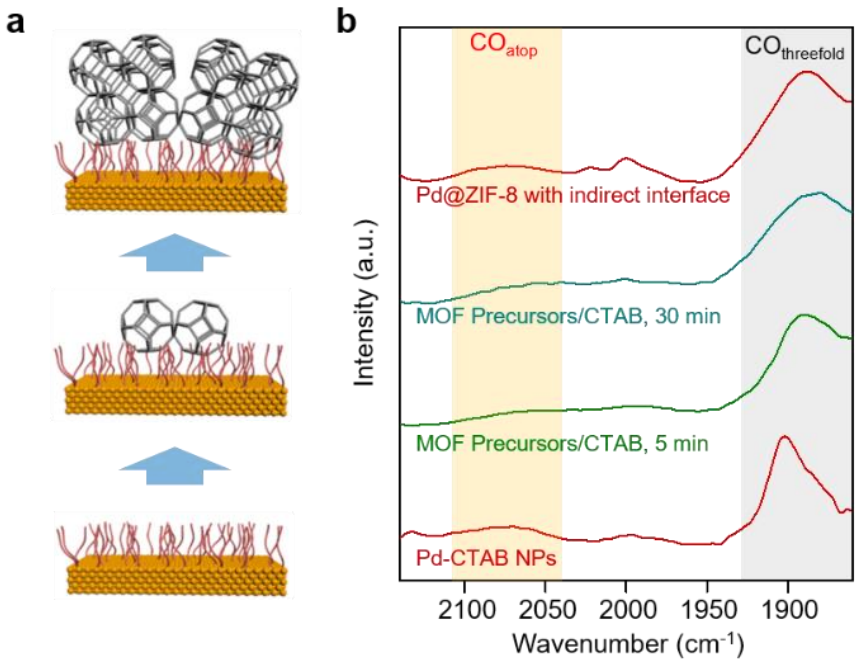

Figure 3.6: (a) Schematic illustration of CTAB dissociation with a higher concentration of CTAB present during MOF coating. (b) CO-DRIFTS spectra of Pd-CTAB NPs, Pd-CTAB NPs incubated in MOF precursor with exogenous CTAB (0.8 mM) for 5 min and 30 min, and Pd@ZIF-8 with indirect interface.

Notably, polycrystalline ZIF-8 coatings (**Figure 3.7b, e, h**) were observed with indirect interfaces formed in the presence of excess exogenous CTAB. This result is in sharp contrast with the single-crystalline Pd@ZIF-8 (**Figure 3.7a, d, g**). When the concentration of CTAB additive further increased, NPs were even only partially coated with ZIF-8 (**Figure 3.7c, f, i**). The homogeneity of the ZIF-8 shell coating, then, has a direct relationship with the amount of CTAB on the metal surface. This idea is further supported by the positive relationship between the amount of surface CTAB and the yield of polycrystalline ZIF-8 coatings (**Figure 3.8**; **Table A3.2**). To have a better understanding on the process, the early stages of both single- and polycrystalline formation were also investigated by EM (**Figure A3.6**). The ZIF-8 crystal growth was found to initiate at a single point to form single-crystalline Pd@ZIF-8 materials. In contrast, for

polycrystalline Pd@ZIF-8, generated via Pd NPs with more CTAB on the surface, multiple ZIF-8 seeds formed and surrounded one NP at an early stage. We thus reason that the interfacial CTAB alters ZIF-8 nucleation and interrupts its growth, generating not only an indirect interface but also polycrystalline coatings. In other words, the dynamic replacement process allows for a capping-agent-free interface with a better-controlled crystal structure. Further impact of the interface on the engendered materials will be discussed in the next section.

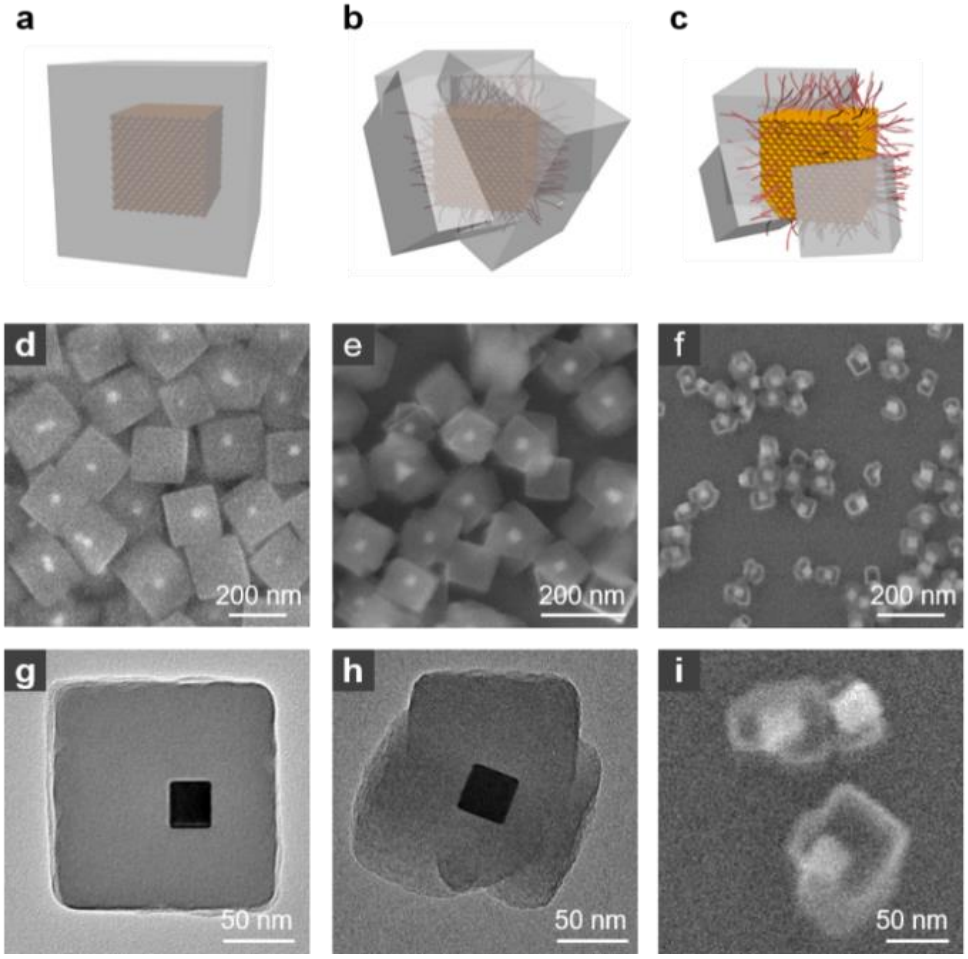

Figure 3.7: The impact of CTAB dissociation on MOF coating. Schematic illustrations, SEM images, and TEM images of Pd@ZIF-8 with a direct interface (a, d, g) and with an indirect interface obtained using an exogenous CTAB concentration of 0.8 mM (b, e, h) and 1.2 mM (c, f, i).

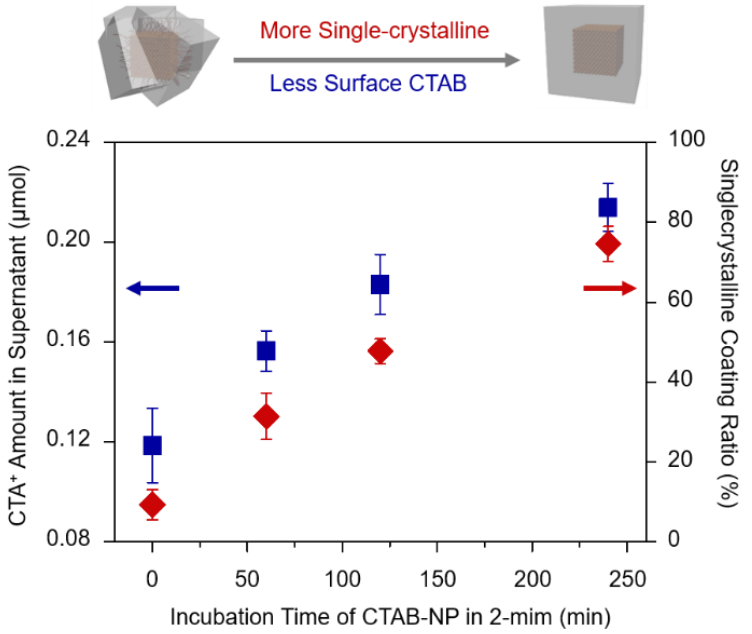

Figure 3.8: Quantitative analysis of the effect of surface CTAB on MOF growth. Blue square ■: The CTAB amount in the supernatant after treating Pd-CTAB NPs with 2-mim (50 mM) for different lengths of time, monitored by ^{1}H NMR. The higher amount in the supernatant, the lower amount of surface CTAB. Red diamond ♦: The ratio of single-crystalline coating in Pd@ZIF-8 samples obtained by treating Pd-CTAB NPs with 2-mim for different lengths of time before encapsulation. The numbers of the single- and polycrystalline Pd@ZIF-8 were counted through SEM images.

The difference between the samples with direct and indirect interfaces were additionally analyzed by thermogravimetric analysis (TGA) and a model hydrogenation reaction. As shown in **Figure A3.7**, the resulting TGA curves showed similar features as pure ZIF-8 crystals for both samples,[20] while the larger weight-loss for the indirect sample was credited to the trapped CTAB molecules. To further verify that the trapped CTAB is on the metal surface at the interface, we used gas-phase ethylene hydrogenation as a probe reaction (**Figure A3.8**). As expected, the sample with a direct interface displayed a reaction rate of 1.78×10^{-3} mol·s^{-1}·g$_{Pd}^{-1}$, which is 3.5-fold higher than that of the sample with an indirect interface (5.02×10^{-4} mol·s^{-1}·g$_{Pd}^{-1}$). This indicates

that the direct interface is cleaner and thus more catalytically active than the indirect interface, where a large number of active sites on the Pd surface were occupied by capping agent.

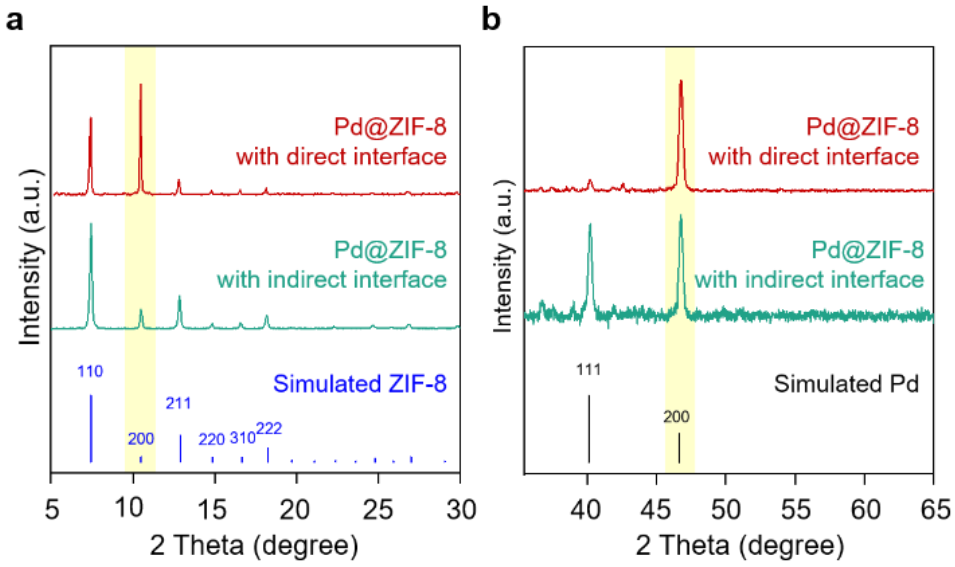

Figure 3.9: PXRD patterns of Pd@ZIF-8 with a direct (red) or an indirect (green) interface. PXRD patterns (a) from 5 to 30 degrees, displaying characteristic ZIF-8 peaks, and (b) from 35 to 65 degrees, displaying characteristic Pd peaks.

PXRD patterns of the two samples drop-casted on substrates were also compared (**Figures 3.9 and A3.14**). For samples with an indirect interface, the XRD patterns were in good agreement with the simulated patterns of ZIF-8 and Pd metal. For sample with direct interface, the cubic Pd@ZIF-8 particles tended to self-assemble on the substrate along the [001] direction of ZIF-8 due to their high uniformity, as evidenced by the enhanced intensity of the (200) diffraction peak. In stark contrast, the (110) peak possessed the highest intensity in the diffraction profile of the sample with the indirect interface (as seen in typical ZIF-8 powders due to its crystal structure).[169] A preferential orientation along the [100] direction of the encapsulated Pd NPs was also observed. The dominant peak of the sample with a direct interface was found to be (200), while the dominant

peak of randomly oriented Pd NPs should be (111).[170] This concerted orientation of both ZIF-8 and Pd crystals further indicates a facet alignment between ZIF-8 and Pd. This global observation of facet alignment was consistent with the result observed via a single particle under electron microscopy: six sets of {100} planes of the Pd NP aligned with six sets of {100} planes of ZIF-8, further supported by the SAED pattern. As shown in **Figure 3.2d**, the {220} planes of Pd and {110} planes of ZIF-8 were well aligned. This relative orientation suggests that the capping agent mediated growth of MOF can generate a better controlled interfaces. The detailed mechanism of alignment is currently under investigation.

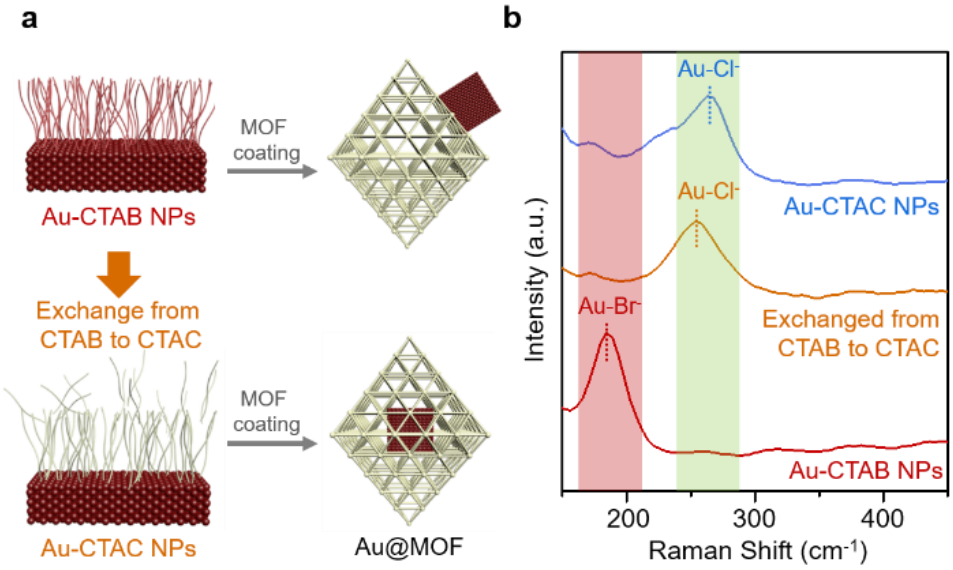

Figure 3.10: Analysis of surface CTAB and CTAC. (a) Schematic illustration of CTAB and CTAC dissociation during MOF coating. (b) Raman spectra of Au-CTAB NPs (red), Au NPs after capping agent exchange from CTAB to CTAC (orange), and Au NPs synthesized directly with CTAC (blue, Au-CTAC NPs).

To test the generality of this direct interfacial growth approach, we explored the possibility of encapsulating metal NPs into another MOF with distinct chemical properties and a different

topology, UiO-66. It is also more chemically and thermally robust than most current MOF materials, including ZIF-8.[171-172] The outstanding stability of the MOF shell can significantly broaden the application of these NP@MOF materials, such as for catalytic reactions requiring harsh conditions.

Direct application of our coating method failed to encapsulate the NPs (**Figure A3.9**). To optimize our conditions for the new MOF, we reviewed the key mechanistic requirements. Our ZIF-8 system has shown that it is important to trigger capping agent dissociation for replacement during MOF coating. We thus hypothesized that the dissociation of CTAB was not sufficient under the conditions of UiO-66 formation. To promote capping agent dissociation, the synthetic condition was modified accordingly. First, to initiate capping agent dissociation, we tried to increase the concentration of linkers. This need could be satisfied by the use of tetrafluoroterephthalic acid (BDC-F_4) as the MOF linker to synthesize UiO-66, which is chosen for its high solubility in aqueous solution.[173-174] Second, cetyltrimethylammonium chloride (CTAC) was used as capping agents to substitute CTAB due to its weaker binding strength with metal surface than that of CTAB.[175] The kinetic capping agent exchange was conducted by exposing Au-CTAB NPs to an aqueous solution with a high concentration of CTAC. SERS spectra were collected to track the exchange process (**Figure 3.10**). SERS analysis indeed indicates the successful replacement of CTAB by CTAC. Compared to Au-CTAB NPs, the signal from Au-Br^- decreased significantly after the CTAB-CTAC exchange. In the meanwhile, a Au-Cl^- peak also appeared around 265 cm^{-1}.[176] After the capping agent exchange, the Au-CTAC NPs were then introduced into MOF precursor solution, following the previously mentioned encapsulation procedure. This optimized synthesis led to a successful encapsulation of NPs by MOF shell in a one-to-one manner, akin to that of the metal NP@ZIF-8 system (**Figure A3.10**). With this

understanding, Au NPs directly synthesized with CTAC were also used to perform the MOF coating (**Figure A3.11**). As shown in **Figure 3.11**, again, each Au NP was encapsulated into a single-crystalline MOF crystal. The PXRD pattern confirmed its identical crystallinity to the simulated UiO-66 (**Figure A3.12**). The single crystallinity was supported by SAED (**Figure 3.11d**). These results clearly demonstrate the generality of this method and the importance of controlling the dissociation dynamics of capping agents for successful encapsulation.

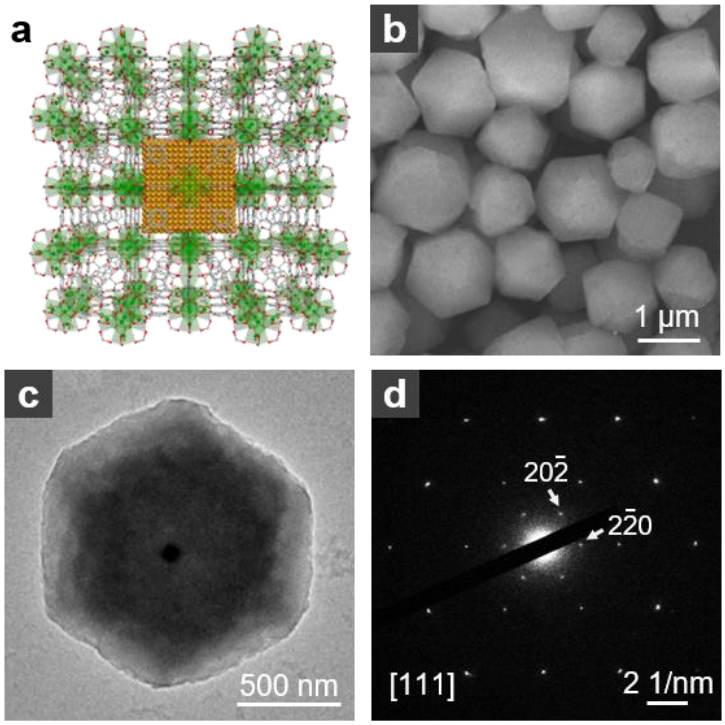

Figure 3.11: A single Au NP encapsulated in UiO-66-F_4. (a) Schematic illustration, (b) SEM image, (c) TEM image, and (d) SAED pattern from (c).

We then tested the hydrogenation of an α,β-unsaturated aldehyde over NP@UiO-66 samples, with and without the direct interface. Unsaturated alcohols are the desired products of this hydrogenation, because they are critical raw materials for pharmaceuticals.[177] However, this organic transformation is challenging, as the hydrogenation of C=C bonds is more

thermodynamically favorable than the hydrogenation of C=O bonds. Applying the MOF coating on metals to promote selectivity of the hydrogenation of C=O bonds has been observed in many studies,[68, 127, 178] and several mechanisms have been proposed such as steric effect.[61] While these mechanisms are different, a direct NP-MOF interface is required for the MOF layer to modulate the intermediates because the reaction takes place on the surface of metals.[1] With this information in mind, we carried out the hydrogenation of cinnamaldehyde over four catalysts, Au NPs with no MOF coating (Au-on-SiO_2), Au NPs on the external surface of MOF (Au-on-MOF), Au NPs with an indirect MOF interface, and Au NPs with a direct MOF interface. To compare their selectivity, the loading of each catalyst was controlled to give the same conversion (**Table A3.3**). For the pure Au catalysts without MOF coating, the selectivity for unsaturated cinnamyl alcohol was 61.8 %, while 3-phenylpropionaldehyde and 3-phenylpropanol were both obtained (**Figure 3.12**). The sample of pure Au NPs on the MOF surface, which served as a control (Au-on-MOF), showed a 53.3 % selectivity to unsaturated cinnamyl alcohol. The catalyst with an indirect interface showed an increase in selectivity toward cinnamyl alcohol to 85.1%, indicating that the MOF coating indeed promotes selectivity. Remarkably, cinnamyl alcohol was the only product detected for the catalyst with a direct interface. As expected from the high stability of UiO-66, the crystal structures of both Au@MOF materials were well maintained after catalysis (**Figure A3.12 and A3.13**). This result clearly highlights the importance of well-defined interfaces for the catalytic performance of NP@MOF materials.

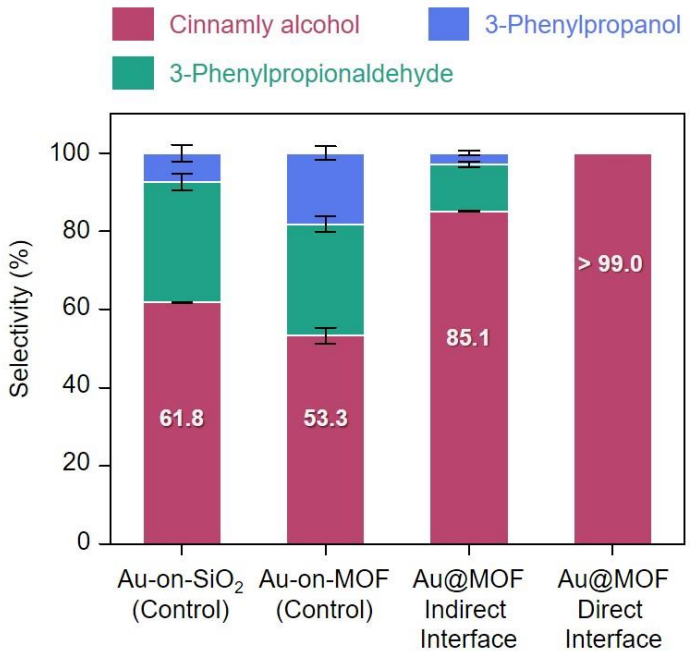

Figure 3.12: Selectivity for cinnamaldehyde hydrogenation over pure Au NPs without a MOF coating, Au NPs on the external surface of MOF, encapsulated Au NPs with an indirect NP-MOF interface, and encapsulated Au NPs with a direct NP-MOF interface. Cinnamyl alcohol is the preferred product, and its selectivity was determined by its ratio to the sum of all three products. Error bars indicate the standard deviation of three independent measurements.

3.3 Conclusions

Here, we have developed an approach to generate well-controlled interfaces between NPs and coated MOFs. Our approach takes advantage of the *in situ* replacement of weakly adsorbed capping agents by MOF precursors during MOF coating. The concept was initially demonstrated on metal NPs capped by CTAB and coated in ZIF-8. Systematic IR and Raman spectroscopic studies showed that CTAB molecules gradually dissociate from the metal surface and are replaced *in situ* by MOFs, resulting in a direct interface between metal NPs and ZIF-8. The well-controlled interface leads to the formation of a single-crystalline MOF coating with a specific crystal facet

alignment. The understanding from the ZIF-8 system was extended to coat UiO-66 type MOF on NPs with a direct interface, where NPs were again individually encapsulated in single-crystalline MOF crystals in a one-in-one fashion. The hydrogenation of an α,β-unsaturated aldehyde was employed to test the catalytic impact of interfacial structure. High selectivity towards the desired unsaturated alcohol product was achieved over the direct interface. In sum, we have demonstrated a new approach to encapsulate defined NPs into MOFs, generating a direct, clean NP-MOF interface *via* the *in situ* replacement of capping agents. This new strategy opens a new route to achieve hybrid materials well-defined interfaces.

This work is supported by National Science Foundation (CHE 1566445), Iowa State University, and Boston College. Authors thank Prof. Matthias Waegele at Boston College for valuable suggestions on the spectroscopic studies.

3.4 Experimental Procedures

Chemicals: Cetyltrimethylammonium bromide (CTAB, Sigma-Aldrich, ≥ 99%), cetyltrimethylammonium chloride (CTAC, Tokyo Chemical Industry Co., Ltd., > 95%), ascorbic acid (Sigma-Aldrich, ≥ 99%), hydrogen tetrachloroaurate trihydrate ($HAuCl_4 \cdot 3H_2O$, Sigma-Aldrich, ~50% Au basis), hydrogen tetrachloropalladate (H_2PdCl_4, Sigma-Aldrich, 98%), zinc nitrate hexahydrate ($Zn(NO_3)_2 \cdot 6H_2O$, J.T.Baker, 99.6%), 2-methylimidazole (2-mim, Alfa Aesar, 97%), sodium borohydride ($NaBH_4$, Sigma-Aldrich, 98.0%), zirconyl chloride octahydrate ($ZrOCl_2 \cdot 8H_2O$, Acros Organics, > 98%), tetrafluoroterephthalic acid (BDC-F_4, Sigma-Aldrich, 97%), zirconium chloride ($ZrCl_4$, Sigma-Aldrich, > 99.5%), terephthalic acid (BDC, Sigma-Aldrich, 98%), acetic acid (Sigma-Aldrich, ≥ 99.7%), deuterium oxide (D_2O, Cambridge Isotope

Laboratories, Inc., D-99.9%), methylsulfonylmethane (Sigma-Aldrich, certified reference materials), sodium citrate tribasic dihydrate (Sigma-Aldrich, ≥ 99.0%), polyvinylpyrrolidone (PVP, MW 40,000, Sigma-Aldrich) were used without further purification. Ultrapure deionized water (DI water, 18.2 MΩ) was used for all solution preparations. Element standard solutions, palladium (1000.00 μg/mL) and zinc (100.00 μg/mL), for ICP-OES were purchased from Inorganic Ventures. Ethylene (Airgas, 99.995%), hydrogen (Airgas, 99.999%) and helium (Airgas, 99.999%) were used for ethylene hydrogenation. Cinnamaldehyde (Sigma-Aldrich, 99.0 %) and hydrogen (Airgas) was used for cinnamaldehyde hydrogenation.

Characterizations: A Bruker AXS D2 Phaser diffractometer was used for the powder X-ray diffraction characterization (PXRD). Transmission electron microscopy (TEM) was performed on a JEOL JEM2010F electron microscope operated at an accelerating voltage of 200 kV. Scanning electron microscopy (SEM) was performed on a JEOL JSM-6340F and JEOL JSM-7001F scanning electron microscope. Selected area electron diffraction (SAED) was taken from JEOL JEM-1400. For sample preparation, the dry sample was dispersed in methanol by sonication. Then the dispersion was dropcast on Cu grids or silicon wafers for TEM or SEM measurements, respectively. Raman spectra were collected with a Micro-Raman system (XploRA, Horiba) with 532 nm laser excitation. Nuclear Magnetic Resonance (NMR) was collected on a Varian Unity INOVA spectrometers (500 MHz). Thermogravimetric analysis (TGA) was conducted in a NETZSCH STA 449F. Diffuse reflectance infrared Fourier transform spectroscopies of chemisorbed carbon monoxide (CO-DRIFTS) was carried out on a Bruker Tensor 27 IR spectrometer with a linearized mercury−cadmium−telluride detector, Harrick diffuse reflection accessory, and Praying Mantis high temperature reaction chamber. For ethylene hydrogenation studies, samples were diluted with low surface area quartz and loaded into glass reactors.

Temperature was controlled by a furnace (CARBOLITE) and PID controller (Diqi-Sense) with a type-K thermocouple. The amount of palladium in each sample was analyzed by inductively coupled plasma optical emission spectrometry on an Agilent 5100 instrument. Gas flows were regulated using calibrated mass flow controllers (Alicat) and reactions were performed using helium as the carrier gas. The product was analyzed by mass spectrometer (MKS special V2000P). For cinnamaldehyde hydrogenation studies, the products were analyzed on a gas chromatograph with flame-ionization detection (Agilent 6850 Network GC with a autosampler, column: HP-1, 30 m × 0.25 mm × 0.25 μm).

Synthesis of Pd-CTAB NPs: Pd-CTAB NPs were synthesized based on a previous report.[1] 50 mg of CTAB was dissolved in 9.3 mL of deionized water (DI water), followed by adding 0.5 mL of 0.01 M H_2PdCl_4 solution. The above solution was placed in 95 °C oil bath for 5 min. Then, 200 μL of 0.04 M ascorbic acid was added with stirring at 200 rpm. The reaction mixture was stirred for 30 min at 95 °C. After cooling to room temperature, the as-synthesized Pd-CTAB NPs were washed once with DI water via centrifugation (8000 rpm, 10 min). Normally, 10 batches of Pd-CTAB NPs were synthesized and dispersed in 5.0 mL of DI water, yielding a 10 mM Pd-CTAB NPs suspension. For the encapsulation, 0.25 mL of the Pd-CTAB NPs suspension was centrifuged (8000 rpm, 10 min) and dispersed in 0.5 mL DI water.

Synthesis of Au-CTAB NPs: The Au-CTAB NP synthesis was modified from a previous report.[2] 550 mg of CTAB was dissolved in 97 mL of DI water. Then, 2.5 mL of 0.01 M $HAuCl_4$ solution and 0.5 mL of 0.1 M trisodium citrate solution were added. The reaction mixture was transferred into a 200-mL pressure vessel and heated in an oven at 110 °C for 24 h. The as-synthesized Au-CTAB NPs were washed once using centrifugation (8000 rpm, 10 min) and dispersed in 2.5 mL of DI water, yielding a 10 mM Au-CTAB NPs suspension. For the

encapsulation, 0.25 mL of the Au-CTAB NPs suspension was centrifuged (8000 rpm, 10 min) and dispersed in 0.5 mL of DI water.

Synthesis of Au-CTAC NPs: In general, Au seeds were synthesized first and added into the growth solution to form Au-CTAC NPs. All the reactions were performed at room temperature (22.0 ± 1.0 ˚C). For the synthesis of Au seeds, 320 mg of CTAC was dissolved in 9.75 mL of DI water, followed by adding 250 μL of 0.01 M $HAuCl_4$ and 450 μL of 0.02 M $NaBH_4$ under stirring at 200 rpm. The above solution of Au seeds was aged for 1 hour at room temperature. The growth step was performed using two batches of the same growth solutions. The growth solution was prepared by dissolving 320 mg of CTAC in 9.625 mL of DI water followed by adding 90 μL of 0.04 M L-ascorbic acid, 250 μL of 0.01 M $HAuCl_4$ and 10 μL of 0.01 M sodium bromide solution. To grow the Au-CTAC NPs, 105 μL of Au seed solution was added to the first growth solution. Upon development (~ 5 s) of a light pink color, 25 μL of the above mixture was immediately transferred into the second growth solution. The solution was stirred for 10 s and left undisturbed for 15 min. The as-synthesized Au-CTAC NPs were washed once with DI water via centrifugation (8000 rpm, 10 min). Normally, 20 batches of Au-CTAC NPs were synthesized and dispersed in 10.0 mL of DI water, yielding a 5 mM Au-CTAC NPs suspension. For encapsulation, 0.375 mL of Au-CTAC NPs suspension was washed twice with DI water via centrifugation and dispersed in 0.1 mL of DI water.

Synthesis of Au-PVP NPs: To form Au-PVP NPs, 1.25 mL of 0.01 M $HAuCl_4$ aqueous solution was introduced into 48.25 mL of DI water in a 100-mL two-neck round bottom flask. Then, the solution was stirred and refluxed at 110 °C oil bath for 20 min. After that, 0.5 mL of the aqueous solution containing 3 wt% sodium citrate tribasic dihydrate was introduced to the above solution and the reaction was held in reflux at 110 °C oil bath for 3 min. The solution was cooled

to room temperature. Then, 1.0 mL of the aqueous solution containing 150.0 mg of polyvinylpyrrolidone was added into the solution to obtain Au-PVP NPs. The formed Au-PVP NPs were centrifuged at 13000 rpm for 20 min to remove the unreacted residues. The as-synthesized Au-PVP NPs were purified by washing with methanol twice via centrifugation (14000 rpm, 20 min). The resulting Au-PVP NPs were dispersed into 0.5 mL of DMF to give a concentration of Au-PVP NPs at 5.0 mg/mL.

Synthesis of metal NP@ZIF-8 with a direct interface: 113.52 mg of 2-mim was dissolved in 1.75 mL of 0.2 mM CTAB aqueous solution to obtain a 2-mim/CTAB solution. 250 μL of 10 mM metal-CTAB NPs were centrifuged (8000 rpm, 10 min) and dispersed in 500 μL of DI water. To form NP@ZIF-8 with a direct interface, 1.75 mL of 2-mim/CTAB solution was mixed with 0.25 mL of 97.5 mM $Zn(NO_3)_2$ solution in a 20-mL glass vial while stirring at 250 rpm at room temperature. After 10 s, 0.5 mL of metal-CTAB NPs in DI water was added into the above mixture. After stirring for 5 min, the mixture was left undisturbed for 3 h at room temperature (22.0 ± 1.0 ˚C). The sample was collected by centrifugation (8000 rpm, 10 min). The sample was washed with methanol three times and was dried under a vacuum condition for 24 h.

Synthesis of metal NP@ZIF-8 with an indirect interface: For NP@ZIF-8 with an indirect interface, 2-mim was dissolved in various concentrations of aqueous CTAB solution (0.8 mM CTAB for polycrystalline shell, 1.2 mM for partially coated shell). 113.52 mg of 2-mim was dissolved in 1.75 mL of aqueous CTAB solution (0.8 mM CTAB, or 1.2 mM CTAB) to obtain a 2-mim/CTAB solution. To form NP@ZIF-8 with an indirect interface, 1.75 mL of 2-mim/ CTAB solution was mixed with 0.25 mL of 97.5 mM $Zn(NO_3)_2$ solution in a 20-mL glass vial while stirring at 250 rpm at room temperature. After 10 s, 0.5 mL of metal-CTAB NPs in DI water was added into the above mixture. After stirring for 5 min, the mixture was left undisturbed for 3 h

under room temperature. The sample was collected by centrifugation (8000 rpm, 10 min). The sample was washed with methanol three times and was dried under a vacuum condition for 24 h.

Synthesis of Au@UiO-66-F_4 with a direct interface: Based on our understanding that was built from the ZIF-8 system, the balance between the rates of dissociation and in situ MOF growth is of critical importance. To optimize our conditions for UiO-66, we propose to initiate capping agent dissociation by increasing the concentration of MOF linkers. Unfortunately, this concept is hard to realize by using the primitive linker of UiO-66, 1,4-benzendicarboxylic acid (BDC), because BDC is insoluble in an aqueous phase. To address this limitation, we make use of tetrafluoroterephthalic acid (BDC-F_4) as the MOF linker for its high solubility in an aqueous solution.

The synthesis of Au@UiO-66-F_4 was carried out in the aqueous phase by using acetic acid as the modulator. Firstly, 0.18 mmole of BDC-F_4 was mixed with 0.5 mL of 6 M acetic acid aqueous solution and denoted as the linker solution. The linker solution was then incubated at a 50 °C oil bath to facilitate the dissolving process of the MOF linker. By using the same concept, 0.18 mmole of $ZrOCl_2 \cdot H_2O$ was dissolved in 0.5 mL of 6 M acetic acid aqueous solution and denoted as the metal solution. Before the synthesis, both linker and metal solutions were preheated at a 50 °C Oil bath for five minutes. Then, the metal solution was subjected to the linker solution in a 20-ml glass vial while stirring at a 50 °C Oil bath. 1 minute after adding the metal solution, 100 uL of the Au NPs solution was injected into the above mixture, which the metal nanoparticle solution concentrations had already been adjusted to 18.75 mmol/L (The Au NPs used here was prepared by centrifuging 0.375 mL of 5 mM as-synthesized Au-CTAC NPs suspension at 10000 rpm for 5 min. The resulting Au NPs were then washed twice with 100 μL of DI water and then dispersed in 100 μL of DI water for further use.). The mixture was stirred for 5 minutes at a 50 °C Oil bath.

Then, the reaction solution was left undisturbed at a 50 °C Oil bath for 3 hours. The resulting solid of Au@UiO-66-F_4 was collected by centrifuge (3000 rpm, 8 min) and washed by DMF and methanol for three times. Then, the sample of Au@UiO-66-F_4 was dried under vacuum overnight before characterizations and catalytic reactions

Capping agent exchange: 375μL of 5 mM Au-CTAB NPs was centrifuged down at 8000 rpm for 10 min and dispersed in 100 μL of 100 mM CTAC aqueous solution. The suspension of Au NPs was left unstirred at room temperature overnight. Then, it was spun down at 8000 rpm for 10 min, washed with 100 μL DI water twice and dispersed in 100 μL DI water for the encapsulation.

Synthesis of Au@UiO-66 with an indirect interface: In general, 25.0 mg of BDC (0.143 mmol) was dissolved in 7 mL of DMF in a 20 mL scintillation vial. Then, 700 μL of acetic acid was added into the solution followed by adding 2 mL of DMF containing 33.4 mg of $ZrCl_4$ (0.143 mmol) and 150 mg PVP. The mixture was sonicated for 20 min at room temperature. Au-PVP NPs (0.25 mL, 5.0 mg Au NPs/mL) was introduced into the above mixture, and the mixture was heated at 120 ˚C in an oil bath for 1 h. After cooling to room temperature, the formed Au@UiO-66 sample was collected by centrifugation (8000 rpm, 10 min). The sample was washed with DMF and methanol three times. The sample was dried under vacuum for 24 h.

Study of the CTAB amount on the metal surface and its impact on forming a direct interface: In this experiment, electron microscopy was carried out to study the impact of CTAB on metal surface to the formation of a direct interface, and ^{1}H-NMR analysis was performed to study the CTAB amount in the supernatant. To study the impact of CTAB on metal surface to the formation of a direct interface, Pd-CTAB NPs were incubated with the 2-mim solution (50 mM) with an incubation time from 1 to 4 h. (A lower 2-mim concentration of 50 mM was used in this study to control the dissociation of CTAB.) After incubating the NPs in the 2-mim solution, the

treated Pd-CTAB NPs were introduced into the MOF precursor solution for encapsulation. The ratio of Pd@ZIF-8 with a single crystalline shell was calculated based on electron microscopy and the results are summarized in **Table A3.2**.

To study the CTAB amount in the supernatant, Pd-CTAB NPs were dispersed in 0.5 mL of deuterium oxide (D_2O) solution containing 50 mM 2-mim. The suspension of Pd-CTAB NPs was left undisturbed in D_2O/2-mim at room temperature for a given time (1, 2, or 4 h). After that, the above suspension was centrifuged and the supernatant was taken for ^{1}H-NMR analysis. The quantitative measurement of absolute CTAB amount in the supernatant was done using methylsulfonylmethane (20 μL, 30.00 mM). **Figure A3.3** shows an example of the quantitative analysis of CTAB amount from the ^{1}H NMR spectrum: Peak A was assigned to the six protons on methyl groups of the internal standard (methylsulfonylmethane); peak E was assigned to the 26 protons on the 13 carbons of the CTAB carbon chain. These two peaks were used to calculate the absolute amount of CTAB in the solution. The results are summarized in **Figure A3.2**. To correlate the amount of CTAB removed from the metal surface and its impact to the formation of a direct interface, **Figure A3.2** and **Table A3.2** were combined in one figure in main text (**Figure 3.8**).

Self-assembly of Pd@ZIF-8 samples for PXRD analysis: Pd@ZIF-8 samples were self-assembled on a silicon wafer. In general, Pd@ZIF-8 samples were dispersed in an aqueous solution containing 0.54 mM CTAB to form a uniform suspension. Next, 10 μL of the suspension was placed on a substrate and dried under atmosphere.

CO-DRIFTS measurement: To carry out CO-DRIFTS analysis, the sample was packed in a sample cup and sealed in a Praying Mantis high-temperature IR reaction chamber under N_2 flow (50 mL/min). A spectrum of the sample was recorded as a background. The adsorption of

carbon monoxide (CO) on the sample was performed by introducing CO (10 mL/min) into the IR reaction chamber for 20 min. Then, the CO-DRIFTS spectra were measured by flushing the samples with N_2 flow (50 mL/min) for 20 min to remove gaseous CO. All spectra were collected with 160 scans at a resolution of 4 cm^{-1} from 1750 cm^{-1} to 3000 cm^{-1}. Probing capping agents on metal surfaces has been an open challenge. We are mindful that CO-DRIFTS cannot exclusively prove that there is absolutely no CTAB on metal surface.

Ethylene hydrogenation: Ethylene hydrogenation is well-known for its structure-independent properties, meaning that the activity is not determined by the shape or size of the catalyst particles. It depends only on the number of active sites.[112] Therefore, it is a very sensitive tool to determine the prevalence of active sites in different catalysts. In general, samples were diluted with low surface area quartz and loaded into U-shaped glass reactors. The glass reactor was then connected to a home-built gas-phase flow system for alkene hydrogenation. Gas flows, including helium, hydrogen, and ethylene, were regulated using calibrated mass flow controllers (Alicat). Gas composition was analyzed with a mass spectroscope (MKS special V2000P). Temperature was controlled by a furnace (CARBOLITE) and PID controller (Diqi-Sense) with a type-K thermocouple. Before the reaction, the catalysts were activated in the glass reactor at 60 ˚C under He flow for 1 h. Gas-phase ethylene hydrogenation was run at 45 ˚C under a continuous system. The activity to ethylene hydrogenation in each sample was summarized by normalizing the amount of palladium in each sample. (The amount of palladium in each sample was analyzed by inductively coupled plasma optical emission spectrometry on an Agilent 5100 instrument.)

Cinnamaldehyde hydrogenation: Catalysts were dispersed in 2 mL of isopropanol solution in the 5.0-mL ampule, and then cinnamaldehyde (0.2 mmol) was added into the above solution. To compare the selectivity of our samples, the conversion of each reaction was kept at

around 6 % (2.60 mg Au-on-SiO_2, 17.5 mg Au@UiO-66 with an indirect interface and 12.0 mg Au@UiO-F_4 with a direct interface). Before catalysis, the high-pressure reactor vessel (Wattacas Inc., 500 mL) was preheated to 70 ˚C. Temperature was controlled using a hot plate (RCT basic, IKA) with a type-K thermocouple. Subsequently, the ampule was transferred into a high-pressure reactor vessel. The autoclave was purged 5 times with H_2 to remove air. Then, the hydrogenation of cinnamaldehyde was carried at 30 bar H_2 at 70 ˚C for 24 h with magnetic stirring at 500 rpm. After that, the catalysts were separated by centrifugation, and the reaction solution was filtered through a filter membrane (0.22 μm). The products were analyzed on a gas chromatograph with flame-ionization detection (Agilent 6850 Network GC with an autosampler, column: HP-1, 30 m × 0.25 mm × 0.25 μm). The results are summarized in **Table A3.3**.

To prepare the control sample of Au NPs deposited on SiO_2, 3 mL of the colloidal Au-CTAC NPs (5 mM) was mixed with 100.0 mg of mesoporous silica (SBA-15) in 5 mL isopropanol in a 20 mL scintillation vial. The mixture was sonicated for 10 min and stirred for 3 h at room temperature. Then, the precipitates were separated by centrifugation (4000 rpm, 10 min), washed with ethanol four times, and dried in the vacuum oven overnight. The resulting sample was denoted as Au-on-SiO_2.

To prepare the control sample of Au NPs deposited on the external surface of UiO-66, 3 mL of the colloidal Au-CTAC NPs (5 mM) was mixed with 100.0 mg of UiO-66 in 5 mL isopropanol in a 20 mL scintillation vial. The mixture was sonicated for 10 min and stirred for 3 h at room temperature. Then, the precipitates were separated by centrifugation (4000 rpm, 10 min), washed with ethanol four times, and dried in the vacuum oven overnight. The resulting sample was denoted as Au-on-UiO-66.

3.5 Appendix

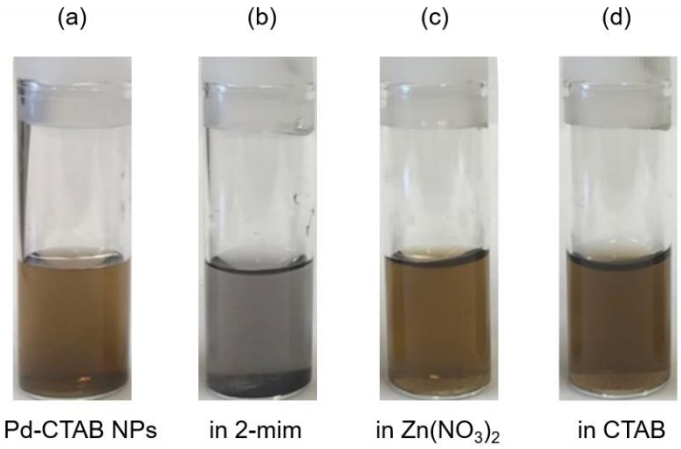

Figure A3.1: Photographs of Pd-CTAB NP suspensions after incubation in (a) pure water, (b) aqueous 2-mim, (c) aqueous $Zn(NO_3)_2$, and (d) aqueous CTAB.

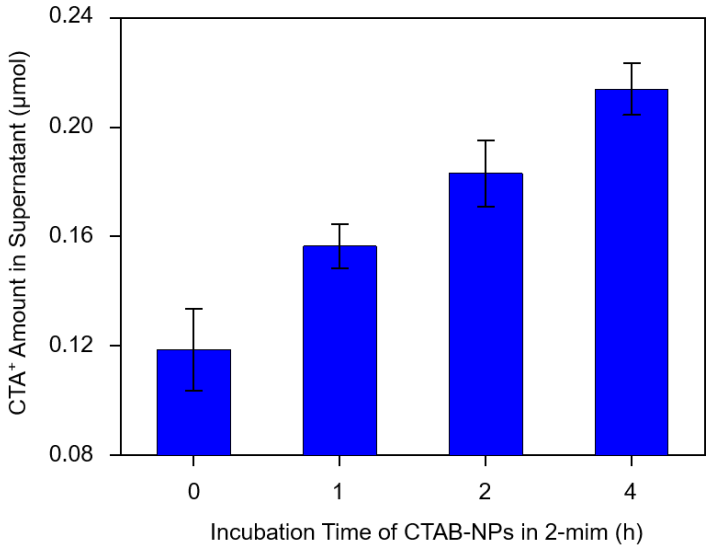

Figure A3.2: Quantitative analysis of CTAB by ^{1}H-NMR.

The amount of CTAB in the supernatant, monitored by ^{1}H NMR, after Pd-CTAB NPs were treated with 2-mim aqueous solution (50 mM) for different lengths of time.

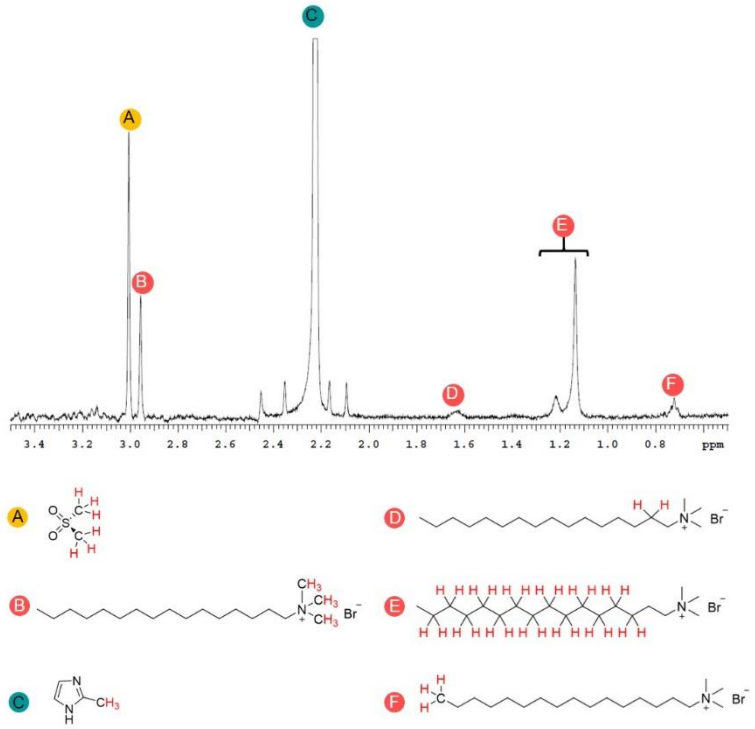

Figure A3.3: Sample 1H NMR spectrum for the quantitative analysis of the amount of CTAB in solution. Peak A was assigned to the six protons of the methyl groups of the internal standard (methylsulfonylmethane); peak E was assigned to the 26 protons of the thirteen carbons of the CTAB carbon chain. These two peaks were used to calculate the absolute amount of CTAB in the solution.

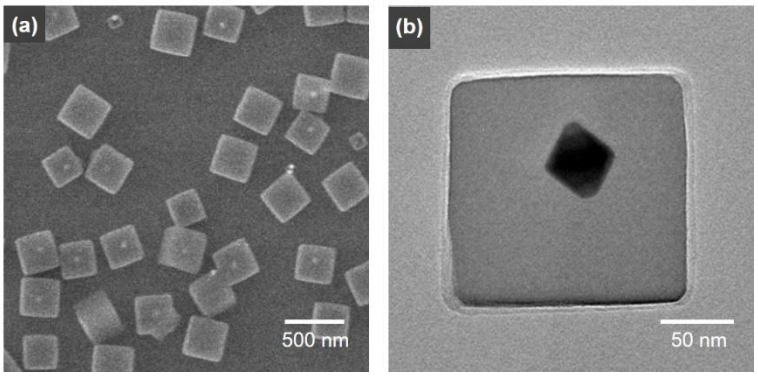

Figure A3.4: Electron microscopy of Au@ZIF-8 with a direct interface by (a) SEM and (b) TEM.

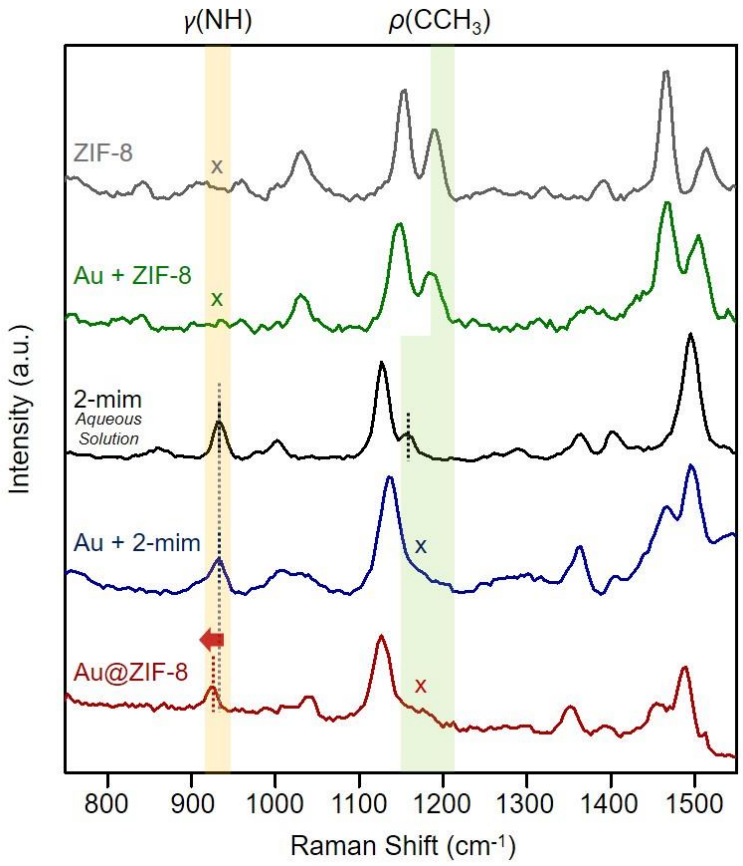

Figure A3.5: Raman spectra of Au@ZIF-8, Au NPs incubated with 2-mim, free 2-mim, Au NPs incubated with ZIF-8 in an aqueous solution and ZIF-8.

Notes for Figure A3.5: The spectrum of Au + 2-mim was measured by using the mixture of Au-CTAB NPs (100 uL, 5 mM) and 2-mim (400 uL, 790 mM). The spectrum of 2-mim was obtained by using the 2-mim aqueous solution (790 mM). The spectrum of Au + ZIF-8 was recorded by using the mixture of Au-CTAB NPs (100 uL, 5 mM) and ZIF-8 (1 mg ZIF-8 in 100 uL DI water). Raman spectrum of Au@ZIF was measured *in situ* during the formation of Au@ZIF-8 with a direct interface. Meanwhile, we are mindful that the chemicals could have different Raman spectra between solid and liquid phase, therefore, we have performed the Raman spectra for all of the samples in an aqueous solution including 2-mim. Two control samples were prepared: Au NPs incubated with 2-mim (Au + 2-mim) and Au NPs mixed with ZIF-8 in an aqueous solution (Au +

ZIF-8). We compared the spectra of Au+2-mim and Au+ZIF-8 with the Au sample during the ZIF-8 coating (Au@ZIF-8), and we focused on the change of peaks from 800 to 1600 cm^{-1}. Firstly, we observed that the sample of Au@ZIF-8 exhibited a similar spectral feature with Au + 2-mim and 2-mim, suggesting that MOF interacted with the metal surfaces through the MOF ligand. Secondly, we hypothesized that the MOF ligand is mostly like to facilitate the MOF-Au interaction through the imidazole "pyridine N", so we compared the spectral feature of out-of-plane bending modes of NH (γ(NH)) at around 935 cm^{-1}. The stretching of NH was absent in bulk ZIF-8 due to the deprotonation of 2-mim when forming Zn-N bonds. Therefore, the observation of NH bending at 928 cm^{-1} in Au@ZIF-8 could be attributed to the 2-mim at the NP-MOF interface. After the NH moiety interacted with the metal surface, the interaction would lead to a weaker NH bending, resulting in a redshift of the N-H bending frequency. In the spectra, Au@ZIF-8 sample exhibits a redshift of the NH bending mode (928 cm^{-1}) compared to free 2-mim (935 cm^{-1}), suggesting the adsorption of ZIF-8 on the metal surface through the imidazole "pyridine N". In contrast, this shift for the sample of Au + 2-mim would be hard to observe because of the interference from the bulk 2-mim

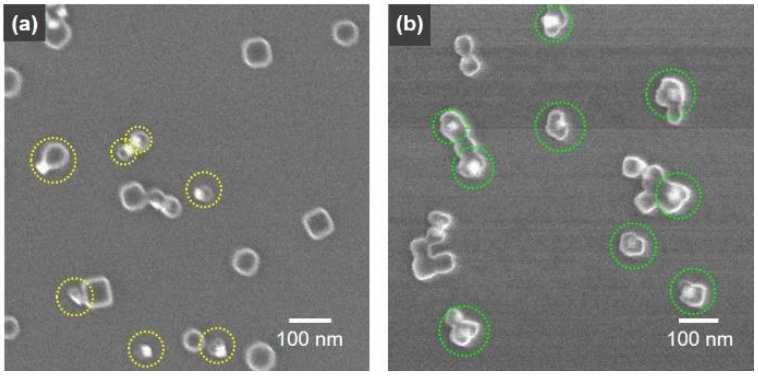

Figure A3.6: Investigation of the early stages of ZIF-8 coating over Pd@ZIF-8 with (a) direct and (b) indirect interfaces.

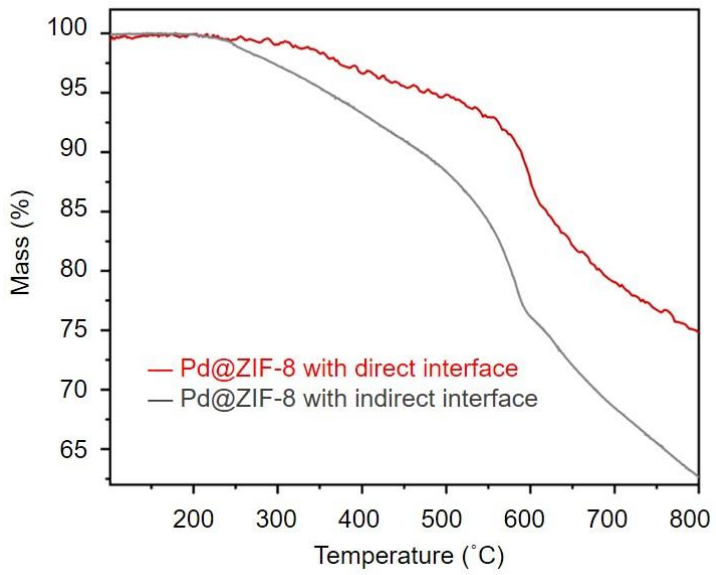

Figure A3.7: TGA analysis of Pd@ZIF-8 with (red) a direct interface and (gray) an indirect interface.

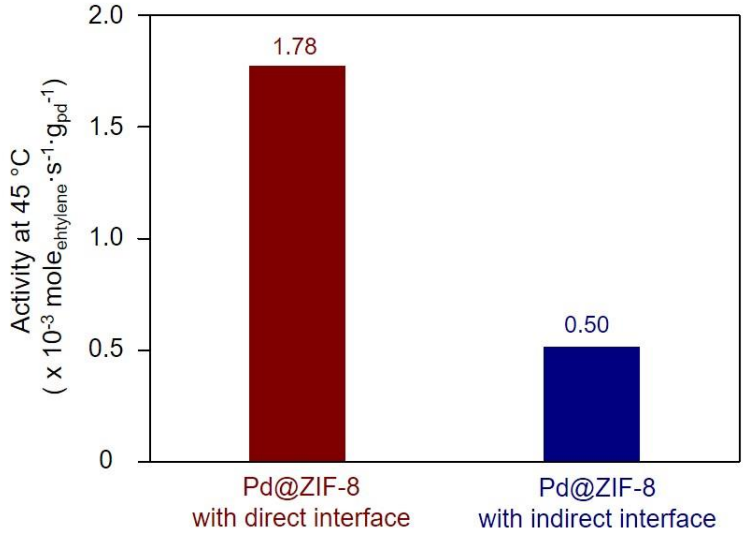

Figure A3.8: Ethylene hydrogenation of Pd@ZIF-8 with (red) a direct interface and (blue) an indirect interface.

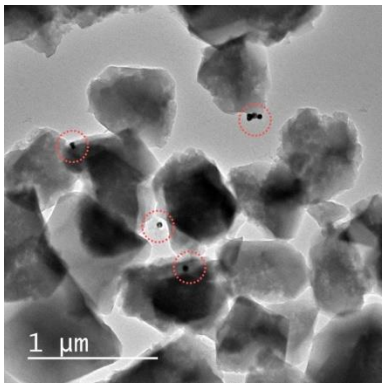

Figure A3.9: TEM image of UiO-66 formation in the presence of Au-CTAB NPs. Au NPs are marked in red circles.

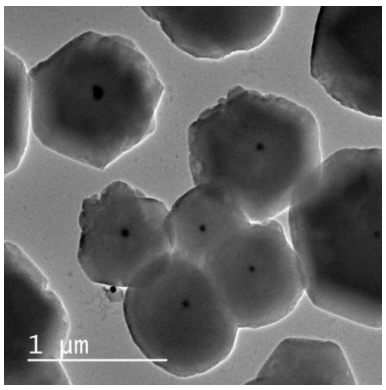

Figure A3.10: TEM image of the UiO-66-F_4 coating of Au-CTAB NPs after capping agent exchange to CTAC.

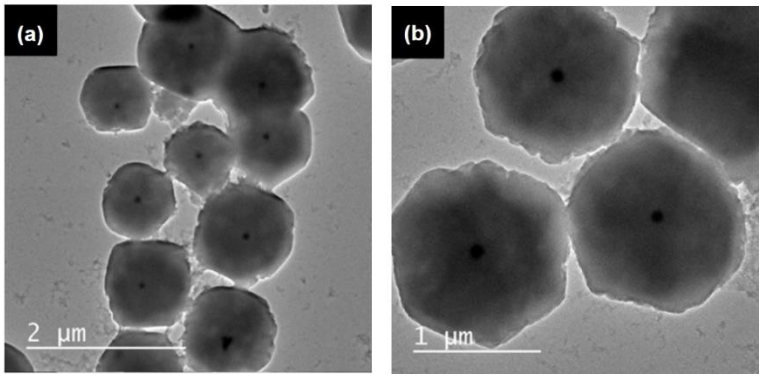

Figure A3.11: TEM images of UiO-66-F_4 coating of Au-CTAC NPs.

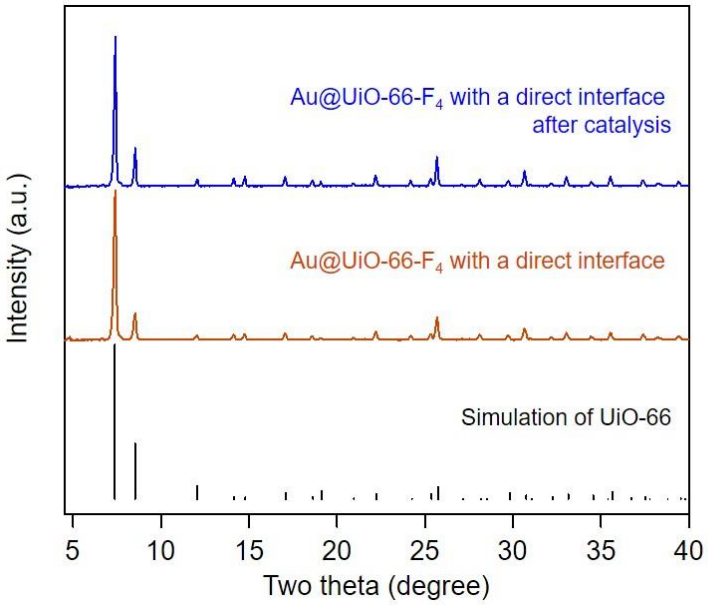

Figure A3.12: PXRD patterns of Au@UiO-66-F_4 with a direct interface (orange) before and (blue) after catalysis.

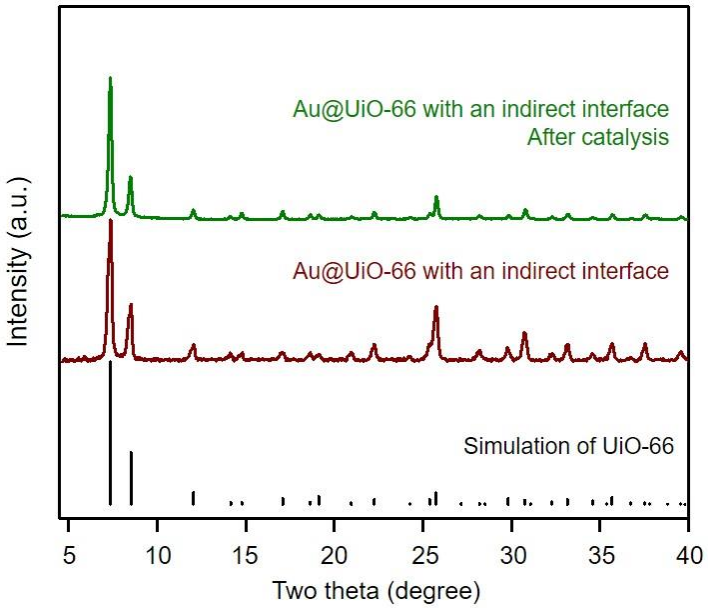

Figure A3.13: PXRD patterns of Au@UiO-66 with an indirect interface (brown) before and (green) after catalysis.

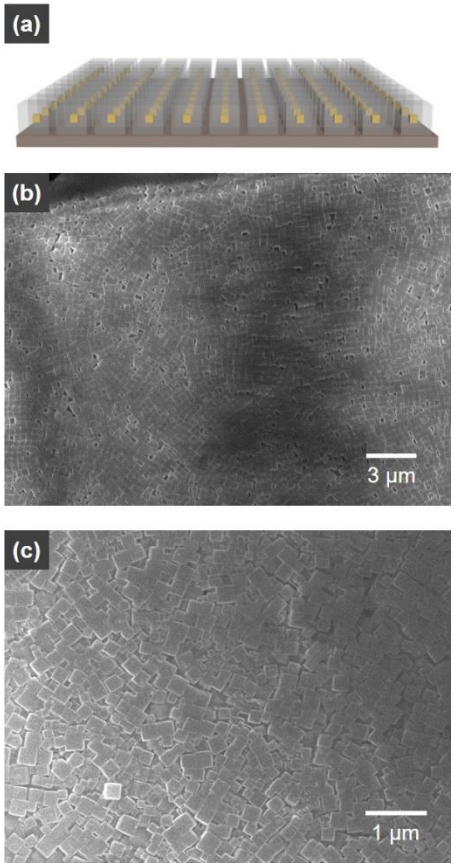

Figure 3.14. Self-assembly of Pd@ZIF-8 with a direct interface. (a) Schematic illustration and (b, c) SEM images.

Table A3.1: Vibrational assignments of surface-enhanced Raman spectroscopy peaks for 2-mim on Au.

Raman Shift (cm^{-1})	Vibrational Assignment[a]
678	$\nu(CCH_3)$
928	$\gamma(NH)$
1123	$\delta(CH)$
1351	$\nu(Ring)$
1486	$\delta_{asym}(CCH_3)$

[a] Signal assignments are based on a previous report of 2-mim on a Ag surface.[166]

Table A3.2: Calculation of the ratio of Pd@ZIF-8 with single-crystalline coating when 2-mim (50 mM)-pretreated Pd NPs were used (treatment time: 1, 2 and 4 h, as labeled).

Time under 2-mim treatment	Ratio of Pd@ZIF-8 with single crystalline shell[a]	Number of crystals used in calculation in each trail[a]
0	9.3 ± 3.7	118
1 hour	31.4 ± 5.8	118
2 hour	47.8 ± 3.1	110
4 hour	74.6 ± 4.3	60

[a] The ratio of Pd@ZIF-8 with single crystalline shell was calculated based on three independent trials, with more than 60 crystals used in the calculation for each trail.

Table A3.3: Summary of selectivity for cinnamaldehyde hydrogenation

Catalyst[a]	Conversion (%)	Selectivity to cinnamyl alcohol (%)	Selectivity to 3-phenylpropionaldehyde (%)	Selectivity to 3-phenylpropanol (%)
Au-on-SiO_2 (Control)	5.0 ± 0.4	61.8 ± 0.1	30.8 ± 2.1	7.4 ± 2.1
Au-on-UiO-66 (Control)	8.0 ± 1.0	53.3 ± 2.0	28.5 ± 2.0	18.2 ± 1.7
Au@UiO-66 with an indirect interface	6.5 ± 0.6	85.1 ± 0.1	12.0 ± 0.6	2.9 ± 0.6
Au@UiO-F_4 with a direct interface	6.1 ± 0.1	> 99.0 [b]	< 1.0 [c]	< 1.0 [c]

[a] Selectivity was determined by its ratio to the sum of all three products (cinnamyl alcohol, 3-phenylpropionaldehyde, and 3-phenylpropanol). The standard deviation was obtained based on three independent measurements. [b] Cinnamyl alcohol is the only product observed in the GC-FID analysis. [c] Product was not observed in the GC-FID analysis.

This page is on purposely left in blank

This page is on purposely left in blank

4.0 Chapter 4:

Investigating Influences of Structural Components on Catalytic Selectivity of Encapsulated Nanoparticles in Metal-Organic Frameworks

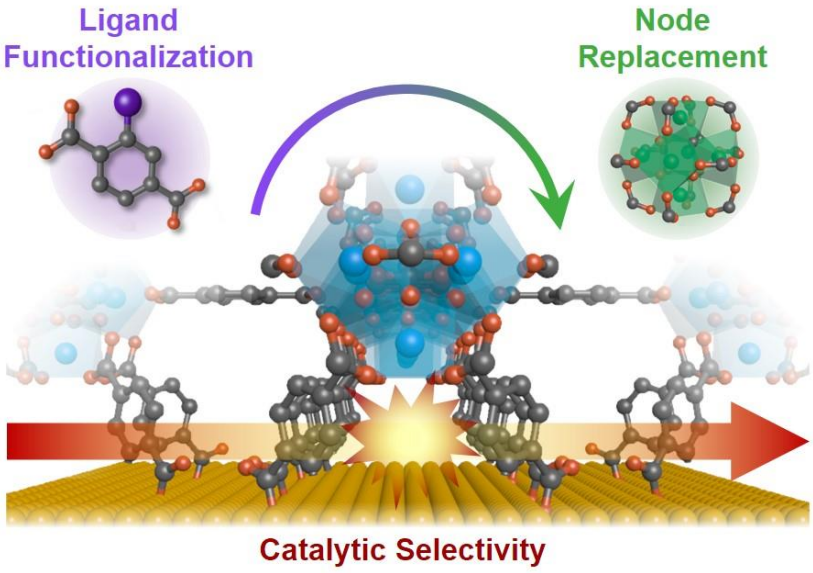

A significant portion of the work described in this chapter will be published in:

Lo, W. –S.; Williams, B. P. Si, X.; Chou, L. –Y.; Huang, W.; Waegele, M. M.; Tsung, C. –K. Investigating Influences of Structural Components on Catalytic Selectivity of Encapsulated Nanoparticles in Metal-Organic Frameworks., In preparation.

4.1 Introduction

Increasing the catalytic activity and selectivity of metal nanoparticles (NPs) is a central topic in heterogeneous catalysis.[24-25, 88] Tailoring the microenvironment around binding sites on the NP surface is critical to achieving this goal. Toward this end, several methods have been employed. For example, deposition of metal NPs on metal oxides can form metal-metal oxide interfacial sites, which can selectively facilitate specific reaction pathways.[28, 31, 179-181] Decoration of metal NPs with organic ligands can promote reaction selectivity through noncovalent reactant-ligand interactions, which can constrain intermediate orientation, favoring reaction at specific sites.[41-42, 182-183] Modification of metal NPs with amorphous polymers can promote reaction selectivity through competitive adsorption.[44-45] More recently, metal-organic frameworks (MOFs) have been utilized to tune the reaction environment around binding sites on catalytic surfaces.

MOFs are crystalline porous materials composed of organic ligands and metal-oxo nodes.[50] In contrast to flexible organic ligands and the ill-defined coverage and often amorphous structure of inorganic oxides and polymers,[33, 39] crystalline MOFs can introduce a more fixed and chemically-ordered environment to the catalytic surface. [101-102, 184-187] Indeed, improved selectivity for several important reactions has been demonstrated using MOFs, including the selective hydrogenation of unsaturated aldehydes,[61, 82] the selective hydrogenation of CO_2, [55, 83-85] and the isomerization of petrochemicals.[99, 188] The proposed mechanism of MOF enhancement combines the strengths of organic ligands and metal oxides. Similar to free organic ligands, the ligands in the MOF structure may facilitate reactant-ligand interactions, directing site-specific selectivity.[56, 61, 68] On the other hand, similar to metal oxides, MOF nodes can activate a specific bond, favoring a particular reaction pathway.[82, 84] In order to build on these successes, understanding which key components most effectively promote selectivity is critical for developing more targeted MOF-

based heterogeneous catalysts.[189] However, previous discussions of MOF enhancement on catalytic selectivity have been limited to either ligands or nodes, introducing significant ambiguity even for the same reaction.[190-192] A solid understanding of how each MOF component affects the catalytic selectivity of metal NPs is therefore needed.

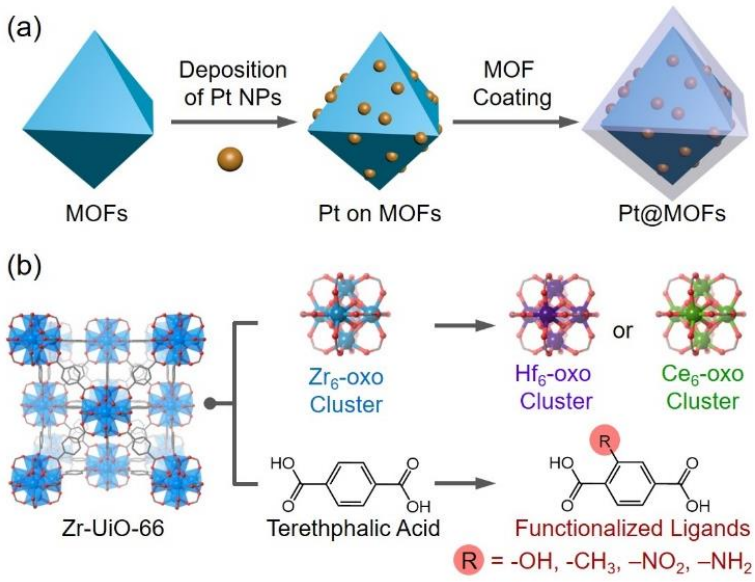

Figure 4.1: (a) Schematic illustration of synthetic routes to generate Pt@MOF analogues with different metal-oxo nodes and organic ligands. (b) Structural components of UiO-based MOFs were tuned by replacing Zr-oxo nodes with Hf-oxo or Ce-oxo nodes and by functionalizing ligands of terephthalic acid with -OH, CH_3, -NO_2, and -NH_2.

In this work, we present a series of MOF-coated metal NPs with different identities of ligand functionalization and metal-oxo node composition to reveal structure−selectivity relationships in the selective hydrogenation of cinnamaldehyde. Pt NPs were first supported on defined MOF crystals and then coated with another layer of MOF to form NP@MOF catalysts (**Figure 4.1a**). Zr-UiO-66 [$Zr_6O_4(OH)_4(BDC)_6$, BDC = 1,4-benzene dicarboxylic acid] is selected as the model system. Seven kinds of NP@MOF catalysts with similar pore structures were

generated by substituting the metal node from Zr-oxo nodes to Hf-oxo and Ce-oxo nodes, and by functionalizing the BDC ligands with various chemical groups, including -OH, -NH_2, -CH_3, and -NO_2 (**Figure 4.1b**). Three metal-oxo nodes with different Lewis acidity and four functionalized ligands with different steric bulkiness can provide systematic analysis of how component identity affects the catalytic selectivity of metal NPs. The resulting NP@MOF catalysts indeed exhibit different selectivity to hydrocinnamaldehyde (undesired product) and cinnamyl alcohol (desired product). The replacement of Zr-oxo nodes with Ce-oxo nodes significantly enhances the catalytic selectivity to cinnamyl alcohol (~87%). In contrast, the functionalization of organic ligands only slightly improves the catalytic selectivity (~58%) relative to the unfunctionalized Zr-UiO-66 (~44%). Reaction kinetics studies suggest that the rate of C=O hydrogenation is increased while the rate of C=C hydrogenation is decreased in Pt@Ce-UiO-66 relative to the rates observed on Pt@Zr-UiO-66. Infrared spectroscopic observations indicate the interaction of the C=O group with the Ce-oxo node may play an important role in the enhanced hydrogenation of this bond. To further demonstrate the generality of the proposed enhancement mechanism, we have shown that the Ti-oxo node can also significantly enhance the catalytic selectivity of cinnamyl alcohol (~90%). This work highlights the critical role of metal-oxo nodes in modulating the catalytic selectivity of metal NPs in selective hydrogenation reactions.

4.2 Results and Discussions

For our study, chemically stable MOFs of Zr-UiO-66 are selected as the model platform due to their structural tunability and Pt NPs are used as the model catalysts.[106, 193] To generate NP@MOF catalysts with identical morphology and defined structure, we sandwiched Pt NPs in core-shell MOF structures through the epitaxial growth of MOF shells on the metal NPs supported on defined

MOF crystals (**Figure 4.1a**).[194] This epitaxial overgrowth has been previously demonstrated by our team, and it allows the Pt NPs to be encapsulated in single-crystalline, core−shell microcrystals. The same method is extended to prepare catalysts with various functional groups including -OH, $-NH_2$, $-CH_3$, and $-NO_2$. (The functionalized Pt@MOF catalysts are denoted as Pt@Zr-UiO-66-X, where X represents the functional group on the benzene motif). Because there is no reported coating method for well-defined Hf- and Ce-based UiO-66, we have developed a method by tuning the synthetic conditions.[195-196] The composites replaced with Hf-oxo and Ce-oxo nodes were named Pt@Hf-UiO-66 and Pt@Ce-UiO-66, respectively.

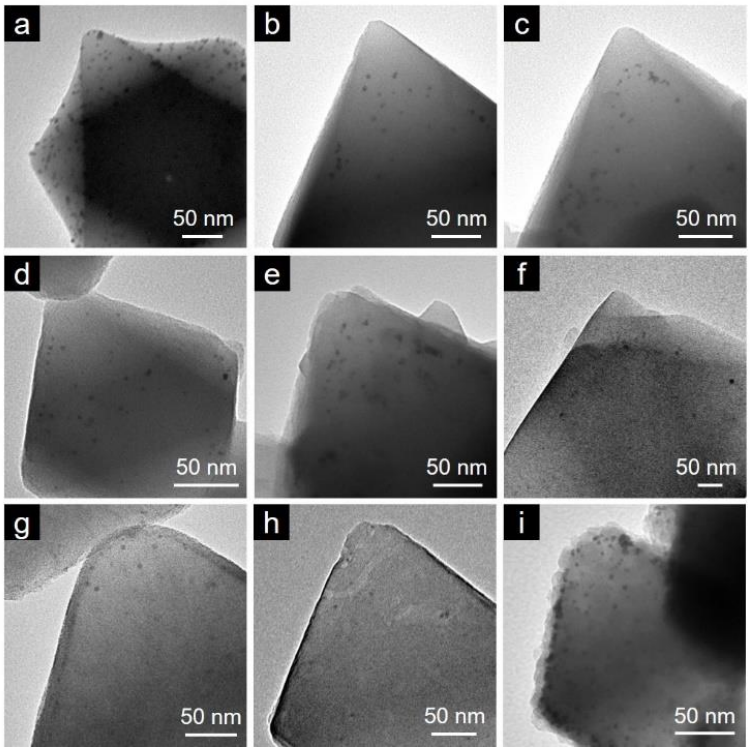

Figure 4.2: TEM images of Pt@MOF analogues: (a) Pt on Zr-UiO-66, (b) Pt@Zr-UiO-66, (c) Pt@Zr-UiO-66-NH_2, (d) Pt@Zr-UiO-66-OH, (e) Pt@Zr-UiO-66-NO_2, (f) Pt@Zr-UiO-66-CH_3, (g) Pt@Hf-UiO-66, (h) Pt@Ce-UiO-66 and (i) Pt@Zr-UiO-66-$(OH)_2$.

Powder X-ray diffraction (PXRD) analysis was used to investigate the phase purity and crystallinity of composites. As shown in **Figure A4.1**, all composites agree well with the simulated UiO-66 with face-centered cubic (fcc) topology. This result suggests that the pore structure of the UiO-66 analogues remains similar despite the difference in ligand functionalization and metal-oxo nodes. Scanning electron microscopy (SEM) revealed that all composites were defined microcrystals with identical octahedral shape**s** (**Figure A4.2**). Transmission electron microscopy (TEM) images show that the Pt NPs were encapsulated within the corresponding UiO-66 analogues (**Figure 4.2**). The average size distribution of encapsulated Pt NPs in each sample is summarized in **Table A4.1** and **Figures A4.3-A4.10**. The average sizes of the Pt NPs in the UiO-66 analogues were estimated to range from 3.2 - 5.1 nm. The similar size of all Pt NPs allows appropriate evaluation of the influence of the identity of the ligands and metal-oxo nodes to catalytic selectivity. The loadings of Pt in the UiO-66 analogues were identified by inductively coupled plasma-optical emission spectrometry (ICP-OES). The results were summarized in **Table A4.2** and were estimated at around 0.3 – 0.6 wt%. Taken together, these results suggest that the pore structure of the MOFs and the size of the Pt NPs are similar for all Pt@UiO-66 analogues.

After establishing a series of NP@MOF catalysts, we evaluated their catalytic performance by carrying out a model reaction, the hydrogenation of cinnamaldehyde. Several studies have shown that applying a MOF coating on metal NPs could influence their selectivity for the hydrogenation of the C=O bond,[61, 82, 190-191] which is originally thermodynamically less favorable than the hydrogenation of the C=C bond.[178] Both structural components of MOFs, the metal-oxo nodes and the organic ligands, have been hypothesized to promote this selectivity. We aim to address this ambiguity by systematically tuning each component. For example, the MOF pore has been hypothesized to constrain intermediates in an up-right orientation, favoring reaction on the

terminal C=O group.[61] Tuning the steric bulkiness of the MOF ligands by functionalization should optimize this orientation control. On the other hand, it has been proposed that metal-oxo nodes can preferentially interact with the C=O group, favoring the hydrogenation of C=O groups.[82] If this mechanism is dominant, tuning the identity of the metal-oxo nodes should determine the selectivity enhancement.

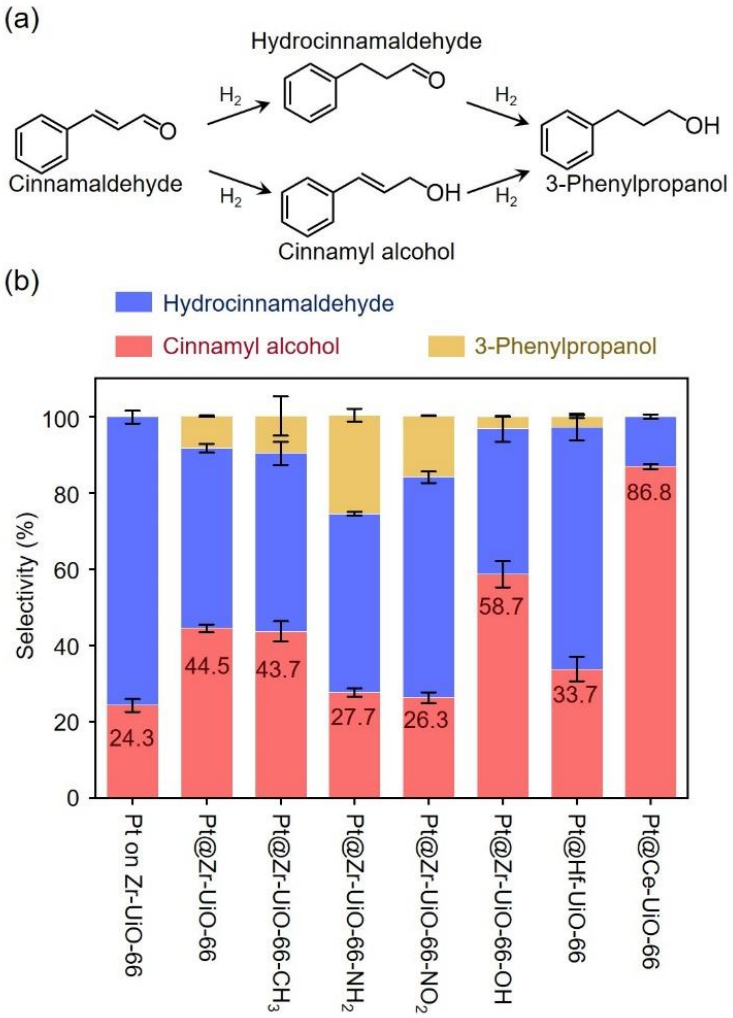

Figure 4.3: (a) Two pathways for the hydrogenation of cinnamaldehyde. (b) Selectivity for cinnamaldehyde hydrogenation over (left to right) Pt NPs on Zr-UiO-66, Pt@Zr-UiO-66, Pt@Zr-UiO-66-CH_3, Pt@Zr-UiO-66-NH_2, Pt@Zr-UiO-66-NO_2, Pt@Zr-UiO-66-OH, Pt@Hf-UiO-66, and Pt@Ce-UiO-66. Selectivity was determined by the ratio of a given product to the sum of all

three products. Error bars indicate the standard deviation of three independent measurements. Reaction conditions: 2 mL of neat methanol containing 25 μL of cinnamaldehyde, 15 μL of triethylamine, 30 bar H_2, and 40 °C.

To compare the selectivity of the Pt@UiO-66 catalysts, the conversion of each reaction was maintained at ~20% (**Table A4.3**). Catalysts were treated under diluted hydrogen to avoid oxidation of the Pt NPs. A similar amount of catalyst was added to each reaction, and the reaction time was adjusted to reach a similar reaction conversion. Cinnamyl alcohol is the preferred product, and selectivity was determined by its ratio to the sum of all three products (**Figure 4.3a**). As shown in **Figure 4.3b**, eight samples were compared: pure Pt NPs on Zr-UiO-66, Pt@Zr-UiO-66, Pt@Zr-UiO-66-X with different functional groups (X = -OH, $-NH_2$, $-CH_3$ and $-NO_2$), Pt@Hf-UiO-66, and Pt@Ce-UiO-66. A control experiment with pristine UiO-66 and its analogues without Pt NPs showed no detectable products (**Table A4.4)**. The sample of pure Pt NPs on the MOF surface (Pt on Zr-UiO-66), which serves as another control, shows a 24.3% selectivity to cinnamyl alcohol. After coating with Zr-UiO-66, the selectivity to cinnamyl alcohol increased to 44.5%, suggesting that the MOF coating improves the catalytic selectivity. The selectivity to cinnamyl alcohol further increases to 58.7% after functionalizing terephthalic acid linker with -OH groups. However, no enhancement in the selectivity to cinnamyl alcohol was observed for the other functional groups ($-NH_2$, $-CH_3$, and $-NO_2$). Guided by this enhancement observed in functionalization of the -OH group, we increased the degree of substitution by using 2,5-dihydroxybenzene-1,4-dicarboxylate ($BDC-(OH)_2$, **Figure 4.1i**), yet the selectivity to cinnamyl alcohol remains similar with the monosubstituted sample (**Table A4.5)**. The replacement of Zr-oxo nodes with Ce-oxo nodes shows the highest selectivity for cinnamyl alcohol (86.8%), whereas switching to Hf-oxo nodes reduces the selectivity to 33.7%. The selectivity in cerium samples remains high at high conversion (82.3%

selectivity at ~60% conversion, **Table S5**). The greater enhancement of the selectivity to cinnamyl alcohol with the replacement of metal-oxo nodes suggests that tuning MOF nodes could be a more effective way to enhance catalytic selectivity than linker functionalization.

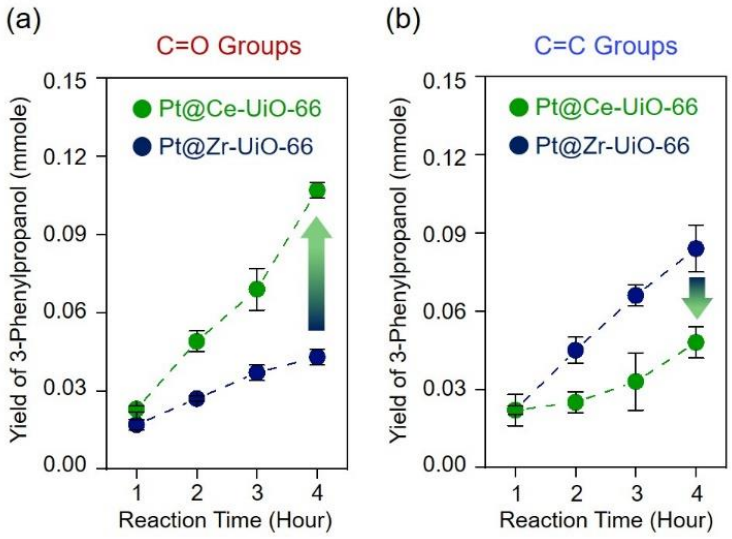

Figure 4.4: Time courses for the hydrogenation of (a) C=O groups using hydrocinnamaldehyde and (b) C=C groups using cinnamyl alcohol over Pt@Zr-UiO-66 and Pt@Ce-UiO-66. Reaction conditions: 2 mL of neat methanol containing 50 μL of reactants, 30 bar, H_2, and 40 °C. Error bars indicate the standard deviation of three independent measurements.

After gaining an initial understanding of the structure-selectivity relationship, we tracked time courses for the hydrogenation of C=O and C=C groups by using hydrocinnamaldehyde and cinnamyl alcohol independently. Each model molecule has only either C=O or C=C bonds and using them individually prevents competitive adsorption. The same amount of catalyst was used to mitigate adsorption effects from the MOF, and the hydrogenation was carried out under the same reaction conditions as with cinnamaldehyde hydrogenation. Two samples were compared:

Pt@Zr-UiO-66 and Pt@Ce-UiO-66. As shown in **Figure 4.4**, relative to Pt@Zr-UiO-66, Pt@Ce-UiO-66 exhibited a faster C=O hydrogenation rate (**Figure 4.4a**) and a slower C=C hydrogenation rate (**Figure 4.4b**). Because mass transport limitations from the MOF coating could also reduce the reaction rate, we also performed C=C group hydrogenation using ethylene. The small size of ethylene allows it to pass easily through the UiO-66 aperture.[71] As shown in **Table A4.6**, Pt@Ce-UiO-66 indeed shows a lower activity to hydrogenate ethylene than Pt@Zr-UiO-66. This result indicates that the cerium catalysts promote C=O hydrogenation and reduce activity for C=C hydrogenation, enhancing the selectivity to unsaturated alcohol.

To investigate the promotion of C=O hydrogenation in Pt@Ce-UiO-66, we carried out two sets of control experiments using diffuse reflectance infrared Fourier transform spectroscopy (DRIFTS). These experiments can distinguish between two separate mechanisms for selectivity enhancement. Firstly, the binding of metal-oxo nodes can alter the electronic structure of metal surfaces, which in turn changes the binding strength of molecular hydrogen. An altered binding strength for molecular hydrogen can influence the barrier to hydrogenation for different chemical groups (in this case, C=O and C=C groups).[197] Secondly, it has been observed that metal-oxo nodes can preferentially interact directly with the C=O group.[82] This preferential interaction may alter the energy landscape of the chemical transformation, enhancing C=O group hydrogenation. Based on these two points, probing changes both in molecular hydrogen and in reactants through DRIFTS may further define the mechanism for the enhanced selectivity to C=O hydrogenation on Pt@Ce-UiO-66.

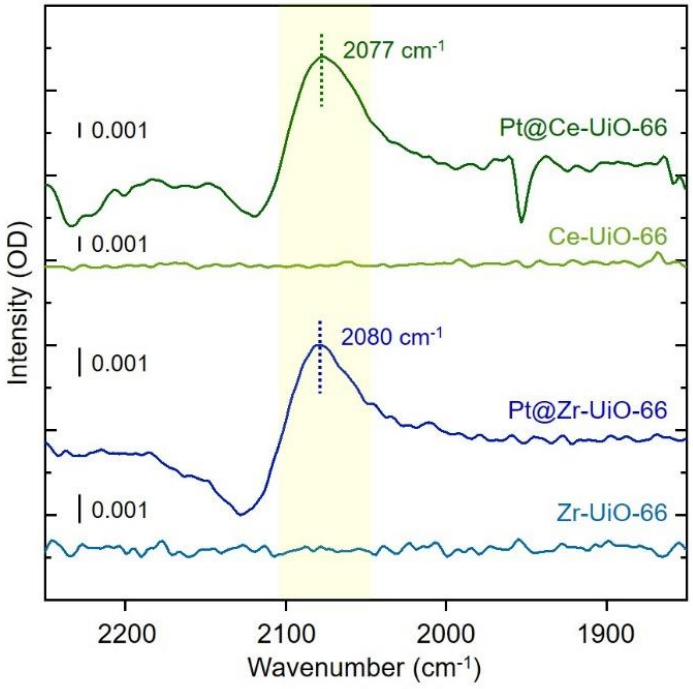

Figure 4.5: DRIFTS measurements of molecular hydrogen adsorbed on Zr-UiO-66, Ce-UiO-66, Pt@Zr-UiO-66, and Pt@Ce-UiO-66. The spectral feature at ~2080 cm^{-1} corresponds to the adsorption of molecular hydrogen atop Pt atoms.

The observed DRIFTS frequency of Pt-H bonds is directly related to the binding strength of molecular hydrogen on the Pt surface.[198] All samples were exposed to diluted hydrogen for one hour before measurements. As shown in **Figure 4.5**, four samples were compared: pure Zr-UiO-66, pure Ce-UiO-66, Pt@Zr-UiO-66, and Pt@Ce-UiO-66. In the spectra, the band at ~2080 cm^{-1} is attributed to molecular hydrogen bound atop Pt atoms (Pt-H_{atop}).[199-200] No spectral feature was observed in control samples of pure Zr-UiO-66 and Ce-UiO-66, reinforcing assignment of the signal to Pt. The spectra for Pt@Zr-UiO-66 and Pt@Ce-UiO-66 show similar features, with Pt-H_{atop} peaks centered at ~2080 cm^{-1} and 2077 cm^{-1}, respectively. The similar Pt-H_{atop} frequency

between both samples indicates that the metal oxide has a minor influence on the binding strength of molecular hydrogen to the Pt surface.

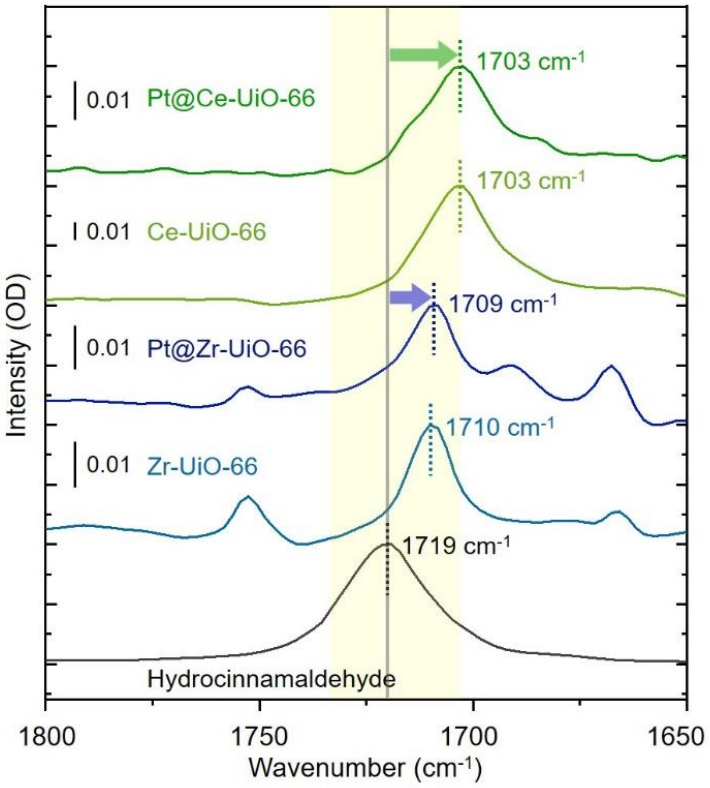

Figure 4.6: DRIFTS of hydrocinnamaldehyde over Zr-UiO-66, Ce-UiO-66, Pt@Zr-UiO-66, and Pt@Ce-UiO-66. The C=O stretch frequency at 1719 cm^{-1} in hydrocinnamaldehyde is presented as a reference for comparison.

To study interactions with the C=O groups in reactant molecules, we performed DRIFTS measurements with hydrocinnamaldehyde. Interaction between metal-oxo clusters and the C=O bond of hydrocinnamaldehyde should lead to a weaker C=O bond, resulting in a red-shift of the C=O stretch frequency.[82] Because of the low vapor pressure of hydrocinnamaldehyde at ambient conditions, it was introduced by bubbling helium gas through pure hydrocinnamaldehyde at 90 ºC. Four samples were compared: Zr-UiO-66, Pt@Zr-UiO-66, Ce-UiO-66, and Pt@Ce-UiO-66. As

shown in **Figure 4.6**, the stretch frequency of C=O at 1719 cm^{-1} in free hydrocinnamaldehyde was used as a reference for comparison. Compared to this reference frequency, the C=O stretch frequency of hydrocinnamaldehyde exposed to Pt@Ce-UiO-66 sample shows a red-shift from 1719 to 1703 cm^{-1}, indicating significant interaction between Ce-oxo nodes and the C=O bond. In contrast, a smaller red-shift (~9 cm^{-1}) of the C=O stretch frequency was observed after exposure to Pt@Zr-UiO-66, signifying less interaction between Zr-oxo nodes and the C=O bond. The greater shift of the C=O frequency on Pt@Ce-UiO-66 implies a greater interaction between the metal-oxo clusters and the reactant C=O bond may play an important role in the enhanced hydrogenation of this bond. With this information in mind, we further carried out cinnamaldehyde hydrogenation with Pt NPs supported on cerium samples, Pt NPs on Ce-UiO-66. As expected, both catalysts can improve the selectivity to cinnamyl alcohol (71.6%, **Table A4.3).** However, the enhancement over the cerium-supported catalysts is not to the degree seen after MOF encapsulation, highlighting the importance of tailoring active sites using the 3-dimensional control of the MOF scaffold.

To test whether this enhancement can be observed on Pt@MOF catalysts with other metal-oxo nodes, we have carried out further studies with another group-4 metal, titanium-based MOFs (Ti-MiL-125).[201] The composite with Ti-oxo nodes is denoted Pt@Ti-MiL-125 (**Figure A4.12**). After introducing hydrocinnamaldehyde into Pt@Ti-MiL-125, the C=O frequency of hydrocinnamaldehyde shows a red-shift from 1719 to 1698 cm^{-1} (**Figure A4.13**). The Pt@Ti-MiL-125 catalyst also shows a lower activity for ethylene hydrogenation (**Figure 4.7**). As a result, Pt@Ti-MiL-125 catalyst indeed enhances the catalytic selectivity to cinnamyl alcohol (90.6%, **Table A4.3**). This agreement encouraged us to revisit the Pt@Hf-UiO-66 catalyst, which only slightly influenced selectivity to cinnamyl alcohol. In Pt@Hf-UiO-66 catalysts, we observed a

redshift of the C=O frequency of hydrocinnamaldehyde, implying activation of the reactant C=O bond (**Figure A4.14**). However, as shown in **Figure 4.7,** the Pt@Hf-UiO-66 catalyst displayed a mass activity of ethylene hydrogenation at around 15.3 $mmol_{ethylene}/g_{Pt}$, which is 1.5~4.0-fold higher than all of the catalysts studied in the report. The low catalytic selectivity to cinnamyl alcohol should thus instead be attributed to its high reactivity to C=C hydrogenation. Taken together, this result further highlights that the enhanced selectivity to unsaturated alcohol is a combination of promoted C=O activation and reduced reactivity to C=C hydrogenation.

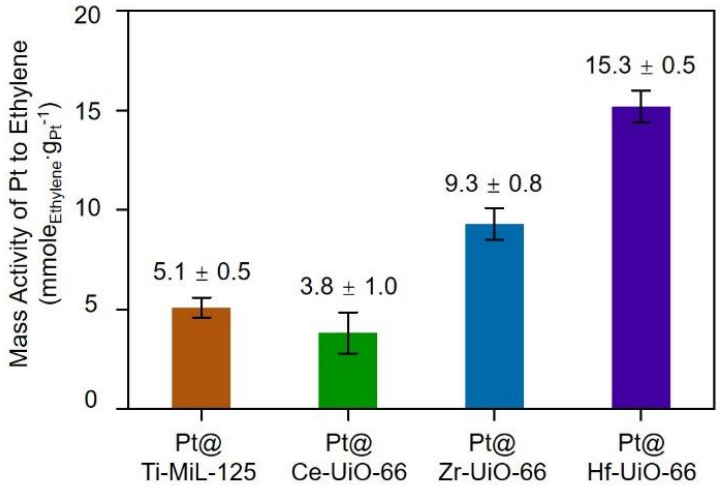

Figure 4.7: Mass activity for ethylene hydrogenation over Pt@Ti-MiL-125, Ce-UiO-66, Pt@Zr-UiO-66, and Pt@Hf-UiO-66.

4.3 Conclusions

In summary, we have established a series of Pt@MOF catalysts with different metal-oxo nodes or ligand functionalization. We have systematically revealed key components of MOF coatings on metal catalysts to promote selectivity. Ligand functionalization of the MOF linker caused minor changes in the catalytic selectivity for the desired unsaturated alcohol. The replacement of inorganic nodes from Zr-oxo nodes to Ce-oxo nodes, on the other hand, greatly enhanced the

selectivity. Infrared spectroscopic observations suggest that the interaction of the C=O group with the Ce-oxo node plays an important role in the enhanced hydrogenation of this bond. This enhancement can be extended to other MOF structures, as Pt@MOF catalysts with Ti-oxo nodes can also enhance the catalytic selectivity of cinnamly alcohol. However, increased interaction between the C=O groups and metal-oxo nodes alone is not enough to enhance selectivity. The relatively poor performance of Pt@Hf-UiO-66 demonstrates that C=C bond hydrogenation must also be suppressed. The encapsulation of metal NPs into MOFs is a route to promising composite catalysts, and our current study shows the critical role of metal-oxo nodes in regulating the catalytic selectivity of metal NPs in specific reactions. The understanding established in this work lays the foundation for further optimization of MOF-based heterogeneous catalyst design.

This work is supported by National Science Foundation (CHE 1566445), Iowa State University, and Boston College. W. -S. Lo acknowledges the Ministry of Education in Taiwan for the financial support.

4.4 Experimental Procedures

Chemicals: Unless otherwise stated, all the reactions were carried out in the air without taking any precaution to protect reactions from oxygen or moisture. Zirconium(IV) chloride ($ZrCl_4$, Alfa Aesar, >99.5%), zirconium(IV) oxychloride octahydrate ($ZrOCl_2 \cdot 8H_2O$, Acros Organic, >98%), N,N-dimethylformamide (DMF, Alfa Aesar, >99.8%), terephthalic acid (BDC, Sigma-Aldrich, 98%), acetic acid (Alfa Aesar, >99%), chloroplatinic acid hexahydrate ($H_2PtCl_6 \cdot 6H_2O$, Sigma-Aldrich, ≥37.50% Pt basis), ethylene glycol (Sigma-Aldrich, ≥99%), sodium hydroxide (NaOH, Alfa Aesar, 98%), hydrochloric acid (HCl, Alfa Aesar, ACS reagent), polyvinylpyrrolidone (PVP,

MW 40,000, Sigma-Aldrich), 2-aminoterephthalic acid (BDC-NH_2, Alfa Aesar, 99%), 2-nitroterephthalic acid (BDC-NO_2, Alfa Aesar, 99%), 2-methylterephthalic acid (BDC-CH_3, Aaron Chemicals, 97%), 2-hydroxyterephthalic acid (BDC-OH, Alfa Aesar, 98%), 2,5-dihydroxyterephthalic acid (BDC-$(OH)_2$, TCI Chemicals, 98%), hafnium(IV) dichloride oxide octahydrate ($HfOCl_2 \cdot 8H_2O$, Alfa Aesar, >98%), glycine (Sigma-Aldrich, 99%), benzoic acid (Sigma-Aldrich, 99.5%), cerium(IV) ammonium nitrate (Alfa Aesar, >98%), sodium chloride (NaCl, Sigma-Aldrich, >99.0%), methanol (Fisher, ACS reagent grade) were purchased from the indicated sources and used without further purification. Hydrogen (Airgas, 99.999%), ethylene (Airgas, 99.995%) and helium (Airgas, 99.999%) were used for the gas-phase hydrogenation. Cinnamaldehyde (Sigma-Aldrich, >95%), triethylamine (Sigma-Aldrich, >99.5%), cinnamyl alcohol (Sigma-Aldrich, >98%), cinnamyl alcohol (Sigma-Aldrich, > 98%), hydrocinnamaldehyde (Alfa Aesar, 95%), methanol (Alfa Aesar, LC-MS grade >99.8%), toluene (Alfa Aesar, HPLC grade >99.7%) and hydrogen (Airgas, 99.999%) were used for the liquid-phase hydrogenation. The Pt standards (1000 ppm, Inorganic Ventures) were used for inductively coupled plasma optical emission (ICP-OES) analysis.

Characterizations: A Bruker AXS D2 Phaser diffractometer was used for the powder X-ray diffraction characterization (PXRD). Transmission electron microscopy (TEM) was performed on the JEOL JEM-F200 electron microscope operated at an accelerating voltage of 200 kV. Scanning electron microscopy (SEM) was performed on a JEOL JSM-6340F scanning electron microscope. Diffuse reflectance infrared Fourier transform spectroscopies were carried out on a Bruker Tensor 27 IR spectrometer with a linearized mercury−cadmium−telluride detector, Harrick diffuse reflection accessory, and Praying Mantis high-temperature reaction chamber. Gas flows were regulated using calibrated mass flow controllers (Alicat Scientific). The amount of platinum

in each sample was analyzed by inductively coupled plasma optical emission spectrometry on an Agilent 5100 instrument. For ethylene hydrogenation studies, the gas composition was analyzed with a mass spectroscope (MKS special V2000P), and the temperature was controlled by a furnace (CARBOLITE) and PID controller (Diqi-Sense) with a type-K thermocouple. For cinnamaldehyde hydrogenation studies, the products were analyzed on a gas chromatograph with flame-ionization detection (Agilent 6850 Network GC with an autosampler, column: HP-1, 30 m × 0.25 mm × 0.25 μm).

Synthesis of Pt NPs: In general, 40.0 mg of $H_2PtCl_6 \cdot 6H_2O$ was dissolved in 6.0 mL of ethylene glycol in a 50-mL single-neck round bottom flask. Then, 2.0 mL of ethylene glycol containing 13.8 mg NaOH was added to the above solution. The reaction mixture was bubbled with N_2 for 20 minutes while stirring at 500 rpm at ambient temperature. After that, the reaction mixture was heated to 160 °C in an oil bath under the nitrogen atmosphere with reflux for 3 hours. After cooling, the formed Pt NPs were mixed with 12 mL of 1.0 M hydrochloric acid and centrifuged at 8000 rpm for 10 minutes to remove the unreacted residues. The resulting Pt NPs were dispersed into 15 mL of DMF for further use.

Synthesis of Zr-UiO-66: In general, 13.3 mg of BDC was dissolved in 7.62 mL DMF in a 20 mL scintillation vial, then 1.38 mL acetic acid was added into the solution to make the final volume to 9 mL. Next, 1 mL of DMF containing 18.6 mg of $ZrCl_4$ was introduced into the above solution. The solution was heated to 120 ˚C in an oil bath for 6 hours. After cooling, the formed Zr-UiO-66 powder was centrifuged at 3000 rpm for 10 minutes. The sample was washed with DMF three times and dispersed in DMF to give a known concentration of MOF particles (e.g., 10.0 mg/mL).

Synthesis of Zr-UiO-66-CH_3: In general, 14.4 mg of BDC-**CH_3** was dissolved in 7.62 mL DMF in a 20 mL scintillation vial, then 1.38 mL acetic acid was added into the solution to make the final volume to 9 mL. Next, 1 mL of DMF containing 18.6 mg of $ZrCl_4$ was introduced into the above solution. The solution was heated to 120 ˚C in an oil bath for 6 hours. After cooling, the formed Zr-UiO-66-**CH_3** powder was centrifuged at 3000 rpm for 10 minutes. The sample was washed with DMF three times and dispersed in DMF to give a known concentration of MOF particles (e.g., 10.0 mg/mL).

Synthesis of Zr-UiO-66-NO_2: In general, 16.9 mg of BDC-NO_2 was dissolved in 7.62 mL DMF in a 20 mL scintillation vial, then 1.38 mL acetic acid was added into the solution to make the final volume to 9 mL. Next, 1 mL of DMF containing 18.6 mg of $ZrCl_4$ was introduced into the above solution. The solution was heated to 120 ˚C in an oil bath for 6 hours. After cooling, the formed Zr-UiO-66-NO_2 powder was centrifuged at 3000 rpm for 10 minutes. The sample was washed with DMF three times and dispersed in DMF to give a known concentration of MOF particles (e.g., 10.0 mg/mL).

Synthesis of Zr-UiO-66-NH_2: In general, 14.5 mg of BDC-NH_2 was dissolved in 7.62 mL DMF in a 20 mL scintillation vial, then 1.38 mL acetic acid was added into the solution to make the final volume to 9 mL. Next, 1 mL of DMF containing 18.6 mg of $ZrCl_4$ was introduced into the above solution. The solution was heated to 120 ˚C in an oil bath for 6 hours. After cooling, the formed Zr-UiO-66-NH_2 powder was centrifuged at 3000 rpm for 10 minutes. The sample was washed with DMF three times and dispersed in DMF to give a known concentration of MOF particles (e.g., 10.0 mg/mL).

Synthesis of Zr-UiO-66-OH: In general, 32.8 mg of BDC-OH was dissolved in 1.2 mL DMF in a 20 mL scintillation vial, then 1.5 mL of DMF containing 42.0 mg of $ZrCl_4$ was

introduced into the above solution. Then, 349 uL DMF solution containing 39.8 mg of PVP was introduced into the above solution. After that, 2.56 mL acetic acid and 0.1 mL DI water were added subsequently. The solution was heated to 120 ˚C in an oil bath for 2 hours. After cooling, the formed Zr-UiO-66-OH powder was centrifuged at 3000 rpm for 10 minutes. The sample was washed with DMF three times and dispersed in DMF to give a known concentration of MOF particles (e.g., 10.0 mg/mL).

Synthesis of Zr-UiO-66-$(OH)_2$: In general, 35.7 mg of BDC-$(OH)_2$ was dissolved in 1.2 mL DMF in a 20 mL scintillation vial, then 1.5 mL of DMF containing 42.0 mg of $ZrCl_4$ was introduced into the above solution. Then, 349 uL DMF solution containing 39.8 mg of PVP was introduced into the above solution. After that, 2.56 mL acetic acid and 0.1 mL DI water are added. The solution was heated to 120 ˚C in an oil bath for 2 hours. After cooling, the formed Zr-UiO-66-$(OH)_2$ powder was centrifuged at 3000 rpm for 10 minutes. The sample was washed with DMF three times and dispersed in DMF to give a known concentration of MOF particles (e.g., 10.0 mg/mL).

Synthesis of Hf-UiO-66: In general, 1.1 g benzoic acid was dissolved in 5.0 mL DMF in a 20 mL scintillation vial, then 1.0 mL of DMF containing 30.0 mg of BDC was introduced into the above solution. Then, 4 mL DMF solution containing 74.2 mg of $HfOCl_2 \cdot 8H_2O$ was introduced into the above solution. After that, the solution was heated to 120 ˚C in an oil bath for 4 hours. After cooling, the formed Hf-UiO-66 powder was centrifuged at 3000 rpm for 10 minutes. The sample was washed with DMF three times and dispersed in DMF to give a known concentration of MOF particles (e.g., 10.0 mg/mL).

Synthesis of Ce_6-clusters: In general, 30.0 g of cerium ammonium nitrate and 9.0 g glycine were dissolved in 27.0 g DI water in a 500-mL PTFE bottle. Then, 321.0 g of a saturated

NaCl solution was introduced into the above solution. The reaction mixture was left at room temperature for 2 days. The formed yellow powders of Ce_6-clusters were filtered and rinsed with DI water to remove the unreacted residues. The formed Ce_6-clusters were dried in the oven at 80 ^oC overnight and stored in a desiccator for further use (product yield at around 10 g).

Synthesis of Ce-UiO-66: In general, 1.5 g benzoic acid was dissolved in 7.0 mL DMF in a 20 mL scintillation vial, then 2.0 mL of DMF containing 66.0 mg of BDC was introduced into the above solution. Then, 1 mL DI water containing 78.0 mg of Ce_6-clusters was introduced into the above solution (Note: Ce_6-clusters are insoluble in DI water at room temperature. So, the aqueous solution containing Ce_6-clusters was placed in a 90 ˚C oil bath for 2 minutes while stirring to give a transparent mixture.) After that, the reaction mixture was heated to 90 ˚C in an oil bath for 4 hours. After cooling, the formed Ce-UiO-66 powder was centrifuged at 3000 rpm for 10 minutes. The sample was washed with DMF three times and dispersed in DMF to give a known concentration of MOF particles (e.g., 10.0 mg/mL).

Synthesis of Ti-MiL-125: In general, 600.0 mg of BDC was dissolved in 9.0 mL DMF in a 30 mL microwave-reaction vial, then 1.0 mL methanol was added into the solution. Next, 0.5 mL acetic acid was introduced into the above solution, and the resulting solution was purged with N_2 for 20 minutes while stirring at 500 rpm at room temperature. Next, 0.37 mL $Ti(OBu)_4$ was introduced into the above solution, and the reaction vial was sealed under a nitrogen atmosphere. The reaction mixture was stirred at 500 rpm in a 100 ˚C oil bath for 15 hours. After cooling, the formed Ti-MiL-125 powder was centrifuged at 3000 rpm for 10 minutes. The sample was washed with DMF three times and dispersed in DMF to give a known concentration of MOF particles (e.g., 10.0 mg/mL).

Synthesis of Pt NPs on the external surface of MOF particles: In general, 50.0 mg of MOF particles (in DMF) was added in a 20 mL scintillation vial. Then, 0.75 mL of Pt NPs in DMF was added dropwise to the above solution with magnetic stirring at 900 rpm. The mixture was stirred at 500 rpm for 24 h at ambient temperature. The sample was centrifuged at 3000 rpm for 10 minutes and washed with DMF twice to remove free Pt NPs. The resulting Pt-on-MOF samples were used for MOF coating without further purification.

If the resulting Pt-on-MOF samples were used as the control in catalysis, as-synthesized Pt-on-MOF samples powder was activated by the solvent exchange to remove residues trapped in the framework. Activation was performed by the solvent exchange. Firstly, the samples were exchanged with fresh DMF every 12 h for one day while stirring at 500 rpm. Next, the samples were exchanged with fresh methanol every 12 h for 5 days while stirring at 500 rpm. The sample was dried in vacuum for 24 h and reduced under a 10 % H_2/He flow (100 mL/min) at 110 °C for 1 h. The activated sample was stored in a desiccator for further use.

Synthesis of Pt@Zr-UiO-66 and the analogues with functionalized ligands: Pt NPs were first supported on defined Zr-UiO-66 crystals and then coated with Zr-UiO-66 to form Pt@Zr-UiO-66 catalysts. The same method is extended to prepare catalysts with various functional groups on BDC ligands, including -NH_2, -CH_3, -NO_2, -OH, and -$(OH)_2$. In general, 0.15 mmol of BDC-based ligands was dissolved in 2.0 mL DMF in a 20 mL scintillation vial. Then, 2.0 mL acetic acid was added to the above solution, followed by 1 mL DMF containing 8.5 mg of Pt-on-MOF samples. The reaction mixture was heated to 90 ˚C for 5 minutes with stirring at 500 rpm. After cooling for 5 minutes, 1 mL DMF containing 10.5 mg $ZrOCl_2 \cdot 8H_2O$ introduce into the above solution, and the resulting mixture was stirred at 90 oC for 4 hours. After that, the formed Pt@Zr-UiO-66 sample was centrifuged at 3000 rpm for 10 minutes. The sample was washed with DMF

three times. The as-synthesized Pt@Zr-UiO-66 powder was activated by the solvent exchange to remove residues trapped in the framework. Activation was performed by the solvent exchange. Firstly, the samples were exchanged with fresh DMF every 12 h for a day while stirring at 500 rpm. Next, the samples were exchanged with fresh methanol every 12 h for 5 days while stirring at 500 rpm. The sample was dried in vacuum for 24 h and reduced under a 10 % H_2/He flow (100 mL/min) at 110 ˚C for 1 h. The activated sample was stored in a desiccator for further use.

Synthesis of Pt@Hf-UiO-66: In general, 400.0 mg benzoic acid was dissolved in 6.5 mL DMF in a 20 mL scintillation vial, then 0.5 mL of DMF containing 15.0 mg of BDC was introduced into the above solution. Then, 2 mL DMF solution containing 37.1 mg of $HfOCl_2 \cdot 8H2O$ was introduced into the above solution. 1 mL DMF containing 18.0 mg of Pt-on-Hf-UiO-66 samples was introduced into the above solution, and the resulting mixture was stirred at 100 ˚C for 2 hours. After that, the formed Pt@Hf-UiO-66 sample was centrifuged at 3000 rpm for 10 minutes. The sample was washed with DMF three times. The as-synthesized Pt@Hf-UiO-66 powder was activated by the solvent exchange to remove residues trapped in the framework. Activation was performed by the solvent exchange. Firstly, the samples were exchanged with fresh DMF every 12 h for one day while stirring at 500 rpm. Next, the samples were exchanged with fresh methanol every 12 h for 5 days while stirring at 500 rpm. The sample was dried in vacuum for 24 h and reduced under a 10 % H_2/He flow (100 mL/min) at 110 ˚C for 1 h. The activated sample was stored in a desiccator for further use.

Synthesis of Pt@Ce-UiO-66: In general, 800.0 mg benzoic acid was dissolved in 8.25 mL DMF in a 20 mL scintillation vial, then 0.5 mL of DMF containing 33.0 mg of BDC was introduced into the above solution. Then, 0.25 mL DI water containing 19.5 mg of Ce_6-clusters was introduced into the above solution. 1 mL DMF containing 20.0 mg of Pt-on-Ce-UiO-66 samples was

introduced into the above solution, and the resulting mixture was stirred at 90 ˚C for 1 hour. After that, the formed Pt@Ce-UiO-66 sample was centrifuged at 3000 rpm for 10 minutes. The sample was washed with DMF three times. The as-synthesized Pt@Ce-UiO-66 powder was activated by the solvent exchange to remove residues trapped in the framework. Activation was performed by the solvent exchange. Firstly, the samples were exchanged with fresh DMF every 12 h for one day while stirring at 500 rpm. Next, the samples were exchanged with fresh methanol every 12 h for 5 days while stirring at 500 rpm. The sample was dried in vacuum for 24 h and reduced under a 10 % H_2/He flow (100 mL/min) at 110 ˚C for 1 h. The activated sample was stored in a desiccator for further use.

Synthesis of Pt@Ti-UiO-66: In general, 100.0 mg of BDC was dissolved in 8.0 mL DMF in a 20 mL scintillation vial, then 1.0 mL methanol was added into the solution. Next, 1.0 mL acetic acid was introduced into the above solution, and the resulting solution was purged with N_2 for 20 minutes while stirring at 500 rpm at room temperature. Next, 62.5 μL $Ti(OBu)_4$ was introduced into the above solution, and the reaction vial was sealed under a nitrogen atmosphere. The resulting mixture was stirred at 90 ˚C for 1 hour. After cooling, the formed Pt@MiL-125 powder was centrifuged at 3000 rpm for 10 minutes. The sample was washed with DMF three times. The as-synthesized Pt@MiL-125 powder was activated by the solvent exchange to remove residues trapped in the framework. Activation was performed by the solvent exchange. Firstly, the samples were exchanged with fresh DMF every 12 h for one day while stirring at 500 rpm. Next, the samples were exchanged with fresh methanol every 12 h for 5 days while stirring at 500 rpm. The sample was dried in vacuum for 24 h and reduced under a 10 % H_2/He flow (100 mL/min) at 110 ˚C for 1 h. The activated sample was stored in a desiccator for further use.

Sample preparation for ICP-OES measurement: Pt@MOF samples at around 5.0 mg were dispersed in 0.5 mL concentrated HCl and 0.15 mL concentrated HNO_3 by sonication for 10 min. The resulting mixture was left at room temperature for 6 hours for digesting the Pt NPs. The resulting solution was then diluted to 10 mL with deionized water using a volumetric flask. Before the ICP-OES measurement, the solution was filtered through a filter membrane (0.22 μm). The quantitative analysis of Pt was carried out against calibration using known concentrations of standard solutions. ICP-OES spectrometry was performed using an Agilent 5100 instrument.

DRIFTS measurement for molecular hydrogen: Before performing DRIFTS analysis, the Praying Mantis high-temperature IR reaction chamber was heated to 150 °C under N_2 flow (10 ft^3/hr) for 1 hour. The heating step was applied to remove trapped residues in the chamber. To carry out DRIFTS analysis, 10.0 mg of MOF samples was diluted with 50.0 mg of KBr. The diluted sample was packed in the sample cup in the IR reaction chamber under He flow (50 mL/min) at ambient temperature. A spectrum of the sample was recorded as a background, and the background was further stabilized by flowing He through the system for 50 min. During the stabilization, a series of spectra were measured with an interval of 5 min, and the differences between spectra were monitored to confirm the stabilization (difference less than 1.0 mOD at the spectral region of interest). The adsorption of molecular hydrogen was performed by introducing 2% H_2/He (50 mL/min) and He (50 mL/min) into the IR reaction chamber for 10 sec. After that, the He flow (50 mL/min) was introduced for another 15 sec. Then, the IR reaction chamber was sealed by closing valves connected to the chamber. The DRIFTS spectra for molecular hydrogen were measured. All spectra were collected with 64 scans at a resolution of 4 cm^{-1} from 1000 cm^{-1} to 4000 cm^{-1}, and the gas flow was controlled by the mass flow controller (Alicat Scientific).

DRIFTS measurement for hydrocinnamaldehyde: Before performing DRIFTS analysis, the Praying Mantis high-temperature IR reaction chamber was heated to 150 °C under N_2 flow (10 ft^3/hr) for 1 hour. The heating step was applied to remove trapped residues in the chamber. To carry out DRIFTS analysis, 10.0 mg of MOF samples was diluted with 50.0 mg of KBr. The diluted sample was packed in the sample cup in the IR reaction chamber at ambient temperature. Before the background stabilization, the sample was treated by an activation process under He flow (75 mL/min) at 110 °C for 30 min to remove the absorbed water. After that, the sample was cooled to 40 °C, and the He flow was adjusted to 50 mL/min. A spectrum of the sample was recorded as a background. The background was further stabilized by flowing He through the system for 50 min. During the stabilization, a series of spectra were measured with an interval of 5 min. The difference between spectra was monitored to confirm the stabilization (difference less than 1.0 mOD at the spectral region of interest). To mimic the reaction condition, all DRIFTS measurement for hydrocinnamaldehyde was carried out at 40 °C.

The adsorption of hydrocinnamaldehyde was performed by introducing the He flow containing hydrocinnamaldehyde, whereas a He flow (20 mL/min) was introduced to the glass bubbler filled with hydrocinnamaldehyde. Because of the low vapor pressure of hydrocinnamaldehyde, the glass bubbler was heated to 90 ºC, and the temperature was monitored by a type-K thermocouple. After that, the He flow (30 mL/min) was introduced to the chamber for 40 min to remove weakly bounded residues of hydrocinnamaldehyde. Then, the DRIFTS spectra for hydrocinnamaldehyde were measured. All spectra were collected with 64 scans at a resolution of 4 cm^{-1} from 1000 cm^{-1} to 4000 cm^{-1}, and the gas flow was controlled by the mass flow controller (Alicat Scientific).

Ethylene hydrogenation: The catalysts were diluted with 1.0 g low surface area quartz and loaded into U-shaped glass reactors. The glass reactor was then connected to a home-built gas-phase flow system for alkene hydrogenation. Gas flows, including helium, hydrogen, and ethylene, were regulated using calibrated mass flow controllers (Alicat Scientific). Gas composition was analyzed with a mass spectroscope (MKS special V2000P). The temperature was controlled by a furnace (CARBOLITE) and PID controller (Diqi-Sense) with a type-K thermocouple. Before the reaction, the catalysts were activated in the glass reactor at 80 ˚C under 10% H_2/He (100 mL/min) for 30 min. Gas-phase ethylene hydrogenation was run at 4 ˚C under a continuous system (C_2H_4/H_2/He=1.2/12/77 mL/min). To compare activity, the conversion of each reaction was kept low (< 20.0 %). The amount of catalysts used in each measurement was shown as followed: Pt@Ti-MiL-125 (5.1 mg, 5.2 mg, 4.9 mg), Pt@Ce-UiO-66 (4.6 mg, 2.6 mg, 2.0 mg), Pt@Zr-UiO-66 (3.6 mg, 1.9 mg, 1.6 mg), and Pt@Zr-UiO-66 (1.4 mg, 1.9 mg, 1.4 mg). The mass activity to ethylene hydrogenation in each sample was calculated based on the amount of platinum in each sample.

Cinnamaldehyde hydrogenation: Pt@MOF catalysts at around 3.5 mg were dispersed in 1.0 mL methanol in the 5.0-mL ampule. Then, 0.5 mL methanol containing 25.0 μL cinnamaldehyde and 15.0 μL triethylamine were added into the above solution, followed by 0.5 mL methanol to make the final volume 2.0 mL. (Note: triethylamine was added to prevent the side reaction of condensation) Before catalysis, the high-pressure reactor vessel (Wattacas Inc., 500 mL) was preheated to 40 ˚C. The temperature was controlled using a hot plate (RCT basic, IKA) with a type-K thermocouple. Subsequently, the ampule was transferred into a high-pressure reactor vessel. The autoclave was purged 5 times with H_2 to remove air. Then, the hydrogenation of cinnamaldehyde was carried at 30 bar H_2 at 40 ˚C with magnetic stirring at 750 rpm. After that, the catalysts were separated by centrifugation, and 1.0 mL reaction solution was mixed with 0.5

mL internal standard (0.2 mL toluene in 4.8 mL methanol). The products were analyzed on a gas chromatograph with flame-ionization detection (Agilent 6850 Network GC with an autosampler, column: HP-1, 30 m × 0.25 mm × 0.25 μm). The reaction conversion was calculated by dividing the amount of all three products (cinnamyl alcohol, hydrocinnamaldehyde and 3-phenylpropanol) observed after catalysis with the amount of cinnamaldehyde observed before catalysis. Because MOF will adsorb reactants, the amount of cinnamaldehyde measured before catalysis was determined by the blank experiment without adding any MOF samples. The catalytic selectivity was determined by its ratio to the sum of all three products (Cinnamyl alcohol, hydrocinnamaldehyde and 3-phenylpropanol). The controlled experiments using pure MOF materials were performed by using 4.0 mg of pure MOF samples. The amount of catalysts used in each measurement was shown as followed: Pt-on-Zr-UiO-66 (3.6 ± 0.1 mg), Pt@Zr-UiO-66 (3.2 ± 0.1 mg), (c) Pt@Zr-UiO-66-CH_3 (5.0 ± 0.1 mg), Pt@Zr-UiO-66-NH_2 (3.1 ± 0.1 mg), Pt@Zr-UiO-66-NO_2 (3.7 ± 0.3 mg), Pt@Zr-UiO-66-OH (3.6 ± 0.2 mg), Pt@Zr-UiO-66-$(OH)_2$ (3.4 ± 0.1 mg), Pt@Hf-UiO-66 (3.7 ± 0.1 mg), Pt@Ce-UiO-66 (3.0 ± 0.2 mg), and Pt@Ti-MiL-125 (4.1 ± 0.1 mg).

Hydrogenation of hydrocinnamaldehyde and cinnamyl alcohol: 2.9 mg of catalysts was dispersed in 1.0 mL methanol in the 5.0-mL ampule. Then, 0.5 mL methanol containing 50.0 μL reactants (hydrocinnamaldehyde or cinnamyl alcohol) and 15.0 μL triethylamine were added into the above solution, followed by 0.5 mL methanol to make the final volume 2.0 mL. Before catalysis, the high-pressure reactor vessel (Wattacas Inc., 500 mL) was preheated to 40 ˚C. The temperature was controlled using a hot plate (RCT basic, IKA) with a type-K thermocouple. Subsequently, the ampule was transferred into a high-pressure reactor vessel. The autoclave was purged 5 times with H_2 to remove air. Then, the hydrogenation was carried at 30 bar H_2 at 40 ˚C

with magnetic stirring at 750 rpm. After that, the catalysts were separated by centrifugation, and 1.0 mL reaction solution was mixed with 0.5 mL internal standard (0.2 mL toluene in 4.8 mL methanol). The targeted product of 3-phenylpropanol was monitored by a gas chromatograph with flame-ionization detection (Agilent 6850 Network GC with an autosampler, column: HP-1, 30 m × 0.25 mm × 0.25 μm).

4.5 Appendix

Table A4.1: Summary of the size of Pt NPs in catalysts

Catalyst	Averaged Size of Pt NPs (nm)[a]
Pt-on-Zr-UiO-66	3.9 ± 1.0
Pt@Zr-UiO-66	3.9 ± 1.0
Pt@Zr-UiO-66-CH_3	5.1 ± 1.1
Pt@Zr-UiO-66-NO_2	3.9 ± 0.9
Pt@Zr-UiO-66-NH_2	3.2 ± 0.8
Pt@Zr-UiO-66-OH	3.7 ± 0.7
Pt@Zr-UiO-66-$(OH)_2$	3.8 ± 0.7
Pt@Hf-UiO-66	4.1 ± 0.8
Pt@Ce-UiO-66	3.4 ± 1.0
Pt@Ti-MiL-125	4.5 ± 1.0

[a] The standard deviation was obtained by measuring 15-20 Pt NPs in the corresponding TEM image.

Table A4.2: Summary of ICP results for the Pt loading in catalysts

Catalyst	**Pt Loading (wt %)[a]**
Pt-on-Zr-UiO-66	0.76 ± 0.02
Pt-on-Ce-UiO-66	0.82 ± 0.01
Pt@Zr-UiO-66	0.65 ± 0.01
Pt@Zr-UiO-66-CH_3	0.38 ± 0.01
Pt@Zr-UiO-66-NO_2	0.30 ± 0.01
Pt@Zr-UiO-66-NH_2	0.18 ± 0.04
Pt@Zr-UiO-66-OH	0.56 ± 0.01
Pt@Zr-UiO-66-$(OH)_2$	0.24 ± 0.02
Pt@Hf-UiO-66	0.59 ± 0.01
Pt@Ce-UiO-66	0.59 ± 0.01
Pt@Ti-MiL-125	0.47 ± 0.01

[a] The standard deviation was obtained based on three independent measurements.

Table A4.3: Summary of selectivity for cinnamaldehyde hydrogenation

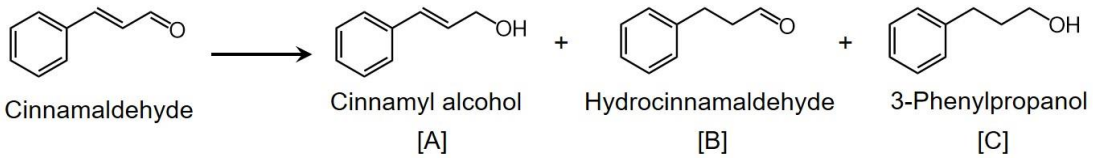

Cinnamaldehyde | Cinnamyl alcohol [A] | Hydrocinnamaldehyde [B] | 3-Phenylpropanol [C]

Catalyst[a]	Reaction Time (Hour)	Reaction Conversion (%)	Selectivity to [A] (%)	Selectivity to [B] (%)	Selectivity to [C] (%)
Pt-on-Zr-UiO-66	0.5	19.7 ± 1.1	24.3 ± 1.7	75.6 ± 1.7	< 1.0 [b]
Pt-on-Ce-UiO-66	1.0	26.9 ± 1.9	71.6 ± 2.0	24.5 ± 1.9	4.0 ± 0.1
Pt@Zr-UiO-66	7.0	26.7 ± 0.6	44.5 ± 1.0	47.2 ± 1.1	8.4 ± 0.2
Pt@Zr-UiO-66-CH_3	17.0	10.2 ± 3.9	43.7 ± 2.6	46.7 ± 3.0	9.8 ± 5.2
Pt@Zr-UiO-66-NO_2	5.0	24.0 ± 2.3	26.3 ± 1.4	57.8 ± 1.5	16.1 ± 0.1
Pt@Zr-UiO-66-NH_2	8.0	19.9 ± 1.6	27.7 ± 1.1	46.8 ± 0.5	25.9 ± 1.7
Pt@Zr-UiO-66-OH	3.0	26.0 ± 2.9	58.7 ± 3.4	38.1 ± 3.4	3.2 ± 0.1
Pt@Hf-UiO-66	8.0	28.0 ± 4.4	33.8 ± 3.2	63.5 ± 3.5	2.7 ± 0.4
Pt@Ce-UiO-66	3.0	24.9 ± 1.7	86.9 ± 0.6	13.1 ± 0.6	< 1.0 [b]
Pt@Ti-MiL-125	16.5	24.7 ± 1.1	90.6 ± 0.7	9.3 ± 0.7	< 1.0 [b]

[a] Selectivity was determined by its ratio to the sum of all three products (A = cinnamyl alcohol, B = hydrocinnamaldehyde, and C=3-phenylpropanol). [b] Product was not observed in the GC-FID analysis.

Table A4.4: Summary of experiments without Pt NPs for cinnamaldehyde hydrogenation

Catalyst[a]	Reaction Time (Hour)	Reaction Conversion (%)
Zr-UiO-66	8.0	< 1.0 [a]
Ce-UiO-66	3.0	< 1.0 [a]
Zr-UiO-66-CH_3	8.0	< 1.0 [a]
Zr-UiO-66-NO_2	8.0	< 1.0 [a]
Zr-UiO-66-NH_2	8.0	< 1.0 [a]
Zr-UiO-66-OH	8.0	< 1.0 [a]
Zr-UiO-66-$(OH)_2$	8.0	< 1.0 [a]
Hf-UiO-66	8.0	< 1.0 [a]
Ti-MiL-125	8.0	< 1.0 [a]

[a] Products (cinnamyl alcohol, hydrocinnamaldehyde, and 3-phenylpropanol) were not observed in the GC-FID analysis.

Table A4.5: Summary of selectivity for cinnamaldehyde hydrogenation at a higher conversion

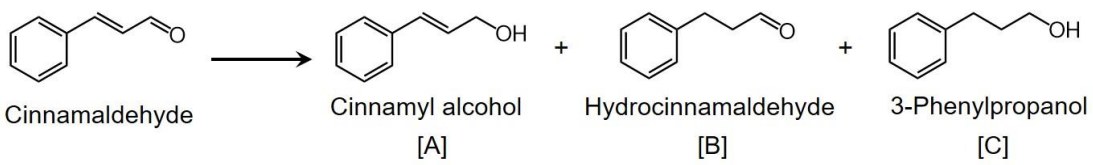

Catalyst[a]	Reaction Time (Hour)	Reaction Conversion (%)	Selectivity to [A] (%)	Selectivity to [B] (%)	Selectivity to [C] (%)
Pt-on-Zr-UiO-66	1.0	39.8 ± 0.2	24.2 ± 0.7	74.1 ± 1.0	1.6 ± 1.4
Pt@Zr-UiO-66-OH	4.0	34.9 ± 6.9	55.8 ± 1.5	40.1 ± 1.6	4.1 ± 0.4
Pt@Zr-UiO-66-$(OH)_2$	6.0	41.9 ± 2.0	73.2 ± 3.4	24.1 ± 3.2	2.8 ± 0.2
Pt@Ce-UiO-66	4.5	60.0 ± 1.9	82.3 ± 1.1	12.1 ± 0.7	6.0 ± 0.4

[a] Selectivity was determined by its ratio to the sum of all three products (A = cinnamyl alcohol, B = hydrocinnamaldehyde, and C=3-phenylpropanol). The standard deviation was obtained based on three independent measurements. [b] Product was not observed in the GC-FID analysis.

Table A4.6: Summary of mass activity for ethylene hydrogenation

Catalyst	Ethylene/Pt ($mmole_{ethylene} \cdot g_{Pt}^{-1}$)[a]
Pt@Hf-UiO-66	15.3 ± 0.5
Pt@Zr-UiO-66	9.3 ± 0.8
Pt@Ce-UiO-66	3.8 ± 1.0
Pt@Ti-MiL-125	5.1 ± 0.5

[a] The standard deviation was obtained based on three independent measurements. The mass activity was calculated by keeping a low conversion of ethylene hydrogenation (< 20.0 %).

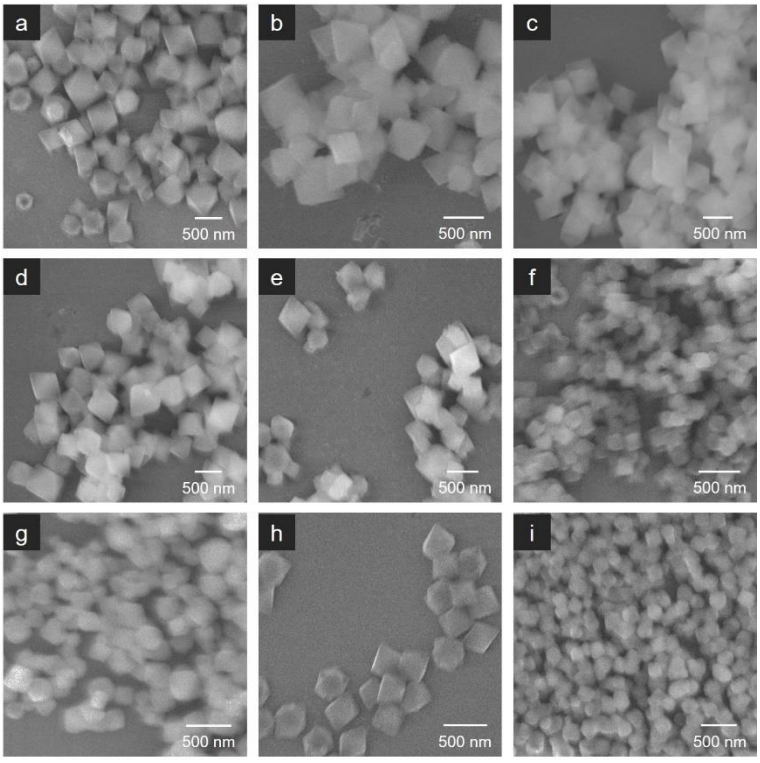

Figure A4.1: SEM images of Pt NPs-based catalysts: (a) Pt-on-Zr-UiO-66, (b) Pt@Zr-UiO-66, (c) Pt@Zr-UiO-66-CH_3, (d) Pt@Zr-UiO-66-NH_2, (e) Pt@Zr-UiO-66-NO_2, (f) Pt@Zr-UiO-66-OH, (g) Pt@Hf-UiO-66, (h) Pt@Ce-UiO-66, and (i) Pt@Zr-UiO-66-$(OH)_2$.

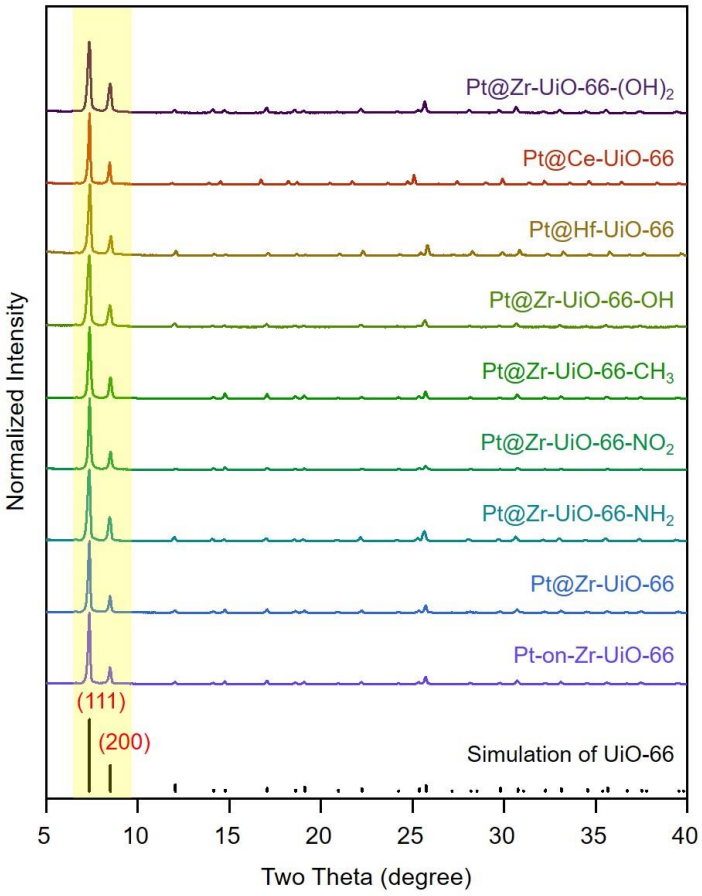

Figure A4.2: PXRD patterns of Pt NPs-based catalysts and the simulation of UiO-66.

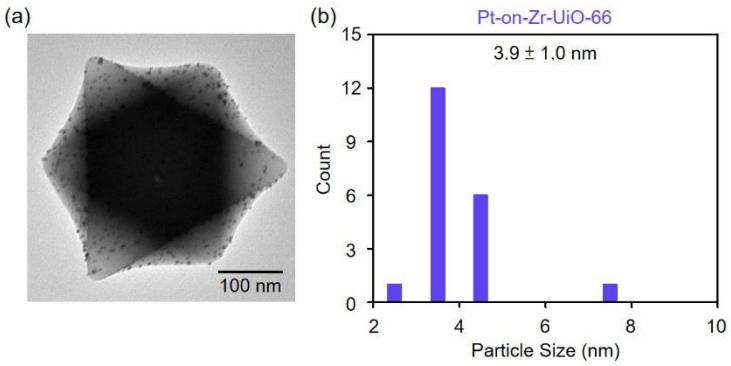

Figure A4.3: (a) TEM image of Pt-on-Zr-UiO-66, and the corresponding (b) size histogram of Pt NPs.

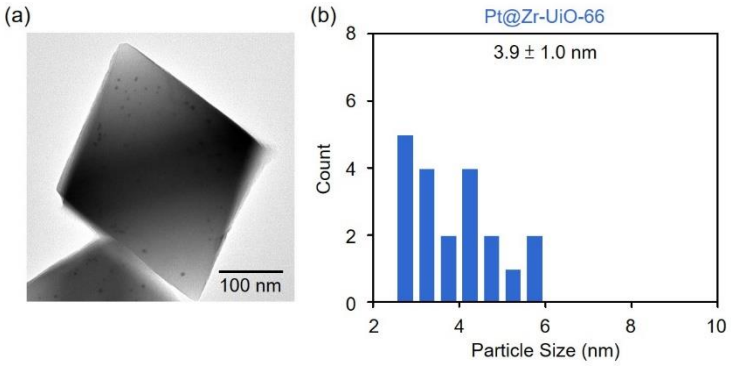

Figure A4.4: (a) TEM image of Pt@Zr-UiO-66, and the corresponding (b) size histogram of Pt NPs.

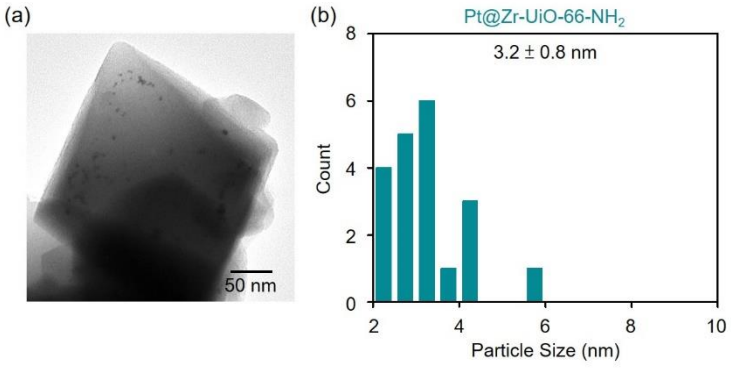

Figure A4.5: (a) TEM image of Pt@Zr-UiO-66-NH_2, and the corresponding (b) size histogram of Pt NPs.

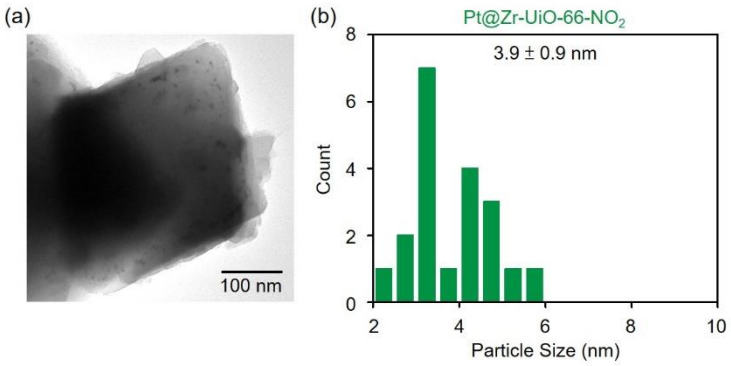

Figure A4.6: (a) TEM image of Pt@Zr-UiO-66-NO_2, and the corresponding (b) size histogram of Pt NPs.

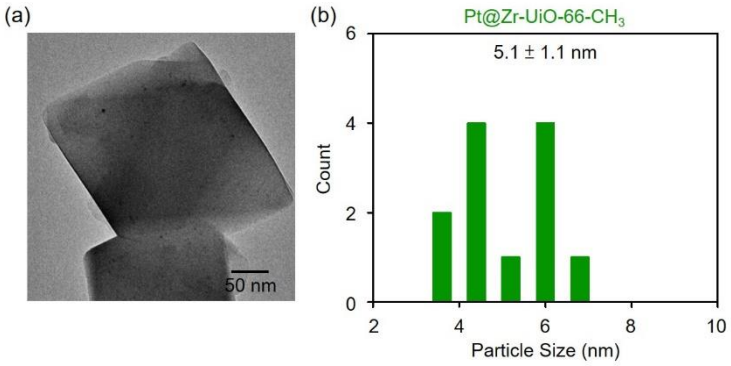

Figure A4.7: (a) TEM image of Pt@Zr-UiO-66-CH_3, and the corresponding (b) size histogram of Pt NPs.

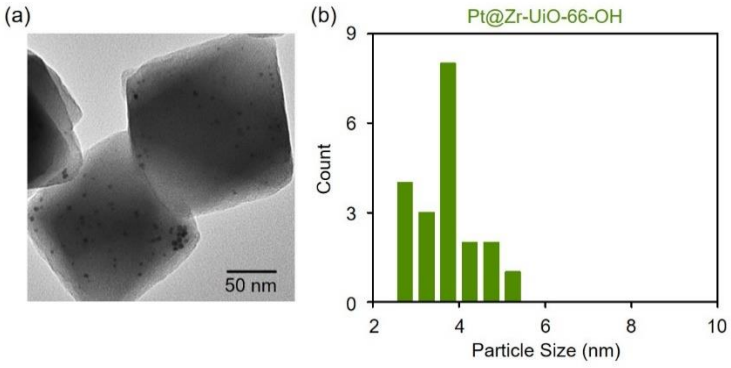

Figure A4.8: (a) TEM image of Pt@Zr-UiO-66-OH, and the corresponding (b) size histogram of Pt NPs.

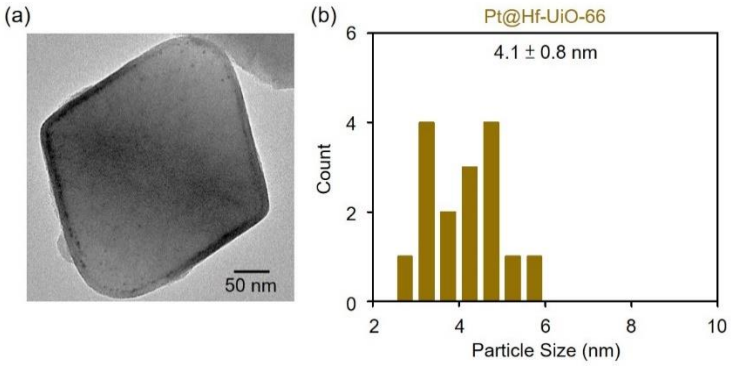

Figure A4.9: (a) TEM image of Pt@Hf-UiO-66, and the corresponding (b) size histogram of Pt NPs.

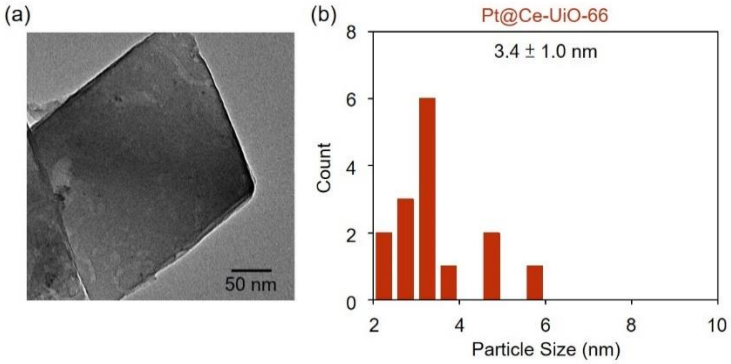

Figure A4.10: (a) TEM image of Pt@Ce-UiO-66, and the corresponding (b) size histogram of Pt NPs.

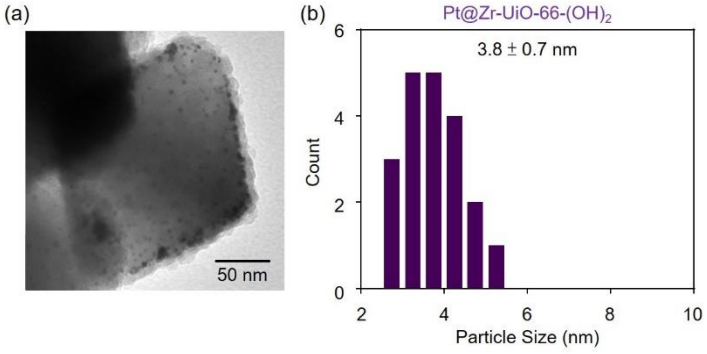

Figure A4.11: (a) TEM image of Pt@Zr-UiO-66-$(OH)_2$, and the corresponding (b) size histogram of Pt NPs.

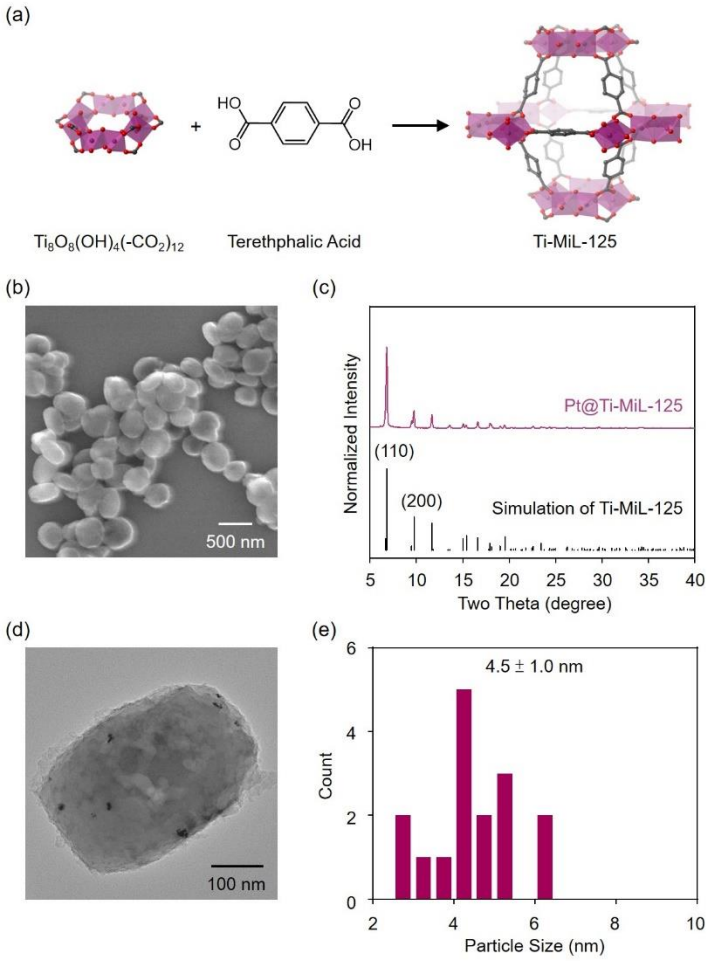

Figure A4.12: (a) Schematic illustration of Ti-MiL-125. Characterization of Pt@Ti-MiL-125: (b) SEM image, (c) PXRD analysis, (d) TEM image and the corresponding (e) size histogram of Pt NPs.

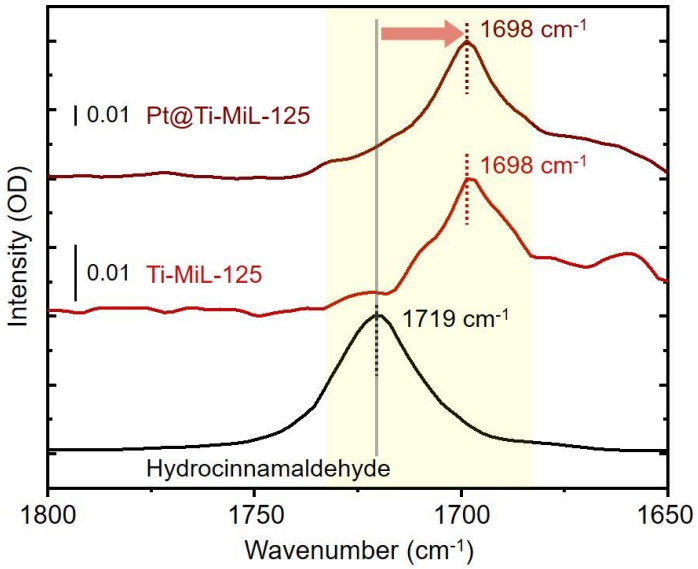

Figure A4.13: DRIFTS of hydrocinnamaldehyde over Ti-MiL-125, and Pt@Ti-MiL-125.

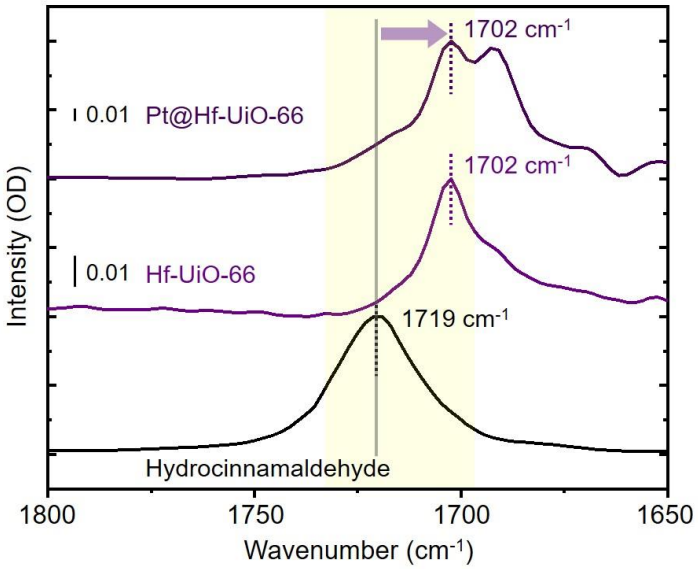

Figure A4.14: DRIFTS of hydrocinnamaldehyde over Hf-UiO-66, and Pt@Hf-UiO-66.

This page is on purposely left in blank

This page is on purposely left in blank

5.0 Chapter 5:

Probing Interactions between Metal-Organic Frameworks and Freestanding Enzymes in a Hollow Structure

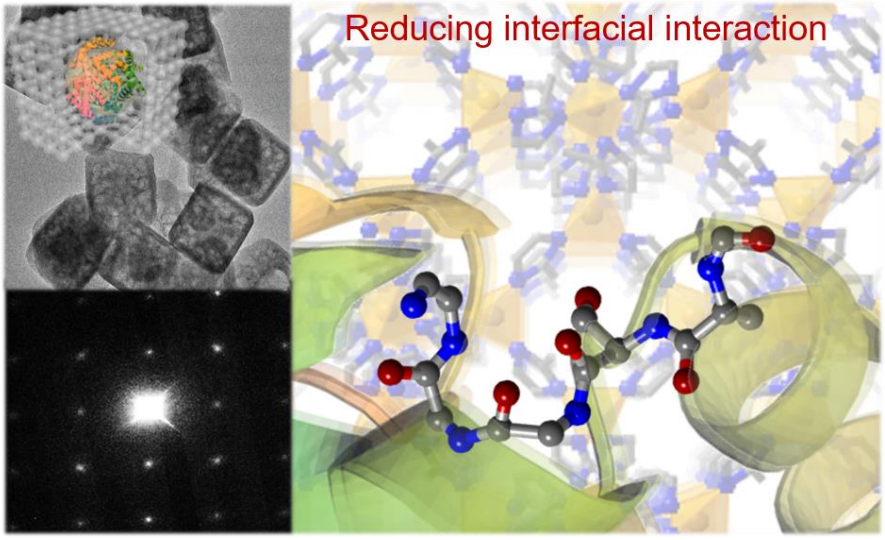

A significant portion of the work described in this chapter has been published in:

Chen, S. –Y.[#]; **Lo, W. –S.[#] (co-first author)**; Huang Y. –D.; Si, X.; Liao, F. -S.; Lin, S. –W.; Williams, B. P.; Sun, T. –Q.; Lin, H. –W.; An, Y.; Sun, T.; Ma, Y.; Yang, H. –C.; Chou, L. –Y.; Shieh, F. –K.; Tsung, C. –K. Probing Interactions between Metal-Organic Frameworks and Freestanding Enzymes in a Hollow Structure. *Nano Lett.* **2020**, 20, 6630–6635. Copyrights 2020 American Chemical Society.

5.1 Introduction

To improve recyclability, enzymes have been immobilized on various supports for different applications.[202-204] The immobilized enzymes have even shown enhanced performance, such as increased activity and stability.[205-206] Immobilization has been carried out through many methods, including adsorption, entrapment, covalent binding, and cross-linking.[207-208] In general, the enzymes are either fixed on the external surfaces of a solid support, or trapped in a porous material.[209-210] While the specific or non-specific interactions between the enzymes and host materials have been reported to increase enzymatic stability,[211-212] these interactions often alter the enzymes from their native state and lead to a change in their biological activity.[213-216] Therefore, it could be beneficial to develop a method to reduce interfacial interactions after the syntheses and allows enzymes to work under a less altered state, which could enhance the activities of immobilized enzymes. Using metal-organic frameworks (MOFs) as host provides such an opportunity because of their post-synthetic modification strategies.[217-219]

MOFs have been used as host materials to impart new enzymatic functions.[220-222] Farha and co-workers have immobilized organophosphorus acid anhydrolase into NU-1000 derivatives.[223-225] Zhou and co-workers have impregnated several enzymes in PCN-333 derivatives.[226-228] Falcaro, Doonan, and co-workers have exhibited the embedding of biomolecules in zeolitic imidazolate framework-8 (ZIF-8).[229-232] Ma and co-workers have incorporated microperoxidase-11 into Tb-mesoMOF.[233-236] We have encapsulated catalase in ZIF-90 and ZIF-8.[237-238] These studies have shown interesting results; however, like other host materials, the interfacial interactions between the enzymes and MOFs impact their biological activities. Herein, to investigate this influence, we propose to hollow out the solid MOFs microcrystals with enzymes encapsulated in and compare the interactions between enzyme and MOFs before and after the

hollowing process. Before hollowing process, the enzymes are confined in the solid MOFs crystals. After hollowing, the enzymes are sealed inside of the central cavity of hollow MOFs crystals in a freestanding form and the permeable MOFs shell allows reactants to go in without leaching of the enzymes (**Figure 5.1**).

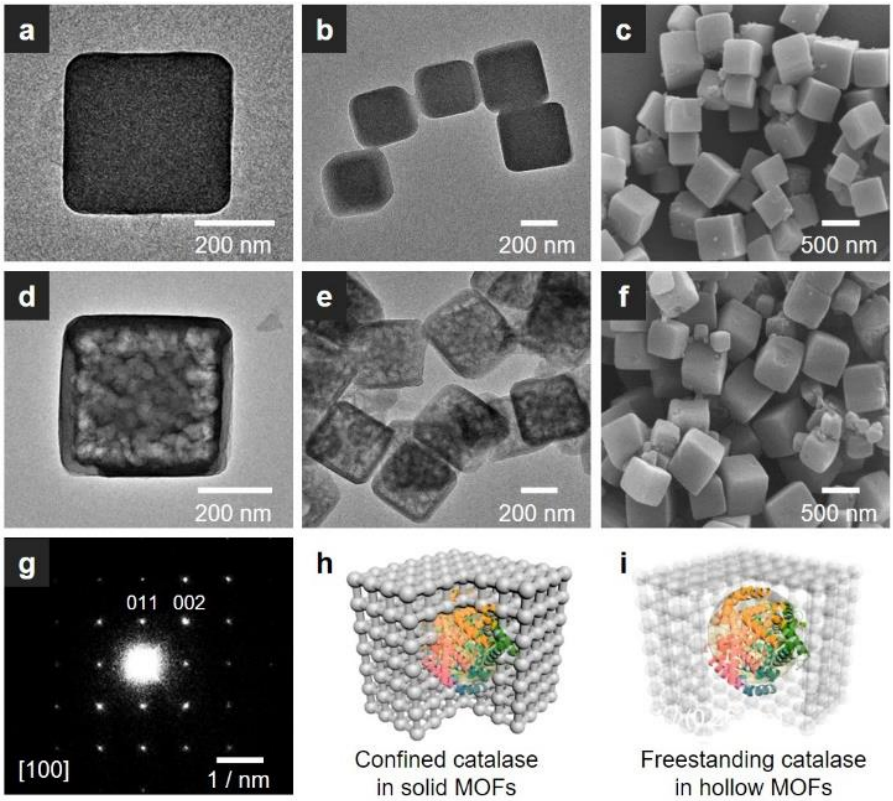

Figure 5.1: TEM and SEM images of catalase encapsulated in (a-c) solid and (d-f) hollow MOFs. (g) The electron diffraction pattern of catalase in hollow ZIF-8. Schematic illustration of catalase encapsulated in (h) solid and (i) hollow MOFs.

5.2 Results and Discussions

To demonstrate this concept, catalase was first encapsulated into ZIF-67 microcrystals and then ZIF-8 shells were overgrown on the ZIF-67 cores.[237] Due to the epitaxial overgrowth, single-crystalline core-shell microcrystals were formed. Then we used a reported method to remove the ZIF-67 cores through a mild hollowing process and form a single-crystalline hollow ZIF-8.[239-240] After the hollowing process, the catalase is held in the central cavity of the hollow ZIF-8 crystal. Both solid and hollow samples were characterized by transmission electron microcopy (TEM) and scanning electron microscopy (SEM). **Figures 5.1a-c** show the uniform solid core-shell MOFs with confined enzymes, and **Figures 5.1d-f** show that the central cavities formed with no change to the morphology of the MOFs crystals after the hollowing process. The hollow sample shows a hysteresis loop in the nitrogen isothermal sorption profiles, indicating central cavity formation (**Figure A5.1**). Powder X-ray diffraction (PXRD) shows that the crystal structure was maintained after the hollowing process (**Figure A5.2**). The electron diffraction pattern reveals that the hollow ZIF-8 microcrystals are single crystalline (**Figure 5.1g**). To verify enzyme encapsulation in solid and hollow MOFs microcrystals, we digested the samples and analyzed them with sodium dodecyl sulfate-polyacrylamide gel electrophoresis (SDS-PAGE). The gels show a characteristic band of catalase, demonstrating that catalase is indeed encapsulated in both solid and hollow samples (**Figure A5.3**). To obtain the enzyme loading, Bradford protein assays were carried out. The loading amounts of confined catalase in the solid MOFs and freestanding catalase in hollow MOFs crystals were quantified to be ~10 wt% (**Table A5.1**).

Table 5.1: Comparison of enzyme-in-MOFs samples in the early stages of the hollowing process per their *in situ* SAXS profile.

Time	Macropore[a] q = 0.01 ~ 0.04 Å^{-1}	Mesopore[a] q = 0.04 ~ 0.07 Å^{-1}	Micropore[b] q = 0.1 ~ 0.4 Å^{-1}
0 min	N/A	(11 × 18 × 4.1)	Sphere: r = 1.1
30 min	(41 × 62 × 11)	(13 × 19 × 4.8)	Sphere: r = 0.9

[a] An elliptical cylinder model was used to fit the macropore and mesopore with results indexed as Minor × Major × Length. [b] A spherical model was used to fit the micropore structure. All dimensions are in nm.

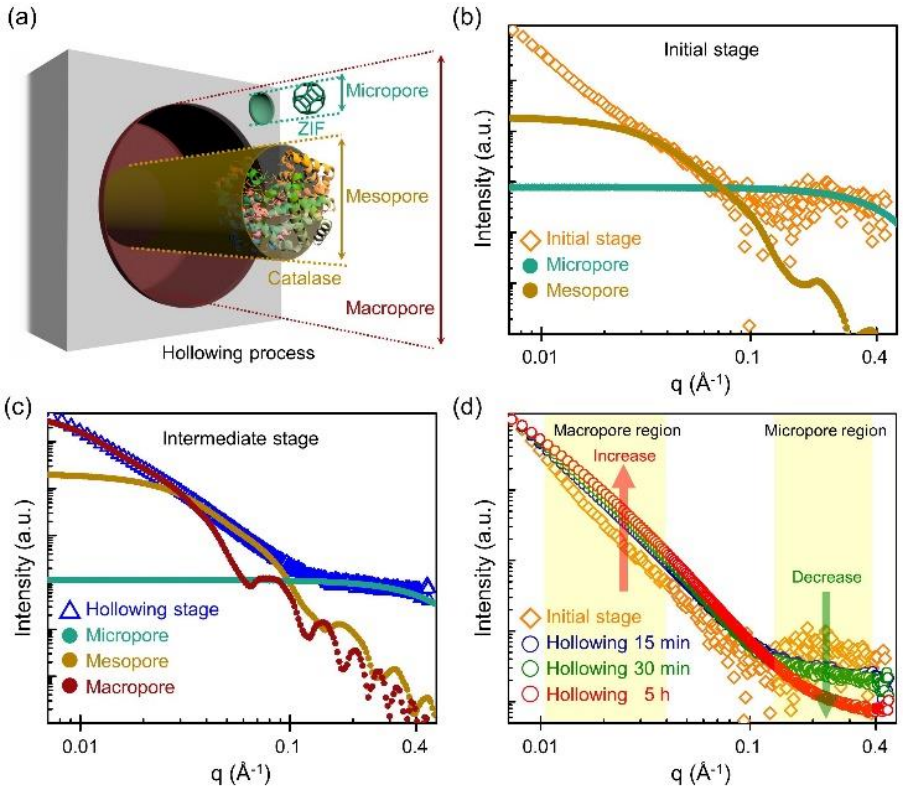

Figure 5.2: Characterization of the hollowing process: (a) Schematic illustration of different pore sizes present in enzyme-in-MOFs samples. (b, c) *in situ* SAXS profile of initial stage and intermediate stage, and (d) time-resolved studies of the hollowing process.

To understand the hollowing process in the presence of enzymes, we have used a synchrotron light source to carry out *in situ* small angle X-ray scattering (SAXS) measurements, which are sensitive to structural changes in the mesostructured range. Detailed parameters are elaborated in **Table 5.1. Figure 5.2** shows the X-ray scattering profiles of the hollowing process. The features at three regions, q = 0.1 ~ 0.4 $Å^{-1}$, 0.04 ~ 0.07 $Å^{-1}$, 0.01 ~ 0.04 $Å^{-1}$, were profiled by computational model to give detailed microporous, mesoporous, and macroporous structures (details are discussed in supporting information). At the initial stage, two structural spaces are observed: the intrinsic MOFs micropores with a diameter of 1.1 nm and the space holding the encapsulated catalase with dimensions of 11 × 18 × 4.1 nm (**Figure 5.2b)**. After 30 min, additional space, representing > 50 nm macroporous cavities, was observed, which supports the formation of central cavities (**Figure 5.2c)**. **Figure 5.2d** shows the profiles of the whole process. There is a clear trend of the intensity increasing in macroporous region (q = 0.01 ~ 0.04 $Å^{-1}$) and intensity decreasing in microporous region (q = 0.1 ~ 0.4 $Å^{-1}$), indicating the increasing of central macropores and decreasing of micropores because the ZIF-67 cores were being removed gradually during the hollowing process.

After investigating the structures and hollowing process, we studied the interfacial interactions between enzyme and MOFs. First, we used infrared (IR) spectroscopy to study the chemical interactions between the encapsulated catalase and MOFs for the two samples. We focused on the amide-I stretches of catalase at 1633 cm^{-1}, which is sensitive to the surrounding coordination environment of the enzyme.[229] The IR spectra reveals a difference between the freestanding and confined samples (**Figure 5.3a)**. Confined catalase exhibits a blue shift of the amide-I stretch (1660 cm^{-1}) compared to free catalase (1633 cm^{-1}), indicating a chemical interaction between the confined catalase and MOFs.[229] We have probed the samples in

intermediate states during the hollowing process and observed a graduate red-shift (**Figure A5.4**), revealing that the states of the enzymes were changed gradually from confined to freestanding state. After hollowing process, the amide-I stretch (1647 cm^{-1}) of freestanding catalase is closer to that of the free catalase (1633 cm^{-1}), showing that the hollow structure reduces chemical interactions between catalase and MOFs. The difference in the amide- I stretch frequencies of free and freestanding catalase can be attributed to the attachment of catalase to the internal surface of the central cavities.[231]

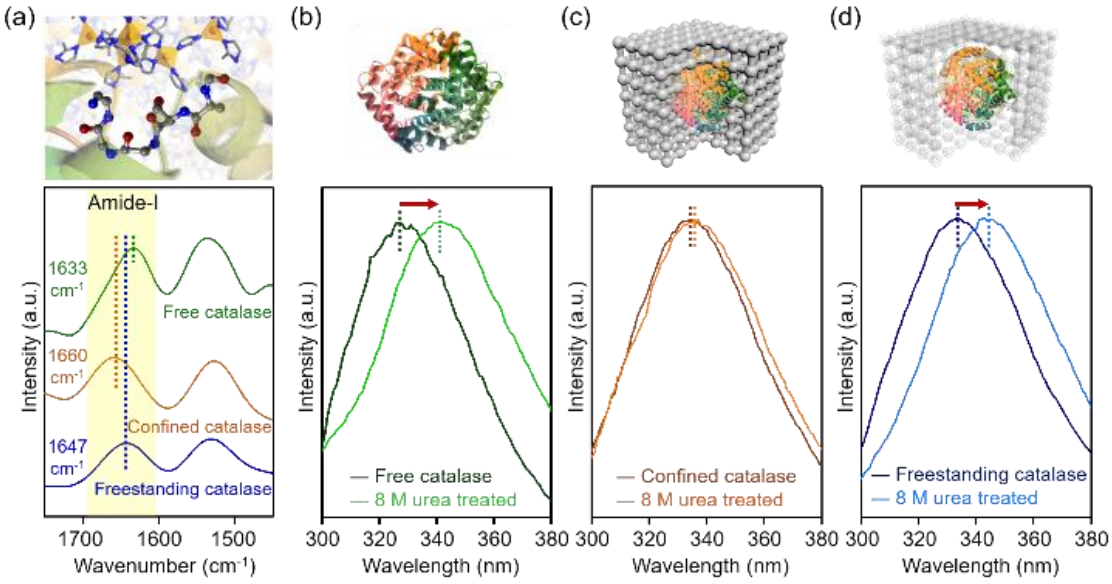

Figure 5.3. (a) Infrared spectra of free catalase, confined catalase, and freestanding catalase in Tris buffer (pH 7.5, 50 mM), respectively. (b-d) Fluorescence spectra of free catalase, confined catalase, and freestanding catalase in Tris buffer (pH 7.5, 50 mM) before and after exposure to 8 M urea.

Next, we studied the structural confinement of enzymes in solid and hollow MOFs. Urea, a universal unfolding agent, has been used as a probe molecule to study structural confinement of enzymes.[241] When exposed to urea, the conformation of free enzymes without confinement can be altered easily.[238] This structural change can be identified by fluorescence spectroscopy because

the emission of the tryptophan of catalase is sensitive to the conformational change.[242] Solid and hollow samples were exposed to 8 M urea solutions and monitored by fluorescence spectroscopy (**Figures 5.3b-d)**. The size of urea molecules is smaller than the pore aperture size so it can diffuse into ZIF-8.[230] After exposure to urea, free catalase shows a redshift (from 330 to 342 nm) of the maximum fluorescence emission (λ_{max}) due to change in its conformation. The solid sample shows no significant shift, indicating that the conformation of catalase in solid MOFs is confined by interfacial interactions.[238] As expected, during the hollowing process, the spectra gradually red-shift (**Figure A5.5)**, and the freestanding catalase shows a large (13 nm) shift after urea exposure, similar to free catalase, which suggests that confinement generated by interfacial interactions gradually decreased during the process. The lesser confined state benefits activity but could negatively impact stability (**Figure A5.6**). This understanding highlights the importance of balancing the tradeoff between stability and activity.

With the observation of lesser interfacial interaction between the MOFs and freestanding enzyme, we tested their biological function by carrying out H_2O_2 degradation over the encapsulated samples. Note that catalase loading is kept consistent and we have characterized the samples after the reaction to show that the structure was not damaged during the reactions (**Figure A5.7**). **Figures 5.4 and A5.8** present the catalytic rate constants (k_{obs}) of encapsulated catalase. The confined catalase shows an observed rate constant of 4.3×10^{-3} s^{-1}, and kinetic study indicates that there is no significant mass transport limitation (**Figure A5.9**). During the hollowing process, activity gradually increased with freestanding catalase showing the highest catalytic rate constant of 1.1×10^{-2} s^{-1}, almost three times greater than confined catalase. Correlating the kinetic studies of H_2O_2 catalysis with the spectroscopic studies suggests that the higher activity of freestanding catalase could be caused by a decrease in the enzyme-MOF interfacial interactions. The Michaelis-

Menten constants, K_M and V_{max}, of the confined catalase, freestanding catalase, and free catalase were compared. Free catalase was reported to decompose H_2O_2 with a K_M of 25.16 mM and a V_{max} of 400.1 $\mu M \cdot s^{-1}$ (**SI**).[243] In **Table A5.2**, compared to free catalase, the confined catalase showed reduced K_M (6.45 mM) and V_{max} (47.30 $\mu M \cdot s^{-1}$), which is in agreement with the previous observations of enzymes immobilized in MOFs.[220, 226] For the freestanding catalase, both K_M (18.71 mM) and V_{max} (432.90 $\mu M \cdot s^{-1}$) are closer to free catalase compared to confined catalase. This phenomenon reasserts that the hollow structure reduces interfacial interactions and allows for better performance. To test whether this phenomenon can be observed on other enzymes, we have carried out the study over chymotrypsin and lipase. In both cases, the freestanding enzyme shows a higher activity than the confined enzymes (**Figure A5.10**).

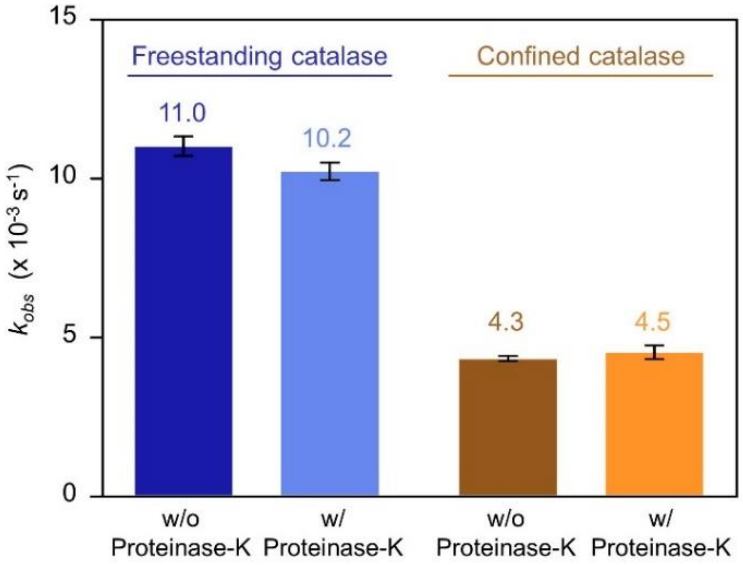

Figure 5.4: Kinetic studies of H_2O_2 degradation for confined and freestanding catalase with and without exposure to proteinase-K. All assays were performed in Tris buffer (pH 7.5, 50 mM). Error bars show the standard deviation of three independent measurements.

Furthermore, the freestanding catalase is protected by MOFs that could shield the enzymes from inhibitors with a large molecule sizes, such as proteinase-K. When exposed to proteinase-K, free catalase shows no detectable activity.[237] While we exposed the freestanding catalase in hollow ZIF-8 to proteinase-K. The proteinase-K treated freestanding catalase exhibits a similar rate constant (1.02×10^{-2} s^{-1}) as before the treatment, indicating that the enzyme is shielded from protease.

Table 5.2: Summary of K_M and V_{max} of confined catalases and freestanding catalases.

	Confined catalase[a]	Freestanding catalase[a]
K_M (mM)	6.45	18.71
V_{max} ($\mu M \cdot s^{-1}$)	47.30	432.90

[a] All measurements were conducted using the same amount of catalase in each test (0.232 mg).

5.3 Conclusions

In summary, we have developed a new strategy to encapsulate enzymes into hollow MOFs with reduced interfacial interaction between enzyme and MOFs. It allows us to investigate the relationship between the interfacial interactions and biological function. Our study indicates that freestanding enzymes have less chemical interaction with the MOFs and that their structure is less confinement. The hollow structure reduces interfacial interactions and is inspired by the cell environment, such as glycolysis enzymes in the cytoplasm of living cells. This study not only highlights the importance of the freestanding state for the biological function of encapsulated enzymes but also presents a new way to immobilize freestanding enzymes in MOFs.

This work made use of the resources of the Instrumental Analysis Center of the SPST at ShanghaiTech University for XRD analysis and gas sorption measurements. The SEM and TEM

analysis was supported by the Center of High-Resolution Electron Microscopy (C*ħ*EM) of the SPST at ShanghaiTech University. S.-Y. C, Y. A and L.-Y. C would like to thank the funding from ShanghaiTech University and Shanghai Natural Science Fund support (Grant No. 18ZR1425300). W.-S. L, B.P. W and C.-K. T acknowledge the support from Boston College. Y.-D. H, F.-S. L T.-Q. S, H.-W. L and F.-K. S would like to thank Ministry of Science and Technology, Taiwan for the funding support (MOST 107-2113-M-008 -008 -MY2). S.-W. L and H.-C. Y would like to thank Ministry of Science and Technology, Taiwan for the funding support (MOST 105-2119-M-030-002-MY2). We also thank the BL23A1 National Synchrotron Radiation Research Center of Taiwan for providing beam time and technical support.

5.4 Experimental Procedures

Chemicals: All chemicals were purchased from commercial chemical vendors and used without any further purification. 2-methyl imidazole (99.0%), hexadecyltrimethylammonium bromide (CTAB, > 98%), catalase from bovine liver, chymotrypsin and proteinase-K from tritirachium album were purchased from Sigma-Aldrich®. Zinc nitrate hexahydrate (99.0%), 4-nitrophenol (pNP, 99%) and 4-nitrophenyl acetate (pNPA, 99%) were purchased from Alfa Aesar®. Bradford reagent, Coomassie brilliant blue R-250, Acryl/bisTM 40.0 % solution, sodium dodecyl sulfate (SDS, 20.0%), ammonium persulfate (APS, > 98.0%), tetramethylethylenediamine (TEMED, > 97.0%) and glycine were from Amresco®. Cobalt (II) nitrate hexahydrate (99.0%), calcium chloride anhydrous (99.0%), and sulfuric acid (95.0 ~ 98.0%) were purchased from Sinopharm Chemical Reagent Co., Ltd. D-sorbital (> 98.0%) and ammonium iron (II) sulfate hexahydrate (99%) were purchased from J&K Scientific. Xylenol orange (ACS reagent) and lipase were

obtained from TCI. Urea (> 99.0%) was purchased from Shanghai Yeasen Biotechnology Co. Ltd. Sodium hydroxide (NaOH, 97.0%) was purchased from SHOWA.

Characterizations: Powder X-ray diffraction (PXRD) analyses were collected using a Bruker D8 Advance X-ray powder diffractometer (Cu Kα radiation, λ= 1.5418 Å). The diffraction patterns were collected between a 2θ range of 5 - 40°. The scanning electron microscopy (SEM) images were obtained using a field emission scanning electron microscope (FE-SEM) Jeol JSM-7800F with an accelerating voltage of 5 kV. Transmission electron microscopy (TEM) images were obtained using a Jeol JEM-2100 plus with an accelerating voltage of 200 kV. The Fourier-transform infrared (FT-IR) spectra were collected using a Thermo Scientific Nicolet iS10 MID-IR Spectrometer with a SMART iTX Base and an ATR IDT/IDX AR-coated diamond crystal for Attenuated total reflectance (ATR) analysis. The IR measurements were performed in 64 scans with a resolution of 2 cm^{-1}. The IR measurements were carried by introducing the samples with an aliquot of deionized H_2O on the ATR crystal. Both the enzyme activity and the quantification of enzymes loading were studied using an Ocean Optics Maya2000 pro UV/Vis spectrometer with a DH-2000-BAL Deuterium-Tungsten light source. The fluorescence tests were conducted using a Horiba Fluorolog®-3 spectrofluorometer with an excitation wavelength at 280 nm. The intrinsic porosities of enzyme in MOFs composite materials were analyzed by nitrogen adsorption-desorption experiments using a Quantachrome Autosorb iQ-2 automated adsorption system. The specific surface areas were calculated using the Brunauer–Emmett–Teller (BET) method around the relative pressure range P/P_0 = 0.06 – 0.20. Pore volumes were calculated around the N_2 adsorbed volumes at P/P_0 = 1.00 (**Table A5.2**).

Synthesis of confined catalase in solid MOFs: To prepare the confined catalase in solid MOFs samples, catalase was first encapsulated into ZIF-67 microcrystals, and then ZIF-8 shells were overgrown on the catalase@ZIF-67 cores. All aqueous solutions were prepared using deionized water (D.I. water). In detail, 0.5 mL 1.925 mM CTAB aqueous solution was added into 0.75 mL 1.843 M 2-methyl imidazole aqueous solution, and the mixture was stirred at 500 rpm for 5 min. Then, a 0.5 mL aqueous solution containing 2.0 mg of catalase was added into the mixture followed by introducing 0.25 mL 97.5 mM $Co(NO_3)_2 \cdot 6H_2O$ aqueous solution. The resulting mixture was stirred at room temperature for 5 min. The reaction solution was then left undisturbed at 4 °C in the refrigerator for 1 h. The precipitate of catalase@ZIF-67 sample was collected by centrifugation (14,000 g).

To overgrow ZIF-8 shells on the catalase@ZIF-67 cores, catalase@ZIF-67 was firstly dispersed into the mixture containing 0.75 mL 1.843 M 2-methyl imidazole aqueous solution and 1 mL 0.9625 mM CTAB aqueous solution followed by an injection of 0.25 mL 97.5 mM $Zn(NO_3)_2 \cdot 6H_2O$ aqueous solution. The resulting mixture was stirred at 500 rpm for 5 min. The reaction solution was then left undisturbed at 4 °C in the refrigerator for 1 h. After this procedure, the precipitate of confined catalase in solid MOFs was collected by filtration and washed by 1 L D.I. water. Next, the obtained products were vacuum-dried at room temperature and stores at 4 °C for the following characterizations. The same procedure was applied to encapsulate lipase and chymotrypsin.

Synthesis of freestanding catalase in hollow MOFs: The freestanding catalase in hollow MOFs samples were prepared by treating the confined catalase in solid MOFs with a mild hollowing process. In detail, after the overgrowth of ZIF-8 layer on the catalase@ZIF-67 cores (as described above), the supernatant was withdrawn. The hollowing process was carried by

incubating the precipitate of confined catalase in solid MOFs with 20 mL D.I. water at 4 °C in the refrigerator for 20 h. After this procedure, the precipitate of freestanding catalase in hollow MOFs was collected by filtration and washed by 1 L D.I. water. Next, the obtained products were vacuum-dried at room temperature and stores at 4 °C for the following characterizations (**Figure S1-S3**). The same procedure was applied to prepare the freestanding lipase and chymotrypsin in hollow MOFs.

Synthesis of confined catalase in solid ZIF-8: To test the diffusion of reactant-H_2O_2 in ZIF-8 microcrystals is without mass transport effect, we performed kinetics study of confined catalase in solid ZIF-8 sample. The kinetic of H_2O_2 decomposition of catalase is a first-order reaction. If there is a mass transport limitation, the diffusion of H_2O_2 will be affected by ZIF-8 microcrystals, therefore, the kinetic of H_2O_2 decomposition of encapsulated catalase will not be first-order reaction. To study this, we synthesized the confined catalase in solid ZIF-8 samples. Catalase was firstly encapsulated into ZIF-8 microcrystals to generate samples of catalase@ZIF-8 cores. Then, ZIF-8 shells were overgrown on the catalase@ZIF-8 cores to form confined catalase in solid ZIF-8 sample.

In detail, a 0.5 mL 1.925 mM CTAB aqueous solution was added into a 0.75 mL 1.843 M 2-methyl imidazole aqueous solution, and the mixture was stirred at 500 rpm for 5 min. Then, a 0.5 mL aqueous solution containing 2.0 mg of catalase was added into the mixture followed by introducing a 0.25 mL 97.5 mM $Zn(NO_3)_2 \cdot 6H_2O$ aqueous solution. The resulting mixture was stirred at room temperature for 5 min. The reaction solution was then left undisturbed at 4 °C in the refrigerator for 1 h. The resulting precipitate of catalase@ZIF-8 sample was collected by centrifugation (14,000 g). To overgrow ZIF-8 shells on the catalase@ZIF-8 cores, the precipitate of catalase@ZIF-8 was then dispersed into the mixture containing 0.75 mL 1.843 M 2-methyl

imidazole aqueous solution and 1 mL 0.9625 mM CTAB aqueous solution. The mixture was stirred at 500 rpm for 5 min followed by an injection of 0.25 mL 97.5 mM $Zn(NO_3)_2 \cdot 6H_2O$ aqueous solution. The resulting mixture was stirred at 500 rpm for 5 min. The reaction solution was then left undisturbed at 4 °C in the refrigerator for 1 h. After this procedure, the precipitate of confined catalase in solid ZIF-8 was collected by filtration and washed by 1 L D.I. water. Next, the obtained products were vacuum-dried at room temperature and stores at 4 °C for the following characterizations (**Figure A5.2** and **A5.3**). The kinetics of H_2O_2 decomposition of catalase in solid ZIF-8 sample fit into a first order reaction (Figure S10) and remained a first-order kinetic in higher concentration of H_2O_2 (1000 μM). This study indicates that there is no significant mass transport limitation of H_2O_2 in ZIF-8 structure.

Examination of catalytic activities for catalase: The biological function of catalase in MOFs samples were examined through the degradation of hydrogen peroxide (H_2O_2) based on the reported ferrous oxidation-xylenol orange (FOX) assay and the standard protocol.[244] The FOX reagent was prepared by mixing 910 mg D-sorbital, 5 mg ammonium iron (II) sulfate hexahydrate, 3.3 mg xylenol orange, and 70 μL sulfuric acid (95.0 ~ 98.0%) in 50 mL D.I. water. Prior to the tests, the corresponding calibration curve of the FOX assay was established through the absorbance at 560 nm using a H_2O_2 solution, which was calibrated spectrophotometrically at 240 nm with an extinction coefficient (ε) of 39.4 $M^{-1} \bullet cm^{-1}$, in concentrations from 0.0 to 100.0 μM by a linear regression with $R^2 = 0.998$. (**Figure A5.8**).[245]

For each trial, catalase in MOFs samples were introduced into a solution containing 100 μL Tris buffer (pH 7.5, 500 mM) and 800 μL D.I. water in a 1.5 mL centrifuge tube. The loading amount of catalase in each trial was kept the same as 0.232 mg. The mixed samples were then vortexed and incubated at room temperature for 10 min. The calibrated H_2O_2 solution as substrate

was introduced to give the initial H_2O_2 concentration of 100 μM and a total volume of 1.0 mL. Each mixture was shaken for a certain time (30 s – 5 min) and followed by a quick centrifugation for 30 s to separate the catalysts and the supernatants. The final concentrations of H_2O_2 were monitored by FOX reagent via its absorbance at 560 nm using a UV-Visible spectrometer (Ocean Optics). The detailed steps of H_2O_2 measurement based on the FOX assay were described as followed. In general, 50.0 μL supernatant of the reaction mixture containing H_2O_2 was added into 950.0 μL FOX reagent in an Eppendorf tube followed by a 30 min incubation at room temperature. The absorbance at 560 nm of each Fox assay was compared with the calibration curve to obtain the corresponding concentration. The kinetic studies of H_2O_2 degradation for each catalase in MOFs sample were plotted in **Figure A5.14**. The observed kinetic constant (k_{obs}) of catalase in MOFs samples were summarized in **Table A5.3**.

Examination of stability of freestanding catalase to extreme conditions: To study the stability to extreme conditions, freestanding catalase samples were exposed to high concentrations of urea (8.0 M) and treated at high temperature (80 ˚C). In the urea study, freestanding catalase samples were introduced into a Tris buffer (pH 7.5, 50 mM) containing final concentrations of 8 M urea, and the mixture was shaken for 30 minutes. Then, hydrogen peroxide as substrate was introduced to give an initial H_2O_2 concentration of 100 μM and a total volume of 1.0 mL. The mixture was shaken for a certain time (1 – 30 min) and the concentrations of hydrogen peroxide were monitored using FOX reagent. A similar procedure was used to study the stability of freestanding catalase at high temperature (80 ˚C). Briefly, freestanding catalase samples were introduced into a Tris buffer (pH 7.5, 50 mM) and the mixture was shaken for 30 minutes. The mixture was placed into 80 ˚C for 3 minutes. Then, the reaction was assayed by adding hydrogen peroxide as substrate to give the initial H_2O_2 concentration of 100 μM and a total volume of 1.0

mL. The mixture was shaken for a certain time (1 – 30 min) and the concentrations of hydrogen peroxide were monitored using FOX reagent. The stability study of freestanding catalase to extreme conditions were summarized in **Figure A5.6**

Examination of catalytic activities for lipase and chymotrypsin: The catalytic function of lipase and chymotrypsin was tested through the hydrolysis of 4-nitrophenyl acetate (pNPA) based on a reported method.[246] The activity was determined based on the change in concentration of 4-nitrophenol (pNP), the product of pNPA hydrolysis. The concentrations of enzyme in each trial were kept the same (0.232 mg). Before each measurement, enzyme in MOF samples were dispersed in 0.5 mL of Tris buffer (50 mM, pH 7.1) containing proteinase-K (0.2 mg • mL^{-1}) and the mixture was incubated at 37 ˚C for 1 hour. Then, the activity measurements were assayed by adding 0.5 mL of pNPA (0.1 mM, containing 50 mM Tris buffer (pH 7.1)) as a substrate and the mixture was shaken for a certain time (1 – 30 min) followed by centrifugation to separate the catalysts and the supernatants. Then, the reaction was terminated by introducing 50.0 μL supernatant of the reaction mixture into 950 μL of NaOH-glycine buffer (0.4 M, pH 10.8). The final concentration of pNP was determined by measuring the absorbance at 405 nm and compared with the calibration curve to obtain the corresponding concentration. The observed kinetic constant (k_{obs}) were calculated by plotting the concentration of pNP (μM) vs reaction time (seconds) and the results were summarized in **Figure A5.10**.

Proteinase-K treatment of catalase in MOF samples: The protection of encapsulated enzyme by MOFs against proteinase-K was tested based on the previous reports.[237] Proteinase-K, a proteolytic enzyme, has a size (68.3 × 68.3 × 108.5 Å) bigger than the aperture (3.5 Å) of ZIF-8 and thus not able to digest the encapsulated catalase in MOFs.[247] In general, catalase in MOFs samples containing 0.232 mg catalase were incubated in a solution containing 500 μL Tris buffer

(pH 7.5, 100 mM), 200 µL aqueous $CaCl_2$ solution (25 mM), and 200 µL D.I. water in a 1.5 mL centrifuge tube. Then, the mixture was added into a 100 µL aqueous proteinase-K solution (1.0 mg mL^{-1}) and shaken at 37 °C for 5 h. After this procedure, the proteinase-K treated samples of catalase in MOFs were collected by centrifugation (14,000 g) for further examination of catalytic activity. The observed kinetic constant (k_{obs}) of proteinase-K treated samples were summarized in **Table A5.3** and plotted in **Figure A5.14**.

The kinetic parameters of catalase in MOF samples: The kinetic parameters were studied based on the Michaelis-Menten equation.[248]

$$V_0 = \frac{V_{max}[S]}{(K_M + [S])}$$

In this equation, V_0 is the initial catalytic velocity; V_{max} is the maximum rate of the enzymatic catalysis when the enzyme is saturated with substrate. K_M is the Michaelis-Menten constant. The kinetic parameters K_M and V_{max} can be obtained by measuring the initial rates of the reaction with different initial substrate concentration using a Lineweaver–Burk plot as shown below.[249]

$$\frac{1}{V_0} = \frac{K_M}{V_{max}[S]} + \frac{1}{V_{max}}$$

In general, the initial velocities of catalase in MOFs samples were determined using the average of observed kinetic constants of H_2O_2 decomposition during t = 0 - 300 s, and the initial substrate concentration was determined at t = 0 s. Depending on the calculated initial velocities at varied substrate concentrations, the Lineweaver-Burk Plot was plotted (**Figure A5. 16** and **A5. 17**), and the two kinetic parameters, K_M and V_{max} were determined from the Lineweaver-Burk plot. All catalytic measurements were conducted using the same catalase amount in each test (0.232 mg).

Quantification of catalase loading in MOFs: Bradford reagent was utilized as the standard method to determine enzyme loading in each MOFs sample. Commercially available Bradford reagent was purchased from Amresco®. The standard operating protocol provided by the supplier was followed. The loadings of encapsulated catalase in MOFs were determined by decomposing the catalase in MOFs samples and reacting with the Bradford reagent. It has been suspected that the MOFs can interfere the analysis of Bradford assay. Therefore, the corresponding calibration curve was established by dissolving ZIF-8 coated ZIF-67 core/shell nanoparticles in aqueous catalase solutions containing varied concentrations of free catalase to MOFs (0 – 30%), 75 mM NaCl, and 50 mM HCl. Followed the standard protocol from the supplier, 100 μL analyte solution was added into 1 mL Bradford reagent, and the mixture was shaken for 2 min. The absorbance of the mixture at 595 nm was measured to plot the calibration curve as shown in **Figure A5.18**.

Sodium dodecyl sulfate polyacrylamide gel electrophoresis: To confirm the existence of encapsulated catalase inside the MOFs, sodium dodecyl sulfate polyacrylamide gel electrophoresis (SDS-PAGE) was carried out. Each catalase in MOFs sample was dissolved in 1 mL 0.2 M HCl. After the powder dissolved completely, the solution was concentrated by centrifugation (14,000 g) with a centrifugal filter (10 kDa). Then, 15 μL concentrated supernatant was mixed with 5 μL loading buffer (Tris buffer, pH = 6.5, 240 mM; 8.0% SDS; 0.04% (w/v) bromophenol blue; 40.0% glycerol; 5.0% β-mercaptoethanol) and heated at 95 °C in water for 5 min. The mixture was loaded on the top of the SDS-PAGE for further electrophoresis at 20 mA. The SDS-PAGE was composed of 4.0% polyacrylamide stacking gel and 12.0% polyacrylamide resolving gel. After electrophoresis, the gel was stained by Commassie Blue. The excess

Commassie Blue on gel was rinsed out with a solution containing 100 mL D.I. water, 80 mL methanol, and 20 mL acetic acid.

Synchrotron small angle X-ray scattering analysis: Small angle X-ray scattering (SAXS) analysis with synchrotron light source was applied to observe the hollowing process applied on the confined catalase in solid MOFs to form the freestanding catalase in hollow MOFs. The solid MOFs nanoparticles with varied hollowing incubation times, 15 min, 30 min, and 5 h, were dispersed in ethylene glycol (1 mg/mL) and loaded into a 4-loaded rocking cell for the SAXS experiment.

The data of small angle X-ray scattering were collected at the BL23A1 SWAXS end station of the National Synchrotron Radiation Research Center (NSRRC), Taiwan. For the instrumental setting, the accelerating voltage of X-rays (wavelength λ= 0.8266 Å) is 15 keV and the sample-to-detector distance is 2,967 mm. The scattering vector q is defined by $4\pi\sin\theta\bullet\lambda^{-1}$ with a scattering angle of 2θ that covered the q range from 0.007 to 0.46 $Å^{-1}$. The reduction of two-dimensional scattering data was processed to an incident count, which was corrected for background radiation, detector sensitivity, buffer transmission, buffer scattering, and sample transmission, and radially averaged to produce *I(q)* vs. q profiles by using conventional procedures.[250]

All data of form-factor scattering analyses were calculated by the elliptical cylinder model via NIST NCNR analysis Macros in IGOR Pro.[251] The elliptical cylinder model function calculated is defined as:

$$I(q) = scale \times \int_0^1 \Psi_{ec}\left[q, a(1-x^2)^{1/2}\right] S^2(qHx/2)dx + bkg$$

with the function:

$$\Psi_{ec}(q,a) = \frac{1}{\pi}\int_0^{\pi} \Lambda_1^2 \left[qa\left(\frac{1+\nu^2}{2} + \frac{1-\nu^2}{2}\cos(y)\right)^{1/2}\right] dy$$

$$\Lambda_1 = 2J_1(t)/t$$

and $J_1(t)$ is the first order Bessel function. The elliptical cylinder is with a total length H, minor radius a, and major radius νa.

$$\nu = R_{major}/R_{minor} \geq 1$$

The value of χ^2 provides the deviation between the model fitting curves and experimental data. The χ^2 equation is defined as:

$$\chi^2 = \frac{1}{\mathrm{N}}\sum\left[\frac{\mathrm{I_{exp}(s_i)} - \mathrm{I_s(s_i)}}{\sigma(\mathrm{s_i})}\right]$$

where N is the number of experimental points, $\mathrm{I_{exp}(s_i)}$is the experiment curve, $\mathrm{I_s(s_i)}$ is model fitting SAXS curves, and $\sigma(\mathrm{s_i})$ is the experiment standard deviation.

5.5 Appendix

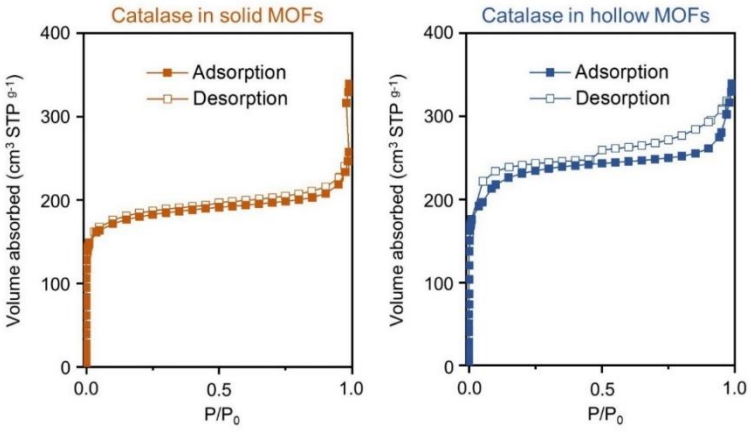

Figure A5.1: Nitrogen isothermal sorption profiles of catalase encapsulated in solid and hollow MOFs.

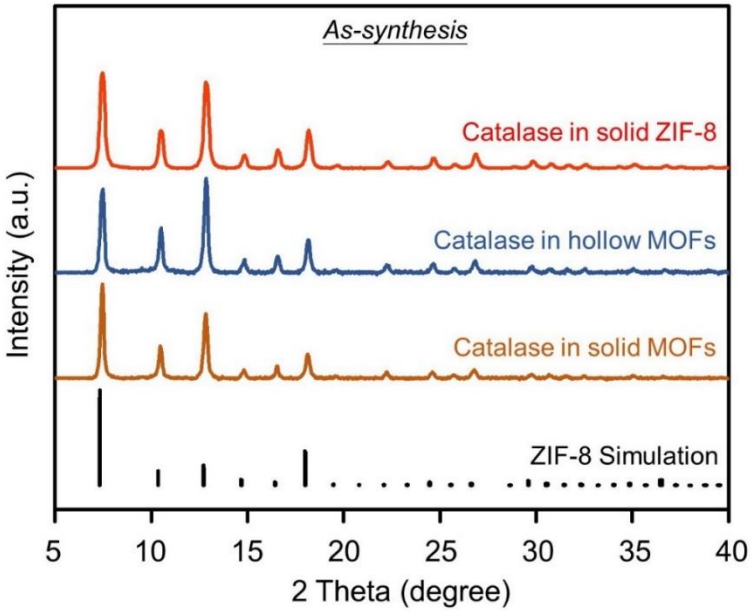

Figure A5.2: PXRD patterns of catalase encapsulated in solid MOFs, hollow MOFs, and solid ZIF-8 as-synthesis.

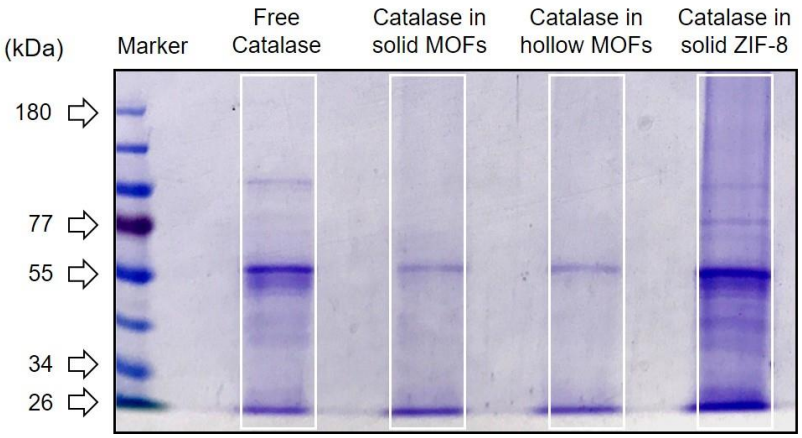

Figure A5.3: SDS-PAGE of free catalase, catalase in solid MOFs, catalase in hollow MOFs, and catalase in solid ZIF-8.

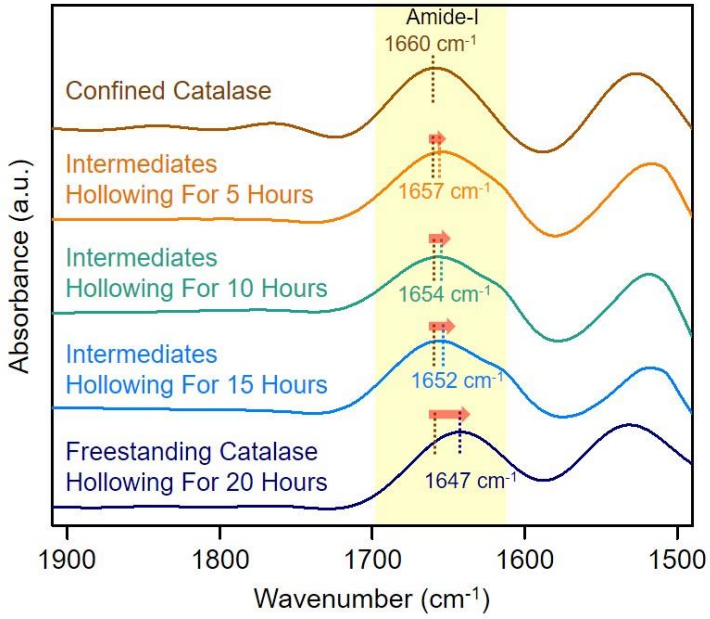

Figure A5.4: Infrared spectra of confined catalase, intermediate and freestanding catalase.

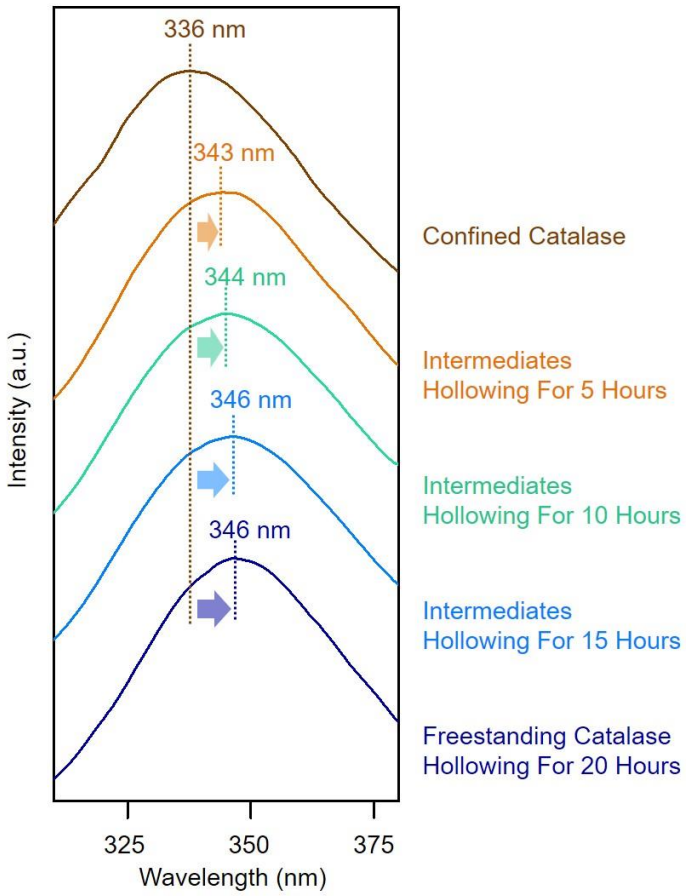

Figure A5.5: Fluorescence spectra of confined catalase, intermediate and freestanding catalase after exposure to 8 M urea. All assays were performed in Tris buffer (pH 7.5, 50 mM).

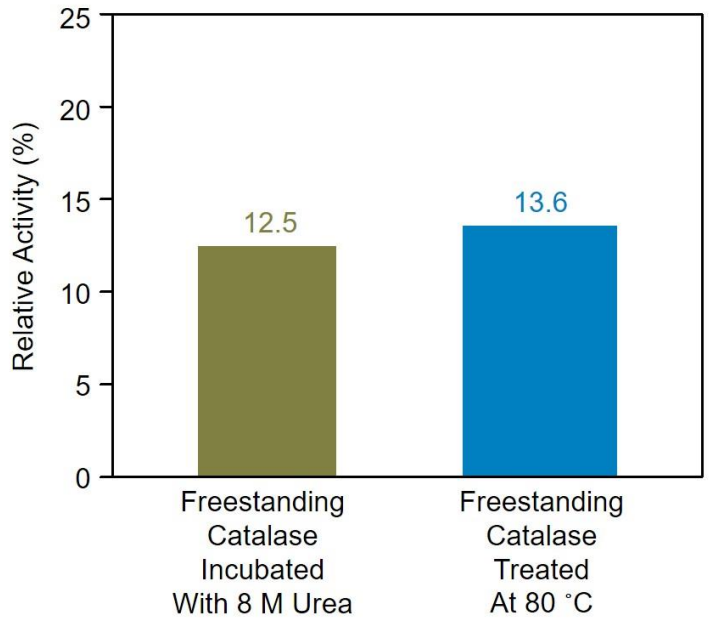

Figure A5.6: Maintained activity for H_2O_2 degradation of freestanding catalase after incubation with 8.0 M urea, and after treatment at 80 °C for 3 min.

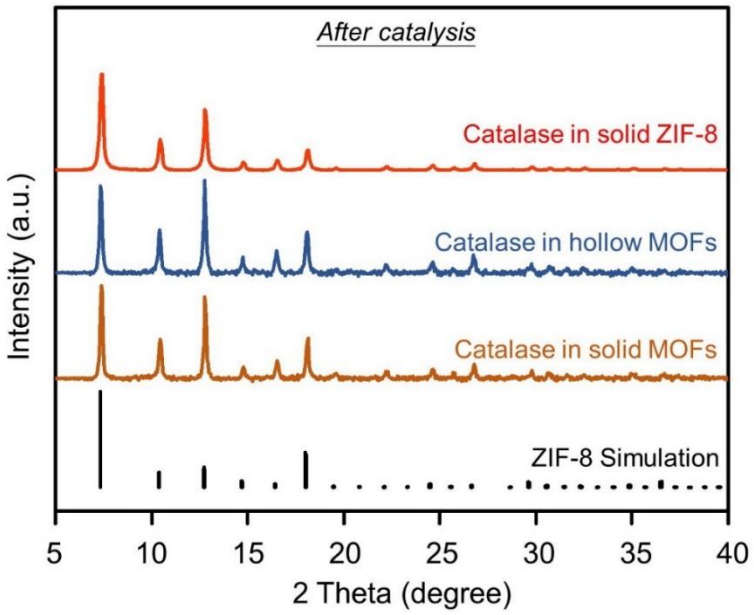

Figure A5.7: PXRD patterns of catalase encapsulated in solid MOFs, hollow MOFs, and solid ZIF-8 after catalysis.

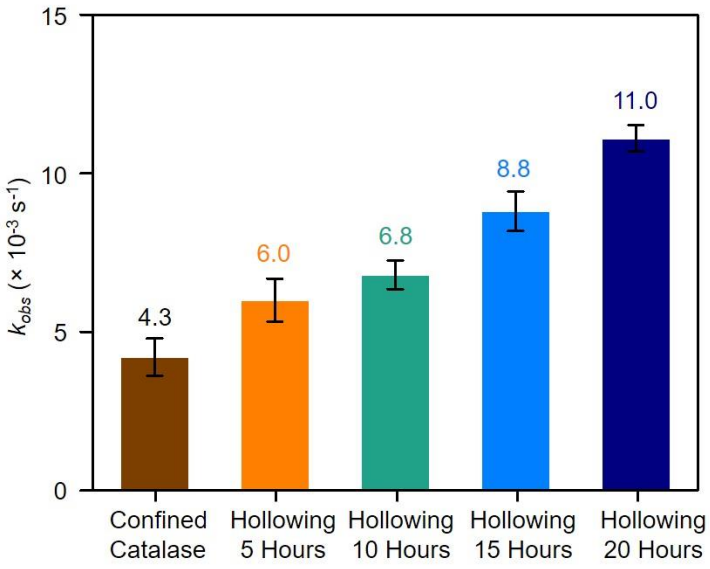

Figure A5.8: Kinetic studies of H_2O_2 degradation for catalase encapsulated in MOF with increasing hollowing time from 0 - 20 h.

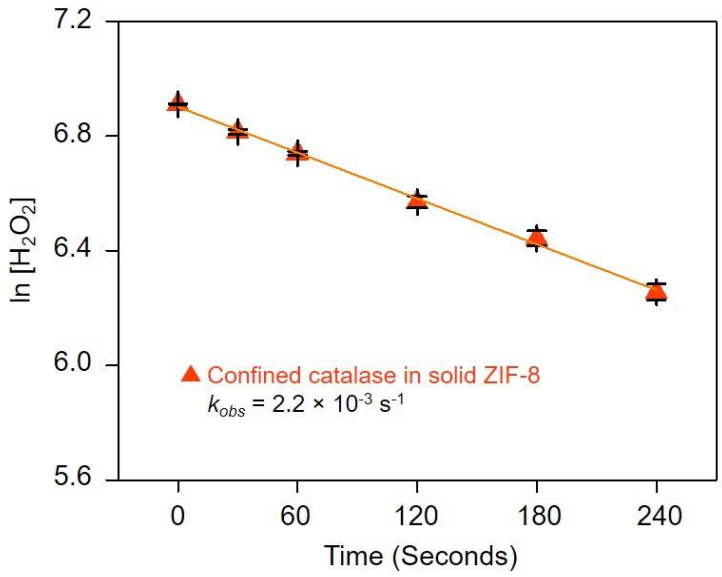

Figure A5.9: Kinetic study of the confined catalase in solid ZIF-8 with higher substrate concentration (H_2O_2, 1000 µM) for diffusion test of H_2O_2.

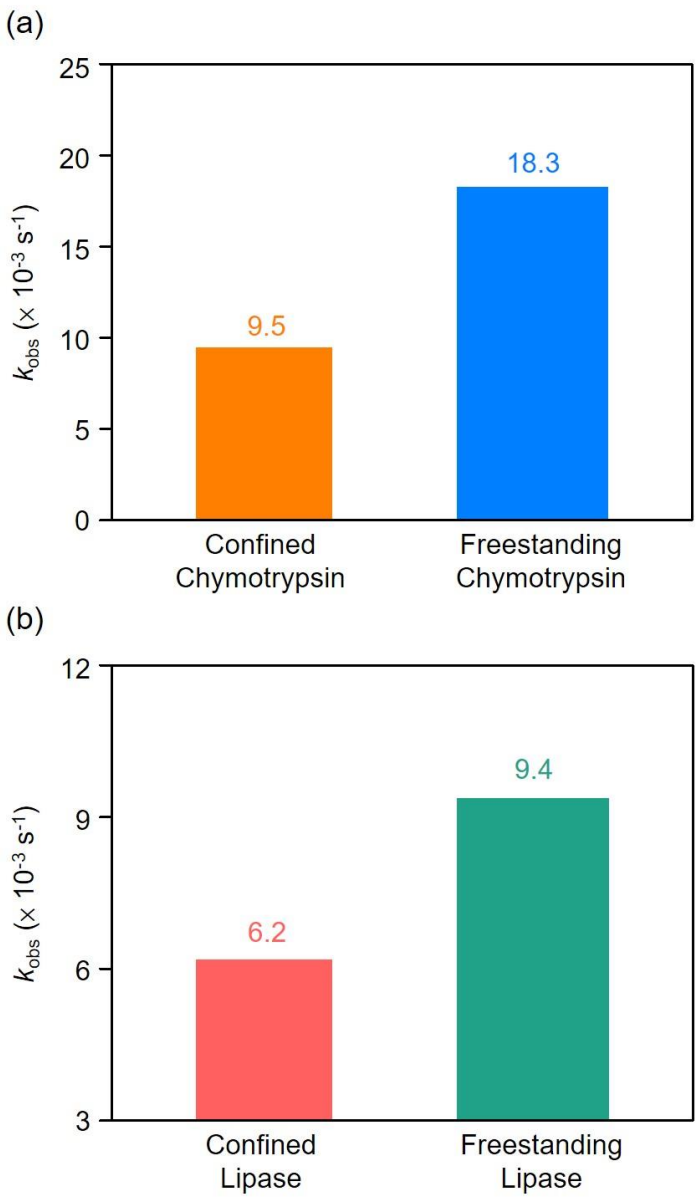

Figure A5.10: Catalytic performance of (a) chymotrypsin and (b) lipase in confined and freestanding states. All assays were performed in Tris buffer (pH 7.5, 50 mM) and the chymotrypsin and lipase in freestanding states were prepared by hollowing the samples for 15 hours.

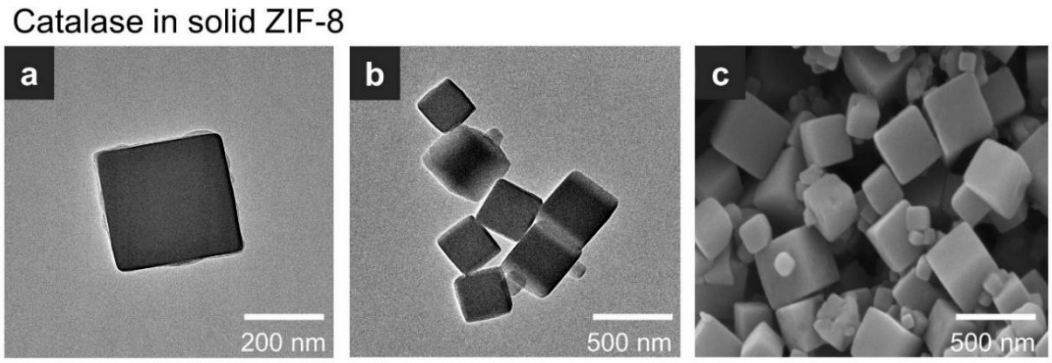

Figure A5.11: TEM and SEM images of catalase in solid ZIF-8.

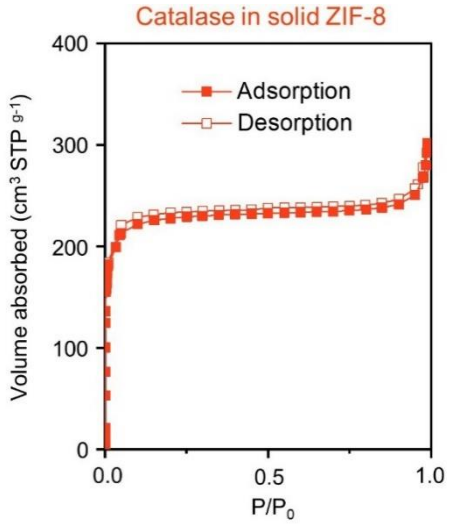

Figure A5.12: Nitrogen isothermal sorption profiles of catalase in solid ZIF-8.

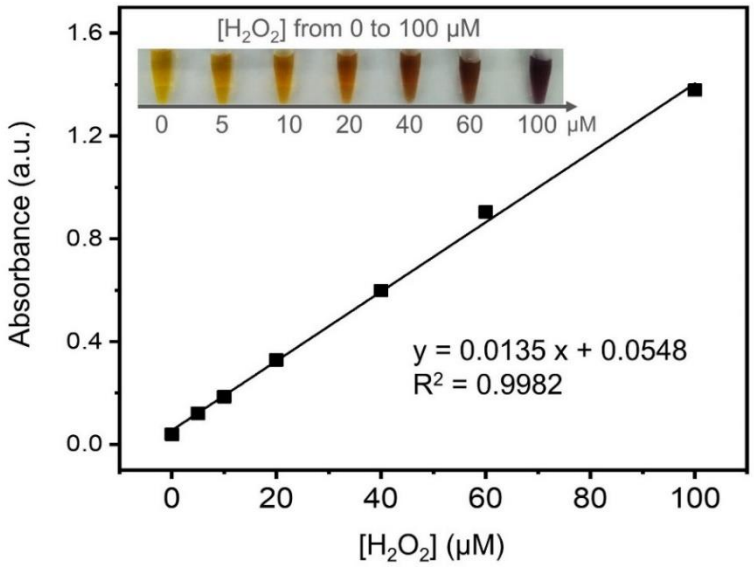

Figure A5.13: The corresponding calibration curve of FOX assay for H_2O_2 measurment.

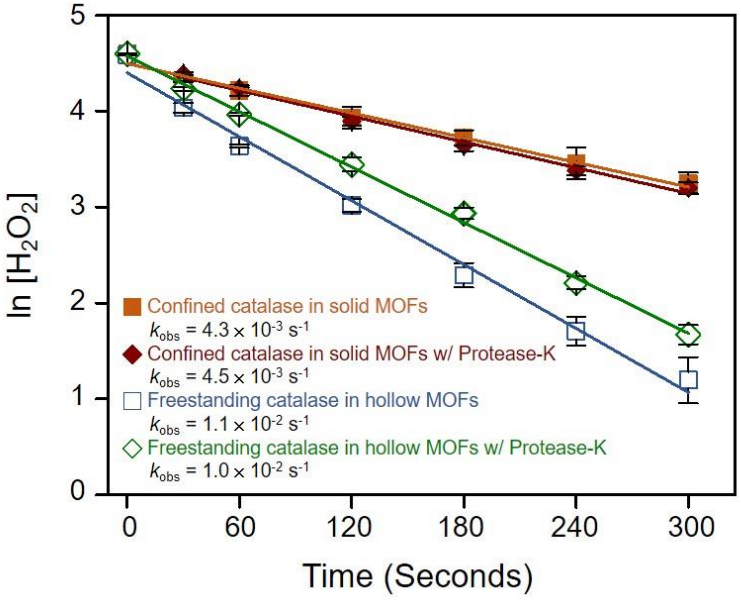

Figure A5.14: The kinetic studies of H_2O_2 degradation for the confined catalase in solid MOFs and freestanding catalase in hollow MOFs before and after the treatment of proteinase-K solution, respectively.

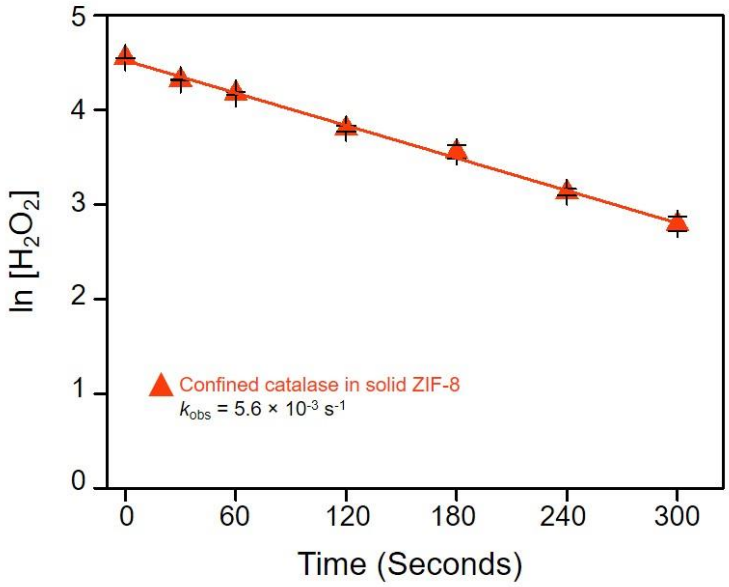

Figure A5.15: The kinetic studies of the confined catalase in solid ZIF-8 with 100 μM of H_2O_2.

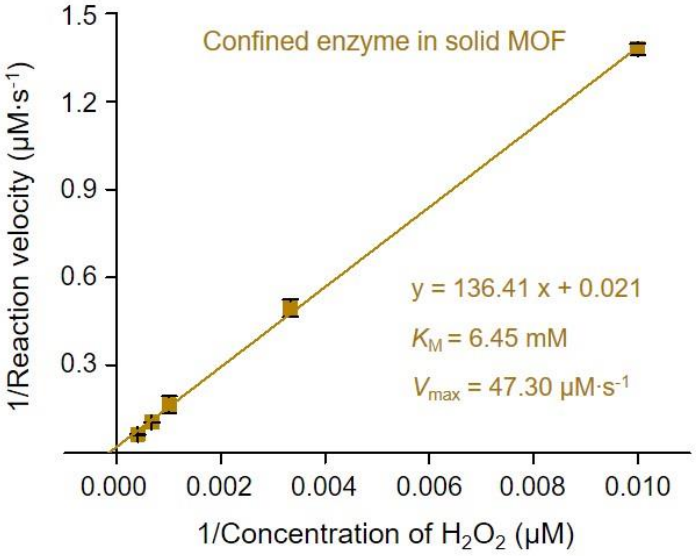

Figure A5.16: Lineweaver–Burk plot for determination of the kinetic parameters for the confined catalase in solid MOFs.

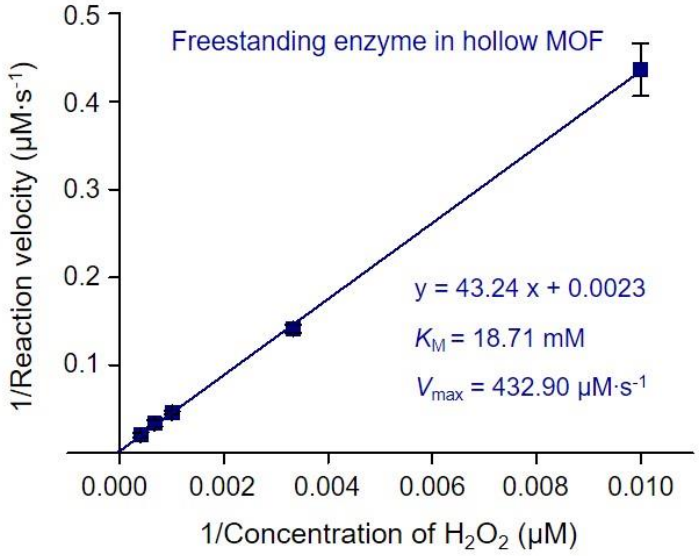

Figure A5.17: Lineweaver–Burk plot for determination of the kinetic parameters for the freestanding catalase in hollow MOFs.

.

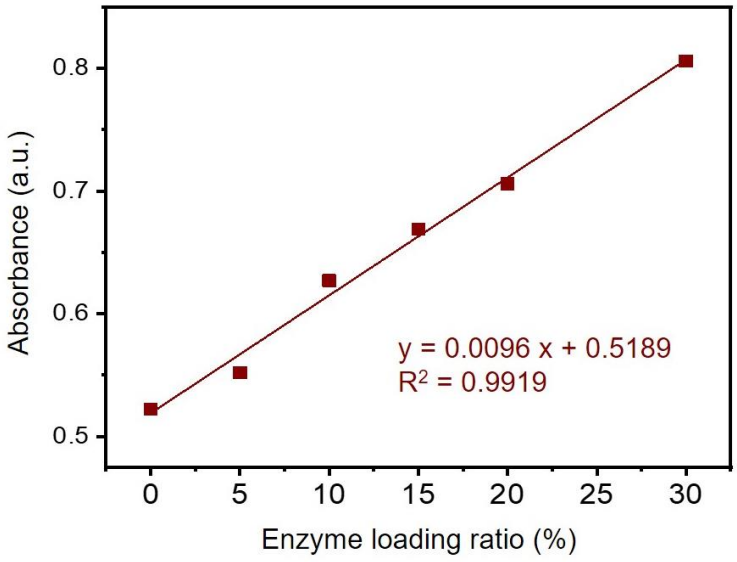

Figure A5.18: The calibration curve of catalase concentration using Bradford assay.

Table A5.1: Enzyme loading amounts of catalase in MOF samples

Sample	**Enzyme loading amount (wt %)**
Confined catalase in solid MOFs	8.29 ± 0.49
Freestanding catalase in hollow MOFs	11.59 ± 0.32
Confined catalase in solid ZIF-8	9.22 ± 0.15

Table A5.2: Nitrogen isothermal sorption profiles of catalase in MOF samples.

	BET Surface area ($m^2\ g^{-1}$)	Total pore volume ($cm^3\ g^{-1}$)
Confined catalase in solid MOFs	686.17	0.526
Freestanding catalase in hollow MOFs	758.24	0.508
Confined catalase in solid ZIF-8	852.42	0.468

Table A5.3: Kinetic parameters – $k_{obs}(s^{-1})$ of catalase in MOF samples.

Samples[a]	**W/O proteinase-K (s^{-1})**	**W/ proteinase-K (s^{-1})**
Confined catalase in solid MOFs	4.3×10^{-3}	4.5×10^{-2}
Freestanding catalase in hollow MOFs	1.1×10^{-2}	1.0×10^{-2}
Confined catalase in solid ZIF-8	5.6×10^{-3}	N/A

[a] All assays performed in Tris buffer (pH 7.5, 50 mM).

This page is on purposely left in blank

6.0 Chapter 6:

Summary and Perspectives

In this thesis, we have established that the hybrid interfaces between heterogeneous catalysts and MOFs can be designed to promote catalytic selectivity. We have systematically probed the NP-MOF interface generated by several commonly used approaches (encapsulation, impregnation, etc.) by IR and Raman spectroscopy. We have revealed the significant differences in structures of the NP-MOF interface between different synthetic methods, despite the similar appearance of the samples observed by electron microscopy. These differences in interfacial structure dramatically impact selectivity to unsaturated alcohol in crotonaldehyde hydrogenation. For example, the interface generated by the coating approach contains trapped capping agents. This trapped capping agent reduces crotyl alcohol selectivity for the hydrogenation of crotonaldehyde.

We have addressed the challenge of controlling the inorganic-organic NP-MOF interface by utilizing weakly adsorbed capping agents during the MOF coating process. Their dynamic nature allows for their gradual dissociation from the NP surface with the assistance of the organic MOF linkers. Thus, direct chemical interactions can be built between NP and MOF, generating a clean and well-defined interface. Combined with conventional techniques, we revealed the relative orientation and facet alignment at NP-MOF interfaces.

We have built a solid understanding of how various MOF components affect the catalytic selectivity catalyzed at the NP-MOF interface. We systematically elucidated how the identity of the ligands and metal-oxo nodes of UiO-66 affects the hydrogenation of cinnamaldehyde. Ligand

functionalization of the MOF linker caused minor changes in the catalytic selectivity for the desired unsaturated alcohol. The replacement of inorganic nodes from Zr-oxo nodes to Ce-oxo nodes, on the other hand, greatly enhanced the selectivity. Infrared spectroscopic observations suggest that the interaction of the C=O group with the Ce-oxo node plays an important role in the enhanced hydrogenation of this bond. We show the critical role of metal-oxo nodes in regulating the catalytic selectivity of metal NPs in specific reactions. The understanding established in this work lays the foundation for further optimization of MOF-based heterogeneous catalyst design.

By extending the concept to other catalysis systems, we have discovered unconventional catalytic behaviors in catalysts confined in MOF microcrystals. Using the catalase enzyme as the model system, we demonstrated that chemical interactions between enzymes and MOFs are critical to maintaining the biological functions of confined enzymes. By systemically tuning the structure of MOF crystals, we observed that the enzymes gradually changed from a confined form in the solid MOF crystals to a freestanding form sealed inside of the central cavity of the hollow MOF crystals. The freestanding enzymes in the hollow MOFs show higher activity, attributed to their lesser chemical interactions and confinement. This study highlights the importance of the freestanding state for the biological function of encapsulated enzymes and presents a new way to immobilize freestanding enzymes in MOFs.

Our achievements in this thesis have established design rules for engineering microenvironments around active sites of catalysts using crystalline MOFs. The spectroscopic protocols established in this thesis allow the study of complicated hybrid interfaces, providing further details on the key MOF component in catalytic performance. Here, we propose some possible directions that may further define important bricks in the foundation for further refining MOF-based heterogeneous catalyst design.

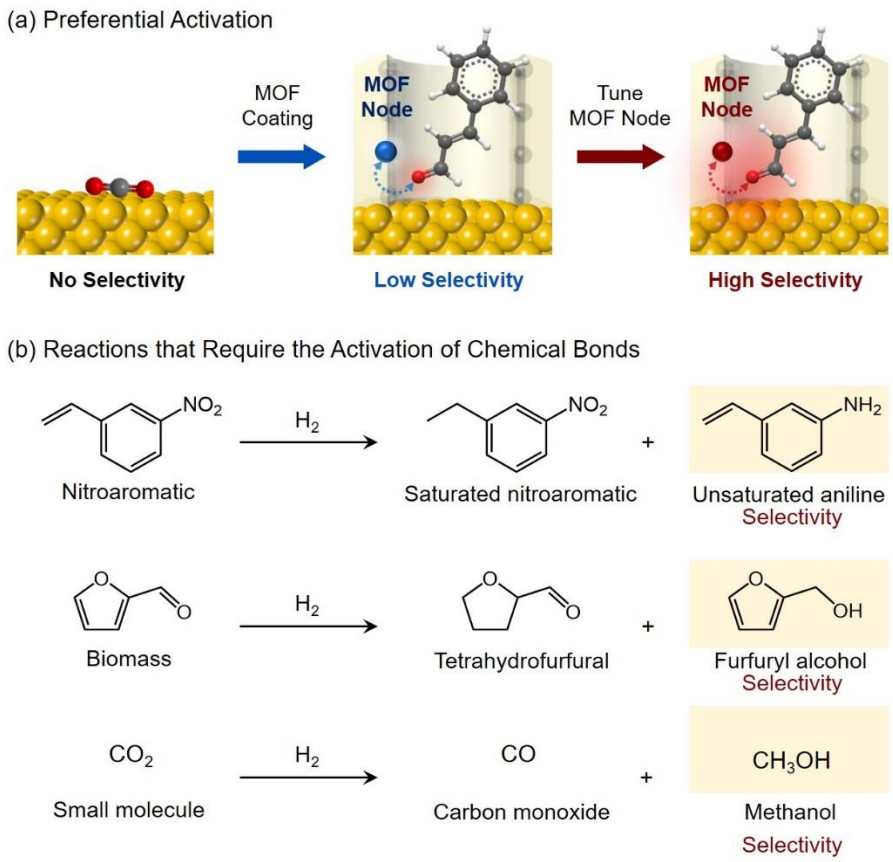

Figure 6.1: Schematic illustration of (a) tuning the identity of metal-oxo nodes to promote the hydrogenation of C=O bonds and (b) three energy-related conversions whereas the catalytic selectivity could be promoted by activating chemical bonds.

We envision an increased focus on exploring broadly the mechanisms that can promote the performance over a wide range of important chemical transformations. For example, we have shown the metal-oxo node plays an important role in the enhanced hydrogenation of C=O bonds (**Figure 6.1**). The activation relies on the identity of the nodes and can potentially benefit several energy-related conversions, such as selective biomass activation, selective hydrogenation of nitroaromatics, and the activation of small molecules. Recently, we have observed that CO_2 molecules favor the bend configuration at the NP-MOF interface.[69, 252] The mechanistic picture of the critical components of this CO_2 activation is unclear. Still, we estimate the outcome of this

mechanistic picture to modify the configuration of intermediates at the NP-MOF interface can broadly influence many challenging reactions, such as the direct C-H carboxylation. Building on the plausible mechanistic pictures, we expect an increased focus on designing well-controlled microenvironments by tuning organic linker ligands, inorganic nodes, and pore structures to promote catalytic performance.

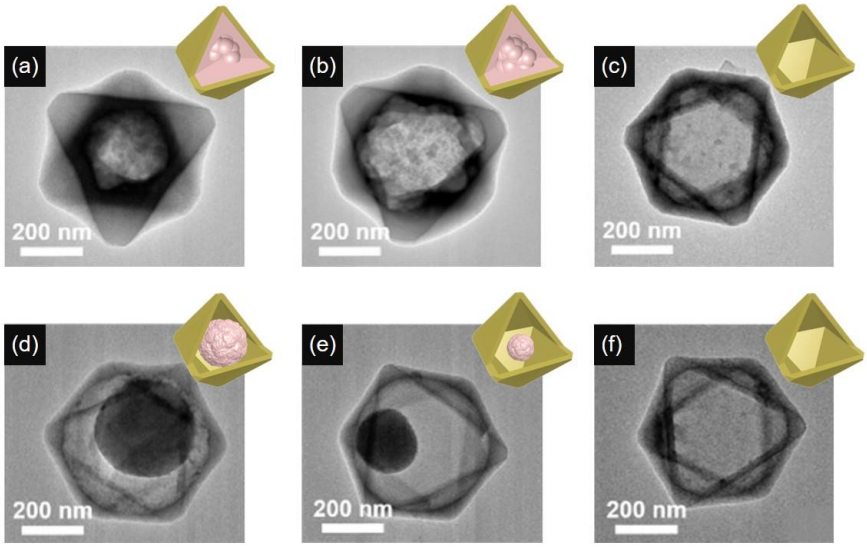

Figure 6.2: TEM images of the core-shell MOF microcrystal with the core consisting of radical-labile ligands etched by HNO_3 for different times, (a): 5 h, (b): 10 h, (c): 24 h. or by reactive oxygen species for different times, (d): 0.5 h, (e): 1.0 h, (f): 1.5 h. Figure adapted from ref. [194]

Beyond the heterogeneous catalysis, we predict the increased observation of unconventional catalytic behaviors in catalysts confined in MOF microcrystals. For example, we have expanded the same concept to enhance the stability of DNA-based hybrid catalysts (DNAzymes).[253] The composite catalyst survived heating at high temperature, exposure to Exonuclease I, and incubation in organic solvents, whereas free DNAzymes were denatured in all cases. Lastly, we expect synthetic methods developed in this thesis could allow precise control over hierarchical structures in the MOF microcrystals (**Figure 6.2**). For example, we have developed a directional engraving process to realize the hierarchical control in the MOF

microcrystals.[194] We presented the oxidative linker cleavage process for selective breakage in single-crystalline MOF microcrystals. By regulating the diffusion of oxidative species, the MOF microcrystals undergo divergent etching routes, producing a series of single-crystalline hollow and yolk−shell MOF structures. The broader impact of this thesis is expected to be the advancement of material design to control chemical catalysis through a tailored microenvironment around the active sites of catalysts.

References

1. Lo, W.-S.; Chou, L.-Y.; Young, A. P.; Ren, C.; Goh, T. W.; Williams, B. P.; Li, Y.; Chen, S.-Y.; Ismail, M. N.; Huang, W.; Tsung, C.-K., Probing the Interface between Encapsulated Nanoparticles and Metal–Organic Frameworks for Catalytic Selectivity Control. *Chemistry of Materials* **2021,** *33* (6), 1946-1953.
2. Li, Y.; Lo, W.-S.; Zhang, F.; Si, X.; Chou, L.-Y.; Liu, X.-Y.; Williams, B. P.; Li, Y.-H.; Jung, S.-H.; Hsu, Y.-S.; Liao, F.-S.; Shieh, F.-K.; Ismail, M. N.; Huang, W.; Tsung, C.-K., Creating an Aligned Interface between Nanoparticles and MOFs by Concurrent Replacement of Capping Agents. *Journal of the American Chemical Society* **2021,** *143* (13), 5182-5190.
3. Chen, S.-Y.; Lo, W.-S.; Huang, Y.-D.; Si, X.; Liao, F.-S.; Lin, S.-W.; Williams, B. P.; Sun, T.-Q.; Lin, H.-W.; An, Y.; Sun, T.; Ma, Y.; Yang, H.-C.; Chou, L.-Y.; Shieh, F.-K.; Tsung, C.-K., Probing Interactions between Metal–Organic Frameworks and Freestanding Enzymes in a Hollow Structure. *Nano Letters* **2020,** *20* (9), 6630-6635.
4. Recognizing the Best in Innovation: Breakthrough Catalyst. *R&D Magazine* 2005.
5. Lindström, B.; Pettersson, L. J., A Brief History of Catalysis. *CATTECH* **2003,** *7* (4), 130-138.
6. Schlögl, R., Heterogeneous Catalysis. *Angewandte Chemie International Edition* **2015,** *54* (11), 3465-3520.
7. Zaera, F., Mechanisms of hydrocarbon conversion reactions on heterogeneous catalysts: analogies with organometallic chemistry. *Topics in Catalysis* **2005,** *34* (1), 129-141.
8. Wisniak, J., The History of Catalysis. From the Beginning to Nobel Prizes. *Educación Química* **2010,** *21* (1), 60-69.
9. Taylor, H., Paul Sabatier 1854-1941. *Journal of the American Chemical Society* **1944,** *66* (10), 1615-1617.
10. Berl, E., Fritz Haber. *Journal of Chemical Education* **1937,** *14* (5), 203.
11. Taylor, H., Fifty Years of Chemical Kineticists. *Annual Review of Physical Chemistry* **1962,** *13* (1), 1-19.
12. Langmuir, I., The Adsorption of Gases on Plane Surfaces of Glass, Mica and Platinum. *Journal of the American Chemical Society* **1918,** *40* (9), 1361-1403.

13. George, S. M., Introduction: Heterogeneous Catalysis. *Chemical Reviews* **1995,** *95* (3), 475-476.
14. Goodman, D. W., Model Studies in Catalysis Using Surface Science Probes. *Chemical Reviews* **1995,** *95* (3), 523-536.
15. Weckhuysen, B. M., Determining the active site in a catalytic process: Operando spectroscopy is more than a buzzword. *Physical Chemistry Chemical Physics* **2003,** *5* (20), 4351-4360.
16. Kang, H. C.; Weinberg, W. H., Modeling the Kinetics of Heterogeneous Catalysis. *Chemical Reviews* **1995,** *95* (3), 667-676.
17. Sattler, J. J. H. B.; Ruiz-Martinez, J.; Santillan-Jimenez, E.; Weckhuysen, B. M., Catalytic Dehydrogenation of Light Alkanes on Metals and Metal Oxides. *Chemical Reviews* **2014,** *114* (20), 10613-10653.
18. Bariås, O. A.; Holmen, A.; Blekkan, E. A., Propane Dehydrogenation over Supported Pt and Pt–Sn Catalysts: Catalyst Preparation, Characterization, and Activity Measurements. *Journal of Catalysis* **1996,** *158* (1), 1-12.
19. Monai, M.; Gambino, M.; Wannakao, S.; Weckhuysen, B. M., Propane to olefins tandem catalysis: a selective route towards light olefins production. *Chemical Society Reviews* **2021,** *50* (20), 11503-11529.
20. Shaffer, C. Catalytic Converter Recycling Is Still Big Business.
21. De Yoreo, J.; Mandrus, D.; Soderholm, L.; Forbes, T.; Kanatzidis, M.; Erlebacher, J.; Laskin, J.; Wiesner, U.; Xu, T.; Billinge, S.; Tolbert, S.; Zaworotko, M.; Galli, G.; Chan, J.; Mitchell, J.; Horton, L.; Kini, A.; Gersten, B.; Maracas, G.; Miranda, R.; Pechan, M.; Runkles, K. *Basic Research Needs Workshop on Synthesis Science for Energy Relevant Technology*; United States, 2016; p Medium: ED; Size: 178 p.
22. Mallat, T.; Baiker, A., Selectivity enhancement in heterogeneous catalysis induced by reaction modifiers. *Applied Catalysis A: General* **2000,** *200* (1), 3-22.
23. Lindlar, H., Ein neuer Katalysator für selektive Hydrierungen. *Helvetica Chimica Acta* **1952,** *35* (2), 446-450.
24. McEwen, A. B.; Guttieri, M. J.; Maier, W. F.; Laine, R. M.; Shvo, Y., Metallic palladium, the actual catalyst in Lindlar and Rosenmund reductions? *The Journal of Organic Chemistry* **1983,** *48* (23), 4436-4438.

25. García-Mota, M.; Gómez-Díaz, J.; Novell-Leruth, G.; Vargas-Fuentes, C.; Bellarosa, L.; Bridier, B.; Pérez-Ramírez, J.; López, N., A density functional theory study of the 'mythic' Lindlar hydrogenation catalyst. *Theoretical Chemistry Accounts* **2011,** *128* (4), 663-673.
26. Hutchings, G. J., Promotion in Heterogeneous Catalysis: A Topic Requiring a New Approach? *Catalysis Letters* **2001,** *75* (1), 1-12.
27. Aika, K.-I.; Ozaki, A., Kinetics and isotope effect of ammonia synthesis over a singly-promoted iron catalyst. *Journal of Catalysis* **1970,** *19* (3), 350-352.
28. Huang, J.; He, S.; Goodsell, J. L.; Mulcahy, J. R.; Guo, W.; Angerhofer, A.; Wei, W. D., Manipulating Atomic Structures at the Au/TiO2 Interface for O2 Activation. *Journal of the American Chemical Society* **2020,** *142* (14), 6456-6460.
29. Kim, J.; Sarma, B. B.; Andrés, E.; Pfänder, N.; Concepción, P.; Prieto, G., Surface Lewis Acidity of Periphery Oxide Species as a General Kinetic Descriptor for CO_2 Hydrogenation to Methanol on Supported Copper Nanoparticles. *ACS Catalysis* **2019,** *9* (11), 10409-10417.
30. Graciani, J.; Mudiyanselage, K.; Xu, F.; Baber, A. E.; Evans, J.; Senanayake, S. D.; Stacchiola, D. J.; Liu, P.; Hrbek, J.; Sanz, J. F.; Rodriguez, J. A., Highly active copper-ceria and copper-ceria-titania catalysts for methanol synthesis from CO_2. *Science* **2014,** *345* (6196), 546-550.
31. Noh, G.; Lam, E.; Bregante, D. T.; Meyet, J.; Šot, P.; Flaherty, D. W.; Copéret, C., Lewis Acid Strength of Interfacial Metal Sites Drives CH_3OH Selectivity and Formation Rates on Cu-Based CO_2 Hydrogenation Catalysts. *Angewandte Chemie International Edition* **2021,** *60* (17), 9650-9659.
32. Noh, G.; Lam, E.; Alfke, J. L.; Larmier, K.; Searles, K.; Wolf, P.; Copéret, C., Selective Hydrogenation of CO_2 to CH_3OH on Supported Cu Nanoparticles Promoted by Isolated TiIV Surface Sites on SiO_2. *ChemSusChem* **2019,** *12* (5), 968-972.
33. Wang, Y.; Qin, R.; Wang, Y.; Ren, J.; Zhou, W.; Li, L.; Ming, J.; Zhang, W.; Fu, G.; Zheng, N., Chemoselective Hydrogenation of Nitroaromatics at the Nanoscale Iron(III)–OH–Platinum Interface. *Angewandte Chemie International Edition* **2020,** *59* (31), 12736-12740.

34. Altenburg, K.; Bosch, H.; Van Ommen, J. G.; Gellings, P. J., The role of potassium as a promoter in iron catalysts for ammonia synthesis. *Journal of Catalysis* **1980,** *66* (2), 326-334.

35. Akira, T.; Motomasa, I.; Toshihiko, O.; Hiroshi, W., Synthesis of Optically Active Common Precursors of Sex Pheromone of Pine Sawfiles: An Application of Enatioface-Differentiating Hydrogenation with Modified Nickel. *Chemistry Letters* **1978,** *7* (1), 61-64.

36. Bürgi, T.; Baiker, A., Heterogeneous Enantioselective Hydrogenation over Cinchona Alkaloid Modified Platinum: Mechanistic Insights into a Complex Reaction. *Accounts of Chemical Research* **2004,** *37* (11), 909-917.

37. Meemken, F.; Maeda, N.; Hungerbühler, K.; Baiker, A., Platinum-Catalyzed Asymmetric Hydrogenation: Spectroscopic Evidence for an O-H-O Hydrogen-Bond Interaction between Substrate and Modifier. *Angewandte Chemie International Edition* **2012,** *51* (33), 8212-8216.

38. Meemken, F.; Hungerbühler, K.; Baiker, A., Monitoring Surface Processes During Heterogeneous Asymmetric Hydrogenation of Ketones on a Chirally Modified Platinum Catalyst by Operando Spectroscopy. *Angewandte Chemie International Edition* **2014,** *53* (33), 8640-8644.

39. Schoenbaum, C. A.; Schwartz, D. K.; Medlin, J. W., Controlling the Surface Environment of Heterogeneous Catalysts Using Self-Assembled Monolayers. *Accounts of Chemical Research* **2014,** *47* (4), 1438-1445.

40. Pang, S. H.; Schoenbaum, C. A.; Schwartz, D. K.; Medlin, J. W., Directing reaction pathways by catalyst active-site selection using self-assembled monolayers. *Nature Communications* **2013,** *4* (1), 2448.

41. Kahsar, K. R.; Schwartz, D. K.; Medlin, J. W., Control of Metal Catalyst Selectivity through Specific Noncovalent Molecular Interactions. *Journal of the American Chemical Society* **2014,** *136* (1), 520-526.

42. Wu, B.; Huang, H.; Yang, J.; Zheng, N.; Fu, G., Selective Hydrogenation of α,β-Unsaturated Aldehydes Catalyzed by Amine-Capped Platinum-Cobalt Nanocrystals. *Angewandte Chemie International Edition* **2012,** *51* (14), 3440-3443.

43. Kwon, S. G.; Krylova, G.; Sumer, A.; Schwartz, M. M.; Bunel, E. E.; Marshall, C. L.; Chattopadhyay, S.; Lee, B.; Jellinek, J.; Shevchenko, E. V., Capping Ligands as Selectivity Switchers in Hydrogenation Reactions. *Nano Letters* **2012,** *12* (10), 5382-5388.
44. Lee, S.; Shin, S.-J.; Baek, H.; Choi, Y.; Hyun, K.; Seo, M.; Kim, K.; Koh, D.-Y.; Kim, H.; Choi, M., Dynamic metal-polymer interaction for the design of chemoselective and long-lived hydrogenation catalysts. *Science Advances* **2020,** *6* (28), eabb7369.
45. Hyun, K.; Park, Y.; Lee, S.; Lee, J.; Choi, Y.; Shin, S.-J.; Kim, H.; Choi, M., Tailoring a Dynamic Metal–Polymer Interaction to Improve Catalyst Selectivity and Longevity in Hydrogenation. *Angewandte Chemie International Edition* **2021,** *60* (22), 12482-12489.
46. Earl, D. J.; Deem, M. W., Toward a Database of Hypothetical Zeolite Structures. *Ind. Eng. Chem. Res.* **2006,** *45* (16), 5449-5454.
47. Muraoka, K.; Sada, Y.; Miyazaki, D.; Chaikittisilp, W.; Okubo, T., Linking synthesis and structure descriptors from a large collection of synthetic records of zeolite materials. *Nat. Commun.* **2019,** *10* (1), 4459.
48. Wang, C.; Liu, D.; Lin, W., Metal–Organic Frameworks as A Tunable Platform for Designing Functional Molecular Materials. *J. Am. Chem. Soc.* **2013,** *135* (36), 13222-13234.
49. Canlas, C. P.; Lu, J.; Ray, N. A.; Grosso-Giordano, N. A.; Lee, S.; Elam, J. W.; Winans, R. E.; Van Duyne, R. P.; Stair, P. C.; Notestein, J. M., Shape-selective sieving layers on an oxide catalyst surface. *Nat. Chem.* **2012,** *4* (12), 1030-1036.
50. Li, H.; Eddaoudi, M.; O'Keeffe, M.; Yaghi, O. M., Design and synthesis of an exceptionally stable and highly porous metal-organic framework. *Nature* **1999,** *402*, 276.
51. Stock, N.; Biswas, S., Synthesis of Metal-Organic Frameworks (MOFs): Routes to Various MOF Topologies, Morphologies, and Composites. *Chem. Rev.* **2012,** *112* (2), 933-969.
52. Zhou, H. C.; Long, J. R.; Yaghi, O. M., Introduction to metal–organic frameworks. *Chem. Rev.* **2012,** *112*, 673-674.
53. Deng, H.; Doonan, C. J.; Furukawa, H.; Ferreira, R. B.; Towne, J.; Knobler, C. B.; Wang, B.; Yaghi, O. M., Multiple Functional Groups of Varying Ratios in Metal-Organic Frameworks. *Science* **2010,** *327* (5967), 846-850.
54. Deng, H.; Grunder, S.; Cordova, K. E.; Valente, C.; Furukawa, H.; Hmadeh, M.; Gándara, F.; Whalley, A. C.; Liu, Z.; Asahina, S.; Kazumori, H.; O'Keeffe, M.; Terasaki, O.;

Stoddart, J. F.; Yaghi, O. M., Large-Pore Apertures in a Series of Metal-Organic Frameworks. *Science* **2012,** *336* (6084), 1018-1023.

55. Rungtaweevoranit, B.; Baek, J.; Araujo, J. R.; Archanjo, B. S.; Choi, K. M.; Yaghi, O. M.; Somorjai, G. A., Copper Nanocrystals Encapsulated in Zr-based Metal–Organic Frameworks for Highly Selective CO_2 Hydrogenation to Methanol. *Nano Letters* **2016,** *16* (12), 7645-7649.
56. Zhang, W.; Zheng, B.; Shi, W.; Chen, X.; Xu, Z.; Li, S.; Chi, Y. R.; Yang, Y.; Lu, J.; Huang, W.; Huo, F., Site-Selective Catalysis of a Multifunctional Linear Molecule: The Steric Hindrance of Metal–Organic Framework Channels. *Advanced Materials* **2018,** *30* (23), 1800643.
57. Na, K.; Choi, K. M.; Yaghi, O. M.; Somorjai, G. A., Metal Nanocrystals Embedded in Single Nanocrystals of MOFs Give Unusual Selectivity as Heterogeneous Catalysts. *Nano Letters* **2014,** *14* (10), 5979-5983.
58. Choi, K. M.; Na, K.; Somorjai, G. A.; Yaghi, O. M., Chemical Environment Control and Enhanced Catalytic Performance of Platinum Nanoparticles Embedded in Nanocrystalline Metal–Organic Frameworks. *Journal of the American Chemical Society* **2015,** *137* (24), 7810-7816.
59. Sabyrov, K.; Jiang, J.; Yaghi, O. M.; Somorjai, G. A., Hydroisomerization of n-Hexane Using Acidified Metal–Organic Framework and Platinum Nanoparticles. *J. Am. Chem. Soc.* **2017,** *139* (36), 12382-12385.
60. Stephenson, C. J.; Hupp, J. T.; Farha, O. K., Postassembly Transformation of a Catalytically Active Composite Material, Pt@ZIF-8, via Solvent-Assisted Linker Exchange. *Inorg. Chem.* **2016,** *55* (4), 1361-1363.
61. Guo, Z.; Xiao, C.; Maligal-Ganesh, R. V.; Zhou, L.; Goh, T. W.; Li, X.; Tesfagaber, D.; Thiel, A.; Huang, W., Pt Nanoclusters Confined within Metal–Organic Framework Cavities for Chemoselective Cinnamaldehyde Hydrogenation. *ACS Catalysis* **2014,** *4* (5), 1340-1348.
62. Wu, H. Q.; Huang, L.; Li, J. Q.; Zheng, A. M.; Tao, Y.; Yang, L. X.; Yin, W. H.; Luo, F., Pd@Zn-MOF-74: Restricting a Guest Molecule by the Open-Metal Site in a Metal–Organic Framework for Selective Semihydrogenation. *Inorg. Chem.* **2018,** *57* (20), 12444-12447.

63. Li, X.; Goh, T. W.; Li, L.; Xiao, C.; Guo, Z.; Zeng, X. C.; Huang, W., Controlling Catalytic Properties of Pd Nanoclusters through Their Chemical Environment at the Atomic Level Using Isoreticular Metal–Organic Frameworks. *ACS Catalysis* **2016,** *6* (6), 3461-3468.

64. Goh, T. W.; Tsung, C.-K.; Huang, W., Spectroscopy Identification of the Bimetallic Surface of Metal–Organic Framework-Confined Pt–Sn Nanoclusters with Enhanced Chemoselectivity in Furfural Hydrogenation. *Acs Appl. Mater. Interfaces* **2019,** *11* (26), 23254-23260.

65. Yang, Q.; Xu, Q.; Yu, S.-H.; Jiang, H.-L., Pd Nanocubes@ZIF-8: Integration of Plasmon-Driven Photothermal Conversion with a Metal–Organic Framework for Efficient and Selective Catalysis. *Angew. Chem. Int. Ed.* **2016,** *55* (11), 3685-3689.

66. Liu, H.; Chang, L.; Bai, C.; Chen, L.; Luque, R.; Li, Y., Controllable Encapsulation of "Clean" Metal Clusters within MOFs through Kinetic Modulation: Towards Advanced Heterogeneous Nanocatalysts. *Angewandte Chemie International Edition* **2016,** *55* (16), 5019-5023.

67. Li, Z.; Yu, R.; Huang, J.; Shi, Y.; Zhang, D.; Zhong, X.; Wang, D.; Wu, Y.; Li, Y., Platinum–nickel frame within metal-organic framework fabricated in situ for hydrogen enrichment and molecular sieving. *Nat. Commun.* **2015,** *6* (1), 8248.

68. Stephenson, C. J.; Whitford, C. L.; Stair, P. C.; Farha, O. K.; Hupp, J. T., Chemoselective Hydrogenation of Crotonaldehyde Catalyzed by an Au@ZIF-8 Composite. *ChemCatChem* **2016,** *8* (4), 855-860.

69. Lee, H. K.; Lee, Y. H.; Morabito, J. V.; Liu, Y.; Koh, C. S. L.; Phang, I. Y.; Pedireddy, S.; Han, X.; Chou, L.-Y.; Tsung, C.-K.; Ling, X. Y., Driving CO_2 to a Quasi-Condensed Phase at the Interface between a Nanoparticle Surface and a Metal–Organic Framework at 1 bar and 298 K. *Journal of the American Chemical Society* **2017,** *139* (33), 11513-11518.

70. Hu, P.; Morabito, J. V.; Tsung, C.-K., Core–Shell Catalysts of Metal Nanoparticle Core and Metal–Organic Framework Shell. *ACS Catalysis* **2014,** *4* (12), 4409-4419.

71. Kuo, C.-H.; Tang, Y.; Chou, L.-Y.; Sneed, B. T.; Brodsky, C. N.; Zhao, Z.; Tsung, C.-K., Yolk–Shell Nanocrystal@ZIF-8 Nanostructures for Gas-Phase Heterogeneous Catalysis with Selectivity Control. *Journal of the American Chemical Society* **2012,** *134* (35), 14345-14348.

72. Lee, H. K.; Koh, C. S. L.; Lee, Y. H.; Liu, C.; Phang, I. Y.; Han, X.; Tsung, C.-K.; Ling, X. Y., Favoring the unfavored: Selective electrochemical nitrogen fixation using a reticular chemistry approach. *Science Advances* **2018,** *4* (3), eaar3208.

73. Hu, P.; Zhuang, J.; Chou, L.-Y.; Lee, H. K.; Ling, X. Y.; Chuang, Y.-C.; Tsung, C.-K., Surfactant-Directed Atomic to Mesoscale Alignment: Metal Nanocrystals Encased Individually in Single-Crystalline Porous Nanostructures. *Journal of the American Chemical Society* **2014,** *136* (30), 10561-10564.

74. Yang, L.-X.; Wu, H.-Q.; Gao, H.-Y.; Li, J.-Q.; Tao, Y.; Yin, W.-H.; Luo, F., Hybrid Catalyst of a Metal–Organic Framework, Metal Nanoparticles, and Oxide That Enables Strong Steric Constraint and Metal–Support Interaction for the Highly Effective and Selective Hydrogenation of Cinnamaldehyde. *Inorganic Chemistry* **2018,** *57* (20), 12461-12465.

75. Hou, C.; Zhao, G.; Ji, Y.; Niu, Z.; Wang, D.; Li, Y., Hydroformylation of alkenes over rhodium supported on the metal-organic framework ZIF-8. *Nano Research* **2014,** *7* (9), 1364-1369.

76. Wang, B.; Liu, W.; Zhang, W.; Liu, J., Nanoparticles@nanoscale metal-organic framework composites as highly efficient heterogeneous catalysts for size- and shape-selective reactions. *Nano Research* **2017,** *10* (11), 3826-3835.

77. Tian, Z.; Chen, D.-L.; He, T.; Yang, P.; Wang, F.-F.; Zhong, Y.; Zhu, W., Theoretical Evidence on the Confinement Effect of Pt@UiO-66-NH_2 for Cinnamaldehyde Hydrogenation. *The Journal of Physical Chemistry C* **2019,** *123* (36), 22114-22122.

78. Chen, X.; Shen, K.; Ding, D.; Chen, J.; Fan, T.; Wu, R.; Li, Y., Solvent-Driven Selectivity Control to Either Anilines or Dicyclohexylamines in Hydrogenation of Nitroarenes over a Bifunctional Pd/MIL-101 Catalyst. *ACS Catal.* **2018,** *8* (11), 10641-10648.

79. Long, Y.; Song, S.; Li, J.; Wu, L.; Wang, Q.; Liu, Y.; Jin, R.; Zhang, H., Pt/CeO_2@MOF Core@Shell Nanoreactor for Selective Hydrogenation of Furfural via the Channel Screening Effect. *ACS Catal.* **2018,** *8* (9), 8506-8512.

80. Chen, L.; Zhan, W.; Fang, H.; Cao, Z.; Yuan, C.; Xie, Z.; Kuang, Q.; Zheng, L., Selective Catalytic Performances of Noble Metal Nanoparticle@MOF Composites: The Concomitant Effect of Aperture Size and Structural Flexibility of MOF Matrices. *Chem, Eur. J.* **2017,** *23* (47), 11397-11403.

81. Zhang, N.; Shao, Q.; Wang, P.; Zhu, X.; Huang, X., Porous Pt-Ni Nanowires within In Situ Generated Metal-Organic Frameworks for Highly Chemoselective Cinnamaldehyde Hydrogenation. *Small* **2018,** *14* (19), 1704318.

82. Zhao, M.; Yuan, K.; Wang, Y.; Li, G.; Guo, J.; Gu, L.; Hu, W.; Zhao, H.; Tang, Z., Metal–organic frameworks as selectivity regulators for hydrogenation reactions. *Nature* **2016,** *539*, 76.

83. Zhu, Y.; Zheng, J.; Ye, J.; Cui, Y.; Koh, K.; Kovarik, L.; Camaioni, D. M.; Fulton, J. L.; Truhlar, D. G.; Neurock, M.; Cramer, C. J.; Gutiérrez, O. Y.; Lercher, J. A., Copper-zirconia interfaces in UiO-66 enable selective catalytic hydrogenation of CO_2 to methanol. *Nature Communications* **2020,** *11* (1), 5849.

84. Gutterød, E. S.; Lazzarini, A.; Fjermestad, T.; Kaur, G.; Manzoli, M.; Bordiga, S.; Svelle, S.; Lillerud, K. P.; Skúlason, E.; Øien-Ødegaard, S.; Nova, A.; Olsbye, U., Hydrogenation of CO_2 to Methanol by Pt Nanoparticles Encapsulated in UiO-67: Deciphering the Role of the Metal–Organic Framework. *Journal of the American Chemical Society* **2020,** *142* (2), 999-1009.

85. Gutterød, E. S.; Pulumati, S. H.; Kaur, G.; Lazzarini, A.; Solemsli, B. G.; Gunnæs, A. E.; Ahoba-Sam, C.; Kalyva, M. E.; Sannes, J. A.; Svelle, S.; Skúlason, E.; Nova, A.; Olsbye, U., Influence of Defects and H_2O on the Hydrogenation of CO_2 to Methanol over Pt Nanoparticles in UiO-67 Metal–Organic Framework. *Journal of the American Chemical Society* **2020,** *142* (40), 17105-17118.

86. Aijaz, A.; Karkamkar, A.; Choi, Y. J.; Tsumori, N.; Rönnebro, E.; Autrey, T.; Shioyama, H.; Xu, Q., Immobilizing Highly Catalytically Active Pt Nanoparticles inside the Pores of Metal–Organic Framework: A Double Solvents Approach. *Journal of the American Chemical Society* **2012,** *134* (34), 13926-13929.

87. Lu, G.; Li, S.; Guo, Z.; Farha, O. K.; Hauser, B. G.; Qi, X.; Wang, Y.; Wang, X.; Han, S.; Liu, X.; DuChene, J. S.; Zhang, H.; Zhang, Q.; Chen, X.; Ma, J.; Loo, S. C. J.; Wei, W. D.; Yang, Y.; Hupp, J. T.; Huo, F., Imparting functionality to a metal–organic framework material by controlled nanoparticle encapsulation. *Nat Chem* **2012,** *4* (4), 310-316.

88. Astruc, D.; Lu, F.; Aranzaes, J. R., Nanoparticles as Recyclable Catalysts: The Frontier between Homogeneous and Heterogeneous Catalysis. *Angewandte Chemie International Edition* **2005,** *44* (48), 7852-7872.

89. Gross, E.; Liu, J. H.-C.; Toste, F. D.; Somorjai, G. A., Control of selectivity in heterogeneous catalysis by tuning nanoparticle properties and reactor residence time. *Nature Chemistry* **2012,** *4* (11), 947-952.
90. Liu, P.; Qin, R.; Fu, G.; Zheng, N., Surface Coordination Chemistry of Metal Nanomaterials. *Journal of the American Chemical Society* **2017,** *139* (6), 2122-2131.
91. Marshall, S. T.; O'Brien, M.; Oetter, B.; Corpuz, A.; Richards, R. M.; Schwartz, D. K.; Medlin, J. W., Controlled selectivity for palladium catalysts using self-assembled monolayers. *Nature Materials* **2010,** *9* (10), 853-858.
92. Zhang, J.; Ellis, L. D.; Wang, B.; Dzara, M. J.; Sievers, C.; Pylypenko, S.; Nikolla, E.; Medlin, J. W., Control of interfacial acid–metal catalysis with organic monolayers. *Nature Catalysis* **2018,** *1* (2), 148-155.
93. Choe, K.; Zheng, F.; Wang, H.; Yuan, Y.; Zhao, W.; Xue, G.; Qiu, X.; Ri, M.; Shi, X.; Wang, Y.; Li, G.; Tang, Z., Fast and Selective Semihydrogenation of Alkynes by Palladium Nanoparticles Sandwiched in Metal–Organic Frameworks. *Angewandte Chemie International Edition* **2020,** *59* (9), 3650-3657.
94. Tong, Y.; Xue, G.; Wang, H.; Liu, M.; Wang, J.; Hao, C.; Zhang, X.; Wang, D.; Shi, X.; Liu, W.; Li, G.; Tang, Z., Interfacial coupling between noble metal nanoparticles and metal–organic frameworks for enhanced catalytic activity. *Nanoscale* **2018,** *10* (35), 16425-16430.
95. Zhao, M.; Deng, K.; He, L.; Liu, Y.; Li, G.; Zhao, H.; Tang, Z., Core–Shell Palladium Nanoparticle@Metal–Organic Frameworks as Multifunctional Catalysts for Cascade Reactions. *Journal of the American Chemical Society* **2014,** *136* (5), 1738-1741.
96. Chen, G.; Xu, C.; Huang, X.; Ye, J.; Gu, L.; Li, G.; Tang, Z.; Wu, B.; Yang, H.; Zhao, Z.; Zhou, Z.; Fu, G.; Zheng, N., Interfacial electronic effects control the reaction selectivity of platinum catalysts. *Nature Materials* **2016,** *15* (5), 564-569.
97. Chen, L.; Luque, R.; Li, Y., Controllable design of tunable nanostructures inside metal–organic frameworks. *Chemical Society Reviews* **2017,** *46* (15), 4614-4630.
98. Delbecq, F.; Sautet, P., Competitive C=C and C=O Adsorption of α-β-Unsaturated Aldehydes on Pt and Pd Surfaces in Relation with the Selectivity of Hydrogenation Reactions: A Theoretical Approach. *Journal of Catalysis* **1995,** *152* (2), 217-236.

99. Gomez-Gualdron, D. A.; Dix, S. T.; Getman, R. B.; Snurr, R. Q., A modelling approach for MOF-encapsulated metal catalysts and application to n-butane oxidation. *Physical Chemistry Chemical Physics* **2015,** *17* (41), 27596-27608.

100. Schweitzer, B.; Archuleta, C.; Seong, B.; Anderson, R.; Gómez-Gualdrón, D. A., Electronic effects due to organic linker-metal surface interactions: implications on screening of MOF-encapsulated catalysts. *Physical Chemistry Chemical Physics* **2020,** *22* (4), 2475-2487.

101. Yang, Q.; Xu, Q.; Jiang, H.-L., Metal–organic frameworks meet metal nanoparticles: synergistic effect for enhanced catalysis. *Chemical Society Reviews* **2017,** *46* (15), 4774-4808.

102. Li, G.; Zhao, S.; Zhang, Y.; Tang, Z., Metal–Organic Frameworks Encapsulating Active Nanoparticles as Emerging Composites for Catalysis: Recent Progress and Perspectives. *Advanced Materials* **2018,** *30* (51), 1800702.

103. Zhang, W.; Lu, G.; Cui, C.; Liu, Y.; Li, S.; Yan, W.; Xing, C.; Chi, Y. R.; Yang, Y.; Huo, F., A Family of Metal-Organic Frameworks Exhibiting Size-Selective Catalysis with Encapsulated Noble-Metal Nanoparticles. *Advanced Materials* **2014,** *26* (24), 4056-4060.

104. Jiang, H.-L.; Liu, B.; Akita, T.; Haruta, M.; Sakurai, H.; Xu, Q., Au@ZIF-8: CO Oxidation over Gold Nanoparticles Deposited to Metal−Organic Framework. *Journal of the American Chemical Society* **2009,** *131* (32), 11302-11303.

105. Li, X.; Goh, T. W.; Xiao, C.; Stanton, A. L. D.; Pei, Y.; Jain, P. K.; Huang, W., Synthesis of Monodisperse Palladium Nanoclusters Using Metal–Organic Frameworks as Sacrificial Templates. *ChemNanoMat* **2016,** *2* (8), 810-815.

106. Cavka, J. H.; Jakobsen, S.; Olsbye, U.; Guillou, N.; Lamberti, C.; Bordiga, S.; Lillerud, K. P., A New Zirconium Inorganic Building Brick Forming Metal Organic Frameworks with Exceptional Stability. *Journal of the American Chemical Society* **2008,** *130* (42), 13850-13851.

107. Chen, L.; Chen, H.; Luque, R.; Li, Y., Metal−organic framework encapsulated Pd nanoparticles: towards advanced heterogeneous catalysts. *Chemical Science* **2014,** *5* (10), 3708-3714.

108. Li, X.; Guo, Z.; Xiao, C.; Goh, T. W.; Tesfagaber, D.; Huang, W., Tandem Catalysis by Palladium Nanoclusters Encapsulated in Metal–Organic Frameworks. *ACS Catalysis* **2014,** *4* (10), 3490-3497.

109. Aoyama, Y.; Kobayashi, H.; Yamamoto, T.; Toriyama, T.; Matsumura, S.; Haneda, M.; Kitagawa, H., Significantly enhanced CO oxidation activity induced by a change in the CO adsorption site on Pd nanoparticles covered with metal–organic frameworks. *Chemical Communications* **2020,** *56* (27), 3839-3842.

110. Wu, L.; Lian, H.; Willis, J. J.; Goodman, E. D.; McKay, I. S.; Qin, J.; Tassone, C. J.; Cargnello, M., Tuning Precursor Reactivity toward Nanometer-Size Control in Palladium Nanoparticles Studied by in Situ Small Angle X-ray Scattering. *Chemistry of Materials* **2018,** *30* (3), 1127-1135.

111. Wang, W.; Wang, Z.; Wang, J.; Zhong, C.-J.; Liu, C.-J., Highly Active and Stable Pt–Pd Alloy Catalysts Synthesized by Room-Temperature Electron Reduction for Oxygen Reduction Reaction. *Advanced Science* **2017,** *4* (4), 1600486.

112. Kuhn, J. N.; Tsung, C.-K.; Huang, W.; Somorjai, G. A., Effect of organic capping layers over monodisperse platinum nanoparticles upon activity for ethylene hydrogenation and carbon monoxide oxidation. *Journal of Catalysis* **2009,** *265* (2), 209-215.

113. Zhu, Q.-L.; Li, J.; Xu, Q., Immobilizing Metal Nanoparticles to Metal–Organic Frameworks with Size and Location Control for Optimizing Catalytic Performance. *Journal of the American Chemical Society* **2013,** *135* (28), 10210-10213.

114. Planas, N.; Mondloch, J. E.; Tussupbayev, S.; Borycz, J.; Gagliardi, L.; Hupp, J. T.; Farha, O. K.; Cramer, C. J., Defining the Proton Topology of the Zr6-Based Metal–Organic Framework NU-1000. *The Journal of Physical Chemistry Letters* **2014,** *5* (21), 3716-3723.

115. Hollins, P.; Pritchard, J., Infrared studies of chemisorbed layers on single crystals. *Progress in Surface Science* **1985,** *19* (4), 275-349.

116. Unterhalt, H.; Rupprechter, G.; Freund, H.-J., Vibrational Sum Frequency Spectroscopy on Pd(111) and Supported Pd Nanoparticles: CO Adsorption from Ultrahigh Vacuum to Atmospheric Pressure. *The Journal of Physical Chemistry B* **2002,** *106* (2), 356-367.

117. Krebs, H. J.; Lüth, H., Evidence for two different adsorption sites of CO on Pt(111) from infrared reflection spectroscopy. *Applied physics* **1977,** *14* (4), 337-342.

118. Primet, M., Electronic transfer and ligand effects in the infrared spectra of adsorbed carbon monoxide. *Journal of Catalysis* **1984,** *88* (2), 273-282.

119. Koczkur, K. M.; Mourdikoudis, S.; Polavarapu, L.; Skrabalak, S. E., Polyvinylpyrrolidone (PVP) in nanoparticle synthesis. *Dalton Transactions* **2015,** *44* (41), 17883-17905.

120. Pastoriza-Santos, I.; Liz-Marzán, L. M., Formation of PVP-Protected Metal Nanoparticles in DMF. *Langmuir* **2002,** *18* (7), 2888-2894.

121. Zheng, Z.; Xu, H.; Xu, Z.; Ge, J., A Monodispersed Spherical Zr-Based Metal–Organic Framework Catalyst, Pt/Au@Pd@UIO-66, Comprising an Au@Pd Core–Shell Encapsulated in a UIO-66 Center and Its Highly Selective CO_2 Hydrogenation to Produce CO. *Small* **2018,** *14* (5), 1702812.

122. Nalbant Esenturk, E.; Hight Walker, A. R., Surface-enhanced Raman scattering spectroscopy via gold nanostars. *Journal of Raman Spectroscopy* **2009,** *40* (1), 86-91.

123. Ren, M.; Jin, Y.; Chen, W.; Huang, W., Rich Capping Ligand–Ag Colloid Interactions. *The Journal of Physical Chemistry C* **2015,** *119* (49), 27588-27593.

124. Baker, L. R.; Kennedy, G.; Van Spronsen, M.; Hervier, A.; Cai, X.; Chen, S.; Wang, L.-W.; Somorjai, G. A., Furfuraldehyde Hydrogenation on Titanium Oxide-Supported Platinum Nanoparticles Studied by Sum Frequency Generation Vibrational Spectroscopy: Acid–Base Catalysis Explains the Molecular Origin of Strong Metal–Support Interactions. *Journal of the American Chemical Society* **2012,** *134* (34), 14208-14216.

125. Rossi, L. M.; Fiorio, J. L.; Garcia, M. A. S.; Ferraz, C. P., The role and fate of capping ligands in colloidally prepared metal nanoparticle catalysts. *Dalton Transactions* **2018,** *47* (17), 5889-5915.

126. Lan, X.; Huang, N.; Wang, J.; Wang, T., Geometric effect in the highly selective hydrogenation of 3-methylcrotonaldehyde over Pt@ZIF-8 core–shell catalysts. *Catalysis Science & Technology* **2017,** *7* (12), 2601-2608.

127. Yuan, K.; Song, T.; Wang, D.; Zhang, X.; Gao, X.; Zou, Y.; Dong, H.; Tang, Z.; Hu, W., Effective and Selective Catalysts for Cinnamaldehyde Hydrogenation: Hydrophobic Hybrids of Metal–Organic Frameworks, Metal Nanoparticles, and Micro- and Mesoporous Polymers. *Angewandte Chemie International Edition* **2018,** *57* (20), 5708-5713.

128. de Jesús, J. C.; Zaera, F., Adsorption and thermal chemistry of acrolein and crotonaldehyde on Pt(111) surfaces. *Surface Science* **1999,** *430* (1), 99-115.

129. Galvagno, S.; Capannelli, G.; Neri, G.; Donato, A.; Pietropaolo, R., Hydrogenation of cinnamaldehyde over Ru/C catalysts: effect of Ru particle size. *Journal of Molecular Catalysis* **1991,** *64* (2), 237-246.

130. Englisch, M.; Jentys, A.; Lercher, J. A., Structure Sensitivity of the Hydrogenation of Crotonaldehyde over Pt/SiO2and Pt/TiO2. *Journal of Catalysis* **1997,** *166* (1), 25-35.

131. Qiu, X.; Zhong, W.; Bai, C.; Li, Y., Encapsulation of a Metal–Organic Polyhedral in the Pores of a Metal–Organic Framework. *Journal of the American Chemical Society* **2016,** *138* (4), 1138-1141.

132. Qin, X.; He, S.; Wu, J.; Fan, Y.; Wang, F.; Zhang, S.; Li, S.; Luo, L.; Ma, Y.; Lee, Y.; Li, T., Tracking and Visualization of Functional Domains in Stratified Metal–Organic Frameworks Using Gold Nanoparticles. *ACS Central Science* **2020,** *6* (2), 247-253.

133. Tsung, C.-K.; Kuhn, J. N.; Huang, W.; Aliaga, C.; Hung, L.-I.; Somorjai, G. A.; Yang, P., Sub-10 nm Platinum Nanocrystals with Size and Shape Control: Catalytic Study for Ethylene and Pyrrole Hydrogenation. *Journal of the American Chemical Society* **2009,** *131* (16), 5816-5822.

134. Kimling, J.; Maier, M.; Okenve, B.; Kotaidis, V.; Ballot, H.; Plech, A., Turkevich Method for Gold Nanoparticle Synthesis Revisited. *The Journal of Physical Chemistry B* **2006,** *110* (32), 15700-15707.

135. Choi, K. M.; Jeong, H. M.; Park, J. H.; Zhang, Y.-B.; Kang, J. K.; Yaghi, O. M., Supercapacitors of Nanocrystalline Metal–Organic Frameworks. *ACS Nano* **2014,** *8* (7), 7451-7457.

136. Nützenadel, C.; Züttel, A.; Chartouni, D.; Schmid, G.; Schlapbach, L., Critical size and surface effect of the hydrogen interaction of palladium clusters. *The European Physical Journal D* **2000,** *8* (2), 245-250.

137. Yoo, H.; Engelke, R.; Carr, S.; Fang, S.; Zhang, K.; Cazeaux, P.; Sung, S. H.; Hovden, R.; Tsen, A. W.; Taniguchi, T.; Watanabe, K.; Yi, G.-C.; Kim, M.; Luskin, M.; Tadmor, E. B.; Kaxiras, E.; Kim, P., Atomic and electronic reconstruction at the van der Waals interface in twisted bilayer graphene. *Nature Materials* **2019,** *18* (5), 448-453.

138. Zhu, Y.; Ciston, J.; Zheng, B.; Miao, X.; Czarnik, C.; Pan, Y.; Sougrat, R.; Lai, Z.; Hsiung, C.-E.; Yao, K.; Pinnau, I.; Pan, M.; Han, Y., Unravelling surface and interfacial structures

of a metal–organic framework by transmission electron microscopy. *Nature Materials* **2017,** *16* (5), 532-536.

139. Grancini, G.; Roldán-Carmona, C.; Zimmermann, I.; Mosconi, E.; Lee, X.; Martineau, D.; Narbey, S.; Oswald, F.; De Angelis, F.; Graetzel, M.; Nazeeruddin, M. K., One-Year stable perovskite solar cells by 2D/3D interface engineering. *Nature Communications* **2017,** *8* (1), 15684.
140. Shi, E.; Yuan, B.; Shiring, S. B.; Gao, Y.; Akriti; Guo, Y.; Su, C.; Lai, M.; Yang, P.; Kong, J.; Savoie, B. M.; Yu, Y.; Dou, L., Two-dimensional halide perovskite lateral epitaxial heterostructures. *Nature* **2020,** *580* (7805), 614-620.
141. Luo, Y.; Li, J.; Liu, X.; Tan, L.; Cui, Z.; Feng, X.; Yang, X.; Liang, Y.; Li, Z.; Zhu, S.; Zheng, Y.; Yeung, K. W. K.; Yang, C.; Wang, X.; Wu, S., Dual Metal–Organic Framework Heterointerface. *ACS Central Science* **2019,** *5* (9), 1591-1601.
142. Falcaro, P.; Okada, K.; Hara, T.; Ikigaki, K.; Tokudome, Y.; Thornton, Aaron W.; Hill, Anita J.; Williams, T.; Doonan, C.; Takahashi, M., Centimetre-scale micropore alignment in oriented polycrystalline metal–organic framework films via heteroepitaxial growth. *Nature Materials* **2017,** *16* (3), 342-348.
143. Jiang, Y.; Song, Y.; Li, Y.; Tian, W.; Pan, Z.; Yang, P.; Li, Y.; Gu, Q.; Hu, L., Charge Transfer in Ultrafine LDH Nanosheets/Graphene Interface with Superior Capacitive Energy Storage Performance. *ACS Applied Materials & Interfaces* **2017,** *9* (43), 37645-37654.
144. Hou, J.; Wang, Z.; Chen, P.; Chen, V.; Cheetham, A. K.; Wang, L., Intermarriage of Halide Perovskites and Metal-Organic Framework Crystals. *Angewandte Chemie International Edition* **2020,** *59* (44), 19434-19449.
145. Chen, Y.-Z.; Wang, Z. U.; Wang, H.; Lu, J.; Yu, S.-H.; Jiang, H.-L., Singlet Oxygen-Engaged Selective Photo-Oxidation over Pt Nanocrystals/Porphyrinic MOF: The Roles of Photothermal Effect and Pt Electronic State. *Journal of the American Chemical Society* **2017,** *139* (5), 2035-2044.
146. Chen, D.; Yang, W.; Jiao, L.; Li, L.; Yu, S.-H.; Jiang, H.-L., Boosting Catalysis of Pd Nanoparticles in MOFs by Pore Wall Engineering: The Roles of Electron Transfer and Adsorption Energy. *Advanced Materials* **2020,** *32* (30), 2000041.

147. Zhu, Q.-L.; Xu, Q., Metal–organic framework composites. *Chemical Society Reviews* **2014,** *43* (16), 5468-5512.

148. Niu, Z.; Li, Y., Removal and Utilization of Capping Agents in Nanocatalysis. *Chemistry of Materials* **2014,** *26* (1), 72-83.

149. Lopez-Sanchez, J. A.; Dimitratos, N.; Hammond, C.; Brett, G. L.; Kesavan, L.; White, S.; Miedziak, P.; Tiruvalam, R.; Jenkins, R. L.; Carley, A. F.; Knight, D.; Kiely, C. J.; Hutchings, G. J., Facile removal of stabilizer-ligands from supported gold nanoparticles. *Nature Chemistry* **2011,** *3* (7), 551-556.

150. Park, K. S.; Ni, Z.; Côté, A. P.; Choi, J. Y.; Huang, R.; Uribe-Romo, F. J.; Chae, H. K.; O'Keeffe, M.; Yaghi, O. M., Exceptional chemical and thermal stability of zeolitic imidazolate frameworks. *Proceedings of the National Academy of Sciences* **2006,** *103* (27), 10186-10191.

151. Alkilany, A. M.; Nagaria, P. K.; Wyatt, M. D.; Murphy, C. J., Cation Exchange on the Surface of Gold Nanorods with a Polymerizable Surfactant: Polymerization, Stability, and Toxicity Evaluation. *Langmuir* **2010,** *26* (12), 9328-9333.

152. Lee, S.; Anderson, L. J. E.; Payne, C. M.; Hafner, J. H., Structural Transition in the Surfactant Layer that Surrounds Gold Nanorods as Observed by Analytical Surface-Enhanced Raman Spectroscopy. *Langmuir* **2011,** *27* (24), 14748-14756.

153. Merrill, N. A.; Sethi, M.; Knecht, M. R., Structural and Equilibrium Effects of the Surface Passivant on the Stability of Au Nanorods. *ACS Applied Materials & Interfaces* **2013,** *5* (16), 7906-7914.

154. Sau, T. K.; Murphy, C. J., Room Temperature, High-Yield Synthesis of Multiple Shapes of Gold Nanoparticles in Aqueous Solution. *Journal of the American Chemical Society* **2004,** *126* (28), 8648-8649.

155. Niu, W.; Li, Z.-Y.; Shi, L.; Liu, X.; Li, H.; Han, S.; Chen, J.; Xu, G., Seed-Mediated Growth of Nearly Monodisperse Palladium Nanocubes with Controllable Sizes. *Crystal Growth & Design* **2008,** *8* (12), 4440-4444.

156. Song, J. H.; Kim, F.; Kim, D.; Yang, P., Crystal Overgrowth on Gold Nanorods: Tuning the Shape, Facet, Aspect Ratio, and Composition of the Nanorods. *Chemistry – A European Journal* **2005,** *11* (3), 910-916.

157. Zaera, F., New advances in the use of infrared absorption spectroscopy for the characterization of heterogeneous catalytic reactions. *Chemical Society Reviews* **2014,** *43* (22), 7624-7663.

158. Eischens, R. P.; Pliskin, W. A.; Francis, S. A., Infrared Spectra of Chemisorbed Carbon Monoxide. *The Journal of Chemical Physics* **1954,** *22* (10), 1786-1787.

159. Hammer, B.; Morikawa, Y.; Nørskov, J. K., CO Chemisorption at Metal Surfaces and Overlayers. *Physical Review Letters* **1996,** *76* (12), 2141-2144.

160. Blyholder, G., Molecular Orbital View of Chemisorbed Carbon Monoxide. *The Journal of Physical Chemistry* **1964,** *68* (10), 2772-2777.

161. Whitford, C. L.; Stephenson, C. J.; Gómez-Gualdrón, D. A.; Hupp, J. T.; Farha, O. K.; Snurr, R. Q.; Stair, P. C., Elucidating the Nanoparticle–Metal Organic Framework Interface of Pt@ZIF-8 Catalysts. *The Journal of Physical Chemistry C* **2017,** *121* (45), 25079-25091.

162. Giorgi, J. B.; Schroeder, T.; Bäumer, M.; Freund, H.-J., Study of CO adsorption on crystalline-silica-supported palladium particles. *Surface Science* **2002,** *498* (1), L71-L77.

163. Talley, C. E.; Jackson, J. B.; Oubre, C.; Grady, N. K.; Hollars, C. W.; Lane, S. M.; Huser, T. R.; Nordlander, P.; Halas, N. J., Surface-Enhanced Raman Scattering from Individual Au Nanoparticles and Nanoparticle Dimer Substrates. *Nano Letters* **2005,** *5* (8), 1569-1574.

164. Boca, S. C.; Astilean, S., Detoxification of gold nanorods by conjugation with thiolated poly(ethylene glycol) and their assessment as SERS-active carriers of Raman tags. *Nanotechnology* **2010,** *21* (23), 235601.

165. Nikoobakht, B.; El-Sayed, M. A., Surface-Enhanced Raman Scattering Studies on Aggregated Gold Nanorods. *The Journal of Physical Chemistry A* **2003,** *107* (18), 3372-3378.

166. Carter, D. A.; Pemberton, J. E., Raman spectroscopy and vibrational assignments of 1- and 2-methylimidazole. *Journal of Raman Spectroscopy* **1997,** *28* (12), 939-946.

167. Carter, D. A.; Pemberton, J. E.; Woelfel, K. J., Orientation of 1- and 2-Methylimidazole on Silver Electrodes Determined with Surface-Enhanced Raman Scattering. *The Journal of Physical Chemistry B* **1998,** *102* (49), 9870-9880.

168. Carter, D. A.; Pemberton, J. E., Surface-enhanced Raman scattering of the acid-base forms of imidazole on silver. *Langmuir* **1992,** *8* (4), 1218-1225.

169. Venna, S. R.; Jasinski, J. B.; Carreon, M. A., Structural Evolution of Zeolitic Imidazolate Framework-8. *Journal of the American Chemical Society* **2010,** *132* (51), 18030-18033.

170. Bharathiraja, S.; Bui, N. Q.; Manivasagan, P.; Moorthy, M. S.; Mondal, S.; Seo, H.; Phuoc, N. T.; Vy Phan, T. T.; Kim, H.; Lee, K. D.; Oh, J., Multimodal tumor-homing chitosan oligosaccharide-coated biocompatible palladium nanoparticles for photo-based imaging and therapy. *Scientific Reports* **2018,** *8* (1), 500.

171. Bai, Y.; Dou, Y.; Xie, L.-H.; Rutledge, W.; Li, J.-R.; Zhou, H.-C., Zr-based metal–organic frameworks: design, synthesis, structure, and applications. *Chemical Society Reviews* **2016,** *45* (8), 2327-2367.

172. Kandiah, M.; Nilsen, M. H.; Usseglio, S.; Jakobsen, S.; Olsbye, U.; Tilset, M.; Larabi, C.; Quadrelli, E. A.; Bonino, F.; Lillerud, K. P., Synthesis and Stability of Tagged UiO-66 Zr-MOFs. *Chemistry of Materials* **2010,** *22* (24), 6632-6640.

173. Huang, Y.-H.; Lo, W.-S.; Kuo, Y.-W.; Chen, W.-J.; Lin, C.-H.; Shieh, F.-K., Green and rapid synthesis of zirconium metal–organic frameworks via mechanochemistry: UiO-66 analog nanocrystals obtained in one hundred seconds. *Chemical Communications* **2017,** *53* (43), 5818-5821.

174. Zhang, F.; Hu, X.; Roth, E. W.; Kim, Y.; Nguyen, S. T., Template-Assisted, Seed-Mediated Synthesis of Hierarchically Mesoporous Core–Shell UiO-66: Enhancing Adsorption Capacity and Catalytic Activity through Iterative Growth. *Chemistry of Materials* **2020,** *32* (10), 4292-4302.

175. Kwon, K. C.; Kim, B. J.; Lee, J.-L.; Kim, S. Y., Effect of anions in Au complexes on doping and degradation of graphene. *Journal of Materials Chemistry C* **2013,** *1* (13), 2463-2469.

176. Corma, A.; Concepción, P.; Domínguez, I.; Forné, V.; Sabater, M. J., Gold supported on a biopolymer (chitosan) catalyzes the regioselective hydroamination of alkynes. *Journal of Catalysis* **2007,** *251* (1), 39-47.

177. Gallezot, P.; Richard, D., Selective Hydrogenation of α,β-Unsaturated Aldehydes. *Catalysis Reviews* **1998,** *40* (1-2), 81-126.

178. Ide, M. S.; Hao, B.; Neurock, M.; Davis, R. J., Mechanistic Insights on the Hydrogenation of α,β-Unsaturated Ketones and Aldehydes to Unsaturated Alcohols over Metal Catalysts. *ACS Catalysis* **2012,** *2* (4), 671-683.

179. van Deelen, T. W.; Hernández Mejía, C.; de Jong, K. P., Control of metal-support interactions in heterogeneous catalysts to enhance activity and selectivity. *Nature Catalysis* **2019,** *2* (11), 955-970.

180. Chen, G.; Zhao, Y.; Fu, G.; Duchesne, P. N.; Gu, L.; Zheng, Y.; Weng, X.; Chen, M.; Zhang, P.; Pao, C.-W.; Lee, J.-F.; Zheng, N., Interfacial Effects in Iron-Nickel Hydroxide–Platinum Nanoparticles Enhance Catalytic Oxidation. *Science* **2014,** *344* (6183), 495-499.

181. Kennedy, G.; Baker, L. R.; Somorjai, G. A., Selective Amplification of C□O Bond Hydrogenation on Pt/TiO2: Catalytic Reaction and Sum-Frequency Generation Vibrational Spectroscopy Studies of Crotonaldehyde Hydrogenation. *Angewandte Chemie International Edition* **2014,** *53* (13), 3405-3408.

182. Makosch, M.; Lin, W.-I.; Bumbálek, V.; Sá, J.; Medlin, J. W.; Hungerbühler, K.; van Bokhoven, J. A., Organic Thiol Modified Pt/TiO2 Catalysts to Control Chemoselective Hydrogenation of Substituted Nitroarenes. *ACS Catalysis* **2012,** *2* (10), 2079-2081.

183. Kahsar, K. R.; Schwartz, D. K.; Medlin, J. W., Selective Hydrogenation of Polyunsaturated Fatty Acids Using Alkanethiol Self-Assembled Monolayer-Coated Pd/Al2O3 Catalysts. *ACS Catalysis* **2013,** *3* (9), 2041-2044.

184. Chen, L.; Xu, Q., Metal-Organic Framework Composites for Catalysis. *Matter* **2019,** *1* (1), 57-89.

185. Shen, Y.; Pan, T.; Wang, L.; Ren, Z.; Zhang, W.; Huo, F., Programmable Logic in Metal–Organic Frameworks for Catalysis. *Advanced Materials* **2021,** *33* (46), 2007442.

186. Jiao, L.; Wang, J.; Jiang, H.-L., Microenvironment Modulation in Metal–Organic Framework-Based Catalysis. *Accounts of Materials Research* **2021,** *2* (5), 327-339.

187. Kim, C. R.; Uemura, T.; Kitagawa, S., Inorganic nanoparticles in porous coordination polymers. *Chemical Society Reviews* **2016,** *45* (14), 3828-3845.

188. Young, L. B.; Butter, S. A.; Kaeding, W. W., Shape selective reactions with zeolite catalysts: III. Selectivity in xylene isomerization, toluene-methanol alkylation, and toluene disproportionation over ZSM-5 zeolite catalysts. *J. Catal.* **1982,** *76* (2), 418-432.

189. Ogiwara, N.; Kobayashi, H.; Inukai, M.; Nishiyama, Y.; Concepción, P.; Rey, F.; Kitagawa, H., Ligand-Functionalization-Controlled Activity of Metal–Organic

Framework-Encapsulated Pt Nanocatalyst toward Activation of Water. *Nano Letters* **2020,** *20* (1), 426-432.

190. Zhang, W.; Ji, W.; Li, L.; Qin, P.; Khalil, I. E.; Gu, Z.; Wang, P.; Li, H.; Fan, Y.; Ren, Z.; Shen, Y.; Zhang, W.; Fu, Y.; Huo, F., Exploring the Fundamental Roles of Functionalized Ligands in Platinum@Metal–Organic Framework Catalysts. *ACS Applied Materials & Interfaces* **2020,** *12* (47), 52660-52667.

191. Zhang, W.; Shi, W.; Ji, W.; Wu, H.; Gu, Z.; Wang, P.; Li, X.; Qin, P.; Zhang, J.; Fan, Y.; Wu, T.; Fu, Y.; Zhang, W.; Huo, F., Microenvironment of MOF Channel Coordination with Pt NPs for Selective Hydrogenation of Unsaturated Aldehydes. *ACS Catalysis* **2020,** *10* (10), 5805-5813.

192. Li, L.; Li, Z.; Yang, W.; Huang, Y.; Huang, G.; Guan, Q.; Dong, Y.; Lu, J.; Yu, S.-H.; Jiang, H.-L., Integration of Pd nanoparticles with engineered pore walls in MOFs for enhanced catalysis. *Chem* **2021,** *7* (3), 686-698.

193. Yuan, S.; Qin, J.-S.; Lollar, C. T.; Zhou, H.-C., Stable Metal–Organic Frameworks with Group 4 Metals: Current Status and Trends. *ACS Central Science* **2018,** *4* (4), 440-450.

194. Luo, L.; Lo, W.-S.; Si, X.; Li, H.; Wu, Y.; An, Y.; Zhu, Q.; Chou, L.-Y.; Li, T.; Tsung, C.-K., Directional Engraving within Single Crystalline Metal–Organic Framework Particles via Oxidative Linker Cleaving. *Journal of the American Chemical Society* **2019,** *141* (51), 20365-20370.

195. Lammert, M.; Wharmby, M. T.; Smolders, S.; Bueken, B.; Lieb, A.; Lomachenko, K. A.; Vos, D. D.; Stock, N., Cerium-based metal organic frameworks with UiO-66 architecture: synthesis, properties and redox catalytic activity. *Chemical Communications* **2015,** *51* (63), 12578-12581.

196. Wasson, M. C.; Otake, K.-i.; Gong, X.; Strathman, A. R.; Islamoglu, T.; Gianneschi, N. C.; Farha, O. K., Modulation of crystal growth and structure within cerium-based metal–organic frameworks. *CrystEngComm* **2020,** *22* (47), 8182-8188.

197. Cheng, G.; Jentys, A.; Gutiérrez, O. Y.; Liu, Y.; Chin, Y.-H.; Lercher, J. A., Critical role of solvent-modulated hydrogen-binding strength in the catalytic hydrogenation of benzaldehyde on palladium. *Nature Catalysis* **2021,** *4* (11), 976-985.

198. Zhu, S.; Qin, X.; Yao, Y.; Shao, M., pH-Dependent Hydrogen and Water Binding Energies on Platinum Surfaces as Directly Probed through Surface-Enhanced Infrared Absorption Spectroscopy. *Journal of the American Chemical Society* **2020,** *142* (19), 8748-8754.
199. Candy, J.-P.; Fouilloux, P.; Primet, M., Adsorption d'hydrogène entre 300 et 873 K sur un catalyseur Pt/MgO. *Surface Science* **1978,** *72* (1), 167-176.
200. Baró, A. M.; Ibach, H.; Bruchmann, H. D., Vibrational modes of hydrogen adsorbed on Pt(111): Adsorption site and excitation mechanism. *Surface Science* **1979,** *88* (2), 384-398.
201. Dan-Hardi, M.; Serre, C.; Frot, T.; Rozes, L.; Maurin, G.; Sanchez, C.; Férey, G., A New Photoactive Crystalline Highly Porous Titanium(IV) Dicarboxylate. *Journal of the American Chemical Society* **2009,** *131* (31), 10857-10859.
202. Kuchler, A.; Yoshimoto, M.; Luginbuhl, S.; Mavelli, F.; Walde, P., Enzymatic reactions in confined environments. *Nature Nanotechnology* **2016,** *11* (5), 409-20.
203. DiCosimo, R.; McAuliffe, J.; Poulose, A. J.; Bohlmann, G., Industrial use of immobilized enzymes. *Chemical Society Reviews* **2013,** *42* (15), 6437-6474.
204. Franssen, M. C.; Steunenberg, P.; Scott, E. L.; Zuilhof, H.; Sanders, J. P., Immobilised enzymes in biorenewables production. *Chemical Society Reviews* **2013,** *42* (15), 6491-533.
205. Palla, K. S.; Hurlburt, T. J.; Buyanin, A. M.; Somorjai, G. A.; Francis, M. B., Site-Selective Oxidative Coupling Reactions for the Attachment of Enzymes to Glass Surfaces through DNA-Directed Immobilization. *Journal of the American Chemical Society* **2017,** *139* (5), 1967-1974.
206. Frenkel-Mullerad, H.; Avnir, D., Sol−Gel Materials as Efficient Enzyme Protectors: Preserving the Activity of Phosphatases under Extreme pH Conditions. *Journal of the American Chemical Society* **2005,** *127* (22), 8077-8081.
207. Chapman, R.; Stenzel, M. H., All Wrapped up: Stabilization of Enzymes within Single Enzyme Nanoparticles. *Journal of the American Chemical Society* **2019,** *141* (7), 2754-2769.
208. Sheldon, R. A.; van Pelt, S., Enzyme immobilisation in biocatalysis: why, what and how. *Chemical Society Reviews* **2013,** *42* (15), 6223-6235.
209. Zou, X.; Wei, S.; Badieyan, S.; Schroeder, M.; Jasensky, J.; Brooks, C. L.; Marsh, E. N. G.; Chen, Z., Investigating the Effect of Two-Point Surface Attachment on Enzyme

Stability and Activity. *Journal of the American Chemical Society* **2018,** *140* (48), 16560-16569.

210. Yiu, H. H. P.; Wright, P. A.; Botting, N. P., Enzyme immobilisation using SBA-15 mesoporous molecular sieves with functionalised surfaces. *Journal of Molecular Catalysis B: Enzymatic* **2001,** *15* (1), 81-92.
211. Yan, M.; Ge, J.; Liu, Z.; Ouyang, P., Encapsulation of Single Enzyme in Nanogel with Enhanced Biocatalytic Activity and Stability. *Journal of the American Chemical Society* **2006,** *128* (34), 11008-11009.
212. Mateo, C.; Abian, O.; Fernandez–Lafuente, R.; Guisan, J. M., Increase in conformational stability of enzymes immobilized on epoxy-activated supports by favoring additional multipoint covalent attachment☆. *Enzyme and Microbial Technology* **2000,** *26* (7), 509-515.
213. Hanefeld, U.; Gardossi, L.; Magner, E., Understanding enzyme immobilisation. *Chemical Society Reviews* **2009,** *38* (2), 453-68.
214. Coscolín, C.; Beloqui, A.; Martínez-Martínez, M.; Bargiela, R.; Santiago, G.; Blanco, R. M.; Delaittre, G.; Márquez-Álvarez, C.; Ferrer, M., Controlled manipulation of enzyme specificity through immobilization-induced flexibility constraints. *Applied Catalysis A: General* **2018,** *565*, 59-67.
215. Böhm, A.; Trosien, S.; Avrutina, O.; Kolmar, H.; Biesalski, M., Covalent Attachment of Enzymes to Paper Fibers for Paper-Based Analytical Devices. *Frontiers in Chemistry* **2018,** *6*, 214.
216. Hoarau, M.; Badieyan, S.; Marsh, E. N. G., Immobilized enzymes: understanding enzyme - surface interactions at the molecular level. *Organic & Biomolecular Chemistry* **2017,** *15* (45), 9539-9551.
217. Wang, Z.; Cohen, S. M., Postsynthetic modification of metal–organic frameworks. *Chemical Society Reviews* **2009,** *38* (5), 1315-1329.
218. Kaneti, Y. V.; Dutta, S.; Hossain, M. S. A.; Shiddiky, M. J. A.; Tung, K.-L.; Shieh, F.-K.; Tsung, C.-K.; Wu, K. C.-W.; Yamauchi, Y., Strategies for Improving the Functionality of Zeolitic Imidazolate Frameworks: Tailoring Nanoarchitectures for Functional Applications. *Advanced Materials* **2017,** *29* (38), 1700213.

219. Gumilar, G.; Kaneti, Y. V.; Henzie, J.; Chatterjee, S.; Na, J.; Yuliarto, B.; Nugraha, N.; Patah, A.; Bhaumik, A.; Yamauchi, Y., General synthesis of hierarchical sheet/plate-like M-BDC (M = Cu, Mn, Ni, and Zr) metal–organic frameworks for electrochemical non-enzymatic glucose sensing. *Chemical Science* **2020,** *11* (14), 3644-3655.

220. Lian, X.; Fang, Y.; Joseph, E.; Wang, Q.; Li, J.; Banerjee, S.; Lollar, C.; Wang, X.; Zhou, H. C., Enzyme-MOF (metal-organic framework) composites. *Chemical Society Reviews* **2017,** *46* (11), 3386-3401.

221. Doonan, C.; Ricco, R.; Liang, K.; Bradshaw, D.; Falcaro, P., Metal-Organic Frameworks at the Biointerface: Synthetic Strategies and Applications. *Accounts of Chemical Research* **2017,** *50* (6), 1423-1432.

222. Li, P.; Modica, J. A.; Howarth, A. J.; Vargas, E.; Moghadam, P. Z.; Snurr, R. Q.; Mrksich, M.; Hupp, J. T.; Farha, O. K., Toward design rules for enzyme immobilization in hierarchical mesoporous metal-organic frameworks. *Chem* **2016,** *1* (1), 154-169.

223. Li, P.; Moon, S.-Y.; Guelta, M. A.; Lin, L.; Gómez-Gualdrón, D. A.; Snurr, R. Q.; Harvey, S. P.; Hupp, J. T.; Farha, O. K., Nanosizing a metal–organic framework enzyme carrier for accelerating nerve agent hydrolysis. *ACS nano* **2016,** *10* (10), 9174-9182.

224. Li, P.; Moon, S.-Y.; Guelta, M. A.; Harvey, S. P.; Hupp, J. T.; Farha, O. K., Encapsulation of a Nerve Agent Detoxifying Enzyme by a Mesoporous Zirconium Metal–Organic Framework Engenders Thermal and Long-Term Stability. *Journal of the American Chemical Society* **2016,** *138* (26), 8052-8055.

225. Chen, Y.; Li, P.; Modica, J. A.; Drout, R. J.; Farha, O. K., Acid-Resistant Mesoporous Metal–Organic Framework toward Oral Insulin Delivery: Protein Encapsulation, Protection, and Release. *Journal of the American Chemical Society* **2018,** *140* (17), 5678-5681.

226. Feng, D.; Liu, T.-F.; Su, J.; Bosch, M.; Wei, Z.; Wan, W.; Yuan, D.; Chen, Y.-P.; Wang, X.; Wang, K.; Lian, X.; Gu, Z.-Y.; Park, J.; Zou, X.; Zhou, H.-C., Stable metal-organic frameworks containing single-molecule traps for enzyme encapsulation. *Nature communications* **2015,** *6*, 5979.

227. Lian, X.; Chen, Y.-P.; Liu, T.-F.; Zhou, H.-C., Coupling two enzymes into a tandem nanoreactor utilizing a hierarchically structured MOF. *Chemical Science* **2016,** *7* (12), 6969-6973.

228. Lian, X.; Erazo-Oliveras, A.; Pellois, J.-P.; Zhou, H.-C., High efficiency and long-term intracellular activity of an enzymatic nanofactory based on metal-organic frameworks. *Nature communications* **2017,** *8* (1), 2075.

229. Liang, K.; Ricco, R.; Doherty, C. M.; Styles, M. J.; Bell, S.; Kirby, N.; Mudie, S.; Haylock, D.; Hill, A. J.; Doonan, C. J., Biomimetic mineralization of metal-organic frameworks as protective coatings for biomacromolecules. *Nature communications* **2015,** *6*, 7240.

230. Liang, K.; Coghlan, C. J.; Bell, S. G.; Doonan, C.; Falcaro, P., Enzyme encapsulation in zeolitic imidazolate frameworks: a comparison between controlled co-precipitation and biomimetic mineralisation. *Chemical communications* **2016,** *52* (3), 473-476.

231. Liang, W.; Xu, H.; Carraro, F.; Maddigan, N. K.; Li, Q.; Bell, S. G.; Huang, D. M.; Tarzia, A.; Solomon, M. B.; Amenitsch, H.; Vaccari, L.; Sumby, C. J.; Falcaro, P.; Doonan, C. J., Enhanced Activity of Enzymes Encapsulated in Hydrophilic Metal–Organic Frameworks. *Journal of the American Chemical Society* **2019,** *141* (6), 2348-2355.

232. Liang, W.; Carraro, F.; Solomon, M. B.; Bell, S. G.; Amenitsch, H.; Sumby, C. J.; White, N. G.; Falcaro, P.; Doonan, C. J., Enzyme Encapsulation in a Porous Hydrogen-Bonded Organic Framework. *Journal of the American Chemical Society* **2019,** *141* (36), 14298-14305.

233. Lykourinou, V.; Chen, Y.; Wang, X.-S.; Meng, L.; Hoang, T.; Ming, L.-J.; Musselman, R. L.; Ma, S., Immobilization of MP-11 into a Mesoporous Metal–Organic Framework, MP-11@mesoMOF: A New Platform for Enzymatic Catalysis. *Journal of the American Chemical Society* **2011,** *133* (27), 10382-10385.

234. Chen, Y.; Lykourinou, V.; Vetromile, C.; Hoang, T.; Ming, L.-J.; Larsen, R. W.; Ma, S., How Can Proteins Enter the Interior of a MOF? Investigation of Cytochrome c Translocation into a MOF Consisting of Mesoporous Cages with Microporous Windows. *Journal of the American Chemical Society* **2012,** *134* (32), 13188-13191.

235. Chen, Y.; Han, S.; Li, X.; Zhang, Z.; Ma, S., Why does enzyme not leach from metal–organic frameworks (MOFs)? Unveiling the interactions between an enzyme molecule and a MOF. *Inorganic chemistry* **2014,** *53* (19), 10006-10008.

236. Pan, Y.; Li, H.; Farmakes, J.; Xiao, F.; Chen, B.; Ma, S.; Yang, Z., How Do Enzymes Orient When Trapped on Metal–Organic Framework (MOF) Surfaces? *Journal of the American Chemical Society* **2018,** *140* (47), 16032-16036.

237. Shieh, F.-K.; Wang, S.-C.; Yen, C.-I.; Wu, C.-C.; Dutta, S.; Chou, L.-Y.; Morabito, J. V.; Hu, P.; Hsu, M.-H.; Wu, K. C.-W., Imparting functionality to biocatalysts via embedding enzymes into nanoporous materials by a de novo approach: size-selective sheltering of catalase in metal–organic framework microcrystals. *Journal of the American Chemical Society* **2015,** *137* (13), 4276-4279.

238. Liao, F.-S.; Lo, W.-S.; Hsu, Y.-S.; Wu, C.-C.; Wang, S.-C.; Shieh, F.-K.; Morabito, J. V.; Chou, L.-Y.; Wu, K. C.-W.; Tsung, C.-K., Shielding against Unfolding by Embedding Enzymes in Metal–Organic Frameworks via a de Novo Approach. *Journal of the American Chemical Society* **2017,** *139* (19), 6530-6533.

239. Liu, X. Y.; Zhang, F.; Goh, T. W.; Li, Y.; Shao, Y. C.; Luo, L.; Huang, W.; Long, Y. T.; Chou, L. Y.; Tsung, C. K., Using a Multi-Shelled Hollow Metal–Organic Framework as a Host to Switch the Guest-to-Host and Guest-to-Guest Interactions. *Angewandte Chemie International Edition* **2018,** *130* (8), 2132-2136.

240. Yang, J.; Zhang, F.; Lu, H.; Hong, X.; Jiang, H.; Wu, Y.; Li, Y., Hollow Zn/Co ZIF Particles Derived from Core–Shell ZIF-67@ZIF-8 as Selective Catalyst for the Semi-Hydrogenation of Acetylene. *Angewandte Chemie International Edition* **2015,** *54* (37), 10889-10893.

241. Monera, O. D.; Kay, C. M.; Hodges, R. S., Protein denaturation with guanidine hydrochloride or urea provides a different estimate of stability depending on the contributions of electrostatic interactions. *Protein Science : A Publication of the Protein Society* **1994,** *3* (11), 1984-1991.

242. Vallée-Bélisle, A.; Michnick, S. W., Visualizing transient protein-folding intermediates by tryptophan-scanning mutagenesis. *Nat Struct Mol Biol* **2012,** *19* (7), 731-736.

243. Çetinus, Ş. A.; Öztop, H. N., Immobilization of catalase on chitosan film. *Enzyme and microbial technology* **2000,** *26* (7), 497-501.

244. Ou, P.; Wolff, S. P., A discontinuous method for catalase determination at 'near physiological' concentrations of H2O2 and its application to the study of H_2O_2 fluxes within cells. *Journal of Biochemical and Biophysical Methods* **1996,** *31* (1), 59-67.

245. Aebi, H., Catalase in vitro. In *Methods in Enzymology*, Academic Press: 1984; Vol. 105, pp 121-126.

246. Anderson, J.; Byrne, T.; Woelfel, K. J.; Meany, J. E.; Spyridis, G. T.; Pocker, Y., The Hydrolysis of p-Nitrophenyl Acetate: A Versatile Reaction To Study Enzyme Kinetics. *Journal of Chemical Education* **1994,** *71* (8), 715.

247. Pähler, A.; Banerjee, A.; Dattagupta, J. K.; Fujiwara, T.; Lindner, K.; Pal, G. P.; Suck, D.; Weber, G.; Saenger, W., Three-dimensional structure of fungal proteinase K reveals similarity to bacterial subtilisin. *The EMBO Journal* **1984,** *3* (6), 1311-1314.

248. Tallarida, R. J.; Murray, R. B., Enzyme Kinetics I: Michaelis—Menten Equation. In *Manual of Pharmacologic Calculations: With Computer Programs*, Tallarida, R. J.; Murray, R. B., Eds. Springer New York: New York, NY, 1987; pp 61-63.

249. Lineweaver, H.; Burk, D., The Determination of Enzyme Dissociation Constants. *Journal of the American Chemical Society* **1934,** *56* (3), 658-666.

250. Yang, H.-C.; Yang, C.-H.; Huang, M.-Y.; Lu, J.-F.; Wang, J.-S.; Yeh, Y.-Q.; Jeng, U. S., Homology Modeling and Molecular Dynamics Simulation Combined with X-ray Solution Scattering Defining Protein Structures of Thromboxane and Prostacyclin Synthases. *The Journal of Physical Chemistry B* **2017,** *121* (50), 11229-11240.

251. Kline, S., Reduction and analysis of SANS and USANS data using IGOR Pro. *Journal of Applied Crystallography* **2006,** *39* (6), 895-900.

252. Lee, H. K.; Koh, C. S.; Lo, W.-S.; Liu, Y.; Phang, I. Y.; Sim, H. Y.; Lee, Y. H.; Phan-Quang, G. C.; Han, X.; Tsung, C.-K.; Ling, X. Y., Applying a Nanoparticle@MOF Interface To Activate an Unconventional Regioselectivity of an Inert Reaction at Ambient Conditions. *Journal of the American Chemical Society* **2020,** *142* (26), 11521-11527.

253. Zhong, H.; Lo, W.-S.; Man, T.; Williams, B. P.; Li, D.; Chen, S.-Y.; Pei, H.; Li, L.; Tsung, C.-K., Stabilizing DNAzymes through Encapsulation in a Metal–Organic Framework. *Chemistry – A European Journal* **2020,** *26* (57), 12931-12935.